National Library of Canada
Acquisitions and Bibliographic Services Branch
395 Wellington Street
Ottawa, Ontario
K1A 0N4

Bibliothèque nationale du Canada
Direction des acquisitions et des services bibliographiques
395, rue Wellington
Ottawa (Ontario)
K1A 0N4

Your file Votre référence

Our file Notre référence

NOTICE

The quality of this microform is heavily dependent upon the quality of the original thesis submitted for microfilming. Every effort has been made to ensure the highest quality of reproduction possible.

If pages are missing, contact the university which granted the degree.

Some pages may have indistinct print especially if the original pages were typed with a poor typewriter ribbon or if the university sent us an inferior photocopy.

Reproduction in full or in part of this microform is governed by the Canadian Copyright Act, R.S.C. 1970, c. C-30, and subsequent amendments.

AVIS

La qualité de cette microforme dépend grandement de la qualité de la thèse soumise au microfilmage. Nous avons tout fait pour assurer une qualité supérieure de reproduction.

S'il manque des pages, veuillez communiquer avec l'université qui a conféré le grade.

La qualité d'impression de certaines pages peut laisser à désirer, surtout si les pages originales ont été dactylographiées à l'aide d'un ruban usé ou si l'université nous a fait parvenir une photocopie de qualité inférieure.

La reproduction, même partielle, de cette microforme est soumise à la Loi canadienne sur le droit d'auteur, SRC 1970, c. C-30, et ses amendements subséquents.

Canada

DIFFUSION BONDING OF SILICON CARBIDE AND SILICON NITRIDE TO MOLYBDENUM

Antonio Eduardo Martinelli

Department of Mining and Metallurgical Engineering
McGill University, Montreal

November, 1995

"A thesis submitted to the Faculty of Graduate Studies and Research in partial fulfilment of the requirements of the degree of Ph.D in Metallurgical Engineering"

National Library
of Canada

Acquisitions and
Bibliographic Services Branch

395 Wellington Street
Ottawa, Ontario
K1A 0N4

Bibliothèque nationale
du Canada

Direction des acquisitions et
des services bibliographiques

395, rue Wellington
Ottawa (Ontario)
K1A 0N4

Your file Votre référence

Our file Notre référence

ISBN 0-612-12431-2

Canada

To my devoted parents and wife,

ABSTRACT

This study focuses on various aspects of solid-state diffusion bonding of two ceramic-metal combinations, namely: silicon carbide-molybdenum (SiC-Mo), and silicon nitride-molybdenum (Si_3N_4-Mo). Single SiC-Mo and Si_3N_4-Mo joints were produced using hot-uniaxial pressing. The microstructure of the resulting interfaces were characterized by image analysis, scanning electron microscopy (SEM), electron probe micro-analysis (EPMA), and X-ray diffraction (XRD). The mechanical properties of the joints were investigated using shear strength testing, depth sensing nanoindentation, and neutron diffraction for residual stress measurement.

SiC was solid-state bonded to Mo at temperatures ranging from 1000°C to 1700°C. Diffusion of Si and C into Mo resulted in a reaction layer containing two main phases: Mo_5Si_3 and Mo_2C. At temperatures higher than 1400°C diffusion of C into Mo_5Si_3 stabilized a ternary phase of composition Mo_5Si_3C. At 1700°C, the formation of

MoC_{1-x} was observed as a consequence of bulk diffusion of C into Mo_2C. A maximum average shear strength of 50 MPa was obtained for samples hot-pressed at 1400°C for 1 hour. Higher temperatures and longer times contributed to a reduction in the shear strength of the joints, due to the excessive growth of the interfacial reaction layer. Si_3N_4 was joined to Mo in vacuum and nitrogen, at temperatures between 1000°C and 1800°C, for times varying from 15 minutes to 4 hours. Dissociation of Si_3N_4 and diffusion of Si into Mo resulted in the formation of a reaction layer consisting, initially, of Mo_3Si. At 1600°C (in vacuum) Mo_3Si was partially transformed into Mo_5Si_3 by diffusion of Si into the original silicide, and at higher temperatures, this transformation progressed extensively within the reaction zone. Residual N_2 gas, which originated from the decomposition of Si_3N_4, dissolved in the Mo, however, most of the gas escaped during bonding or remained trapped at the original Si_3N_4-Mo interface, resulting in the formation of a porous layer. Joining in N_2 increased the stability of Si_3N_4, affecting the kinetics of the diffusion bonding process. The bonding environment did not affect the composition and morphology of the interfaces for the partial pressures of N_2 used. A maximum average shear strength of 57 MPa was obtained for samples hot-pressed in vacuum at 1400°C for 1 hour.

RESUME

Le présent travail traite de l'adhésion à diffusion à l'état solide appliquée à deux combinaisons céramique-métal: carbure de silicium-molybdène (SiC-Mo) et nitrure de silicium-molybdène (Si_3N_4-Mo). Des joints simples de SiC-Mo et Si_3N_4-Mo ont été fabriqués en utilisant le pressage uniaxe à haute température. La microstructure des interfaces a été caractérisée à l'aide de l'analyse d'image, balayage électronique, analyse par la microsonde électronique, et la diffraction des rayons X. Les propriétés mécaniques des joints ont été étudiées en analysant la résistance en cisaillement, indentation avec sondage de la profondeur de pénétration, et la diffraction de neutrons pour mesurer les forces résiduelles.

SiC a été lié à Mo à l'état solide à des températures variantes entre 1000°C et 1700°C. La diffusion du Si et du C dans Mo a résulté à une zone de réaction constituée de deux phases: Mo_5Si_3 et Mo_2C. Pour des températures supérieures à 1400°C, la

diffusion du C dans Mo_5Si_3 a stabilisé la phase ternaire de composition Mo_5Si_3C. A 1700°C, la formation de MoC_{1-x} a été observée due à la diffusion en volume du C dans Mo_2C. Une valeur maximale moyenne de la résistance en cisaillement de 50 MPa a été obtenue pour des échantillons fabriqués à 1400°C pour 1 heure. Des températures plus élevées et des temps plus longs ont contribué à la réduction de la force de tondre des joints, due à la croissance excessive de la couche de réaction à l'interface. Si_3N_4 a été joint à Mo sous vide et sous azote dans l'intervalle de température 1000°C - 1800°C pour des temps variants entre 15 minutes et 4 heures. La dissociation du Si_3N_4 et la diffusion du Si au Mo ont causé la formation d'une couche de réaction constituée, initialement, de Mo_3Si. A 1600°C (sous vide) Mo_3Si a été partiellement transformé en Mo_5Si_3 par diffusion du Si envers le siliciure original. À des températures plus élevées, telle transformation a développé considérablement dans la zone de réaction. Le gaz N_2 résiduel, qui est créé de la décomposition du Si_3N_4, a été dissous dans le Mo, cependant, la plus part du gaz a échappé pendant l'adhésion ou a resté piégé a l'interface original du Si_3N_4-Mo, causant la formation d'une membrane poreuse. Le joint sous N_2 a augmenté la stabilité de Si_3N_4, affectant les cinétiques du procès d'adhésion à diffusion. L'environnement de l'adhésion n'a pas affecté la composition et la morphologie de l'interface avec les pressions partielles du N_2 utilisés. Une valeur maximale de la résistance en cisaillement de 57 MPa a été obtenue pour les échantillons pressés sous vide à 1400°C pour 1 heure.

ACKNOWLEDGMENTS

This work was made possible thanks to the support of several individuals and institutions, to whom I wish to express my gratitude. Firstly, I would like to thank the National Research Council of Brazil (CNPq), the Energy and Nuclear Research Institute (IPEN) and Dr. R. Muccillo for the scholarship grant, and the Natural Science and Engineering Research Council of Canada (NSERC) for partially financing this research project.

I would also like to express my appreciation to Atomic Energy of Canada Ltd. (AECL), through Dr. John Root and Mr. Ronald Rogge, for the opportunity to use the NRU facilities in Chalk River, and for all the support in performing neutron diffraction tests. Also, to the Institute for Aerospace Research (IAR), through Dr. Jean-Pierre Immarigeon and Dr. Rhida Berriche, for the nanoindentation analysis; and to Carborundum Co. and Ceradyne Inc. for supplying the ceramic materials used in this

work.

Many thanks to the technical staff at McGill for their indispensable contribution: Mr. Glenn Poirier for the use of the EPMA equipment, and carbon coatings on very short notice; Mrs. Helen Campbell for the helpful hints on SEM imaging; Mr. Martin Knoepfel and the workshop crew for their patience and promptness; and Mr. Luisito "Chito" Edovas for his support with the shear tests, and mainly for bringing to my attention the great American Football.

Finally, I would like to express my gratitude to my supervisor, Professor Robin A.L. Drew, for the guidance and patience throughout this work, and for the opportunity to present this work to the Canadian, American, and Mexican (NAFTA) scientific communities. Also, to the various members of the ceramic group for the valuable discussions, especially when things were not progressing well: Dr. Ali Hadian, Dr. Daniel Muscat, Mr. Majid Entezarian, Mr. Thomas Lebeau, Mr. Mohamed Guermazi, Dr. Youngmin Baik, Dr. Mehdi Allaverdhi, and Ms. Priti Wanjara. Special thanks also go to Mr. Mohamed Guermazi for the translation of the abstract into French. Thanks to you all.

TABLE OF CONTENTS

LIST OF FIGURES

CHAPTER 1:

CHAPTER 2:

CHAPTER 4:

CHAPTER 6:

CHAPTER 7:

LIST OF TABLES

CHAPTER 7:

APPENDIX I:

CHAPTER 1:

INTRODUCTION

During the past few years the use of ceramics in structural applications has gradually increased. Conventional heavy metallic structures have been replaced by lighter ceramic materials, capable of providing high strength as well as good corrosion and wear resistance at high temperatures. Ceramics such as silicon carbide (SiC) and silicon nitride (Si_3N_4) are also able to resist severe mechanical stresses, in the presence of radiation and in chemically hostile environments, particularly at high temperatures, exceeding by far the capabilities of metals. Among the properties

that make SiC and Si_3N_4 suitable for structural applications are low density, high-strength at high temperatures, high modulus of rupture, good wear-resistance, and relatively good oxidation resistance as compared to other high-temperature structural materials, such as nickel and iron based superalloys (Figure 1.1 and Appendix I).

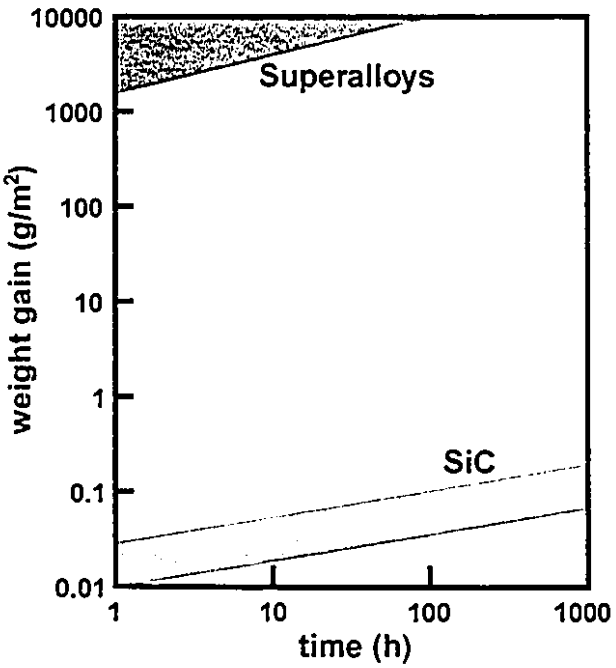

Figure 1.1- Oxidation of SiC and structural Ni-Fe superalloys at 1250°C [1].

Because of this combination of properties, engines and gas-turbines containing Si_3N_4 and SiC parts can operate at higher temperatures with improved thermodynamic combustion efficiency [2,3]. In addition, the use of light materials also represent advantages from the economical point of view. Reducing engine weight enhances fuel economy (Figure 1.2), and decreases the emission of gaseous and particulate pollutants

into the atmosphere: a benefit that helps companies to meet increasingly rigorous environmental regulations [4].

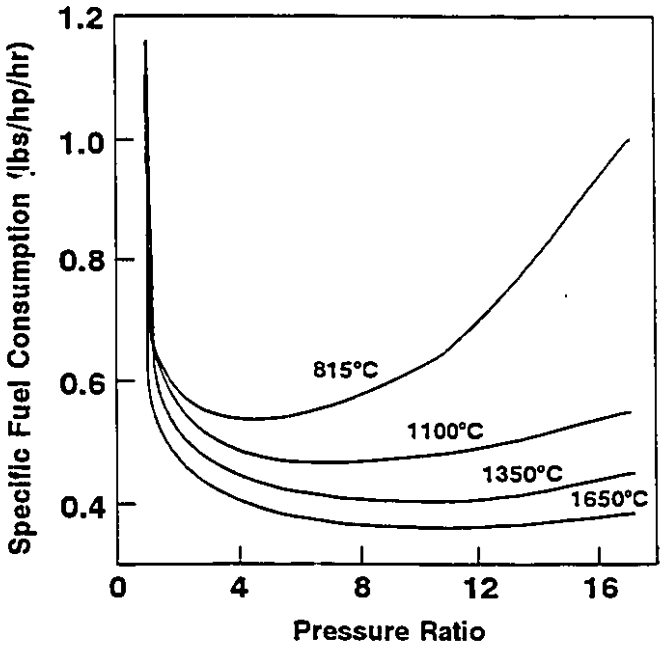

Figure 1.2- Specific fuel consumption for different turbine inlet temperatures. Engines operate at typical pressure ratios of 7 and 16 [5].

The automotive industry has profited from the recent developments in ceramics such as SiC and Si_3N_4, fabricating turbochargers and other engine components for service temperatures in excess of 1000°C [1,2]. Figure 1.3 shows a Si_3N_4 turbocharger rotor manufactured by Garrett Turbo Inc., and employed by Nissan in the 1990 Skyline model. The use of the light-weighted Si_3N_4 turbine wheels reduced rotating inertia by 40% and improved time-to-boost by 30%, delivering 280 hp with nearly instantaneous acceleration [6].

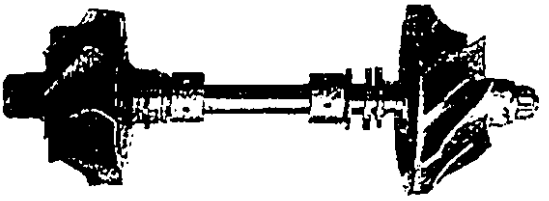

Figure 1.3- Si_3N_4 turbocharger rotor used in the Nissan 1990 Skyline model [2].

Other automobile manufacturers have also investigated the use of ceramic materials for turbocharger engines. For example, Toyota Motor Corporation has already introduced injection molded Si_3N_4 rotors into the Celica model, improving overall engine performance, as depicted in Figure 1.4. Volkswagen AG is another company developing SiC and Si_3N_4 rotors aiming at turbocharger inlet temperatures of 1230°C [6].

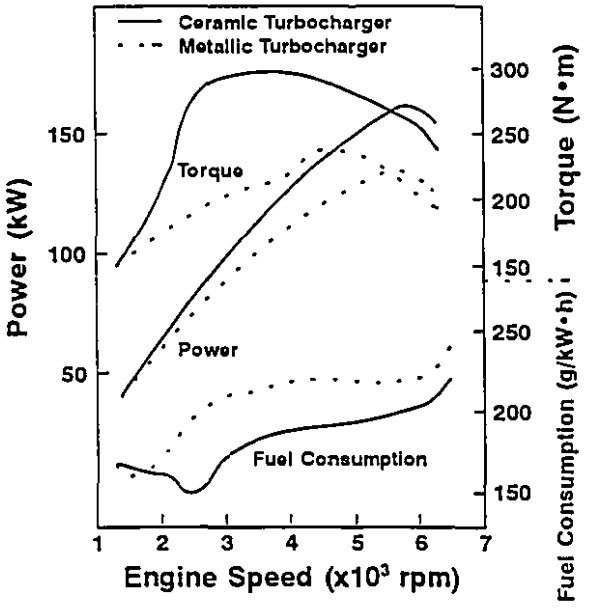

Figure 1.4- Comparative performance of Toyota engines equipped with metallic and Si_3N_4 turbochargers [6].

SiC and Si_3N_4 have also being used as aeroengine materials (Figure 1.5) permitting aerospace companies to improve the thrust to weight ratio by 50% in military aircrafts and 25% in civil airplanes [8]. For military engines this equates to better aircraft performance, increased capability for carrying weapons, and prolonged operating ranges. For civilian engines these benefits translate into reduced specific fuel consumption, lowering life cycle costs. Modern engines run in an environment of about 900°C to 1000°C, requiring extensive cooling of the metallic components, such as exhaust nozzles. With the use of SiC or Si_3N_4, the operating temperatures of such engines can be raised to 1200°C or higher, without cooling. As an example, Rolls-Royce have researched the manufacturing process of SiC, expecting to enhance the materials properties to withstand engine cycles of 1400°C [6]. In addition, ceramic components have the potential to last up to four times longer than similar metal parts exposed to high temperature conditions.

Elsewhere, SiC has been used in the electronic industry and in nuclear fusion reactors. Structural materials for fusion reactors require chemical and oxidation resistance along with improved mechanical properties at high-temperatures. SiC has these characteristics and it can be used as a protective coating of reactors first wall materials such as Mo, due to their similar thermal-expansion characteristics and refractoriness [9]. For microelectronics applications, although silicon-based devices are used in 99% of the cases, there are certain service requirements for which they are not appropriate, *i.e.*, exposure to radiation and high-temperatures. For these purposes, alternative combinations of semiconductors (GaAs and SiC) and refractory metals (Mo and W) have been studied.

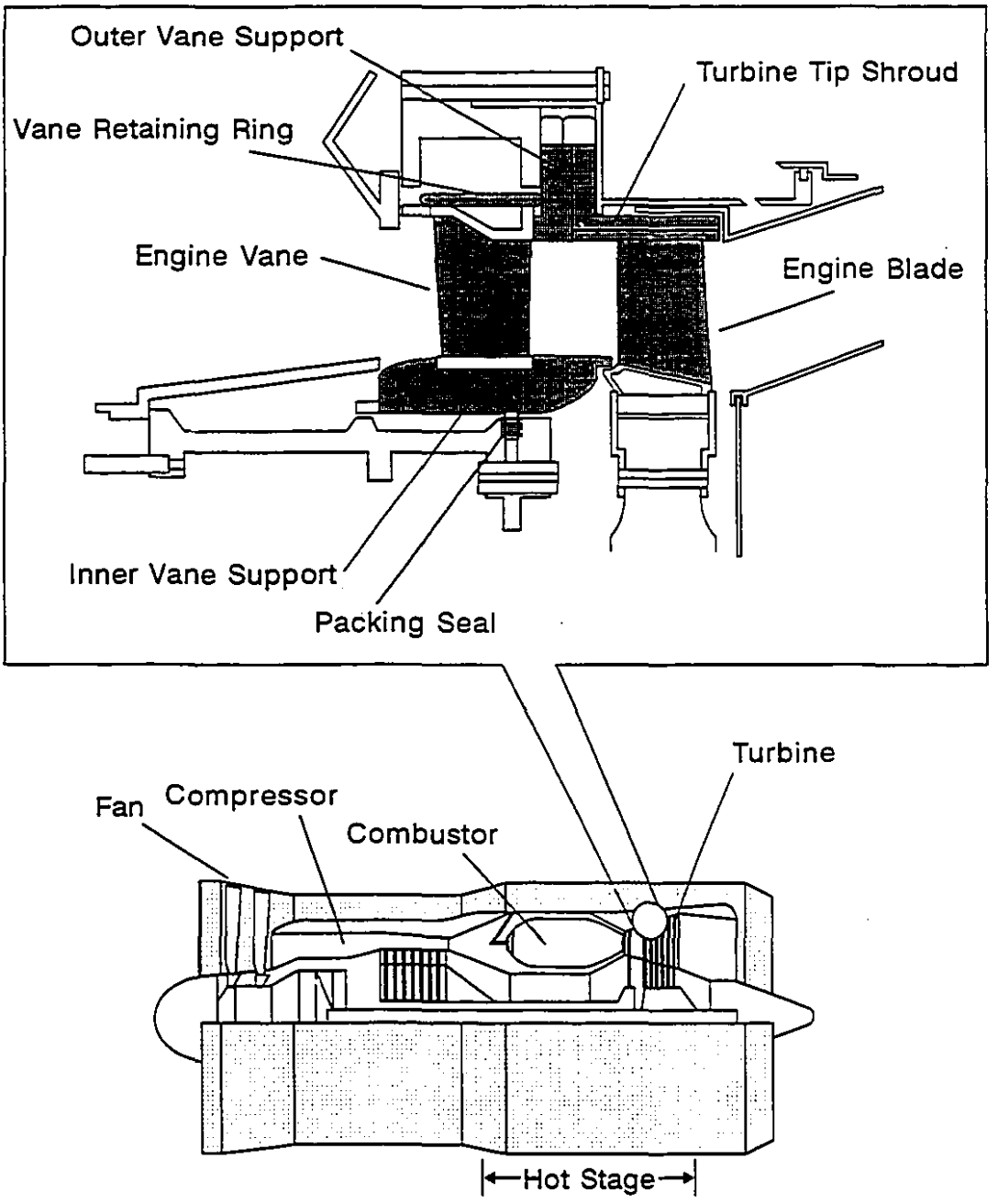

Figure 1.5- Schematics of aircraft-type turbine engine with ceramic components [7].

Refractory metals are important in electronic applications because they react with the ceramic promoting the formation of ohmic contacts with low electrical resistance within the interfacial region.

The use of ceramics also have a few associated disadvantages. For example, as an outcome of their brittle behaviour, ceramics usually have large scatter in their strengths and they are difficult to machine. Consequently, ceramics are used in conjunction with metals to fabricate composites, ceramic-coated components, and joined structures. When bulk ceramic parts are used, they are usually small and replace specific components. However, this situation implies that the ceramic parts have to be joined to various metallic structures, as in the case of the ceramic turbine rotor to the metallic shaft of an engine. Therefore, the practical use of ceramics in engineering devices largely depends on the ability to join them to metals. Reliable joining processes are necessary for the production of sound joints with good mechanical properties at the required service temperature and environment [2,3].

Several methods to join ceramics to metals have been developed over the years. The appropriate approach depends on the materials to be joined, joint design, and the anticipated operating conditions. Among the various joining methods currently available, metal-brazing is known to produce sound ceramic-metal joints with good mechanical properties. However, brazed joints are usually not resistant to temperatures in excess of 500°C because of the typical brazing temperatures, and limited melting temperature and oxidation resistance of the available brazing alloys [10]. Solid-state diffusion bonding

arises as an alternative method to produce temperature-resistant interfaces. Diffusion bonded joints are able to withstand higher service temperatures than brazed components, as well as to resist chemically hostile environments.

Solid-state joining requires the application of pressure at high-temperatures in order to promote intimate contact between the parts, which is essential for high-quality bonding. This requirement, however, is a shape-restrictive aspect, limiting the geometry of the joints to flat components. However, the most relevant problem in ceramic-metal joining by solid-state diffusion comes from the different thermal expansion behaviour of the materials. Highly covalent ceramics, such as SiC and Si_3N_4, have generally lower coefficients of thermal expansion (CTE) than metals. Whereas Si_3N_4 and SiC have CTEs of $3.5 \times 10^{-6} °C^{-1}$ and $4.4 \times 10^{-6} °C^{-1}$ respectively, metals and alloys of technological interest have CTEs ranging from $8 \times 10^{-6} °C^{-1}$ up to $25 \times 10^{-6} °C^{-1}$. These metals and alloys contract more than the ceramic during cooling of the diffusion couple from the relatively high bonding temperatures. Consequently, residual stresses are created, affecting the mechanical integrity of the joint. In particular, the presence of tensile stresses in the region adjacent to the interface and close to the edges of the ceramic, increases the probability for brittle fracture [11]. Several approaches can be used to overcome this difficulty. The main alternatives are the optimization of sample design avoiding geometries with points of high stress concentration such as rectangular faces, and the use of metallic interlayers with CTE between those of the ceramic and base metal.

The use of metallic interlayers is based on metals with CTE close to that of the ceramic. Although a few Ni-alloys have low thermal expansion characteristics, this behaviour is limited to a narrow temperature range. Therefore, the comparative analysis carried out, herein, is limited to metals that do not show discontinuities in their thermal expansion curves as a function of the temperature. Figure 1.6 shows thermal expansion coefficients for a few low-expansion metals as compared to those of SiC and Si_3N_4. From the thermal expansion point of view, refractory metals such as tungsten (W) and molybdenum (Mo) are the most attractive materials to be used as interlayers for joining SiC and Si_3N_4 to other metals. Their CTEs are close to those of the ceramics and they can be used to reduce the thermal mismatch between SiC/Si_3N_4 and metals or metal alloys with higher CTEs.

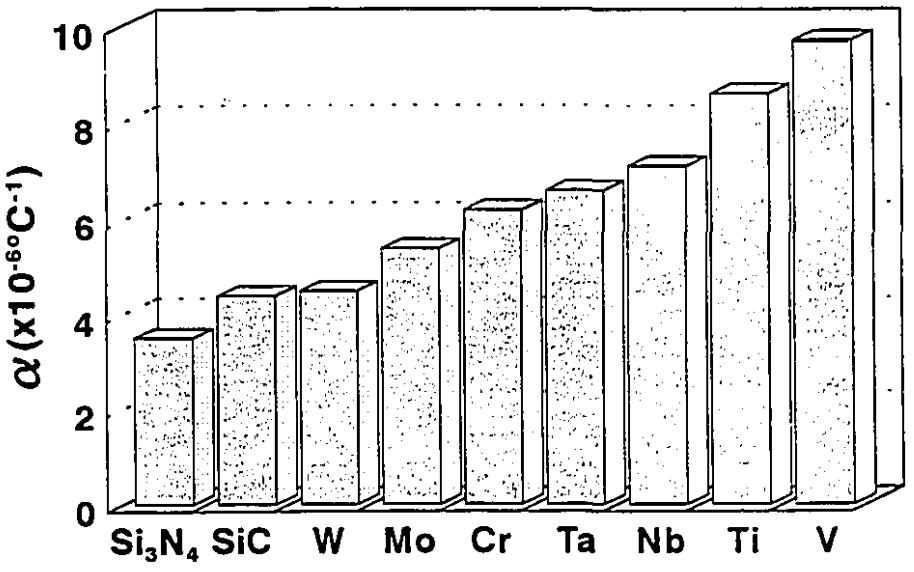

Figure 1.6- Linear coefficient of thermal expansion (α, 20°C to 1600°C) of SiC, Si_3N_4, and low-expansion metals [4,11].

Mo-interlayers can be readily used to join SiC and Si_3N_4 to metals, even if the joint is required to function in corrosive environments, as Mo is resistant to high-temperature corrosion by most types of molten glasses and acids found in chemical plants [12]. On the other hand, if the service conditions involve exposure to oxidizing atmospheres, the Mo-interlayer has to be protected. An exception occurs if the joint design keeps the interlayer isolated from the oxidizing environment, such as in the case of ceramic-metal seals, exhaust valves, and fuel nozzles [3]. Moreover, it has been reported that unprotected Mo is capable of sustaining short term use (up to 100 hours) in fuel-rich sections of turbine engines, operating at temperatures up to 1400°C [13]. However, the fast rates of oxidation of Mo at temperatures higher than 540°C in oxidizing atmospheres, prevent long term use of the material [14]. For service temperatures up to 1300°C, the Mo-layer can be protected by a double coating consisting of a Ni-Cr and a Au-Pd layer [13]. For applications where higher temperatures are involved, silicide coatings provide the most efficient protection. $MoSi_2$, for example, melts at temperatures above 2000°C, and its resistance to oxidizing environments results in service temperatures of the order of 1900°C [15,16].

An additional parameter to be considered in selecting an intermediate material is the mismatch in the elastic modulus between the ceramic and metallic interlayer. A misfit in elastic modulus generates very large tensile and shear stresses in the region adjacent to the edges of the joint, regardless of the sign of the mismatch, enhancing the propensity to fracture [11]. In the case of Si_3N_4, for example, although the CTE mismatch with W

is smaller compared to Mo, the elastic modulus mismatch is considerably smaller for Si_3N_4-Mo (Figure 1.7), which decreases the contribution of the elastic mismatch term to the overall residual stresses. From a general perspective, therefore, Mo has a better set of properties than W as an intermediate material between Si_3N_4 and metal or metal alloys.

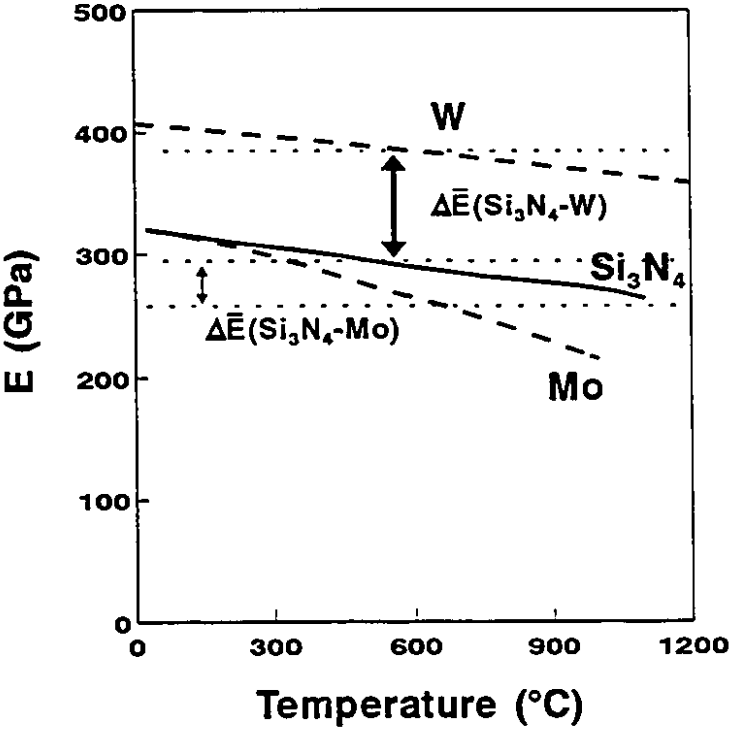

Figure 1.7- Mismatch in the elastic modulus for Si_3N_4-W and Si_3N_4-Mo combinations [4,11].

Therefore, in order to assess the potential of a specific ceramic-metal combination for structural applications, the physical and mechanical properties of the joining materials is an important aspect. However, it is also relevant to understand the mechanism of

interface formation between the metal and ceramic. In particular, the SiC-Mo and the Si_3N_4-Mo systems are reactive, and the presence of an interfacial reaction layer may affect the final properties of the joint, especially if brittle intermetallics are formed. For this reason, it is important to investigate the reaction behaviour of SiC and Si_3N_4 in the presence of Mo, upon the fabrication of diffusion couples, and to correlate the microstructure of the ceramic-metal interfaces with the mechanical properties of the joints.

CHAPTER 2:

CERAMIC-METAL JOINING PROCESSES

Ceramics and metals can be combined for the production of composites or coated devices. Composites are fabricated by methods such as powder metallurgy (hot pressing or hot isostatic pressing), squeeze casting, and infiltration processes (liquid or vapour infiltration). In the fabrication of structural composites, ceramics are used as whiskers, particles, or fibres to reinforce a metallic matrix. Ceramics are also used as protective coatings on metallic substrates. In this case, a ceramic film is deposited on a metallic substrate to produce a thermal barrier, or to

prevent wear and corrosion of the substrate. Ceramic coatings are commonly produced by methods such as chemical vapour deposition (CVD), plasma-assisted chemical vapour deposition, and physical vapour deposition (PVD).

Another possibility to integrate ceramics and metals is to produce bulk joints. This method is particularly useful when sintered ceramic components have to be incorporated into engineering devices largely composed of metallic parts. For example, a ceramic turbocharger rotor joined to a metal shaft in a combustion engine. Several methods have been developed over the years to produce sound and reliable joints between bulk ceramics and metals. The choice of appropriate joining method depends on the materials to be joined, joint design, and the anticipated service conditions. The main techniques used to join ceramics to metals can be divided into three groups: mechanical, indirect, and direct joining [17].

2.1 MECHANICAL JOINING

Bolting, shrink fitting, and clamping are some of the processes used to mechanically attach ceramic parts to metallic structures. Shrink fitting, for example, is used to join turbine components, such as a Si_3N_4 rocker arm insert to an aluminum arm. Clamping has been used to hold ceramic leading edges to the structure of space shuttles [18]. Although mechanical joining provides low-cost products, several disadvantages are associated with these processes, including design restrictions and the presence of points of high stresses that increase the probability of failure of the ceramic component [19].

2.2 INDIRECT JOINING

Indirect joining refers to the use of adhesives, glasses, or metallic brazing alloys to join a ceramic to a metal. Adhesives provide a simple and inexpensive method of joining ceramics to metals, however, the service temperatures are limited. Organic adhesives such as epoxies, can form strong bonds suitable for temperatures as high as 175°C. In one application, epoxy film adhesives are used to bond ceramic tiles to the interior of offshore oil pipes made of steel. The role of the ceramic is to protect the inside of the pipe from abrasion. Epoxies are also used to mount ceramic magnets in electrical motors [17]. As for glass interlayers, they are used, for example, to bond Al_2O_3 to niobium (Nb) in the production of sodium vapour lamps [17]. However, the use of glass interlayers can only be employed to join ceramics that form intergranular glassy phases, as bonding occurs by a reaction between this phase and the glass interlayer. A glass phase that can carry out such a reaction does not exist in every non-oxide ceramic, as in the case of SiC [4].

Brazing is commonly used in the manufacture of high-integrity joints with good mechanical properties. Complex designs and shapes can also be produced without major complications. However, brazing requires wetting of the ceramic (contact angles less than 90°), which is often difficult to achieve because of the high stability of ceramic compounds. One way to overcome this problem is to metallize the ceramic surface. Metallizing methods, such as the molybdenum-manganese process, consists of applying a thin metallic layer to the ceramic substrate, thus improving the wettability of the

ceramic to the braze [17]. Although widely used in industry, metallizing processes are generally restricted to oxide ceramics [4]. Another alternative, available for non-oxide ceramics, is to add small percentages of a reactive metal, *e.g.* titanium (Ti), in order to promote wetting of the ceramic surface by the braze. One example is given in Figure 2.1 for the alloy Cusil (72 Ag-28 Cu, in wt.%). The contact angle of Cusil on Si_3N_4 decreases drastically when titanium is added to form Cusil ABA (65 Ag-33.5 Cu-1.5 Ti, in wt.%), clearly indicating a major improvement in the wetting properties of the alloy [17].

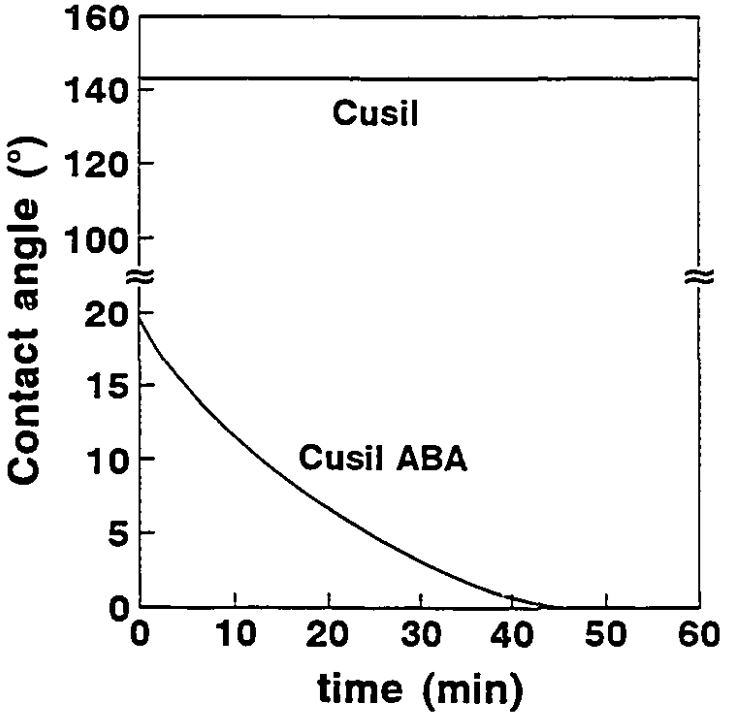

Figure 2.1- Contact angle of Ag-Cu based alloys on the surface of Si_3N_4 substrates at 900°C [17].

Nevertheless, brazed joints are usually not resistant to high temperatures and oxidizing environments. Typical brazes have limited melting points and oxidation resistance, and brazing itself is carried out at relatively low temperatures [10]. Brazing of Si_3N_4 using Cusil ABA, for example, takes place at temperatures between 800°C and 900°C, where the reaction between the alloy and the ceramic is already quite extensive [17]. This results in strength degradation of the brazed joints using Cusil ABA, which has been observed even in vacuum [17].

2.3 DIRECT JOINING

Direct joining includes processes where the ceramic is joined to the metal without interlayers. Welding and solid-state diffusion are the most common examples. Welding involves fusion of one of the components at the interfacial region to promote joining. In solid-state diffusion, the aim of the process is to produce a joint without melting any of the components. Bonding occurs with or without mass transfer across the interface. In the latter case, bonding is a result of charge transport across the interface with the establishment of van der Waals forces between the materials (physical bonding). Mass transfer occurs when the atomic species of the original materials diffuse across the interface (chemical bonding). In this case the resulting interface can have a diffusion layer (diffusive interface) or a reaction layer (reactive interface), depending on the thermodynamics of the system and the joining conditions [20].

2.4 MECHANISM OF SOLID-STATE BONDING

2.4.1 GENERAL ASPECTS OF DIFFUSION-BONDING

The first requirement for solid-state diffusion is the establishment of interatomic contact between the materials to be joined. For that, the bonding surfaces have to be free of impurities and they must have minimum roughness [19]. In addition to a good contact, there should be enough diffusion between the materials in a reasonable time. To fulfil this requirement, solid-state joining is a pressure-assisted process carried out at high temperatures. Pressure can be applied uniaxially (hot-press, HP) or isostatically (hot-isostatic press, HIP) on a diffusion couple. In HIPping, complicate geometries can be produced whereas uniaxial hot-pressing is limited to flat components. Among the disadvantages of HIPping, the cost of hot-isostatic pressed products is extremely high.

There are several benefits of solid-state joining. Direct bonding makes it possible to join materials with different refractoriness. Moreover, diffusion-bonded joints are usually able to withstand higher service temperatures than the brazed ones. The interfaces also offer good corrosion, oxidation, and radiation resistance at high temperatures. Another characteristic of diffusion bonding is that minimum distortion or deformation takes place, resulting in accurate dimensional control. This is particularly important in the fabrication of components where flatness and lateral tolerances are a decisive aspect [21]. Solid-state bonding can also be used to assess the mechanism of interface formation in metal-ceramic systems prior to the fabrication of composites or coatings. To successfully produce a ceramic-metal composite, or to coat a metal substrate with a

ceramic film, it is important to understand how the ceramic interacts with the metal, especially from the aspect of interface formation.

Among the disadvantages, direct bonding is a batch process, which means limited production. In addition, the misfit in the CTEs of the joining materials can result in areas of high stresses. To minimize this problem, geometries that favour the development of high stress concentrations have to be avoided, or interlayers that reduce the CTE mismatch have to be employed.

2.4.2 ESTABLISHMENT OF CERAMIC-METAL INTERFACES

The driving force for interface formation in solid-state bonding is the reduction in the surface energy, that occurs when intimate contact between the metal and the ceramic is achieved. This energy change per unit area (ΔG) is expressed by the Young-Dupré equation [22]

$$\Delta G = \gamma_m + \gamma_c - \gamma_{cm} \tag{2.1}$$

where γ_m and γ_c are the surface energies of the metal and the ceramic respectively, and γ_{cm} is the ceramic-metal interfacial energy. If physical bonding occurs, *i.e.*, no reaction takes place, ΔG is identical to the work of adhesion W_{ad}, which corresponds to the energy necessary to separate a unit area of interface into the two original surfaces [23]. Substituting W_{ad} for ΔG in equation (2.1) and rearranging the terms yield

$$\gamma_{cm} = \gamma_m + \gamma_c - W_{ad} \tag{2.2}$$

which shows that the ceramic-metal interfacial energy, γ_{cm}, decreases as W_{ad} increases,

which facilitates bonding. Therefore, in systems with high W_{ad}, strong interfaces are formed between the metal and the ceramic. This trend is illustrated in Figure 2.2 for different ceramic-metal systems [23].

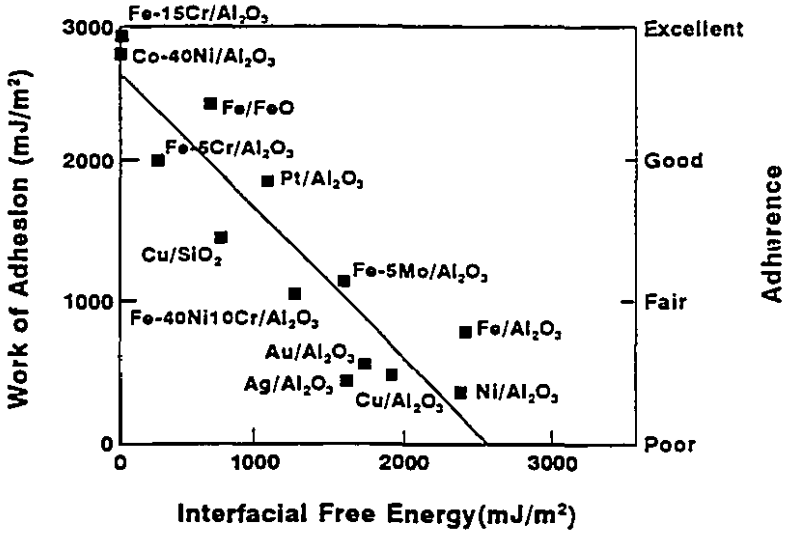

Figure 2.2- Correlation between W_{ad}/adherence and γ_{cm} [23].

There are two ways to calculate W_{ad} depending on the ceramic-metal system. If there is melting at the ceramic-metal interface, W_{ad} is calculated by

$$W_{ad} = \gamma_m (1 + \cos\Theta) \tag{2.3}$$

where Θ is the contact angle between the metal and the ceramic, which can be measured by sessile drop experiments [17], and values of γ_m for most metals can be found in the literature. On the other hand, if the ceramic-metal is a solid-solid system, W_{ad} can be estimated by measuring the dihedral angle, ϕ, associated with residual voids on diffusion-bonded interfaces [24]. If the interface ruptures in a brittle fashion, ϕ can be measured

using an atomic force microscope and W_{ad} is then obtained by

$$W_{ad} = \gamma_m (1 - \cos\phi) \quad (2.4)$$

Another important consequence of equation (2.1) is that a stable interface requires a positive ΔG (or W_{ad}). For a number of ceramic-metal systems, W_{ad} varies with the temperature, which provides an explanation for minimum temperature requirements to achieve bonding [22]. Chemical reactions, when present, further lower the free energy of the system, improving bonding [25]. Values of γ_{cm} are available in the literature for just a few solid-solid systems, most of them involving Al_2O_3. From Table 2.1 it can be seen that, in general, γ_{cm} for Al_2O_3-metal systems tends to increase with the cohesive energy of the metal, which is directly related to its melting temperature. In other words, the higher the melting point of the metal, the higher is the energy necessary to establish an interface with the ceramic substrate [23].

Table 2.1- Interfacial Energies of Solid-Solid Al_2O_3-Metals Systems [23]

System	γ_{cm} (mJ/m^2)	T_m of metal (°C)
Al_2O_3-Ag	1570 (700°C)	962
Al_2O_3-Au	1800 (1000°C)	1064
Al_2O_3-Cu	2210 (850°C)	1085
Al_2O_3-Ni	1730 (1002°C)	1455
Al_2O_3-Fe	2200 (1000°C)	1538

2.4.3 MODELLING SOLID-STATE BONDING

Solid-state diffusion bonding occurs when mass transfer mechanisms act to close the voids formed upon the contact between ceramic and metal, as shown in Figure 2.3.

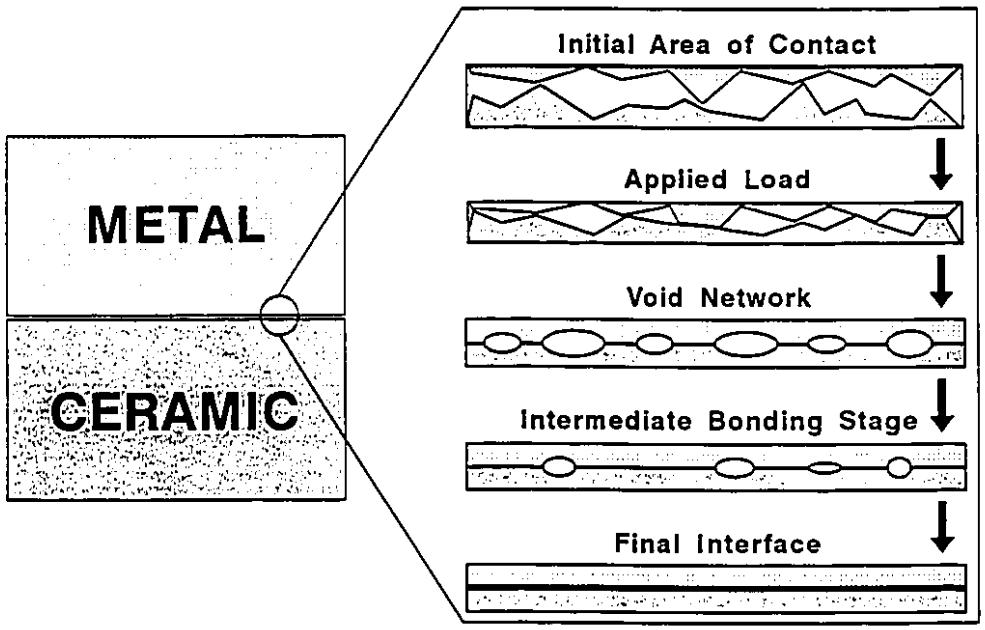

Figure 2.3- Mass transport by diffusion mechanisms closes the void network in a ceramic-metal interface resulting in bonding.

Several models have been proposed to explain diffusion bonding. Each of them is based on a distinct representation of surface roughness, and different bonding stages and mechanisms. In the currently accepted model [26], contact between the metal and the ceramic surfaces form an interface with a void network consisting of parallel cylinders of elliptical cross-section. The closure of a section perpendicular to the longitudinal axis

occurs by the simultaneous action of different mass diffusion mechanisms. The elliptical profile is a simple and acceptable representation of the complex void geometries observed in real systems. Void geometry is an important aspect of theoretical modelling because it determines the contribution from the different diffusion mechanisms to bonding. In assuming an elliptical void geometry, for example, it is implicit that the dominating diffusion mechanism shifts depending on the instantaneous void aspect ratio: from surface sources to interface sources as the aspect ratio approaches unity and vice-versa. The mechanisms responsible for diffusion bonding include plastic yielding, creep, and mass transport processes. They are listed below and illustrated in Figure 2.4 [27]:

1. Initial plastic yielding.
2. Surface diffusion from a surface source to a neck.
3. Volume diffusion from a surface source to a neck.
4. Evaporation from a surface source and condensation at a neck.
5. Grain boundary diffusion from an interfacial source to a neck.
6. Volume diffusion from an interfacial source to a neck.
7. Power-law creep.

These mechanisms can be generally classified into plastic deformation, diffusion from surface and interface sources to necked regions, and power-law creep.

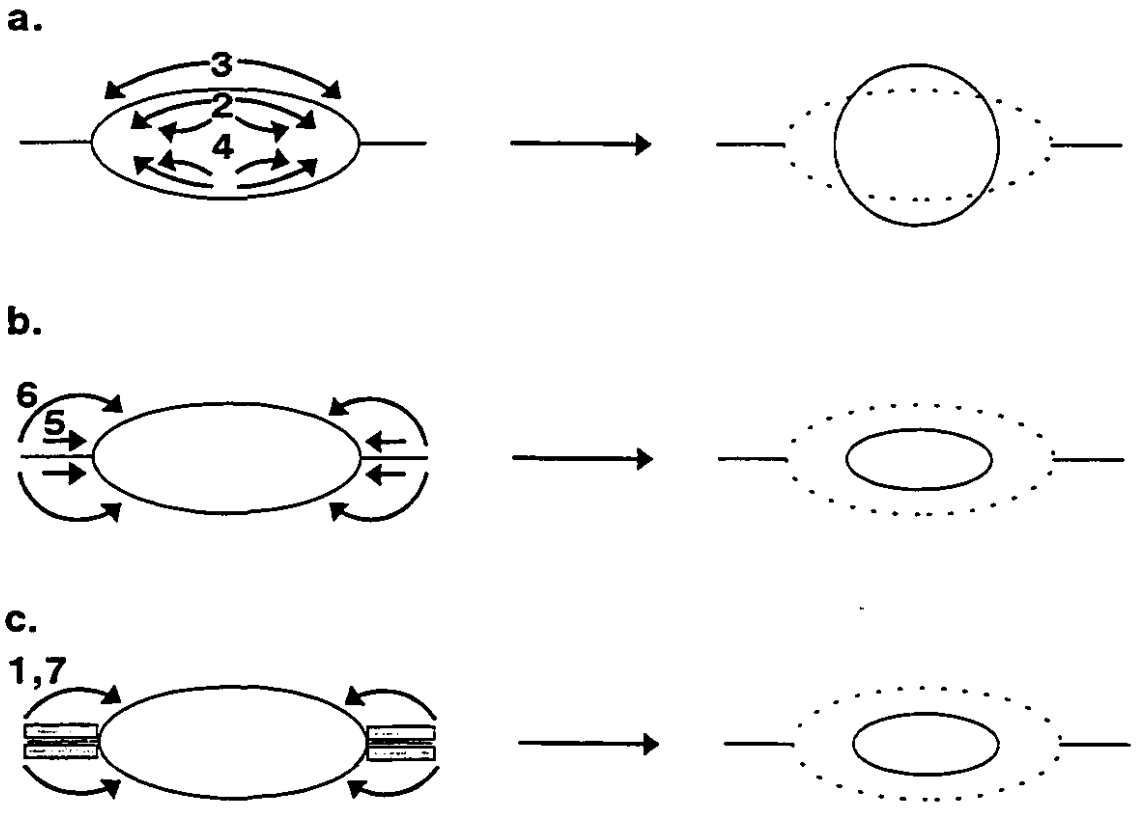

Figure 2.4- Schematic representation of sources and sinks of material during diffusion bonding [27].

a. Mechanism 1- Initial plastic deformation

The initial contact between metal and ceramic occurs within the area of asperities (Figure 2.3). The applied load on the diffusion couple causes plastic deformation which increases the initial area of contact by mutual indentation of the asperities. Plastic deformation occurs mainly in the metal, as a consequence of rapid loss in strength at elevated temperatures. The initial area of contact grows until the applied load can be

supported, *i.e.*, the local stress falls below the yield strength of the metal [27]. Bonding occurs when the local shear stress in the metal reaches a maximum value required for plastic flow. Following this plastic deformation, diffusion and power-law creep take place. These are time dependent stages and one or more of six diffusion and creep mechanisms may contribute to bonding [26].

b. Mechanisms 2 to 4- Diffusion from surface sources to necked regions

Mechanisms 2 to 4 are activated by the change in chemical potential that accompanies any change in the curvature of a void. Matter diffuses in the direction of increased curvature, *i.e.*, towards the sharp neck of the void (Figure 2.4a). As a result, elliptical cross-sections change into circular ones. When the aspect ratio of the voids approaches one (circular cross-section), the diffusion rates of mechanisms 2 to 4 tend to zero. Each mechanism is governed by a diffusion coefficient, properly selected: for surface diffusion (mechanism 2), the assumed two-dimensional geometry is a thin surface layer and the relevant diffusion coefficient is that of surface diffusion; for volume diffusion (mechanism 3), matter is transported through the area of the neck. Hence, the diffusion coefficient is that of volume diffusion. For the evaporation and condensation mode (mechanism 4), the rate of mass transfer is governed by the vapour pressure [3].

c. Mechanisms 5 and 6- Diffusion from interface sources to necked regions

The rate of diffusion from interfacial sources is determined by the chemical

potential gradient along the bond interface, which depends on the void neck radius and the applied pressure [26]. Although mechanisms 5 and 6 have the same interfacial source, the routes of material transfer are different (Figure 2.4b). Considering the interface to be a high-angle grain boundary, mechanism 5 transfers matter along a thin boundary layer. The coefficient for boundary diffusion would therefore be applicable. Bulk diffusion, which is associated with mechanism 6, should employ the coefficient for volume diffusion.

d. Mechanism 7- Power-law creep

Diffusion bonding is usually carried out at high-temperatures for relatively short times. Although macro-creep is undesirable because it causes specimen distortion, micro-creep of asperities can contribute to void closure [26]. The power-law creep mechanism is modelled as a two-stage process. In the first stage, a change in void height occurs, *i.e.*, an elliptical hole grows in plane-strain condition under the power-law creep. The second stage consists of filling the void with material displaced from the neighbouring area of contact (Figure 2.4c) [3].

The total bonded area is calculated based on the assumption that the contribution from each diffusion mechanism can be added linearly. A major problem in calculation comes from the lack of representative values for diffusion coefficients, activation energies, and creep constants. Such data are not readily available, particularly for

ceramics, limiting the practical application of the model to a few systems.

2.5 INFLUENCE OF EXPERIMENTAL PARAMETERS ON BONDING

Experimental parameters that affect solid-state bonding are temperature, time, pressure, and, in some cases, environment [27]. Their influence on the final properties of the interface are discussed below.

2.5.1 TEMPERATURE

Temperature is the most important parameter in solid-state joining because it controls the kinetics of the thermally activated processes involved in diffusion bonding. Joining at high temperatures enhances atomic mobility across the interface and assists in the movement of dislocations [23]. In fact, all diffusion mechanisms are sensitive to temperature. The temperature required to obtain sufficient joint strength is typically between $0.5T_m$ and $0.9T_m$, where T_m is the absolute melting point of the base metal [27]. A compromise has to be reached to assure the formation of a reliable interface with minimum residual stresses. Although stress concentration increases with increasing bonding temperature, for each ceramic-metal system there is an optimum value that maximizes the strength of the interface. To a certain extent, increasing the temperature enhances bonding, provided that time is controlled to prevent the development of detrimental reaction products in reactive systems. An example of the dependence of bond strength as a function of the temperature is given for Al_2O_3-Nb joints in Figure 2.5.

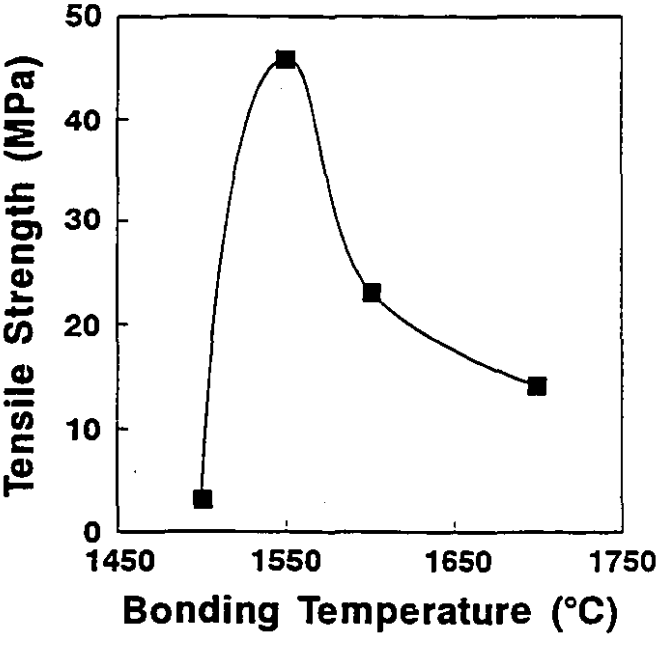

Figure 2.5- Tensile strength of Al_2O_3-Nb joints as a function of the bonding temperature [23].

The increase in strength for the Al_2O_3-Nb joints, at temperatures up to 1550°C, was related to an increase in the fraction of bonded surface. The loss of strength above 1550°C was due to the formation of a thick reaction zone ($\geq$ 20 μm) detrimental to the strength of the joints [23]. For a given pressure and time, a minimum temperature is often necessary to achieve complete bonding, as can be seen for the Al_2O_3-Pt system (Figure 2.6a). This minimum temperature increases with the melting point of the metallic component of the joint (T_m), as shown in Figure 2.6b [23].

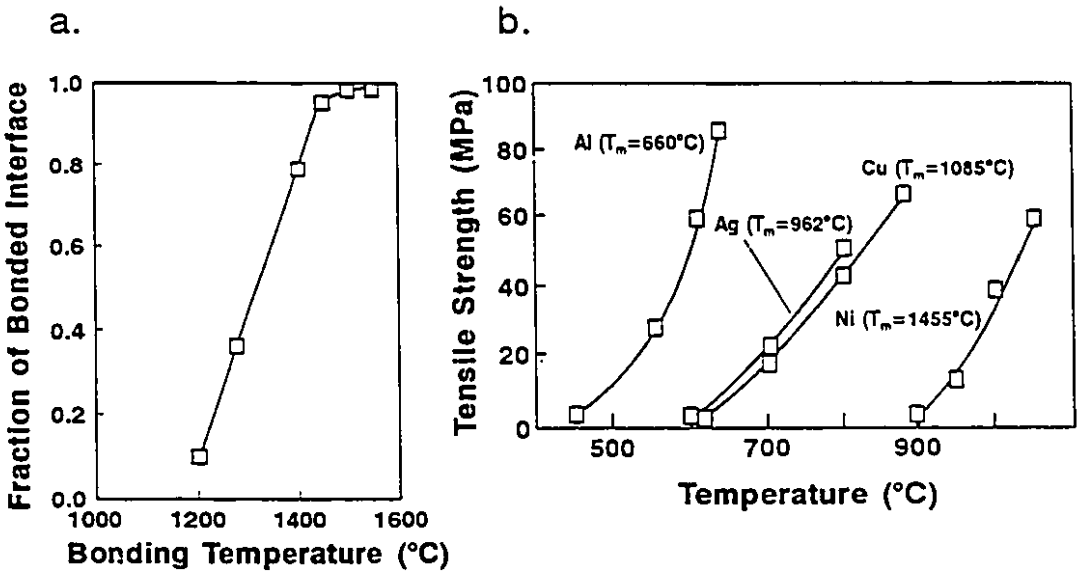

Figure 2.6- (a) Fraction of bonded interface as a function of the temperature for Al_2O_3-Pt joints; (b) bond strength as a function of temperature for several Al_2O_3-metal combinations [23].

2.5.2 TIME

Bonding times may vary from one second to several hours depending on the ceramic-metal combination and the joining temperature [17]. For each temperature, there is a corresponding minimum time required to promote complete bonding. This value decreases when the temperature or pressure increases. For reactive systems, bonding times also have to be adjusted to promote bonding with limited reaction. Because solid-

state diffusion is frequently described by non-equilibrium thermodynamics, time may affect not only the amount of reaction, but also the nature of the reaction products. In Si_3N_4-W, for example, time affects the amount of Si present at the interface, which determines the type of W-silicide that precipitates (W_5Si_3 or WSi_2) [20].

2.5.3 LOAD

Representative uniaxial pressures used in hot-pressing of ceramics to metals range from 1 to 100 MPa. These values are typically a fraction of the room temperature yield strength of the metal, thus avoiding macroscopic deformation of the component [27]. The role of pressure on bonding is not limited to establishing contact between the materials and to promote micro-creep. Pressure is also responsible for breaking the stable oxide film present on the surface of most ceramics, exposing the material to interact with the metallic component of the joint.

2.5.4 SURFACE ROUGHNESS

The presence of asperities on the bonding surfaces limits the total area of contact between the metal and oxide-free ceramic, and, in addition, large voids are rarely closed [23]. Interfacial flaws are detrimental to the strength of the joint in the sense that they act as fracture initiation sites. Therefore, it is necessary to polish the bonding surfaces prior to joining, improving the initial area of contact between the metal and ceramic and preventing the formation of large voids. However, unjoined areas are still likely to

remain at the interface, especially close to the edges [2]. Unjoined edges are a weakening factor as they create notches at the interface. Not only the average joint strength decreases, but also the local strength becomes position dependent. Large variations in strength have been observed comparing different positions of such interfaces, as can be seen in Figure 2.7 for Si_3N_4-Fe-Si_3N_4 joints.

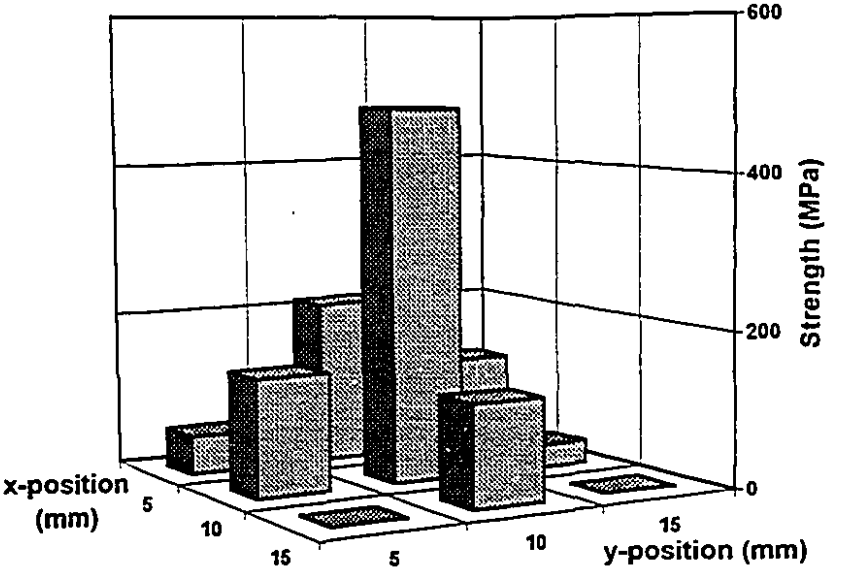

Figure 2.7- Strength of Si_3N_4-Fe-Si_3N_4 at different positions of the joint [2].

The strength of Si_3N_4-Fe-Si_3N_4 joints reached 500 MPa at the centre of the joint. Close to the edges, the strength drastically decreased to 10% of that value. Limited bonding at joint edges occurs for several reasons. One is the curvature of the interface.

Mechanical finishing of bonding surfaces inevitably removes extra volume from the edge region. Another cause is the inhomogeneity in the deformation of the metal layer under the applied load [2]. Figure 2.8 shows the distribution of load on a sandwich type sample depicting the loss of contact stress close to the border of the specimen [23]. Another possibility occurs in reactive systems where gas is released: the reaction in the outer region of the joint may be promoted by continuous evacuation, causing excessive thinning of the edge of the ceramic.

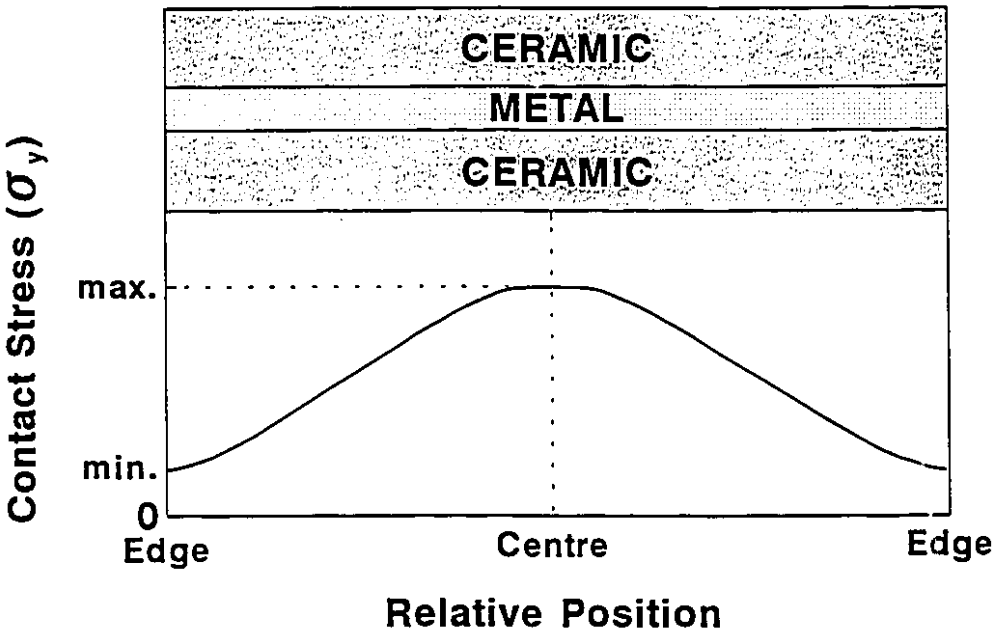

Figure 2.8- Contact stress distribution in sandwich-type joints [23].

2.5.5 ENVIRONMENT

Diffusion bonding is usually carried out in vacuum or in the presence of a gas with low oxygen activity, *e.g.* argon (Ar) or nitrogen (N_2). Although bonding pressure is usually sufficient to break down the protective oxide layer of the ceramic, its recovery may occur rapidly if the partial pressure of oxygen is sufficiently high [27]. If one of the reaction products is a gas, such as N_2 in Si_3N_4-metal systems, the environment affects the thermodynamics of the system and the kinetics of the reaction. In such cases, increasing the partial pressure of N_2 in the environment may promote the formation of metal-nitrides, a situation not observed when joining is carried out under vacuum.

CHAPTER 3:

THE FORMATION OF CERAMIC-METAL INTERFACES

Ceramic-metal interfaces can be classified into three categories, as illustrated in Figure 3.1 [18]:

1. Interfaces with no reaction or diffusion layer: planar interfaces with possible epitaxial growth, as in the case of Al_2O_3-Nb, Al_2O_3-Pt, and ZrO_2-Pt [20].

2. Interfaces with a diffusion layer: originating from interdiffusion between the metal and ceramic, as in the case of Si_3N_4-stainless steel [20].

3. Interfaces with a reaction layer: new phases result from a chemical reaction between a ceramic and metal, as in the SiC-Ni system. As atomic diffusion is far easier in metals than in ceramics, reaction layers grow extensively in metals but to a limited extent in ceramics [18].

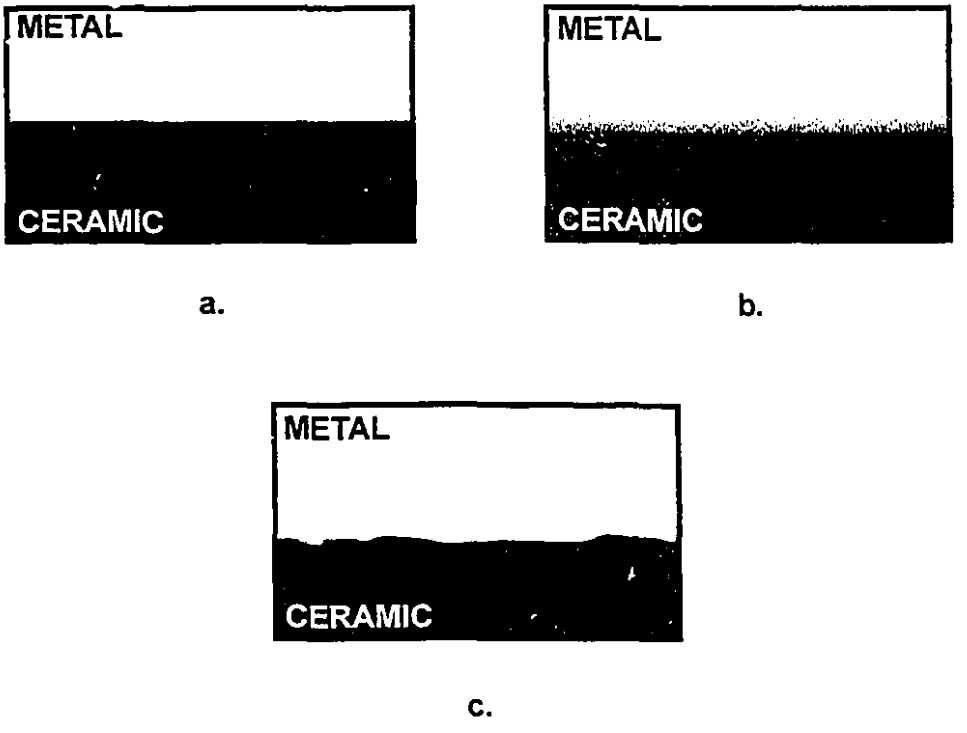

Figure 3.1- Common classes of ceramic-metal interfaces. (a) Non-diffusive and non-reactive, (b) diffusive, and (c) reactive.

The growth of interfacial reaction layers initially enhance bonding, forming an adherent interface between the metal and ceramic. However, if the new phases are

brittle, thick reaction layers can result in excessive concentrations of thermal stresses, degrading the quality of the bond [20,28]. Thus, the chemistry of a ceramic-metal interface has to be established in order to determine the best parameters for the production of mechanically sound joints, capable of fulfilling demanding service requirements.

3.1 INTERFACIAL CHEMICAL REACTION

Chemical reaction during solid-state bonding occurs when mass is transferred across the interface, resulting in the formation of new phases. Some degree of reaction is important because it lowers the interfacial energy of the system, enhancing the adherence of the interface, according to Figure 2.2 [23]. As an example, Al_2O_3 forms non-reactive interfaces with nickel (Ni) and copper (Cu), with relatively high interfacial energies. However, when Ni-O and Cu-O alloys are bonded to Al_2O_3, a chemical reaction take place resulting in the formation of a spinel layer, lowering the interfacial energy (Table 3.1).

Table 3.1- Interfacial Energy (γ) of Solid Ceramic-Liquid Metal Systems [23]

System	T(°C)	γ(mJ/m^2)	Reaction
Al_2O_3-Ni	1500	2440	No
Al_2O_3-Ni(O)	1600	1600	Yes
Al_2O_3-Cu	1100	2080	No
Al_2O_3-Cu(O)	1230	1000	Yes

Whether new phases are formed at ceramic-metal interfaces depends on the thermodynamic properties of the joining materials and on the experimental conditions. Some systems change their nature from non-reactive to reactive according to the bonding parameters. For instance, Al_2O_3 may react with Nb depending on the partial pressure of oxygen in the environment [23]. Chemical reactions take place when the formation of a reaction product reduces the total Gibbs free energy of the system. Because interfacial reactions are irreversible processes, they should be described using irreversible thermodynamics, where entropy is determined by the flow of heat, mass, and chemical potentials of the reacting species [23]. Since such data are not available for most of the ceramic-metal systems of practical interest, equilibrium thermodynamics are used in first approximation. Equilibrium values are usually available for various reactive systems as a function of temperature and atmosphere.

The thermodynamic behaviour of a particular ceramic-metal system is described considering the variation in the Gibbs free energy (ΔG) of all possible reactions and solid-solutions involving its constituents. The system spontaneously undergoes the transformation that results in the lowest energy state. Alternatively, the reactivity of a system can be assessed comparing the standard free energy of formation of reaction products (ΔG^0) with that of the ceramic. If a particular reaction product is more stable than the original ceramic, it will form, and the system is reactive. This method is useful if an automated thermodynamic database is readily available and if not many elements are involved, as in the case of systems containing SiC and a metal (Me). The

decomposition of SiC results in Si and C, and thus only the formation of Me-carbides and Me-silicides has to be investigated.

Figure 3.2 shows ΔG^0 for Me-carbides and Me-silicides considering a variety of metals. As an example, Figure 3.2b indicates that Ni_2Si is more stable than SiC. On the other hand, Figure 3.2a shows that Ni_3C has $\Delta G^0 > 0$ for the entire temperature range under consideration. Hence, the interface of SiC-Ni diffusion couples would probably contain a reaction layer consisting of Ni_2Si and free C. This analysis is in good agreement with experimental results obtained for this system [23].

An advantage of the use of a thermodynamic database is that it provides a view over an entire temperature range. This way, it is possible to identify changes in the composition of ceramic-metal interfaces, as one particular compound becomes more stable than another as the temperature changes. An example of this fact is seen in Figure 3.2a comparing the stability of WC and W_2C. On the other hand, isotherms of ternary phase diagrams are available only for a limited combination of elements and for specific temperatures, which could impair a thorough thermodynamic analysis of a particular ceramic-metal system.

Some disparities between thermodynamic predictions and experimental results have been observed. One of them involves the reaction between SiC and Al resulting in Al_4C_3, which is thermodynamically less stable than SiC. A possible explanation for this result is that there is a discrepancy between the literature and the real value of ΔG^0 for the formation of SiC. The literature suggests that the SiC used in the production of

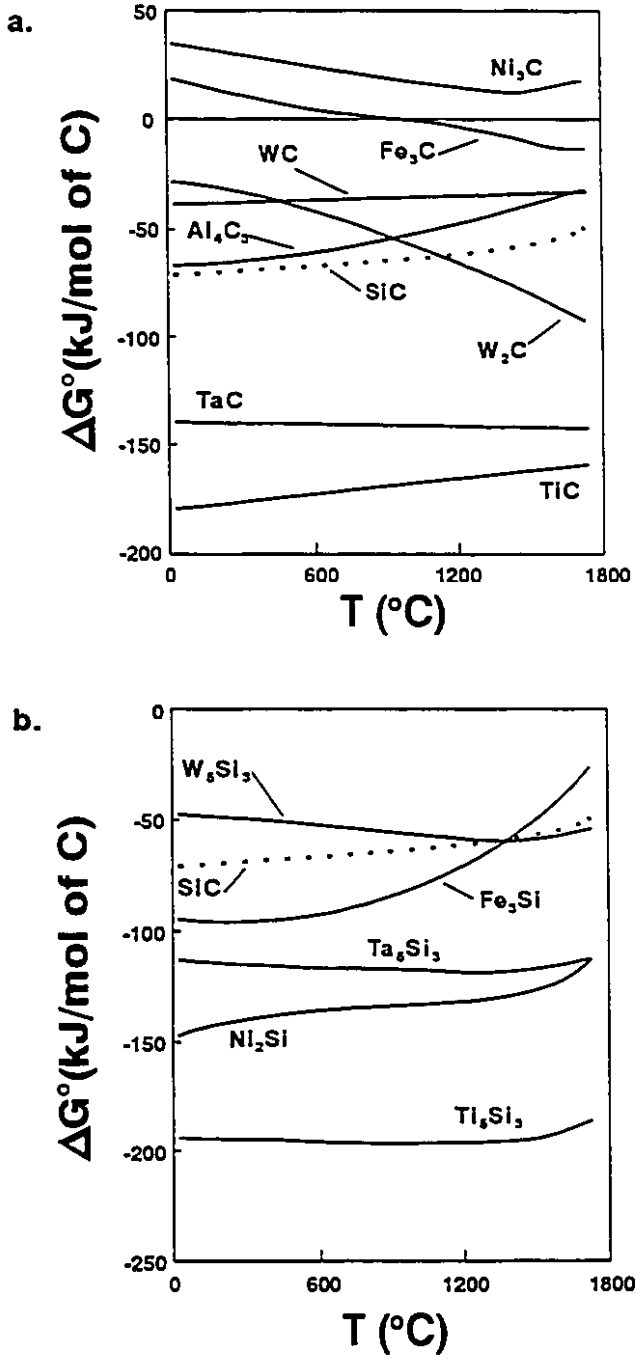

Figure 3.2- Standard free energy of formation of SiC, (a) metal-carbides and (b) metal-silicides (data obtained from F*A*C*T database).

SiC-Al joints is somehow less stable than the variety considered in the thermodynamic evaluation of the system [20].

In the case of systems involving Si_3N_4, an additional difficulty is introduced by the presence of a gas phase. N_2 gas is formed upon the dissociation of Si_3N_4, and it may or may not diffuse into the metal, depending on its solubility at the bonding temperature. For metals with low solubility for N_2, the gas remains trapped inside the interfacial voids, resulting in porosity. Metals with high solubility for N_2 dissolve the gas to a certain extent, and the interfaces have limited or no porosity, depending on the amount of Si_3N_4 that dissociated. Alternatively, N_2 can also react with the metal or a component of a metallic alloy, resulting in the formation of a nitride phase within the interface. Examples of N_2 solubilities in different metals, at 1200°C are: close to zero for cobalt (Co), molybdenum (Mo), nickel (Ni), and tungsten (W); 1.5 at.% for niobium (Nb); 5 at.% for iron (Fe); 6.5 - 7 at.% for chromium (Cr), tantalum (Ta), and vanadium (V); and larger for manganese (Mn), titanium (Ti), and zircon (Zr). Titanium is also a strong nitride former, and it is used as an alloying element to minimize interfacial porosity [20].

Many ceramic-metal combinations are classified as reactive systems. The thickness of an interfacial reaction zone, as a function of temperature and time, can be expressed by [27]

$$x = K_p t^n \tag{3.1}$$

where x is the thickness of the reaction layer, K_p is the coefficient of penetration, and t is the time. The temperature term is implicit in the coefficient of penetration which

follows an Arrhenius-type relationship

$$K_p = K_o \exp(-Q/RT) \tag{3.2}$$

where K_o is the pre-exponential factor, Q is the activation energy for interface formation, R is the gas constant, and T is the absolute temperature.

The rate constant, K_o, in equation (3.2) contains the frequency factor of atomic migration at the interface. In a study where different types of SiC were joined to Nb, K_o was evaluated [29]. For pressureless sintered SiC (PLS-SiC), K_o was 3.22×10^{-3} m^2/s; lower than that of reaction bonded SiC (RBSC): 2.38 m^2/s. This indicated that Nb combined more readily with Si at the interface with RBSC than with PLS-SiC.

For most of the reactive ceramic-metal combinations, interfaces grow parabolically with time, *i.e.*, following equation (3.1) with n equal to 0.5 (Fick's law). However, a few exceptions to this rule have been reported. Figure 3.3 illustrates the thickness of SiC-Ni interfaces as a function of the time, for different temperatures. During the initial stages of diffusion, Si penetrated into Ni but did not form intermetallic compounds, due to its large solubility in the metal. The nucleation of Ni_2Si was then delayed. At low temperatures, this resulted in a slow interfacial growth during the entire process, as a result of the slow kinetics of diffusion. At higher temperatures, an initial incubation period was observed, after which the growth rate of the reaction layer increased considerably with time, deviating from the parabolic growth [20]. Another exception to Fick's law was observed in the TiC-Mo system, where the growth rate of Mo_2C was constant for low concentrations of free C in TiC [20].

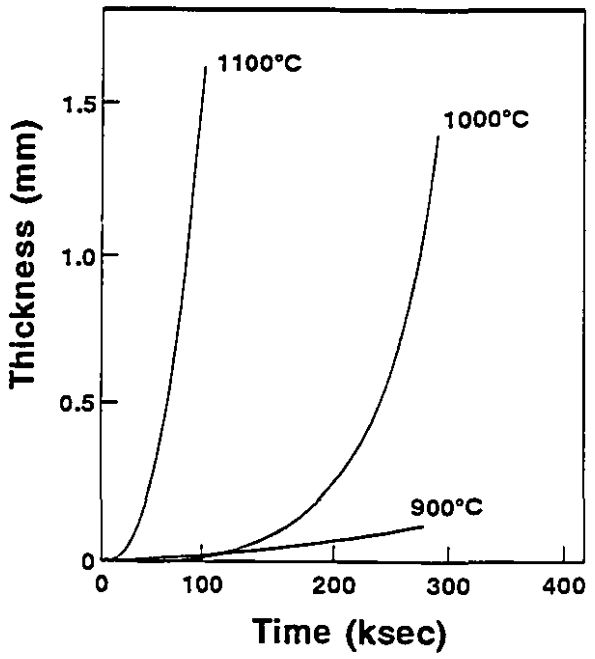

Figure 3.3- Thickness of SiC-Ni reaction layer as a function of the time, for different temperatures [20].

3.2 THE SiC-Mo SYSTEM

The SiC-Mo system has been studied for its importance in the fabrication of composites, and for the matching thermal expansion behaviour and refractoriness of these materials. Another important feature of this system is molybdenum disilicide ($MoSi_2$). This compound is a potential material for the fabrication of high temperature intermetallic composites and coatings. $MoSi_2$ has high melting point (2032°C), excellent high-temperature oxidation resistance, and high electrical and thermal conductivity [16].

Because of its low CTE, Mo has been considered as an intermediate material for

joining SiC to metals and alloys. Although much work has been done in joining SiC to metals such as Nb, Ti and Al, little data are available concerning the physical and mechanical properties of SiC-Mo interfaces. It is known that no liquid phase is expected to form up to 1800°C within the SiC-Mo interface [30]. Therefore, solid-state diffusion is the only mechanism that can result in bonding of SiC to Mo, for temperatures between 1100°C and 1700°C.

The reaction between SiC and Mo has been studied for pyrolitic β-SiC coatings on Mo substrates, and for resistance-welded joints [31]. The temperature investigated was 1200°C, and a reaction layer was formed, consisting of a region with two intermixed phases (Mo_5Si_3 and Mo_2C) and a thin layer of a ternary compound (Mo_5Si_3C) in contact with SiC. The mixed aspect of the Mo_5Si_3/Mo_2C layer was attributed to a ternary diffusion phenomenon, assuming diffusion of carbon (C) as the rate-determining step. Considering volume diffusion of C through the Mo_5Si_3 layer, the reaction to form Mo_2C would proceed faster at those points where C had to travel the shortest distance through Mo_5Si_3. A similar argument applies considering that C diffused along grain boundaries of the Mo_5Si_3 phase towards Mo [31].

Figure 3.4 shows a cross section of the Mo-Si-C phase diagram at 1200°C [31]. In this diagram, Mo_5Si_3 is shown as coexisting with Mo_5Si_3C and SiC by the presence of a compatibility triangle joining these phases. This situation was not observed at 1600°C, according to the corresponding isotherm (Figure 3.5). At that temperature, $MoSi_2$ coexists with Mo_5Si_3C and SiC [30]. Conversely, the presence of Mo_5Si_3 and

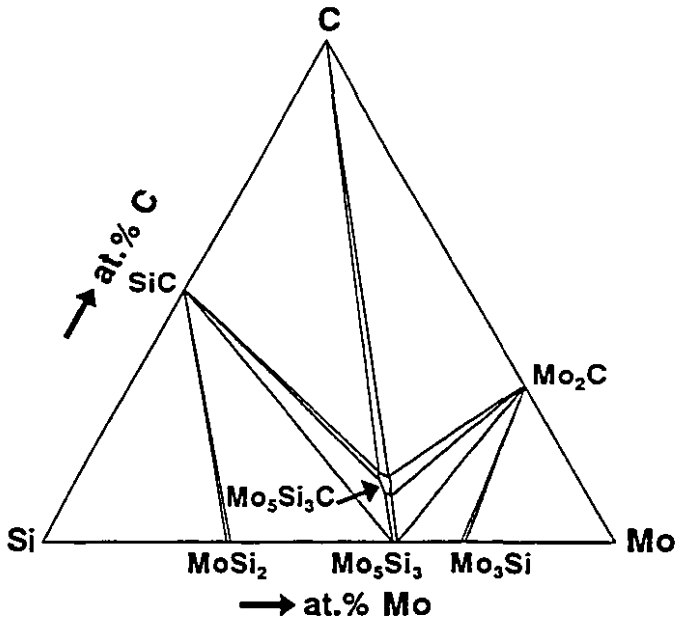

Figure 3.4- Cross-section of the Mo-Si-C phase diagram at 1200°C [31].

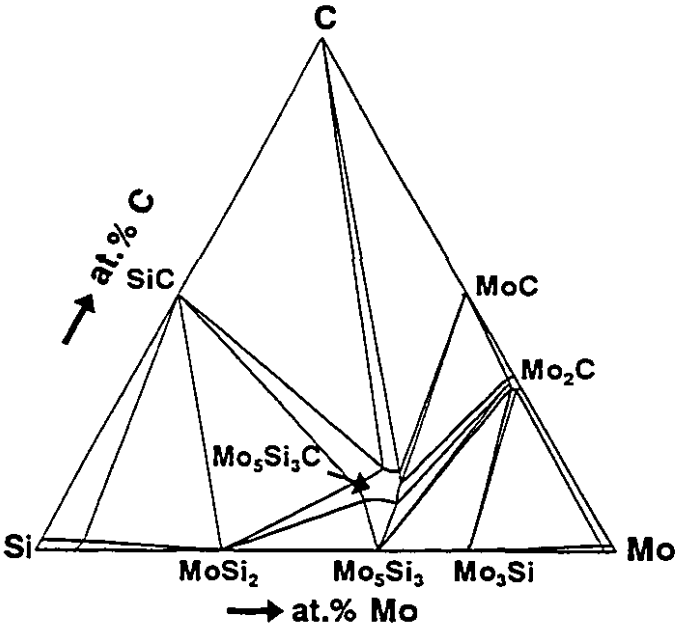

Figure 3.5- Cross-section of the Mo-Si-C phase diagram at 1600°C [30].

Mo_5Si_3C were observed at 1700°C [32], in a study consisting of joining SiC to Mo by hot-pressing and hot-isostatic pressing (HIPping). The diffusion couples were annealed for 1 hour under pressures of 100 MPa upon hot-pressing, and 1 GPa upon HIPping. The reaction products and diffusion paths were the same as the ones observed at 1200°C, but they were obtained for shorter times at the higher temperature. Finally, the reaction between SiC and Mo has also been studied at 1100°C, and the reaction products observed were Mo_2C and Mo_5Si_3. The formation of the ternary phase was not reported at that temperature [33].

3.3 THE Si_3N_4-Mo SYSTEM

Some aspects of the reaction between Mo and Si_3N_4 have been previously studied, particularly when the starting materials were in powder form. It has been reported [34] that Mo has a low solubility for N_2, and that the dissolution of the gas in the metal occurs endothermically, *i.e.*, the concentration of N_2 dissolved in Mo increases with the temperature at a constant partial pressure of N_2. Based on this work, the solubility of N_2 in Mo was calculated for two different partial pressures of the gas at 1600°C (Table 3.2).

Si_3N_4 and Mo powders have been observed to react at temperatures as low as 1000°C, forming Mo_5Si_3 and N_2. Similar results have been obtained by annealing a powder mixture of Mo and Si blended with Si_3N_4 at 1700°C. In this work, no phase transformation was observed between 1000°C and 1700°C [34]. In another study, the formation of Mo_2N was observed upon annealing of Si_3N_4 with 50 vol.% Mo at 1000°C

for 30 minutes under a vacuum of 10^{-2} torr (1 Pa). At 1200°C, the reaction products observed were $MoSi_2$, Mo_5Si_3 and Mo_3Si [35].

Table 3.2- Solubility of N_2 in Mo at 1600°C [34]

Partial Pressure of N_2 (kPa)	Concentration of N_2 in Mo (at.%)
0.02	10^{-3}
120	10^{-2}

The influence of the atmosphere on the reaction between Si_3N_4 and Mo powders has also been studied [36]. In one investigation, different mixtures of Si_3N_4 and Mo were annealed at 1300°C in environments with partial pressures of N_2 varying from 6×10^{-8} to 10^4 kPa. The reaction products obtained in this work are summarized in Table 3.3.

Table 3.3- Reaction between Si_3N_4 and Mo Powders at 1300°C [36]

	Partial Pressure of N_2 (kPa)			
$Mo:Si_3N_4$	6×10^{-8}	2×10^{-3}	80	1×10^{4}
3:1	$MoSi_2$, Mo_5Si_3	$MoSi_2$, Mo_5Si_3	Si_3N_4, Mo_5Si_3	Mo_2N, Si_3N_4
6:1	Mo_5Si_3, Mo_3Si	Mo_5Si_3, Mo_3Si	Mo_5Si_3, Mo_3Si	Mo_2N, Si_3N_4
20:1	Mo_3Si, Mo	Mo_3Si, Mo	Mo_3Si, Mo	Mo_2N, Si_3N_4

Because the Si_3N_4-Mo system contains a gas phase (N_2), the Mo-Si-N phase diagram depends on the partial pressure of the gas. Figure 3.6 illustrates the 1300°C cross-sections of the Mo-Si-N phase diagram for different partial pressures of N_2 [36]. The results contained in Table 3.3 showed, in general, good agreement with the thermodynamic predictions based on the 1300°C cross-section of the Mo-Si-N phase diagram [36], except when the partial pressure of N_2 was equal to 10 MPa. In the same study, however, it was observed that in the production of Si_3N_4-Mo diffusion couples at 1300°C, the external partial pressure of N_2 influenced the reaction only at the triple points where Mo, Si_3N_4, and N_2 were in contact. Away from the triple points, the interface was formed exclusively by Mo_3Si. At the triple points, both Mo_5Si_3 and $MoSi_2$ were observed along with Mo_3Si. It was concluded that in these areas the Mo-rich silicides were formed through the reaction between Mo and the more Si-rich silicides. The reaction at the triple points were not observed at 1100°C. Also, no Mo-nitride was formed, indicating that the N_2 coming from the decomposition of Si_3N_4 remained at the interface between Mo and Si_3N_4, forming a porous layer with internal pressures being estimated between 700 and 8800 kPa [36].

Additional contributions to the study of Si_3N_4-Mo couples can also be found in the literature. Whereas one investigation reported Mo_5Si_3 as the only reaction product observed when Si_3N_4 and Mo were hot-pressed at 1750°C, a second study reported, not only the formation of Mo_5Si_3, but also Mo_3Si at the interface of diffusion couples pressed at 1717°C [35]. Finally, it has been reported that the thickness of the Mo substrate

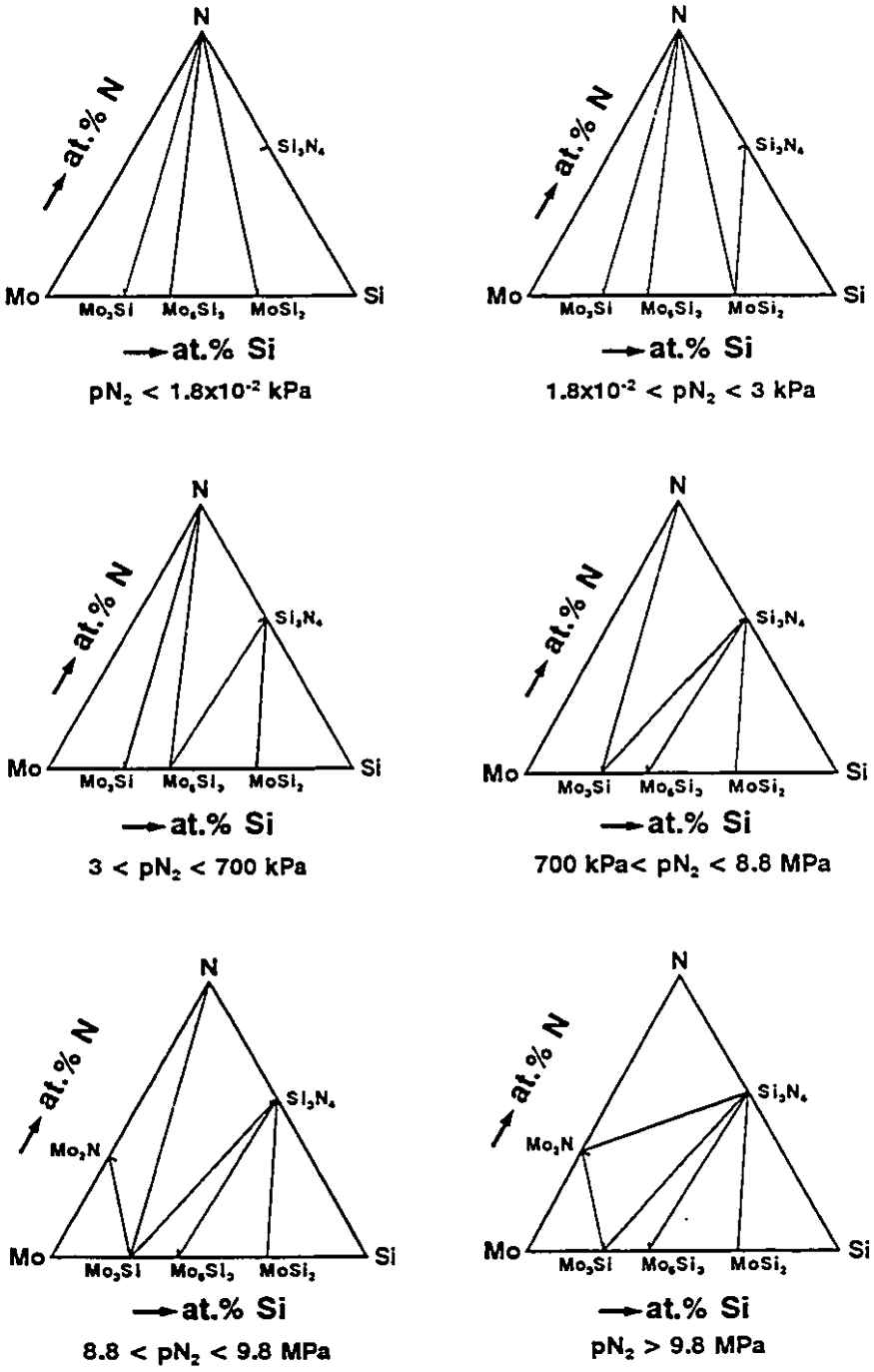

Figure 3.6- The 1300°C cross-section of the Mo-Si-N phase diagram for different partial pressures of N_2 [36].

influenced the mechanical integrity of Si_3N_4-Mo couples. When Si_3N_4-Mo couples were hot-pressed at temperatures between 1170°C and 1500°C, the presence of thermal stresses prevented the formation of reliable joints when the thickness of the Mo block was of the order of 15 mm. In that case, joining could only be achieved using a Mo-W laminate interlayer to reduce the amplitude of thermal residual stresses [10].

3.4 MOLYBDENUM CARBIDES

The Mo-C phase diagram is illustrated in Figure 3.7 [37]. The melting temperature of molybdenum is estimated to be approximately 2610°C, which is good agreement with the value given in Table AI.3 (Appendix I). At 2207°C the solubility of carbon in Mo reaches its maximum (1.1 at.%), with a marked reduction as the temperature decreases. The Mo-C phase diagram also shows that carbon forms four interstitial compounds with Mo. They have compositions Mo_2C and MoC_{1-x}, and each one has two distinct crystallographic structures. Mo_2C has an orthorhombic polymorph (α-Mo_2C) stable at low temperatures, and an hexagonal modification (β-Mo_2C) stable at high temperatures. The transformation temperature between the α and β structures depend on the concentration of carbon. As for the MoC phases, they are both non-stoichiometric carbides. The hexagonal phase (η-MoC_{1-x}) has a composition near Mo_3C_2, and is stable above 1655°C. The cubic phase (α-MoC_{1-x}) has composition near $MoC_{0.7}$, and is stable above 1860°C. A few physical and mechanical properties of Mo_2C are included in Table 3.4.

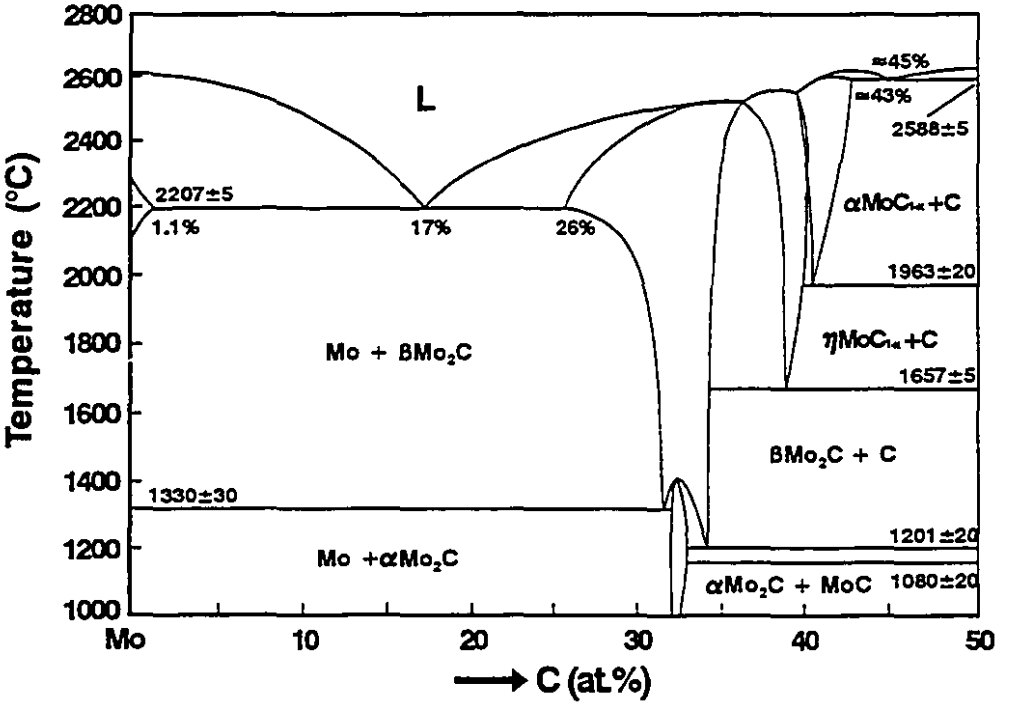

Figure 3.7- The Mo-C phase diagram [37].

Table 3.4- Properties of Mo_2C [38]

Hexagonal (ß)	Lattice Parameters	a = 7.244 Å
		c = 4.734 Å
Orthorhombic (α)	Lattice Parameters	a = 7.244 Å
		b = 6.004 Å
		c = 5.199 Å
	Density (X-Ray)	9.06 g/cm^3
	CTE (x10^{-6})	4.9°C^{-1} // a
		8.2°C^{-1} // c
	Microhardness (HV)	15 GPa
	Elastic Modulus	227 GPa at 25°C

As mentioned earlier, Mo crystallizes in a bcc structure, where two types of interstitial sites are found: the larger ones are tetrahedral sites situated at the positions (½,¼,0) and equivalents, and the smaller are distorted octahedral sites situated at the positions (0,0,½), (½,½,0) and equivalents. Figure 3.8 illustrates the geometry of the bcc interstitial sites [39].

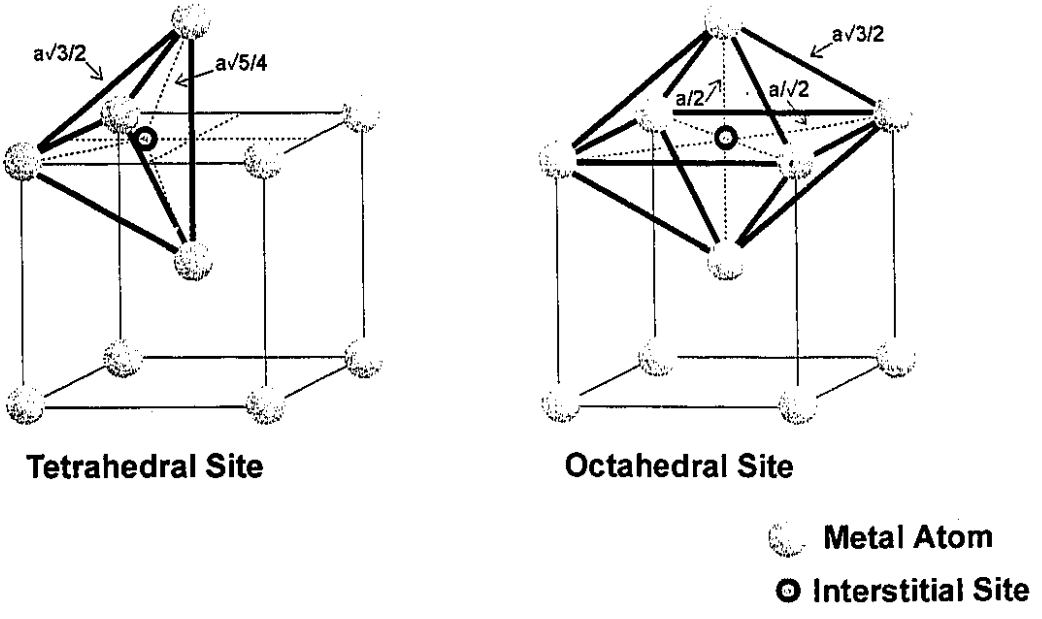

Figure 3.8- Interstitial sites in the bcc structure [39].

Carbides are usually interstitial compounds. Carbon has a preference for octahedral sites, since the tetrahedral geometry results in interstices which are too large for such a small atom. However, the octahedral sites in the Mo bcc structure are too small to accommodate carbon, which accounts for its limited solubility in Mo. In order

to provide larger octahedral sites, Mo transforms from bcc to hcp, which contains larger octahedral interstitial positions (Figure 3.9). The geometry of the new octahedral sites are adequate to accommodate carbon, and hence, the precipitation of a Mo-carbide takes place. The chemical bonding in Mo-carbides consists of a combination of metallic (Mo-Mo) and covalent (Mo-C) character. The dominating nature of the bonding changes from covalent to metallic in the series α-MoC_{1-x} → η-MoC_{1-x} → Mo_2C [40]. The Mo-C bonds are made by hybridization of Mo_{4d}-C_{2p} orbitals and they are responsible for the high hardness and brittleness of these compounds, due to their strongly localized character. As for the Mo-Mo bonds, they contribute to the high melting point and extensive concentration range and stability, characteristic of Mo-carbides [38].

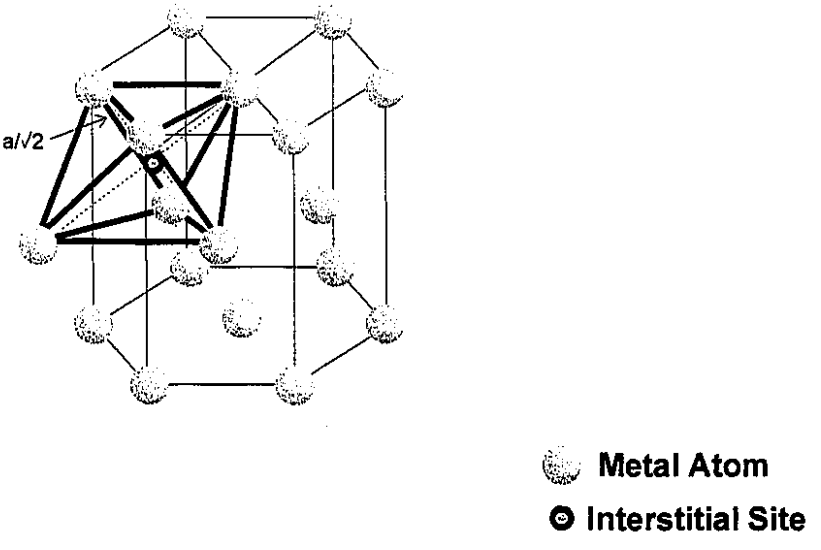

Figure 3.9- Octahedral interstitial sites of the hcp structure [39].

3.5 MOLYBDENUM SILICIDES

The Mo-Si phase diagram is illustrated in Figure 3.10. The melting point of Mo is established as 2623°C. The solubility of Si in Mo increases as the temperature increases, until it reaches 5.4 at.% at 2070°C. Two eutectic points have been observed in the Mo-Si system: one at 2070°C corresponding to 16.5 at.% Si, and another at 1410°C corresponding to 95 at.% Si. In addition, evidence of a third eutectic has been found at approximately 1900°C, and corresponding to 55 at.% Si [41].

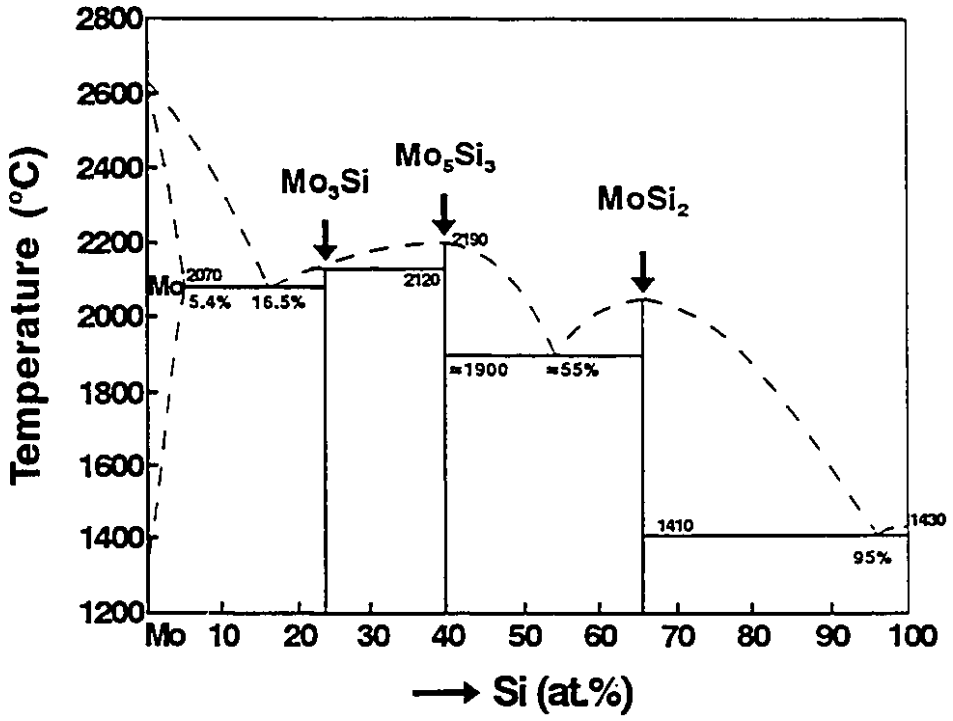

Figure 3.10- The Mo-Si phase diagram [41].

Three Mo-silicides are known. They are Mo_3Si (β-phase) with cubic symmetry, $MoSi_2$ (δ-phase), and Mo_5Si_3 (γ-phase), both with tetragonal symmetry [16]. Mo-silicides have low solubility for C. In particular, addition of C to Mo_5Si_3 stabilizes the hexagonal structure of the ternary phase with composition Mo_5Si_3C [16]. This phase is built on parallel chains of Mo_6C octahedra, with each octahedron sharing two opposite faces with its neighbour, as shown in Figure 3.11.

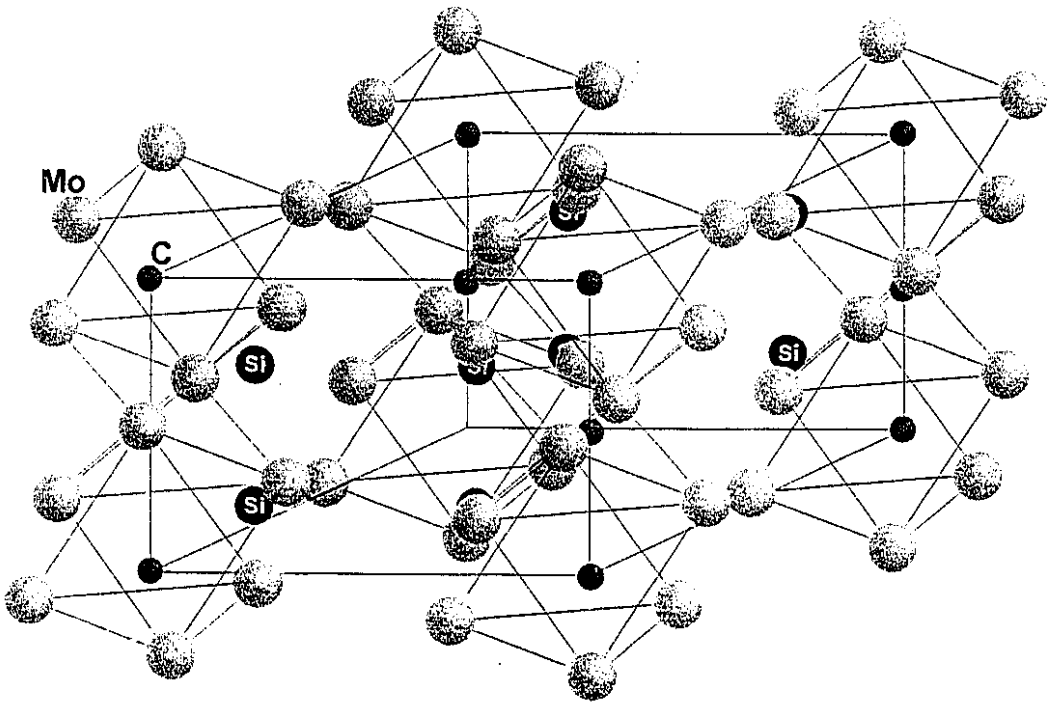

Figure 3.11- The Mo_5Si_3C structure showing its building blocks of Mo_6C [31].

Not all the interstitial sites of the Mo_5Si_3C are occupied by C atoms, resulting in a rather broad range of composition over which the compound is stable. Mo_5Si_3C is an unusual example of a Me_5Si_3 (Me = metal) structure stabilized by C. The Me_5Si_3 family contains numerous interstitial free binary phases and ternary solid solutions $Me_5Si_3(C)$, but only a few true ternary compounds. A few properties of Mo_5Si_3 and Mo_5Si_3C are contained in Table 3.5.

Table 3.5- Properties of Mo_5Si_3 [16,31,35,42] and Mo_5Si_3C [38,43]

Mo_5Si_3	Structure	Tetragonal
	Lattice Parameters	a = 9.645 Å
		c = 4.912 Å
	Melting Point	2180°C
	Density (X-Ray)	8.24 g/cm^3
	CTE ($\times 10^{-6}$)	6.4°C^{-1} (20 - 1000°C)
	Elastic Modulus	50 GPa at 1000°C
	Oxidation Resistance	-67 mg/cm^2 (1500°C/4h)
Mo_5Si_3C	Structure	Hexagonal
	Lattice Parameters	a = 7.286 Å
		c = 5.046 Å
	Density (X-Ray)	7.86 g/cm^3

CHAPTER 4:

THE MECHANICAL BEHAVIOUR OF CERAMIC-METAL JOINTS

A thorough description of the mechanical behaviour of ceramic-metal joints requires the determination of their strength along with the distribution of residual thermal stresses. This chapter reviews the basic aspects involved in evaluating the mechanical strength and residual stresses, especially for the case of hot-pressed diffusion couples.

4.1 MECHANICAL STRENGTH

The mechanical properties of hot-pressed diffusion couples depends on the properties of the joining materials (CTE, elastic modulus), joint geometry, and bonding conditions. A mechanically reliable joint is not only a strong joint, but also one characterized by small scatter in strength. Scatter in strength is mainly caused by the presence of interfacial imperfections and the occurrence of brittle debonding. Figure 4.1 schematically shows some of the common interfacial defects resulting from diffusion bonding. Among the most common interfacial deformities, unjoined or weakly bonded islands result in substantial scatter and reduction in the average joint strength. Moreover, if a reaction layer is excessively thick, cracking is also likely to occur, weakening the joint [2].

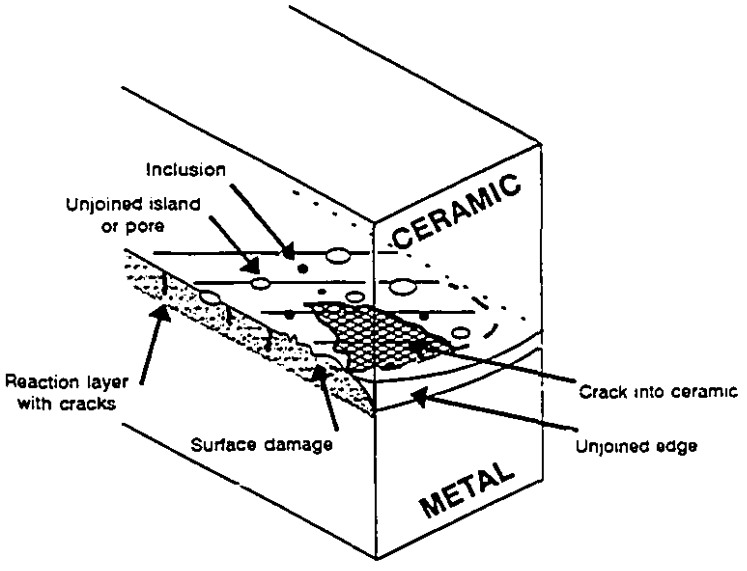

Figure 4.1- Schematic representation of interfacial flaws commonly encountered in ceramic-metal diffusion couples [2].

Several approaches have been used to measure joint strength. The most common methods include tensile, bending (or flexural), and shear tests. The schematics of these tests are illustrated in Figure 4.2. Tensile tests (Figure 4.2a) are generally performed in double joint specimens (ceramic-metal-ceramic), whereas three-point bending can be performed in both single and double joints, as shown in Figure 4.2c and Figure 4.2d. Shear tests (Figure 4.2b) can only be performed on single joints as a consequence of their intrinsic geometry.

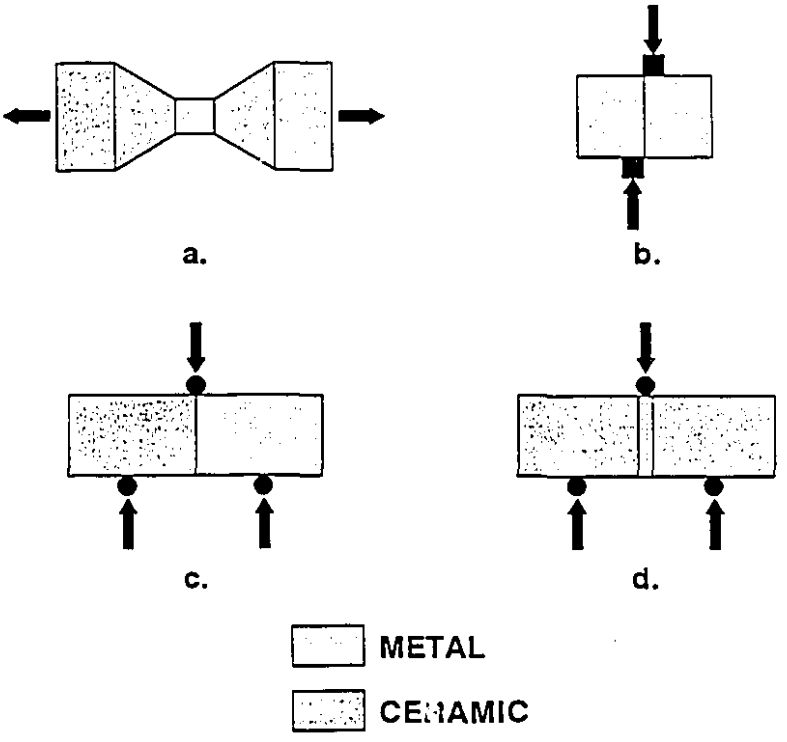

Figure 4.2- Schematics of mechanical tests performed on ceramic-metal joints. (a) Tensile; (b) shear; (c) flexural on single joint; (d) flexural on double joint [1,17].

The characterization of the interfacial strength by pull-off or shear-off tests have several limitations. The first one is related to the variety of techniques used by different research groups, making it difficult to establish a mutual comparison of results. Efforts to calculate a transferability factor from one test to another have found little success. In one attempt, tensile and three-point bend were compared for Si_3N_4-Al-Invar[1] joints [44]. The bend strength of the joint was predicted to be 1.7 times the tensile strength whereas, experimentally, a factor of 2.5 was obtained. The discrepancy was attributed to a difference between the calculated and the observed stress distributions, and to different contributions of the plastic deformation to the tensile and bend values. Similar adversities are expected when three and four-point bend tests are compared. The shear test provides an alternative way to assess the mechanical strength of interfaces. Samples are easily produced, but the results are generally lower than those obtained for bend and tensile tests.

Tensile, bend, and shear tests yield the load at which the joint ruptures. Fracture is caused by the load-induced propagation of the most severe flaw within the bonded interface. The fracture load is a function of the stress intensity at the flaw and of the crack propagation resistance of the interface. However, if the crack deviates from the interface line, the fracture becomes a function of the crack surface, limiting the accuracy of the measurement of the inherent bond strength of the interface [23].

[1]Invar: 64 at.%Fe, 36 at.%Ni.

In order to restrain the crack trajectory to the interface line, notched or pre-cracked double joints are used in three-point bending tests. Figure 4.3 illustrates the geometry of a ceramic-metal-ceramic specimen notched between the metal and one of the ceramic layers [11].

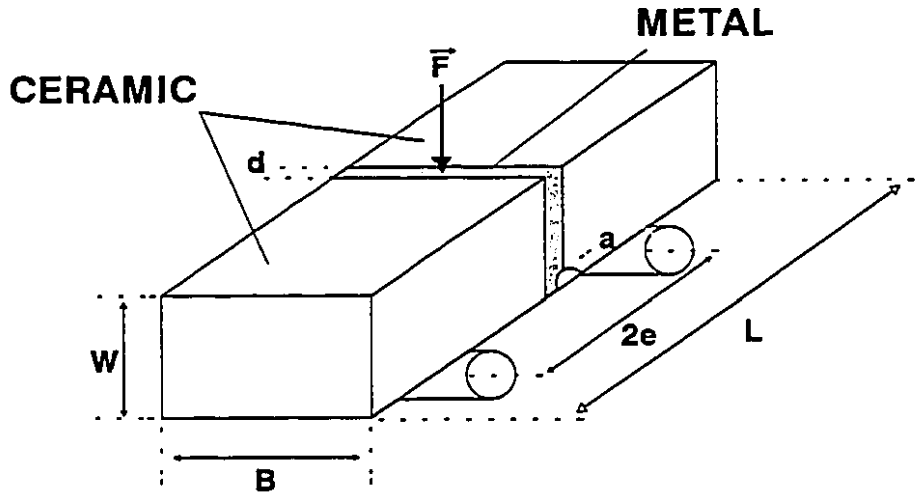

Figure 4.3- Pre-notched ceramic-metal-ceramic sample used in three-point bending tests [11].

In this approach, the measured parameter is the interfacial fracture energy G_c, obtained from the fracture load, F_c, by

$$G_c = F_c^2\left(\frac{9e^2\pi}{B^2W^3}\right)\frac{Y_G}{E^*} \qquad (4.1)$$

where e, B, and W are related to the geometry of the specimen. Y_G is a geometric correction function and E^* is the effective elastic modulus. Equation (4.1) is valid if the

load *vs.* deflexion curve is linear up to the point of rupture. The effective elastic modulus is expressed by

$$\frac{1}{E^*} = \frac{1}{16}\left(\frac{1+k_1}{\mu_1}+\frac{1+k_2}{\mu_2}\right) \qquad (4.2)$$

where μ is the shear modulus of the material, k is the stress intensity factor, and the subscripts 1 and 2 refer to the joining materials. The stress intensity factor, k, is equal to $(3\text{-}4\nu)$ for plain strain conditions, which is the case for the geometry of the sample depicted in Figure 4.3. The term ν is the Poisson's ratio of the material. The reversible fraction of G_c corresponds to the work of adhesion W_{ad}, as given by equations (2.3) and (2.4). Hence, if W_{ad} is known, it is possible to estimate the irreversible fraction of G_c, which is the dissipated energy that accompanies interface fracture [11]. Once G_c is obtained, a fracture resistance parameter K_c can be calculated according to

$$K_c = [E^* G_c/(1-\beta^2)]^{1/2} \qquad (4.3)$$

where β is one the Dundurs parameters [45]. If the crack tip region is small compared with the crack length, the interface fracture energy does not depend on the crack tip model, and K_c can be considered a material property [11]. Accurate measurements of G_c can be obtained if residual stresses, crack trajectories, and pre-cracking are carefully controlled.

One problem with this method is in the production of samples using a hot-press equipment. Because of their geometry and typical dimensions, samples have to be pressed individually, which can lead to differences in the experimental conditions from one

specimen to another. In addition, it is difficult to measure the dihedral angle necessary to calculate W_{ad}, particularly if a reaction zone is present. Reactive systems frequently fracture in a brittle manner, leaving chips of interfacial material attached to the original components (metal and ceramic), which prevents an accurate assessment of the dihedral angle. Finally, very little work has been done on the determination of fracture resistance parameters, which prevents comparison of results. Consequently, shear tests were performed on the joints produced in this work. Shear tests usually yield results which are lower than in tensile and bending tests. The reason for this is in the parameter that relates test geometry to crack trajectory, namely the phase angle of loading ψ [11]. In the case of two brittle solids, ψ is given by

$$\psi = tan^{-1}(k_{II}/k_I) \tag{4.4}$$

where k_I and k_{II} are the mode I and mode II stress intensity factors as shown in Figure 4.4.

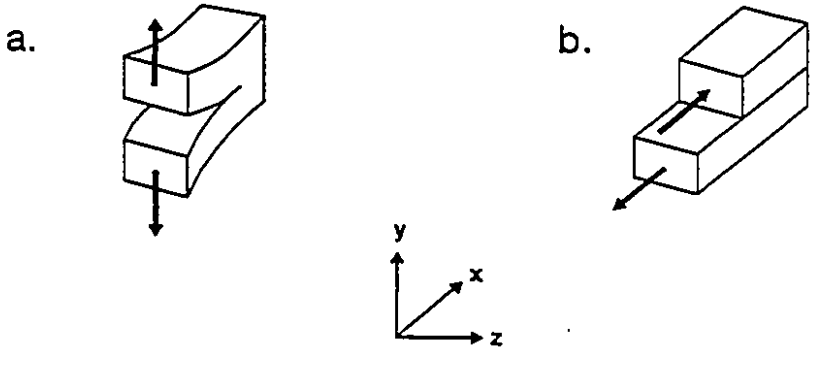

Figure 4.4- (a) Mode I and (b) mode II loading corresponding to the *Re(k)* and *Im(k)* in $k = k_I - ik_{II}$ [1].

Since $\psi = 0$ for mode I loading and $\pi/2$ for pure mode II, ψ is directly related to the fraction of mode II loading on the interface crack [11]. Different specimen geometries provide different phase angles, which results in different dominant stress states, according to Figure 4.5. Notably, if the sample is subjected to shear loadings, the crack tends to deviate from the interface into the ceramic, resulting in lower values for interfacial strength [40].

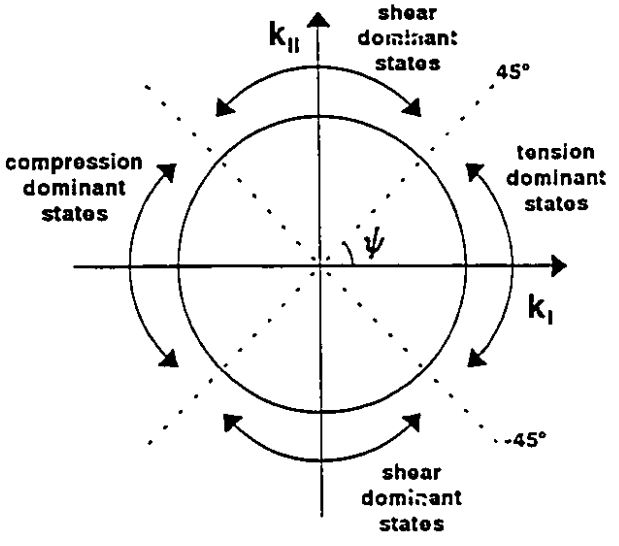

Figure 4.5- Stress dominant states as a function of the phase angle ψ [46].

Ceramic-metal interfaces can fracture in a ductile or brittle fashion depending on the joining materials and the type of interface. If a reaction zone is present, its mechanical properties also influence the fracture mode. Figure 4.6 illustrates the most

common fracture mechanisms observed in ceramic-metal systems.

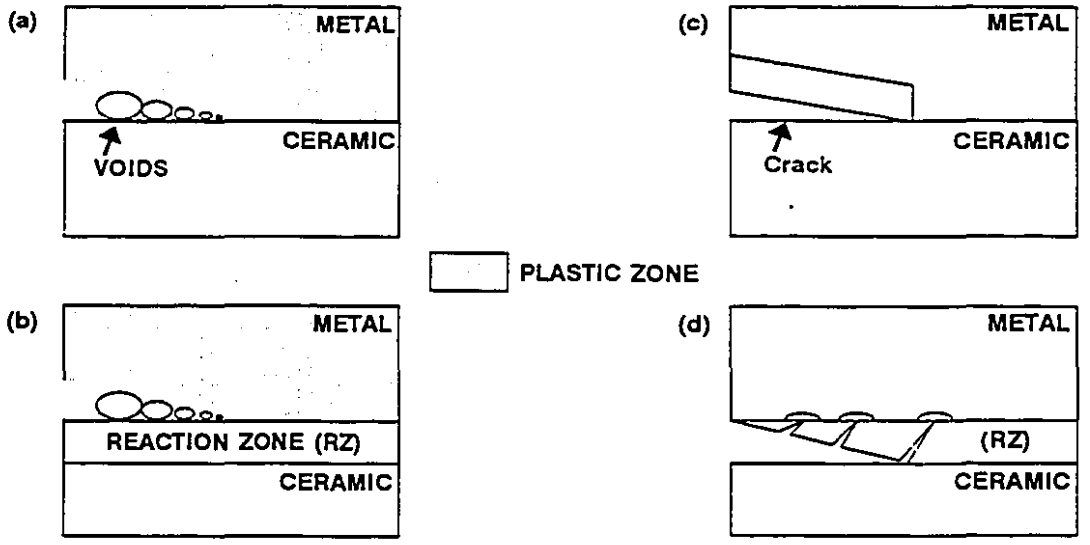

Figure 4.6- Fracture mechanisms of ceramic-metal interfaces: (a) and (b) ductile fracture; (c) and (d) brittle fracture [24].

Only a small number of systems fracture in a ductile way. Examples include the Al_2O_3-Al (non-reactive), and the Al_2O_3-Al/Mg (reactive) systems [24]. Ductile fracture occurs by nucleation and coalescence of voids, caused by plastic flow of the metal in the region adjacent to the interface, as shown in Figure 4.6a. The majority of metal-ceramic combinations fracture by brittle debonding. Systems such as Al_2O_3-Nb, Al_2O_3-Pt, and SiO_2-Cu are examples of non-reactive systems that fail by brittle debonding, whereas

SiC-Ni is a reactive system that fractures in the same fashion. Brittle debonding differs from ductile fracture in the sense that no metal remains attached to the ceramic, indicating that the crack propagates at the interface plane by bond rupture (Figure 4.6c). However, if the diffusion couple consists of a ductile metal and a brittle ceramic, the fracture behaviour also becomes sensitive to the sign of the phase angle. Figure 4.7 illustrates this situation.

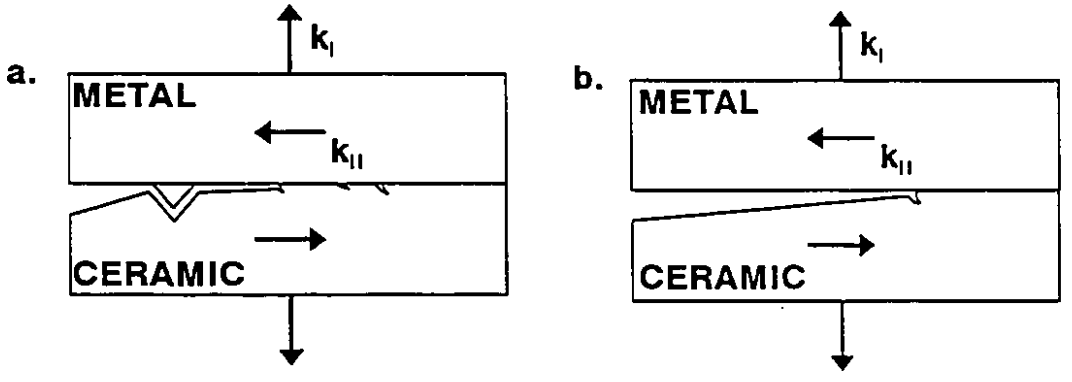

Figure 4.7- Interfacial fracture mode of ductile metal-brittle ceramic diffusion couple as a function of the phase angle ψ. (a) $\psi < 0$; (b) $\psi > 0$ [11].

When the phase angle is positive, the crack path is influenced by its magnitude. The crack moves away from the interface, preferentially into the brittle material, as ψ approaches 70°. On the other hand, if ψ is negative, the usually large fracture energy of the metal compared with the interface, prevents the propagation of the crack out of the

interface. In this case, one of two possibilities occurs depending on the yield strength of the ductile metal. If the yield strength of the metal is low, plastic blunting of the interface cracks leads to ductile fracture involving hole nucleation at the interface. Alternatively, if the metal has a high yield strength, the stress field of the interface crack interacts with pre-existing flaws in the brittle ceramic. Because these flaws are subject to substantial mode II loading, the crack is deviated back towards the interface. As a result, chips of the ceramic remain attached to the fracture surface [11].

4.2 RESIDUAL STRESSES

The amplitude and distribution of residual stresses in a joint depends on parameters such as CTE and elastic modulus of the metal and ceramic. Geometry of the joint, bonding temperature, and thickness of reaction layers also have an important influence. The presence of residual stresses not only limits the strength of a joint, but also increases the scatter in strength [2]. High concentrations of residual stresses are generally found close to the interface and to the free surface. In cylindrical samples, the amplitude of stresses increases with the diameter of the joint. For the rectangular geometry, the corners of the bond faces act as points of high stress concentration.

The presence of residual stresses in ceramic-metal joints with rectangular geometry can be visualized in Figure 4.8 [47]. Residual stresses do not form during heating of the ceramic-metal system, since the materials are not constrained. However, upon cooling from the joining temperature, the metal develops a smaller lateral

dimension than the ceramic, because of its larger CTE. As a result, large tensile stresses are formed in the direction parallel to the interface (in-plane component, σ_x), especially close to the ceramic side. To counteract this effect, compressive in-plane stresses originate in the vicinity of the interface, on the ceramic side. Along the edges of the joint, high stress intensities are also created, especially in the direction perpendicular to the interface (normal component, σ_z). Large shear stresses (τ_{xz}) occur in that region, as well. In addition, a mismatch in elastic modulus of the joining materials contributes to the formation of tensile stresses at the edge, enhancing the propensity to fracture. Thus, a substantial mode II contribution to edge failure is expected in all situations [11].

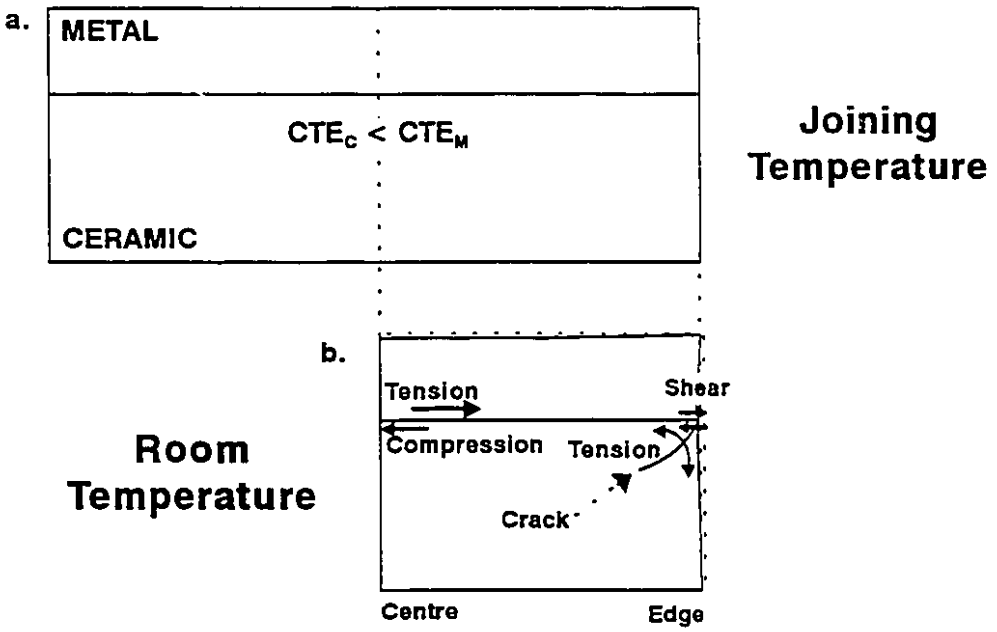

Figure 4.8- Residual stresses in rectangular single joints. (a) Stress-free joint at the joining temperature; (b) stresses developed during cooling [47].

The vectors of the principal stresses, σ_1 and σ_2, are obtained from measurements of σ_x, σ_z, and τ_{xz} according to

$$\begin{pmatrix}\sigma_1\\ \sigma_2\end{pmatrix} = \frac{1}{2}(\sigma_x+\sigma_z)\pm\frac{1}{2}[(\sigma_x-\sigma_z)^2+4\tau_{xz}^2]^2 \qquad (4.5)$$

Figure 4.9 shows an example of a typical distribution of σ_1 and σ_2 as a function of the relative position and orientation with respect to the interface. The stresses were estimated using FEM analysis on Si_3N_4-SM50 stainless-steel joints. The bonding temperature was set at 700°C [48].

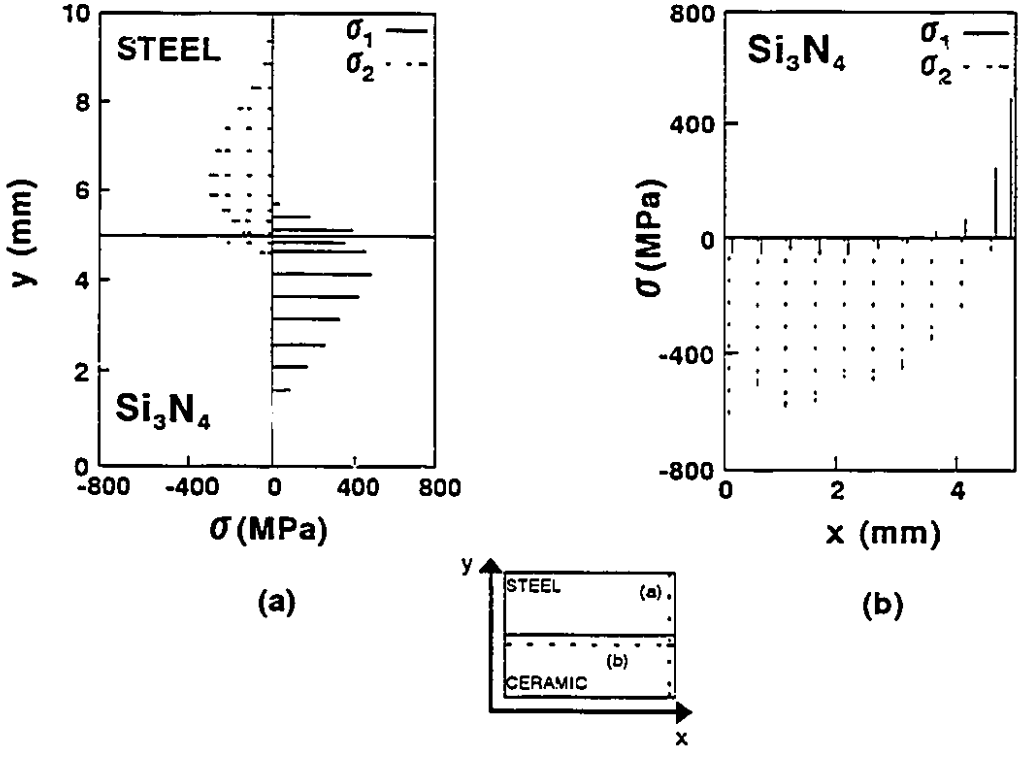

Figure 4.9- Distribution of σ_1 and σ_2 in diffusion couples of Si_3N_4-SM50 [48].

According to Figure 4.9a, σ_1 reaches its maximum close to the edge of the sample, where the ceramic is subjected to large tensile stresses. The σ_2 component is strongly compressive in the ceramic side along the bond line (Figure 4.9b). Consequently, the position where σ_1 reaches its maximum determines the most probable location for crack initiation, and the direction of crack propagation is governed by σ_2 [48]. Therefore, it is important to minimize σ_{1max} in order to inhibit crack initiation, thus improving the average strength of the joint, and reducing scattering. Several methods have been studied to achieve this objective, such as the use of interlayers, and the optimization of the joint geometry [48].

Interlayers are used to minimize the CTE mismatch between ceramics and metals, thus reducing the amplitude of residual stresses. One of the approaches is the graded-α technique, where a number of buffer layers are inserted between the metal and the ceramic (Figure 4.10). By controlling the composition of each layer, it is possible to adjust the individual CTEs to closely matched values [17]. Although this configuration can be easily produced in hot-press equipment, a large number of layers are necessary and their thermal expansion behaviour must be well understood. Another possibility is the use of a metallic interlayer with a closely matched CTE to that of the ceramic, and relatively low yield strength and high ductility. Refractory metals, such as molybdenum (Mo) and tungsten (W), are a few candidates.

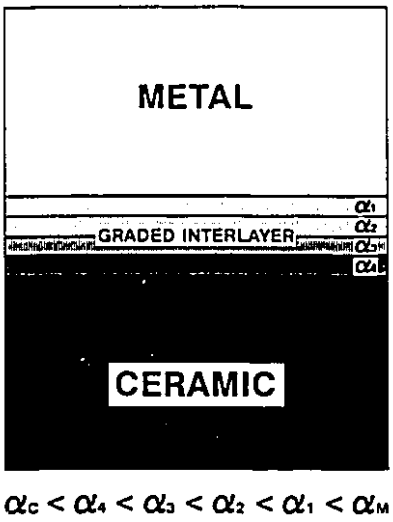

Figure 4.10- Graded-α attachment technique used to reduce the thermal expansion mismatch between ceramic and metal [17].

The geometry of the sample can also be optimized to reduce the formation of residual stresses. The effect of geometry change on σ_{1max} is shown in Figure 4.11. Inserting the metal between the ceramic substrates reduces σ_{1max} by 30% (Figure 4.11a). Instead, if a ceramic interlayer is inserted between metal substrates, σ_{1max} increases by 35% of the original value. Another possibility is to change the neutral axis of bending, which affects the bending moment. In the geometry illustrated in Figure 4.11b, σ_{1max} decreases by 15%, and in Figure 4.11c by 40%. When the ceramic and metal substrates are reversed in Figure 4.11c, σ_{1max} increases by 13% of the original value because σ_{1max} is further from the bond line, which increases the bending moment [48].

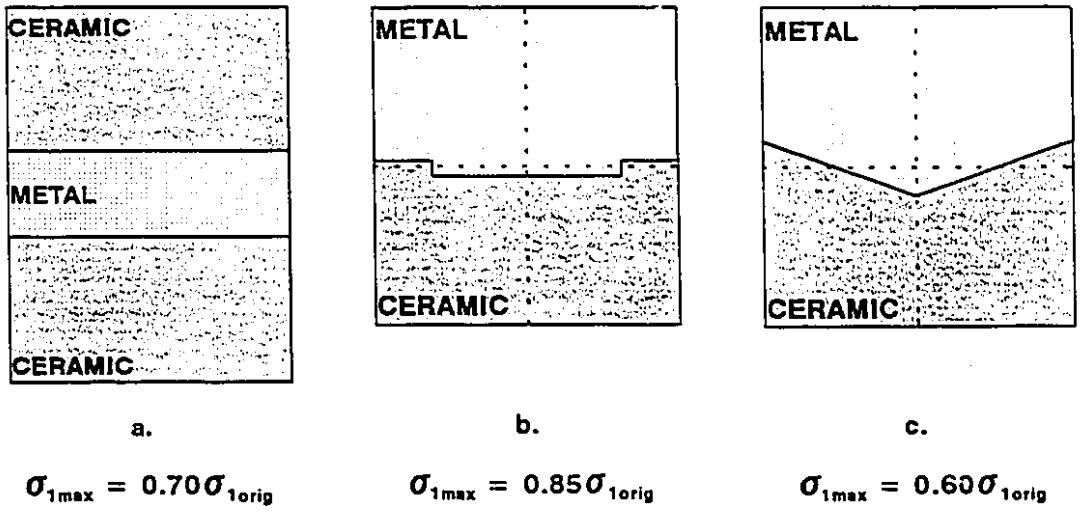

Figure 4.11- Effect of joint geometry on σ_{1max}. (a) Double joint; (b) and (c) change in neutral axis of bending. Values of σ_{1max} are compared to that of a single joint with straight interface (σ_{1orig}) [48].

Several methods can be used to evaluate the distribution of residual stresses in ceramic-metal joints. The most common techniques are the finite element method (FEM), X-ray diffraction (XRD), and neutron diffraction. FEM is a numerical approach where the properties of the ceramic and metal are used along with the joining conditions, to obtain a computerized map of the stress distribution in the joint. The disadvantage of this technique is that it does not take into consideration the effect of the reaction layer and the properties of the reaction products into the final results. The thickness and nature of reaction zones can affect drastically the distribution of residual stresses, and therefore the mechanical strength of the joint.

Diffraction techniques are also employed to evaluate residual stresses. They are based on a change of the position of the diffraction peaks as a result of strain. Combining the strain measurements with the properties of the ceramic and metal, it is possible to calculate the stresses to which the material is exposed. XRD is a non-destructive technique more popular than neutron diffraction, as a result of the availability of equipment. However, one serious limitation results from the poor penetration of X-rays, which restricts the stress analysis to the surface of the material. Neutron diffraction is also a non-destructive method used to measure residual stresses in engineering materials. The technique is similar to XRD, however, neutrons have higher penetration than X-rays, making it possible to determine bulk properties rather than surface effects [49]. This technique was employed to obtain the stress distribution of the SiC-Mo diffusion couples hot-pressed in this work.

CHAPTER 5:

OBJECTIVES

The interaction between SiC and Si_3N_4 with Mo has not yet been thoroughly investigated. However, Mo is an important material from the standpoint of integrating monolithic ceramics into engineering devices, as well as developing ceramic-metal composites.

Previous studies have addressed the problem of joining SiC and Si_3N_4 to Mo. Nevertheless, a variety of different techniques have been used, which prevents a mutual comparison of results. Moreover, fundamental aspects of the subject have been

overlooked. In particular, questions concerning the evolution of the microstructure of the interfaces and its relation to the mechanical properties of the joints remain unanswered.

In addition, no study has been conducted on the determination of residual stresses by neutron diffraction on hot-pressed SiC-Mo and Si_3N_4-Mo joints. Estimates of the distribution of residual stresses in hot-pressed diffusion couples have been made for similar systems, such as Si_3N_4-stainless steel, however, the finite element method has been used. Despite the fact that numerical models usually provide reliable approximations, important aspects such as the presence of reaction zones, incomplete bonding, and the rate employed to cool the joints from the bonding temperature are not taken into account.

Finally, very little attention has been paid to the production of hot-pressed diffusion couples using these materials, yet, this technology can become available if a basic understanding of the optimum joining parameters is obtained. In summary, it is necessary to establish a complete guide on the fabrication and characterization of hot-pressed SiC-Mo and Si_3N_4-Mo joints. Only with that information will it be possible to turn these systems into effective ceramic-metal combinations for structural applications.

This work addresses some of the aspects of joining SiC and Si_3N_4 to Mo by solid-state diffusion, using the hot-uniaxial pressing technique. The optimum parameters were studied in relation to the mechanism of interface formation, and joint strength. In addition, residual stresses were also determined for SiC-Mo joints by neutron diffraction. The main steps followed during this work are summarized as follows:

1. Prepare a series of hot-pressed SiC-Mo and Si_3N_4-Mo diffusion couples using commercially available materials, and vary production parameters such as joining temperature, bonding time, cooling rate, surface roughness, and atmosphere (for the Si_3N_4-Mo system).
2. Investigate the microstructural evolution of the ceramic-metal interfaces and compare the results with thermodynamic analyses carried out for both the SiC-Mo and Si_3N_4-Mo systems.
3. Measure joint strength by shear testing and the mechanical properties of the interfacial reaction products using a novel nanoindentation technique.
4. Correlate the microstructure of interfaces with joint strength.
5. Evaluate residual stresses by neutron diffraction and investigate ways to minimize the amplitude of those stresses.

CHAPTER 6:

EXPERIMENTAL TECHNIQUES, ANALYSIS AND CHARACTERIZATION OF DIFFUSION COUPLES

The bonding characteristics of SiC-Mo and Si_3N_4-Mo joints were investigated. Initially, the thermodynamic behaviour of these systems was studied, followed by hot-pressing, microstructural analysis of the ceramic-metal interfaces, and characterization of the mechanical properties of the joints. This chapter describes the main techniques used to carry out these analyses, as well as the equipment employed for the production and characterization of ceramic-metal diffusion couples.

6.1 THERMODYNAMIC ANALYSIS

Thermodynamic analyses of SiC-Mo and Si_3N_4-Mo systems were performed with the aid of a computer program named F*A*C*T (Facility for the Analysis of Chemical Thermodynamics). The results obtained from this automated database were used in conjunction with available literature information, and isothermal cross-sections of Mo-Si-C and Mo-Si-N phase diagrams.

F*A*C*T is a program capable of performing thermochemical calculations and supplying thermodynamic properties of various stoichiometric compounds and binary solutions [50]. The analyses carried out herein were based on the routine REACTION to calculate the standard Gibbs free energy for the formation of Mo-Si-C and Mo-Si-N compounds (ΔG^0). REACTION calculates changes in extensive thermochemical functions such as enthalpy (H), entropy (S), internal energy (U), and Gibbs free energy (G) for a specified change in the state of a system. The input consisted of a balanced chemical equation and a subscript line to specify the temperature, hydrostatic pressure, phases, and activities of each reactant and product. According to data retrieved from the F*A*C*T database, a tabular print-out was generated, containing the change in the required thermodynamic properties of the system for a particular temperature or range of temperatures.

For the Mo-Si-C system, ΔG^0 for the formation of SiC was obtained and plotted along with ΔG^0 for the formation of Mo-Si (Mo_3Si, Mo_5Si_3, $MoSi_2$), and Mo-C (Mo_2C, MoC) compounds. Temperatures up to 1800°C were investigated, and a hydrostatic

pressure of 0.01 atm. (minimum value accepted by F*A*C*T) was chosen to simulate vacuum conditions. The values of ΔG^0 were normalized for 1 mol of SiC, *i.e.*, the formation of any reaction product corresponded to the decomposition of the same amount of SiC. A similar procedure was followed for the Mo-Si-N system. The ΔG^0 for the formation of Si_3N_4 was obtained and plotted along with the ΔG^0 for the formation of Mo-Si (Mo_3Si, Mo_5Si_3, $MoSi_2$), and Mo-N (Mo_2N) compounds. Temperatures up to 2000°C were studied along with pressures of 0.01 and 1 atm. In the latter case, $N_{2(g)}$ was included as a reactant to simulate joining in a N_2 atmosphere. The values of ΔG^0 were normalized for 1 mol of Si_3N_4.

6.2 STARTING MATERIALS

The starting materials used in the preparation of diffusion couples were pressureless sintered α-SiC Hexoloy grade SA™ (Carborundum Co., Niagara Falls, USA), Ceralloy 147-3® Needlelok Si_3N_4 (Ceradyne Inc., Costa Mesa, USA), and Mo sheet 99.95% pure (Johnson & Matthey, Toronto, Canada). SiC was sintered by the manufacturer using small amounts of carbon (C) and boron (B) as additives. A sample taken from one of the plates was analyzed by X-ray diffraction (XRD) using Cu$K\alpha$ radiation. The resulting spectrum, shown in Figure 6.1, revealed that the plates consisted of hexagonal α-SiC polymorph 6H with a slight texture in the (103) and (116) planes. Table 6.1 contains a few physical and chemical properties of this material, relevant to this work [50,51].

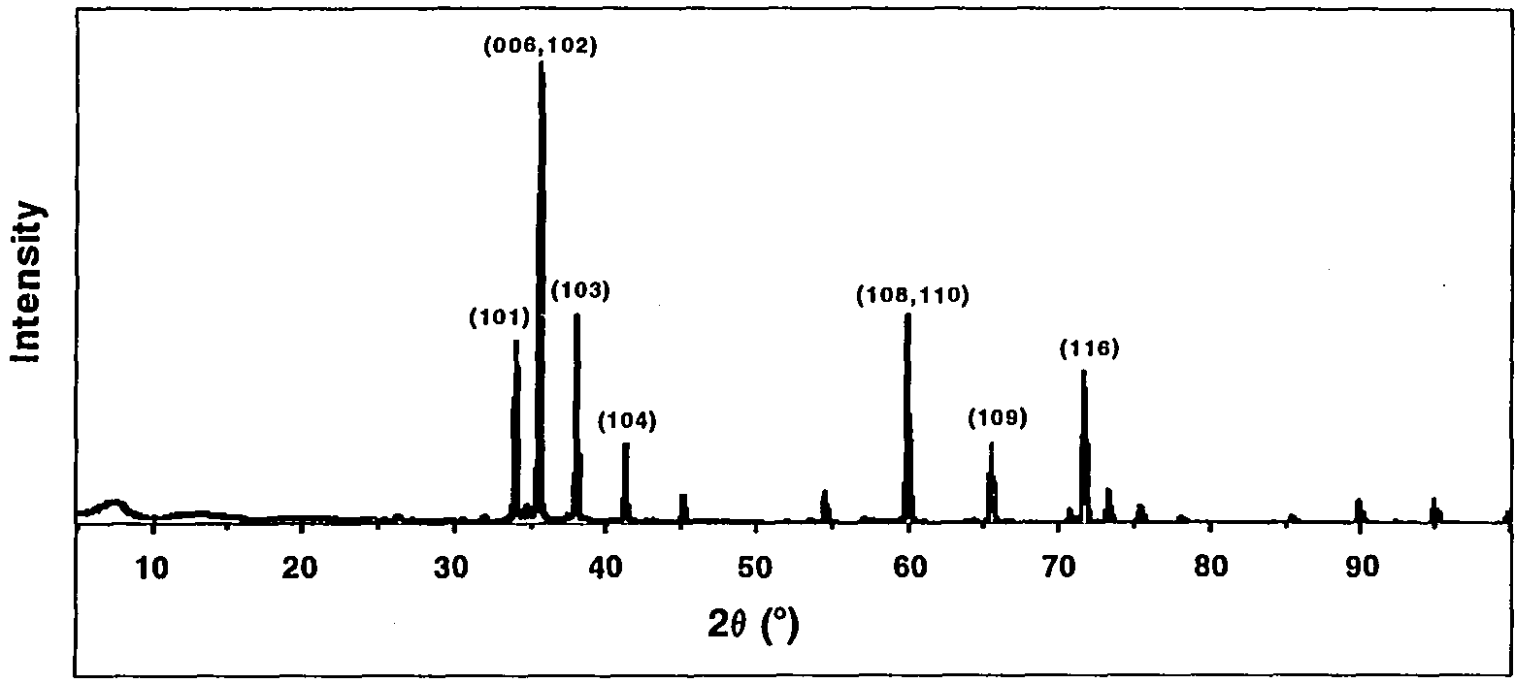

Figure 6.1- XRD pattern of Carborundum α-SiC.

Table 6.1- Properties of Carborundum Sintered α-SiC [51,52]

Physical Properties	
Decomposition Temperature	2300 - 2500°C
Density	3.13 g/cm^3 (97.5% Theoretical Density)
CTE	4.5×10^{-6}°C^{-1} (20°C - 1000°C)
Mechanical Properties	
Elastic Modulus	414 GPa at RT
Modulus of Rupture	335±55 MPa at RT
Vickers Microhardness	33.00 GPa
Poisson's Ratio	0.14

The variety of Si_3N_4 used in this work was sintered reaction-bonded β-Si_3N_4 (SRBSN) Ceralloy® 147-3. This material was produced by adding the sintering additives Al_2O_3 and Y_2O_3 to silicon, prior to shaping. The material was then nitrided, as for reaction-bonded Si_3N_4 (Appendix I), and fired in N_2 at temperatures between 1800 and 2000°C, using a protective powder-bed consisting of boron nitride (BN). The final product achieved 99% of the theoretical density with reduced linear shrinkage. Table 6.2 shows some of the properties of Ceralloy® 147-3 [53]. A sample of Ceralloy® 147-3 was also analyzed by XRD (Figure 6.2). The diffraction pattern indicated the presence of β-Si_3N_4, and an additional crystalline phase having composition $Si_3N_4 \cdot Y_2O_3$. The latter was identified as N-melilite, an intergranular phase often found in Y_2O_3 sintered Si_3N_4. Although Al_2O_3 was also used as a sintering additive, no peaks corresponding to any

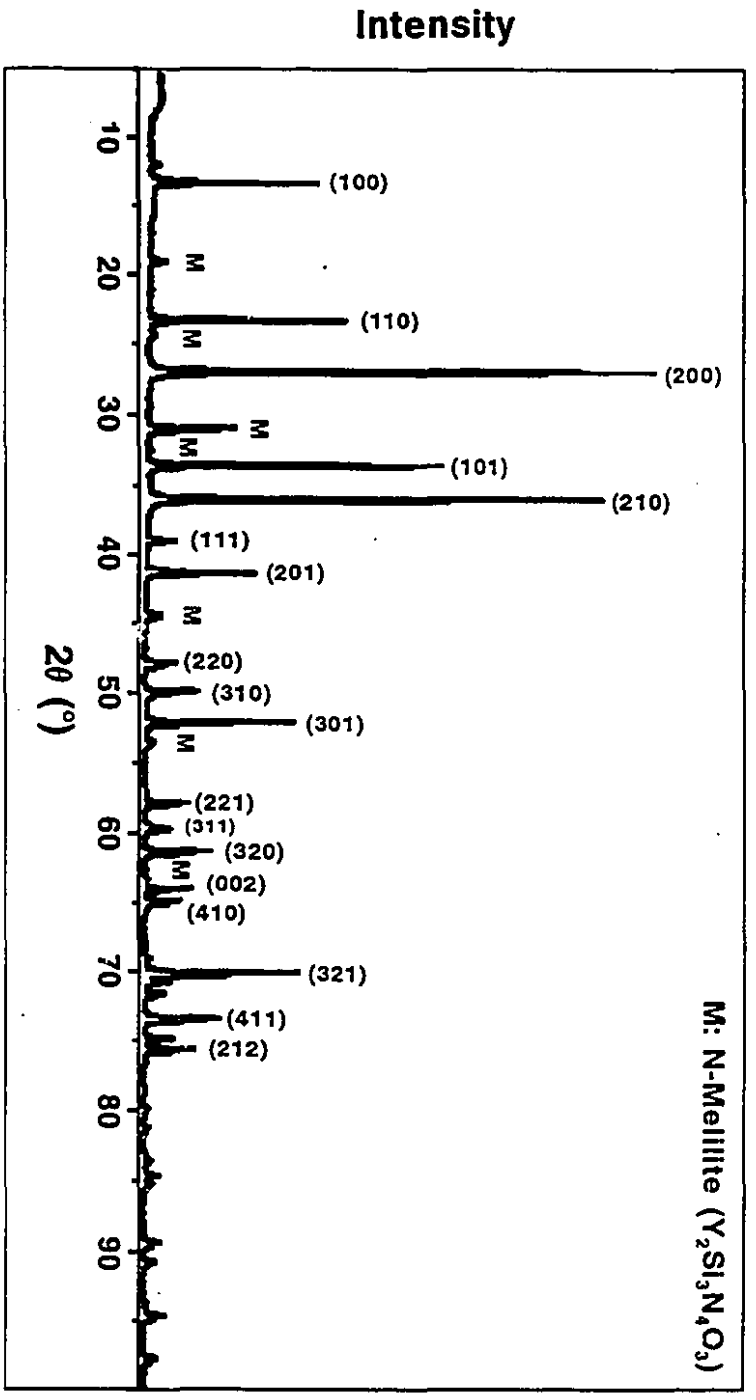

Figure 6.2- XRD pattern of Ceralloy 147-3 Si_3N_4.

other compound were found, possibly indicating the presence of a vitreous intergranular phase containing both Al_2O_3 and SiO_2.

Table 6.2- Properties of Ceralloy 147-3 Si_3N_4 [53]

Physical Properties	
Density	3.30 g/cm^3 (99.3% of Theoretical Density)
CTE	3.5×10^{-6}°C^{-1} (20°C - 1000°C)
Thermal Conductivity	35 W/m.K at RT 17 W/m.K at 1000°C
Mechanical Properties	
Elastic Modulus	320 GPa at RT
Modulus of Rupture	800 MPa at RT 737 MPa at 1000°C 545 MPa at 1200°C 366 MPa at 1400°C
Vickers Microhardness	15.5 GPa
Poisson's Ratio	0.28
Fracture Toughness	6.0 - 7.5 MPa$\sqrt{m}$

A collection of properties for the rolled Molybdenum sheets supplied by Johnson & Matthey is shown in Table 6.3 [54]. XRD was also performed, confirming the bcc structure and high purity of the material (Figure 6.3). At high values of the diffraction angle, it was visible that some of the doublets were resolved due to the different angles of diffraction corresponding to CuKα_1 and CuKα_2 wavelengths [55].

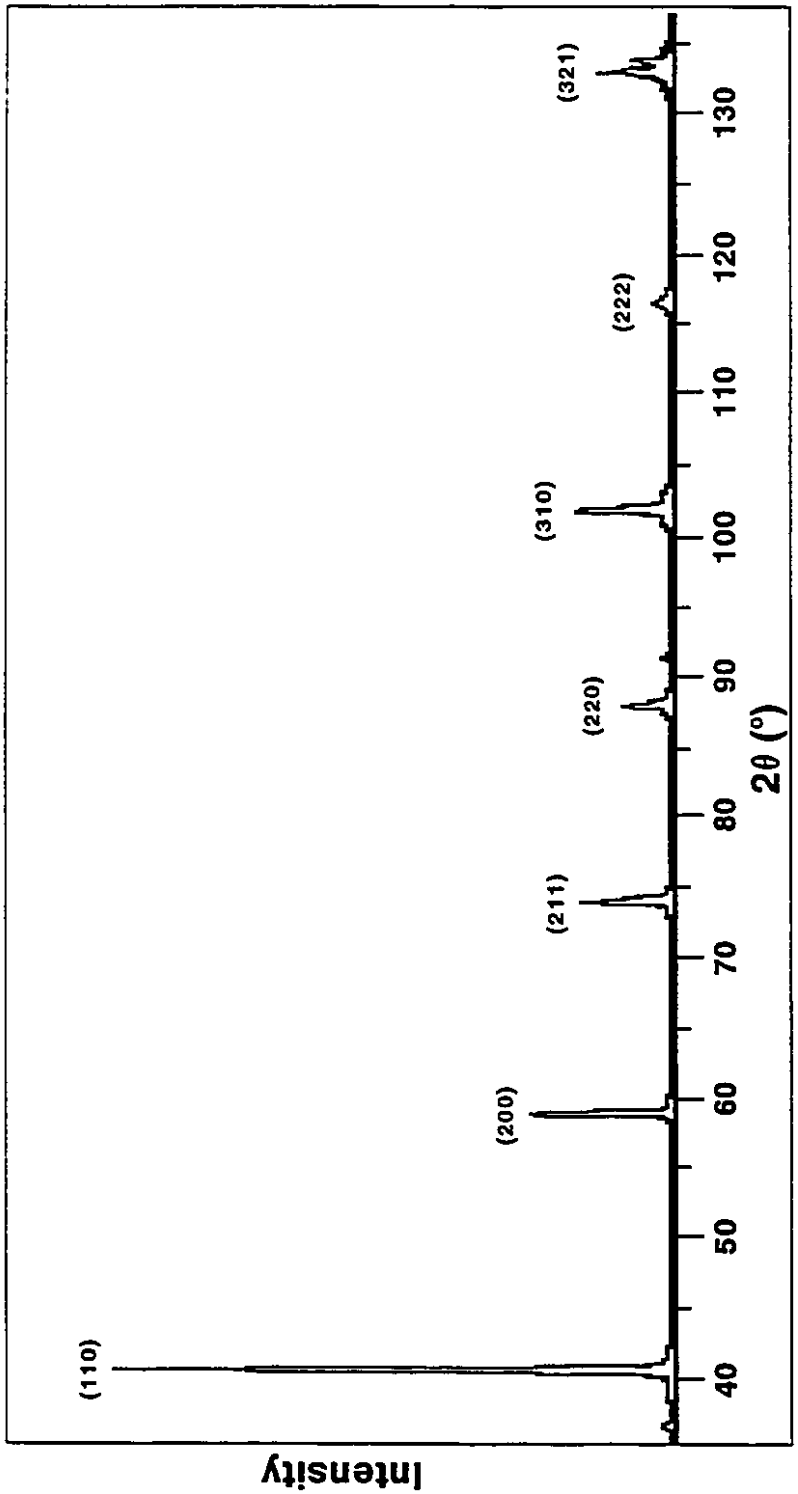

Figure 6.3- XRD spectrum of rolled Mo-sheet.

Table 6.3- Properties of Rolled Molybdenum Sheet [54]

Physical Properties	
Melting Point	2622±10°C
Density	10.14 g/cm^3
CTE	5.35x10^{-6}°C^{-1} (20°C - 1600°C)
Electrical Resistivity	5.65x10^{-6} Ω.cm at RT 35.2x10^{-6} Ω.cm at 1130°C
Thermal Conductivity	124.77 W/m.K at RT
Mechanical Properties	
Elastic Modulus	324 GPa at RT 289 GPa at 540°C 262 GPa at 1100°C 103 GPa at 1650°C
Vickers Microhardness	2.30 GPa
Poisson's Ratio	0.324

6.3 JOINING EXPERIMENTS

Joining experiments started with the preparation of the diffusion couples. SiC and Si_3N_4 were supplied as plates of 150x150x6 mm^3 and 20x20x5.4 mm^3 respectively, and Mo was supplied as 50x50x2.5 mm^3 rolled sheets. The original plates were cut into small blocks having a cross-section 9.0x9.0 mm^2 and the thicknesses of the supplied plates, using a diamond blade and a high-speed wafering saw. The surfaces to be joined were then ground and polished with 1.0 μm diamond paste finish and cleaned with isopropanol in an ultrasound probe for 5 minutes. The diffusion couples consisted of a block of SiC

or Si_3N_4 mounted axially with a block of Mo such that their polished surfaces were in contact. The experimental apparatus used to join the diffusion couples consisted of a hot-press, a rotary vacuum pump, and a N_2 gas supply, as depicted in Figure 6.4.

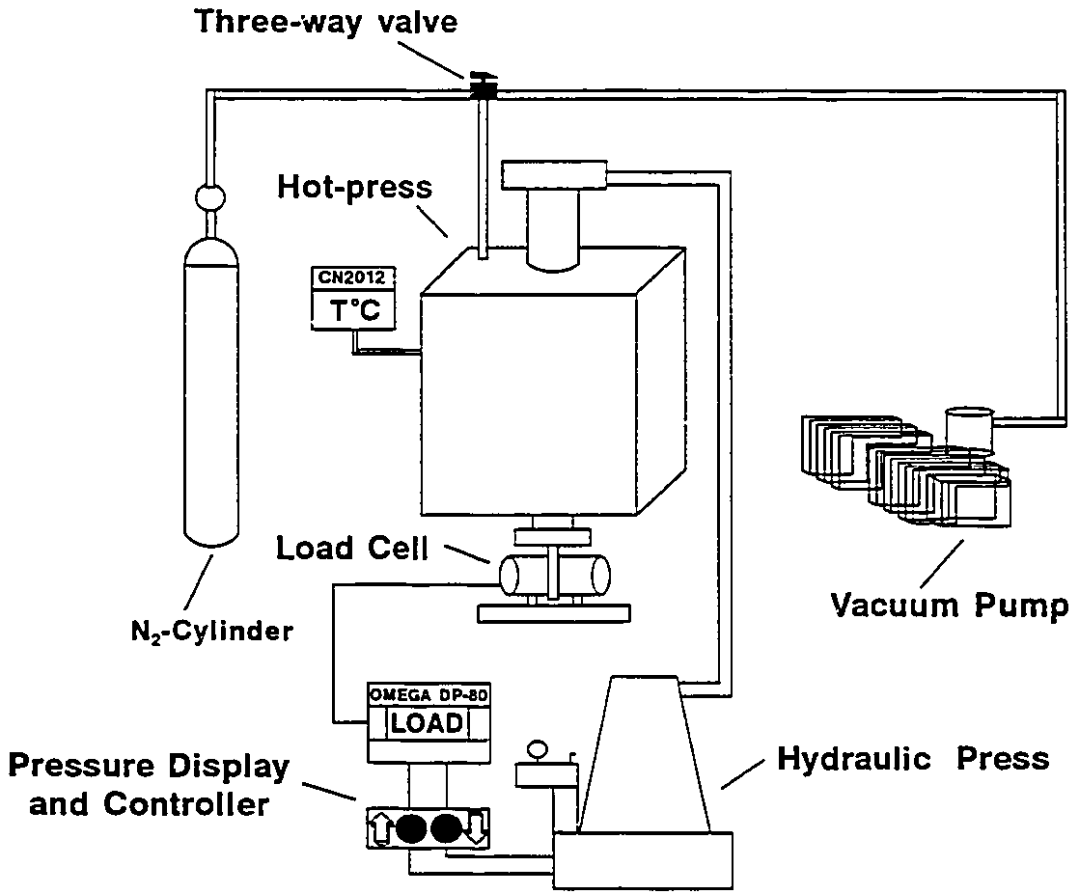

Figure 6.4- Experimental apparatus used to join SiC and Si_3N_4 to Mo.

Once a diffusion couple was assembled, it was then positioned in the furnace. Individual samples were inserted in a graphite die and embedded in BN powder 99.5% pure (Johnson & Matthey, Toronto, Canada). The role of the powder-bed was to avoid

contact between the sample and the internal walls of the graphite die, and to aid in the distribution of the hydraulic pressure applied to the sample. The graphite die containing the sample and the powder-bed was then placed in-line with the remaining graphite punches. Figure 6.5 shows a schematic representation of the sample assembly and the hot-press chamber. The sample holder and punches used to apply the uniaxial load to the diffusion couple were manufactured from a graphite grade used especially for hot-pressing applications (AQ-30, Speer Canada, Montreal). Table 6.4 shows some of the properties of this material [56].

Table 6.4- Properties of Graphite Speer Grade AQ-30 [56]

Density	1.75 g/cm^3
Compressive Strength	98.5 MPa
Thermal Conductivity	105 W/m.K
CTE	3.5×10^{-6} °C^{-1}
Ash Content	100 ppm

The pressure applied to a sample during hot-pressing was provided by a hydraulic pump ENERPAC IPE-2560 and monitored by a load cell placed underneath the furnace (Figure 6.4). This load cell generated an output voltage signal that was sent to an OMEGA DP-80 digital display. Calibration of the load cell was performed periodically

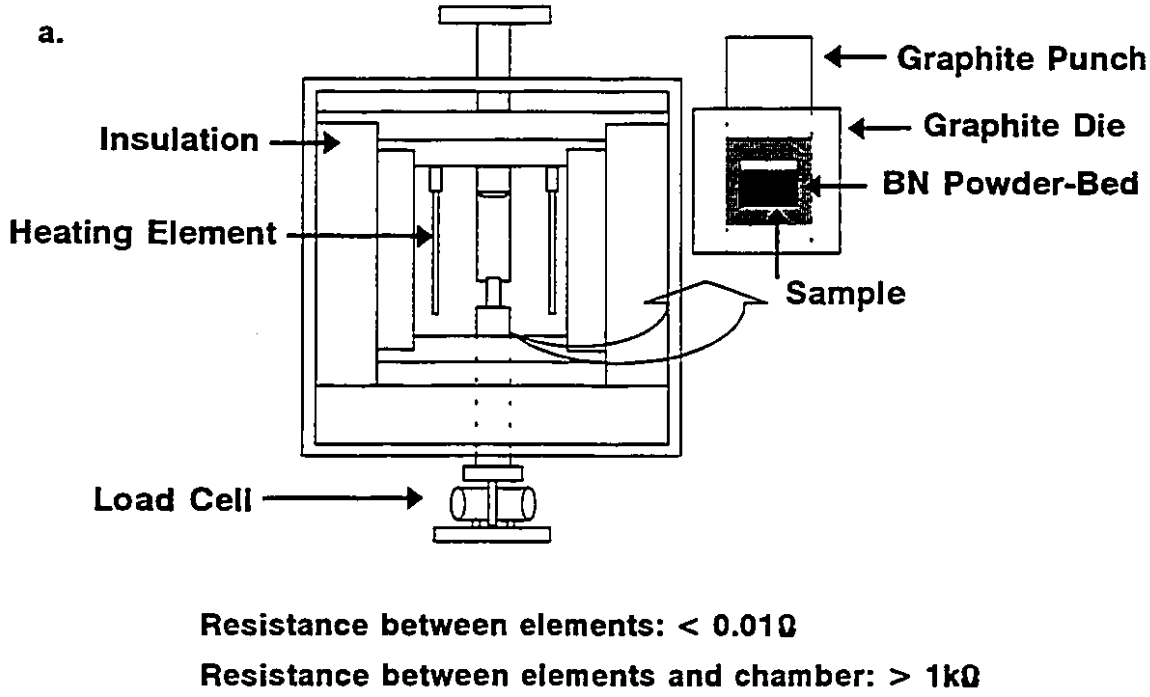

Figure 6.5- (a) Front and (b) side views of the hot-press chamber.

against the ENERPAC gauge, maintaining a precision of 5% of the nominal applied load.

The joining temperature was measured by an infrared pyrometer MIKRON M-600 inserted at the back of the furnace (Figure 6.5b). Its target tube consisted of a glassy-graphite cylinder connected to a fibre-optic lens assembly. As the temperature increased the target tube glowed, and the fibre-optics sent a signal, in the form of infrared radiation, to a control box. There, an output voltage signal was generated, simulating a type-C thermocouple, and sent to a programmable temperature controller OMEGA CN2012. The pyrometer was periodically calibrated against a type-C thermocouple[1] placed in contact with the sample. Hence, the testing temperatures were within a range of 5°C of the nominal value.

Once a sample was in position, the furnace was closed and evacuated to a pressure of 2×10^{-4} atm. (20 Pa), at room temperature. For the experiments carried out in N_2, the furnace was backfilled to pressures slightly above 1 atm. (110 to 120 kPa). After the joining environment was established, the furnace was heated up to the preset joining temperature at a rate of 15°C/min. Two graphite elements were used for heating, and the hot zone was surrounded by graphite fibre insulators on all six sides (Figure 6.5). During joining experiments in N_2, the expansion of the gas was controlled using the three-way valve shown in Figure 6.4. When the temperature in the furnace was 10°C lower than the set point, the load was applied to the sample.

[1] Tungsten - 5%Rhenium / Tungsten - 26% Rhenium.

Joining of SiC to Mo was carried out for temperatures ranging from 1000°C to 1700°C under vacuum. Si_3N_4 was joined to Mo under vacuum and in N_2 for temperatures between 1000°C and 1800°C. For both systems, the holding times varied from 10 minutes to 4 hours, and the hydraulic pressures from 5 to 100 MPa. Figure 6.6 shows the temperature and pressure profiles followed in the joining experiments.

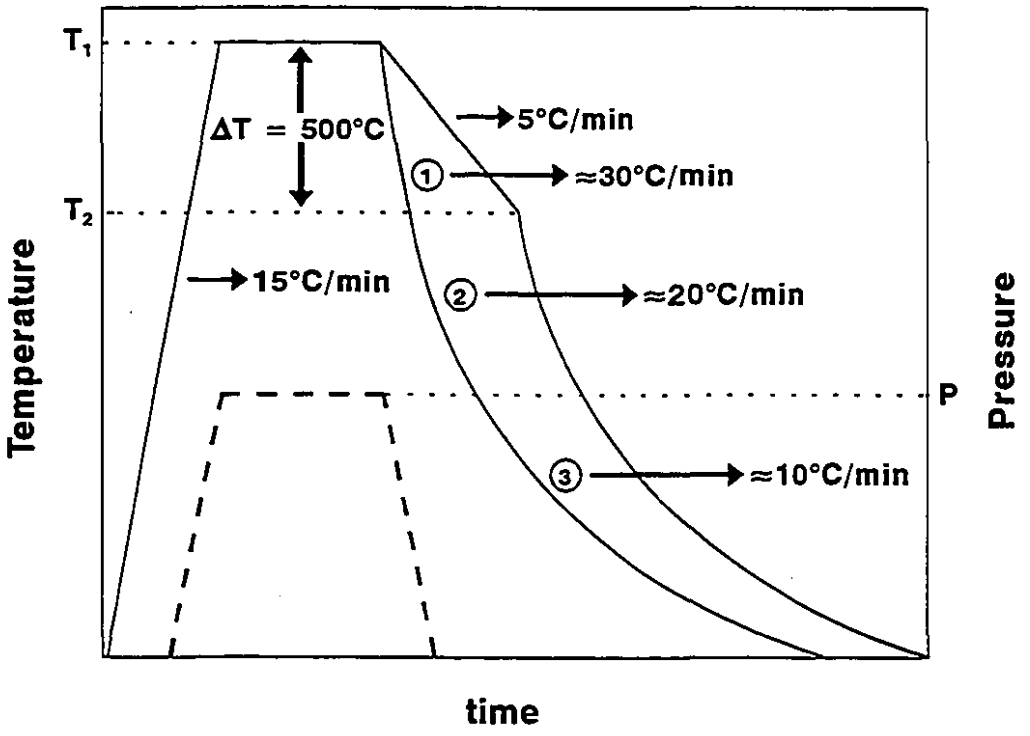

Figure 6.6- Temperature and pressure profiles followed in joining experiments.

After the holding time elapsed, the sample was cooled to room temperature. The applied load was carefully removed during the initial stages of cooling. Two cooling

profiles were employed. In the first one, the sample was simply furnace cooled. Typical cooling rates for this profile are estimated in Figure 6.6. Furnace cooling was used to produce samples to calculate the activation energy for the formation of interfaces. In this case, slow cooling would result in continued reaction beyond the holding time stipulated, affecting the final value of activation energy. The second profile consisted of cooling the sample slowly (5°C/min) for the first 500°C. The sample was then furnace cooled for the remainder of the cycle. This profile was used in the preparation of specimens for mechanical testing.

6.4 MICROSTRUCTURAL CHARACTERIZATION

In order to investigate the composition and morphology of the SiC-Mo and Si_3N_4-Mo interfaces, cross-sections of each joint were cut using a low-speed diamond saw and mounted in a cold-setting epoxy resin. Specimens were then polished with diamond paste and alumina suspension (0.05 μm finish). Although the hardness of Al_2O_3 (23.7 GPa) is lower than that of SiC (33.0 GPa) [1], this last polishing step was effective in improving the surface conditions of Si_3N_4 (hardness of 15.5 GPa), Mo (hardness of 2.30 GPa), and the interfacial reaction products.

The thickness of the interfaces were measured using a LECO 2005 image analyzer. Micrographs were obtained from a JEOL JSM-840A scanning electron microscope, using mainly the back-scattered electron image mode (BEI). The backscattered signal is proportional to the average atomic number of the sampling

volume, producing a contrast between regions of a specimen with different compositions. Electron probe micro-analysis (EPMA) of interfacial phases was performed in a CAMEBEX electron microprobe with wavelength dispersive system (WDS) using a beam current of 0.7 nA and an accelerating voltage of 10 kV. Quantitative analysis of carbon was performed using a polymeric window (NORAN®) with enhanced transmission properties. X-ray line analysis was carried out in a JEOL-8900 superprobe using a beam diameter of 1 μm, step size of 0.5 μm (to allow overlapping and therefore continuous analysis), and beam penetration of 2 μm (to minimize interference from underlying material). For SEM and EPMA characterization, the samples were carbon-coated using an EDWARDS E306A Coating System.

6.5 X-RAY DIFFRACTOMETRY

X-ray diffraction was carried out on fracture surfaces of the joint components, using CuKα radiation on a RIGAKU ROTAFLEX RU-200B diffractometer. CuKα radiation consists of two lines (Kα_1 and Kα_2) with wavelengths 1.544390 Å and 1.540562 Å, respectively. The angular range between 5 and 100° was investigated with an angular velocity of 0.6°/min, accelerating voltage of 50 kV, and current of 150 mA. Similar conditions were used on samples of the starting materials, except for the angular range which was adjusted individually, as can be seen in Figures 6.1 through 6.3.

6.6 SHEAR STRENGTH TESTING

The interfacial strength of SiC-Mo and Si_3N_4-Mo joints was determined by fracture shear loading using a INSTRON Dynamic Testing System Model 8500, and a shear jig represented schematically in Figure 6.7. The specimens consisted of butt-joined ceramic-metal diffusion couples. Prior to shearing, the samples were surface ground to assure parallelism between the sample and the plunger. They were then carefully placed in the bottom part of the jig, with the interface plane parallel to the plane of vertical displacement of the plunger. The position of the specimen was adjusted so the contact area between the bottom of the plunger and specimen included all the specimen cross-section. The sample was held in position by two screws. These screws applied a slight pressure on the Mo side of the sample to prevent any bending moment and specimen movement during testing. The sample assembly was then moved up towards the plunger at a vertical speed of 0.5 mm/min until the applied load resulted in fracture of the specimen.

The load-displacement curves were obtained on a *x-y* chart recorder connected to the testing equipment. The shear strength of the joint was then calculated by

$$\tau = \frac{P_{max}}{2A} \tag{6.1}$$

where τ is the shear strength, P_{max} is the fracture load, and A is the specimen cross-sectional area. For each set of experimental conditions studied (temperature, time, and environment for the case of Si_3N_4-Mo joints), an average of six samples were used to

determine the shear strength. The error bars were assumed to be plus or minus one standard deviation.

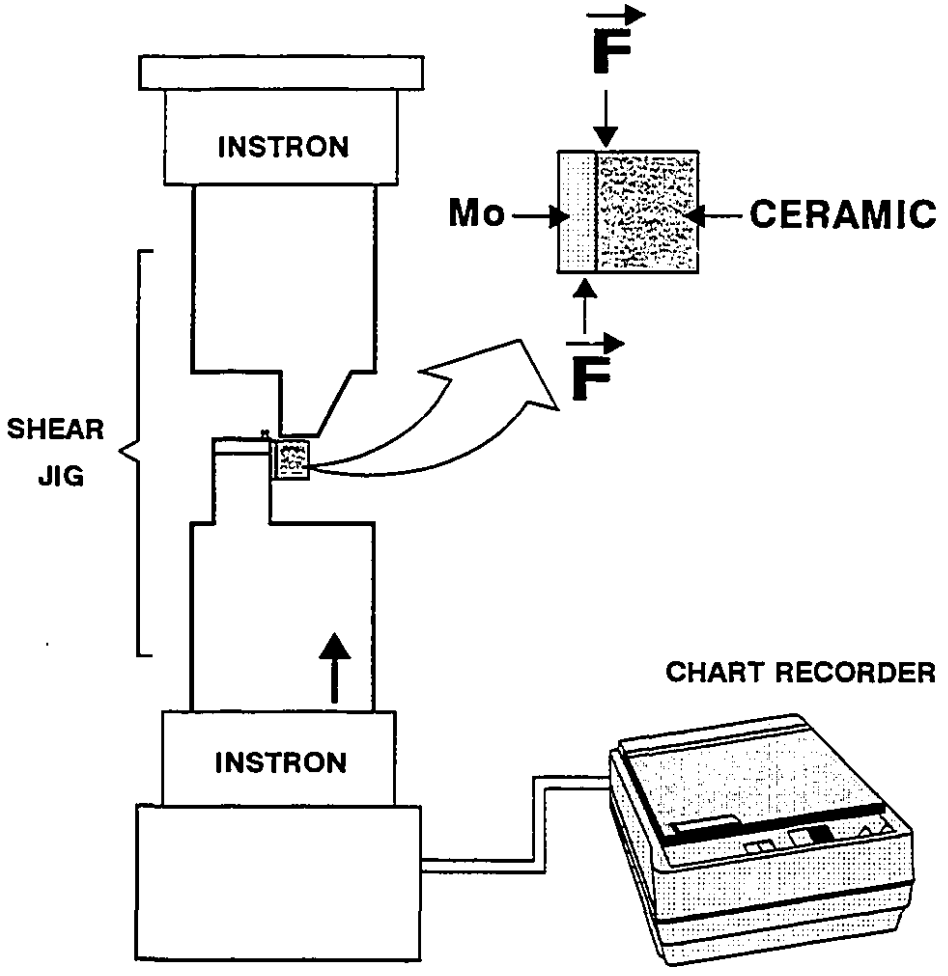

Figure 6.7- Assembly used in shear loading tests.

6.7 NEUTRON DIFFRACTOMETRY

The effect of the joining temperature on the distribution of residual stresses in SiC-Mo joints was studied using neutron diffraction. A series of SiC-Mo diffusion

couples was hot-pressed at temperatures ranging from 1200°C to 1500°C for 1 hour, under a pressure of 10 MPa. The samples were cooled slowly from the joining temperature as illustrated in Figure 6.6. In addition, the effect of the cooling rate on the distribution of residual stresses was also studied, using a sample hot-pressed at 1400°C for 1 hour, under a pressure of 10 MPa. This sample was cooled directly from the joining temperature.

Neutrons are generated in a nuclear reactor as a product of the nuclear fission of Uranium-235 (^{235}U) atoms (Figure 6.8). Because of its quantic nature, a neutron with velocity v has associated with it a particular wavelength, λ, according to the equation [62]

$$\lambda = h/mv \tag{6.2}$$

where h is the Planck's constant, and m is the mass of the neutron. Neutrons with different velocities are generated in the process. Fast neutrons (short wavelengths) are slowed down or *thermalized* inside the reactor by collisions with moderators such as graphite and heavy water (D_2O). Thermalization is necessary, mainly, to produce neutrons with wavelengths of the order of magnitude of the atomic spacing in crystalline structures. Hence, it is possible to investigate the arrangement of the atoms of a particular specimen by analyzing the diffraction of the neutron beam with the atomic planes of the material, as in X-ray diffraction.

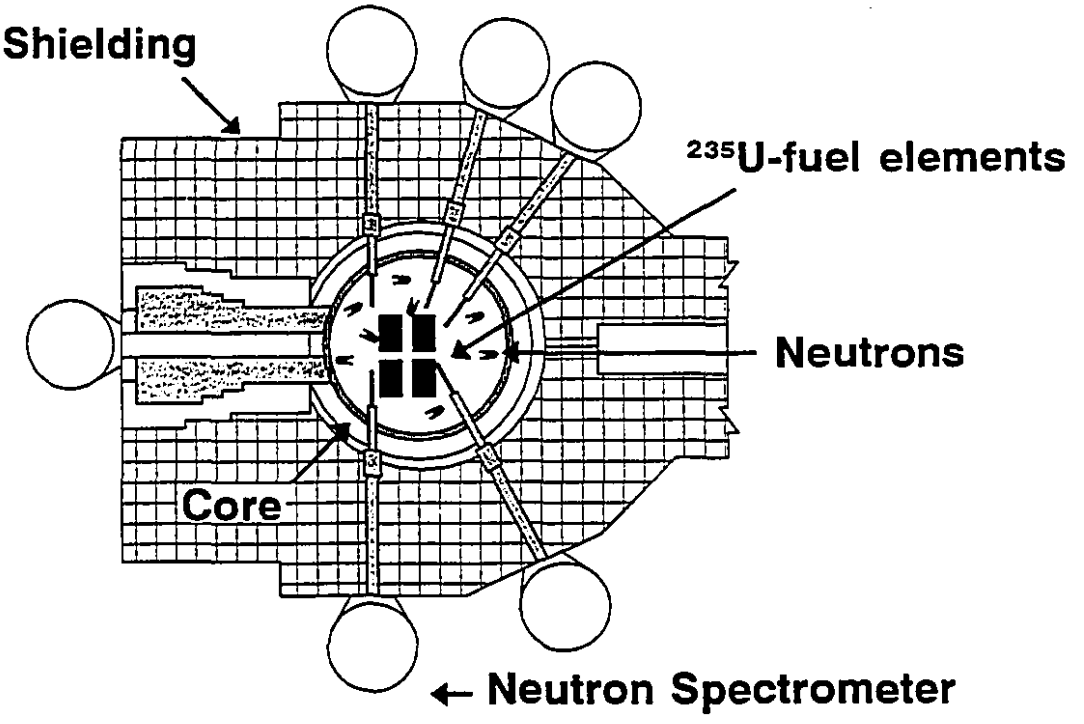

Figure 6.8- Schematics of a nuclear reactor showing its core, shielding, and neutron spectrometers [57].

Neutrons with different velocities, and therefore different wavelengths, form a polychromatic, or white beam, as they are collimated towards a neutron spectrometer. There, a crystal diffracts part of the white beam generating a monochromatic diffracted beam. The wavelength of the monochromatic beam, λ, is related to the atomic spacing, *d*, of a selected set of planes *(hkl)* of the monochromator crystal, by the Bragg's law

$$\lambda = 2d.sin\theta \qquad (6.3)$$

where θ is the angle of diffraction. Only 1% of the white beam is diffracted by the crystal. The remainder is undeviated and absorbed to avoid being counted as background, and to reduce the level of radiation surrounding the neutron detector. Imperfections in the crystal and horizontal divergence of the white beam result in a band for the wavelength of the monochromatic beam ($\lambda \pm d\lambda$). The width of the band $d\lambda$ is of the order of 0.05 Å.

The monochromatic beam is then collimated towards the sample under investigation. As the neutron beam penetrates the sample, diffraction occurs in all directions selected by the Bragg's law. By adjusting the position of the neutron detector, a particular set of planes is selected according to the corresponding angle of diffraction. The diffracted beam enters the detector and is electronically counted. Neutrons being uncharged (n^0), do not produce ionization. Thus, the detection process depends on neutron absorption by atoms whose subsequent decay results in ionizing products. In a ^{3}He detector the reaction can be expressed as [49]

$$^3He + n^0 = H^+ + {}^3H^+ + 0.76\ MeV \qquad (6.4).$$

In a subsequent step, H^+ and $^3H^+$ ionize the ^{3}He gas generating a voltage pulse. The energy released (0.76 MeV) is in form of γ radiation, which originates an electric pulse of intensity equal to 1% of the intensity of the pulse produced by the neutrons. In the counting process, neutrons are separated in electronic channels according to the angle of incidence, which is directly related to the angle of diffraction with the crystallographic

planes of the sample. Using equation (6.3) it is then possible to calculate the atomic spacing of the particular set of planes, which is the foundation of the stress analysis by diffraction methods.

The set-up employed in the neutron diffraction experiments is illustrated in Figure 6.9. A germanium (Ge) crystal was used as monochromator, where a beam of wavelength 1.8533 Å was generated by diffraction of the white beam of neutrons with the (331) planes of the crystal. The monochromatic beam, arising from the Ge-crystal, was collimated towards a SiC-Mo sample, placed on top of a moving table. The spacial position of the sample was adjusted by a set of independent stages for the x, y, and z coordinates. The x and y coordinates selected a specific position within the sample, and the z coordinate was fixed. The beam height, as selected by the slit, was greater than the sample height, allowing an integrated diffraction process through the entire sample. The angular position of the neutron detector, Φ, was adjusted to collect the neutrons diffracted by a particular set of crystallographic planes of SiC or Mo. The strain in the SiC side of the sample was studied using the $(2\bar{1}2)$ planes which diffracted at $\Phi = -89.84°$. For Mo, the (211) planes were used corresponding to $\Phi = -92.40°$. These particular sets of planes were chosen taking into account the intensity of the diffracted peak and its angular position [58]. The diffracted peak had to be relatively intense, as a consequence of the inherent low intensity of the monochromatic neutron beam. As mentioned earlier, the typical intensity of a monochromatic beam is of the order of 1% of the intensity of the white beam. In addition, the number of neutrons generated in a nuclear reactor is four

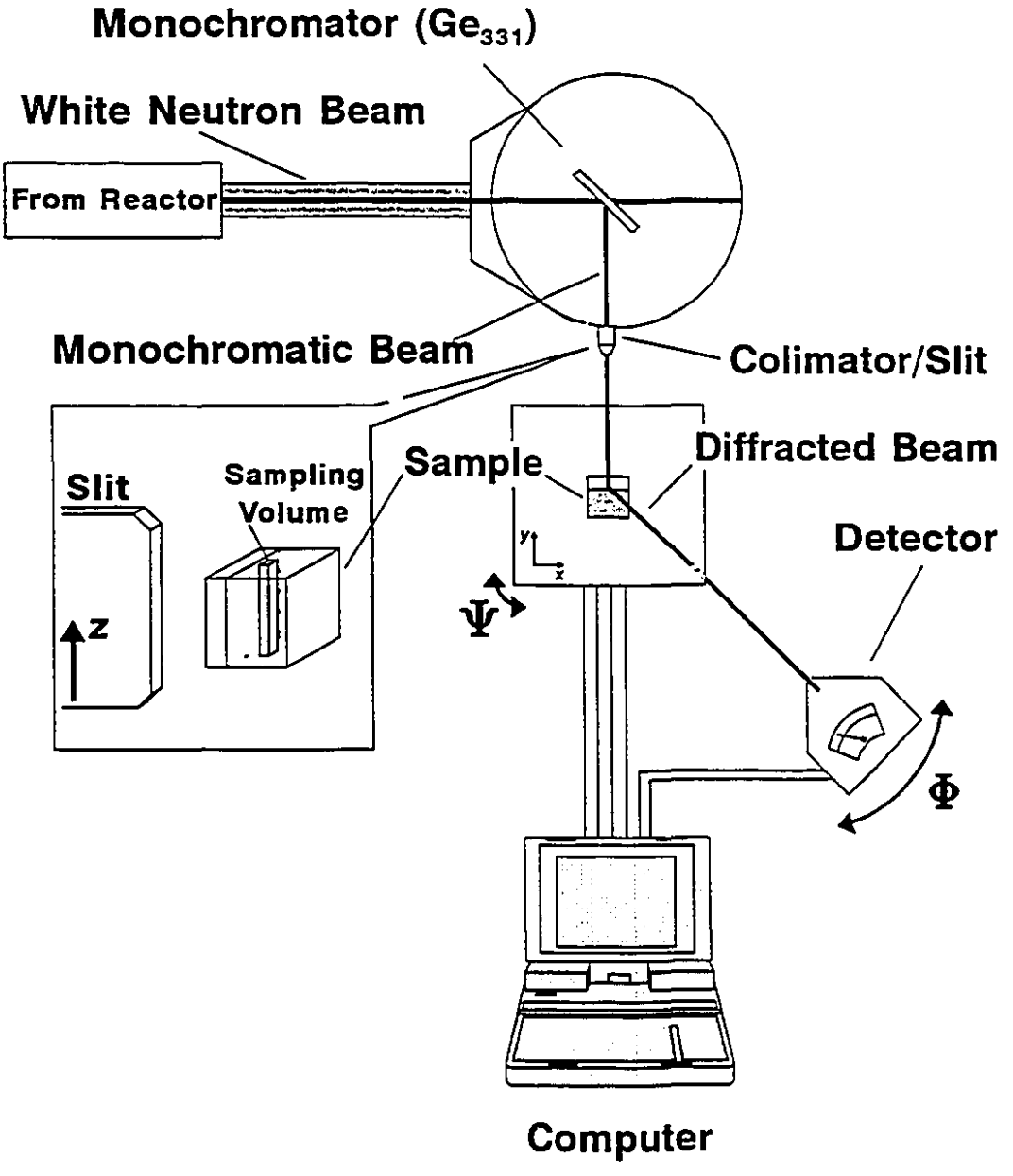

Figure 6.9- Set-up for neutron diffraction analysis of SiC-Mo joints.

orders of magnitude lower than the number of quanta generated in an X-ray tube. Also, the angle Φ had to be preferentially close to 90°, since the distortion of the sampling volume is minimum in that situation, as shown in Figure 6.10. This last feature is important from the spacial resolution standpoint, since 75% of the diffracted beam is concentrated around the centre of the sampling volume, in an area which accounts for 25% of the total value [58].

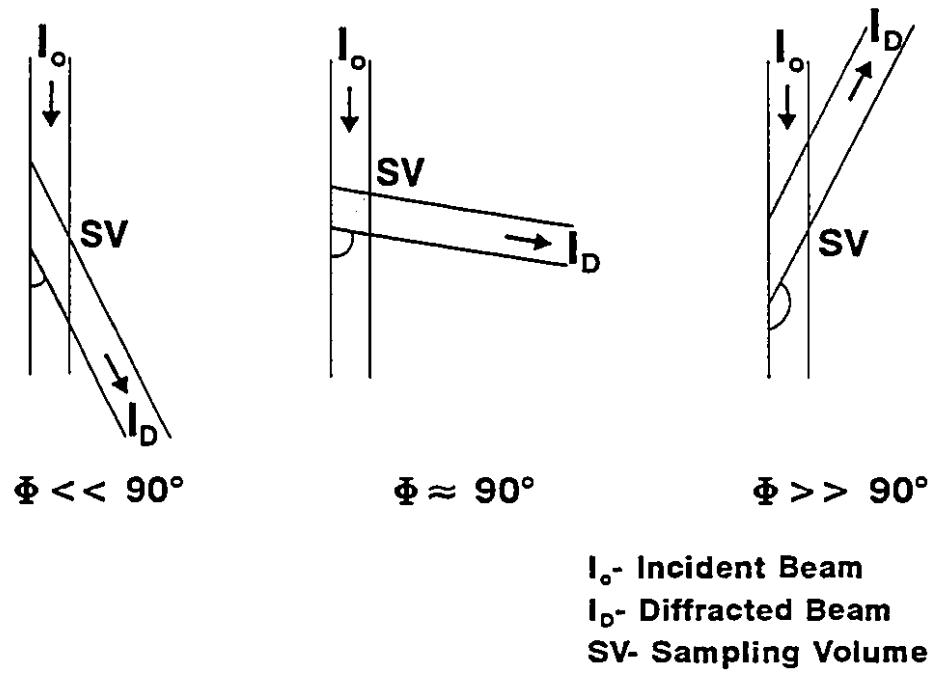

Figure 6.10- Geometry of sampling volume as a function of Φ.

The angle of rotation of the table, Ψ, was adjusted in order to select the geometry of the diffraction process, and therefore the component of strain to be studied (Figure 6.11). Normal components of strain are studied setting the angle of rotation of

the sample Ψ to Φ/2, and in-plane components setting Ψ to Φ/2 + 90°. Therefore, the corresponding values of Ψ for SiC were 45.08° for the in-plane component, and -44.92° for the normal component. For Mo, Ψ was equal to 43.80° for the in-plane component, and -46.20° for the normal component. Symmetry was assumed between the two in-plane components of strain.

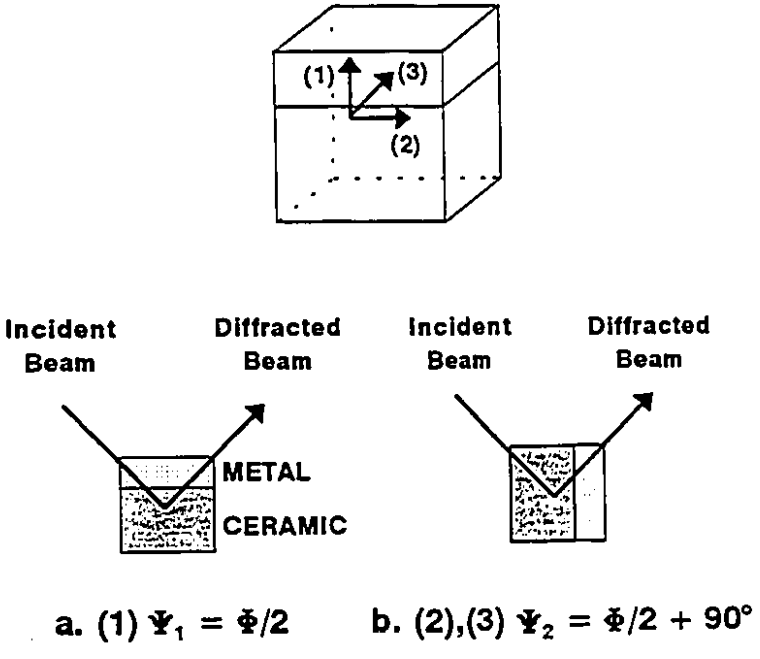

Figure 6.11- Sample orientation selected by the angle Ψ for (a) normal strain component, and (b) in-plane strain component.

The angle Φ is related to the angle of diffraction θ in (6.3) by

$$\Phi = 2\theta \tag{6.5}$$

Thus, by measuring Φ, it is possible to calculate θ, and therefore the interplanar distance,

d, corresponding to the *(hkl)* planes observed. When the material is under tension, the planes are pulled slightly apart so that d increases with respect to a strain-free value, d_o. Likewise, if the sample is under compression, the planes are pushed together and d decreases with respect to d_o. The measured strain, ε, is then defined by

$$\varepsilon = (d-d_o)/d_o \tag{6.6}$$

Strain can also be expressed in terms of the diffraction angles for peaks in the specimen and strain-free sample (if λ is the same). Errors in strain measurements are sometimes of the order of the strain values because if the number of collected points is small, the error in the peak fit (Gaussian function) can be of the order of the peak shift itself. The error in the Gaussian fit is related to the quality of the statistics generated during measurements, and not necessarily to peak width, *i.e.*, a broad peak can be collected with reasonable statistics yielding satisfactory results, whereas a sharp peak can be collected with a reduced number of points, resulting in a poor fit. Once the strain is obtained, the corresponding stress can be calculated according to

$$\sigma_x = \frac{E}{1+\nu}\left[\varepsilon_x + \frac{\nu}{1-2\nu}(\varepsilon_x+\varepsilon_y+\varepsilon_z)\right] \tag{6.7}$$

where E is the elastic modulus, and ν is the Poisson's ratio. The values of E and ν for SiC and Mo are included in Tables 6.1 and 6.3, respectively. A cyclic permutation of indices in equation (6.7) yields the other two components of stress (σ_y and σ_z). On the basis of sample symmetry, it was assumed that the strain along both in-plane components were equivalent ($\varepsilon_x = \varepsilon_y$). Hence, the set of three equations implied in (6.7) was reduced

to two: one to calculate the in-plane components of the strain (ε_x and ε_y), and another to calculate the normal component (ε_z).

6.8 NANOINDENTATION ANALYSIS

Depth sensing nanoindentation was used to determine the hardness and elastic modulus of the reaction products existing within SiC-Mo interfaces. Whereas typical microhardness measurements use fixed loads from 1 to 10 N, nanoindentation tests are performed in the ultra-low load regime (less than 1 N). The advantage of this test over conventional microhardness is that small volumes of material can be analyzed (layer thickness between 2 to 3 μm).

A schematic representation of the nanomechanical probe used in this work is shown in Figure 6.12 [59]. The sample was placed on a set-up consisting of independent x, y, and z stages controlled by a computer. A microscope was used to select the areas of the sample for the indentation tests. The tests were performed using a diamond indenter attached to a load cell. The load cell resolution was 10 mN for the applied load of 0.055 N. The depth resolution was 0.3 nm, and the spacial resolution was 100 nm. The load and depth of penetration were collected from the time the indenter touched the sample until it was completely removed from it, resulting in a load *vs.* depth plot from where the elastic modulus and the microhardness of the tested material were obtained.

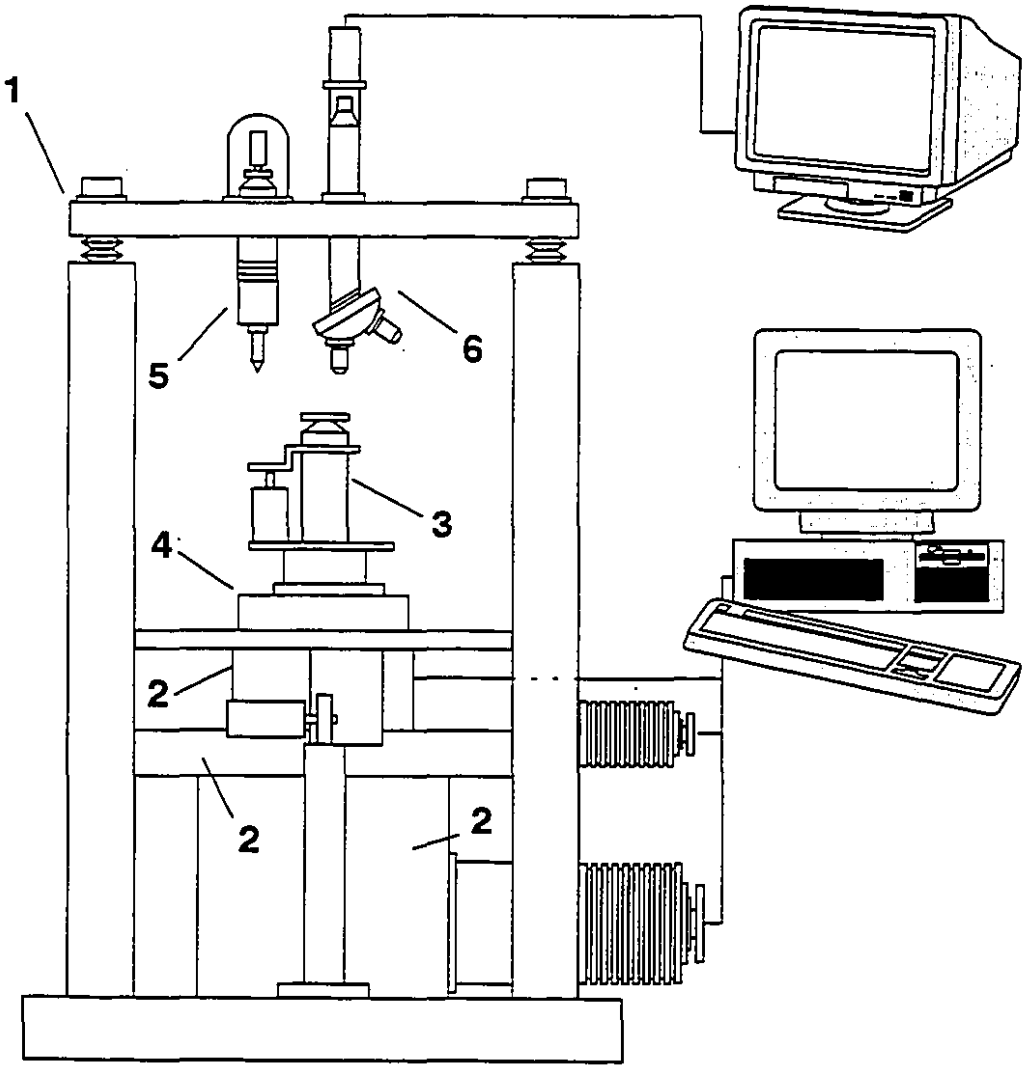

1.Frame
2.{xyz} Stages
3.Transducer
4.Ball slide
5.Load Cell/Indenter
6.Microscope

Figure 6.12- Diagram of probe used in nanoindentation tests [59].

The Vickers hardness (HV) was calculated from load-depth plots according to the equation [60]

$$HV = 113.51\frac{W_p}{h_p^3} \tag{6.8}$$

where W_p is the plastic work in μJ and h_p is the plastic depth in μm. The elastic modulus was calculated from the slope of the unloading segments of load-depth plots using the following equation [61]:

$$\left(\frac{1-\nu^2}{E}+\frac{1-\nu_0^2}{E_0}\right)\frac{dP}{dh} = 2\sqrt{\frac{A_c}{\pi}} \tag{6.9}$$

where dP/dh is the slope of the linear portion of the unloading curve, ν is the Poisson's ratio of the material being tested, ν_0 and E_0 are the Poisson's ratio and the elastic modulus of the diamond indenter, and A_c is the contact area between the indenter and the sample.

CHAPTER 7:

THE SiC-Mo SYSTEM

Initially a thermodynamic analysis of the Mo-Si-C system was carried out and followed by the hot-pressing and characterization of SiC-Mo diffusion couples. A correlation was established between the microstructure of the resulting ceramic-metal interfaces and the mechanical properties of the joints.

7.1. THERMODYNAMIC EVALUATION OF THE SiC-Mo SYSTEM

When SiC is in contact with Mo, a reaction is expected to take place. In

Figure 7.1 the stability of Mo-Si-C compounds, represented by their respective standard Gibbs free energy of formation (ΔG^0), is plotted for temperatures up to 1800°C.

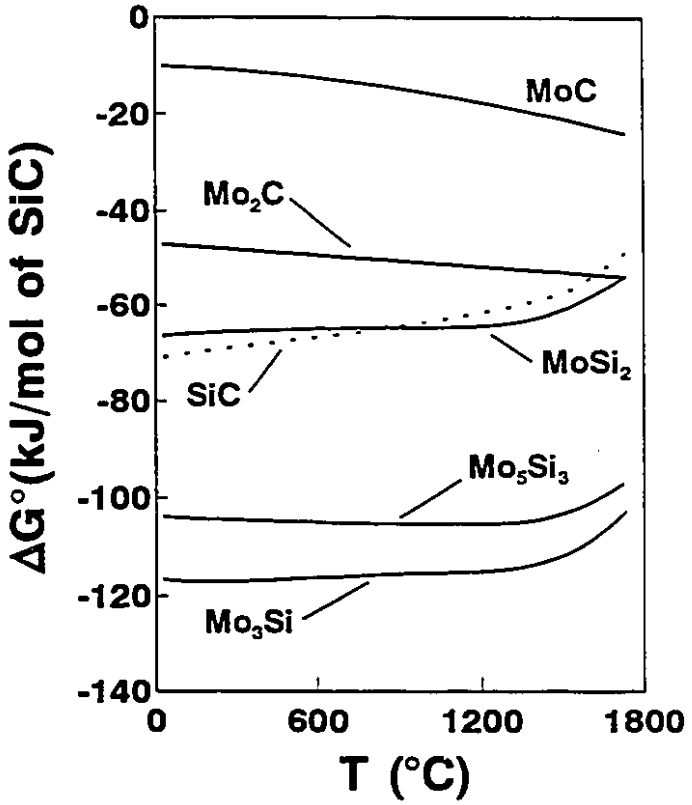

Figure 7.1- Standard free energy of formation of Mo-Si-C compounds as a function of the temperature (data obtained from F*A*C*T).

Because Mo_3Si and Mo_5Si_3 have lower ΔG^0 of formation compared to SiC, they are expected to form. The process starts with the decomposition of SiC into silicon (Si) and carbon (C) according to

$$SiC = Si + C.....\Delta G_1^0 \quad (7.1)$$

where $\Delta G_1^0 > 0$, since the formation of SiC has associated with it a $\Delta G^0 < 0$. Subsequently, Si diffuses into Mo and reacts with it to form Mo_3Si following

$$3\,Mo + Si = Mo_3Si.....\Delta G_2^0 \quad (7.2)$$

Combining equations (7.1) and (7.2), and selecting 1200°C as the joining temperature gives

$$SiC = Si + C.....\Delta G_1^0 = 61\ kJ$$

$$3\,Mo + Si = Mo_3Si.....\Delta G_2^0 = -115\ kJ$$

yielding

$$SiC + 3\,Mo = Mo_3Si + C.....\Delta G_3^0 = \Delta G_1^0 + \Delta G_2^0 = -54\ kJ \quad (7.3)$$

Carbon originating from the decomposition of SiC also diffuses into Mo. This step of the process should be thermodynamically evaluated considering two possible routes: the formation of a stable carbide (Mo_2C),

$$2\,Mo + C = Mo_2C.....\Delta G_4^0 \quad (7.4)$$

and the formation of a solid-solution between Mo and C according to

$$Mo_2C = 2\,Mo + [C]_{Mo}.....\Delta G_5 \quad (7.5)$$

Although ΔG_5 is not available, the Mo-C phase diagram (Figure 3.7) indicates that C has a very small solubility in Mo for temperatures lower than 2100°C. In addition, Mo has a high affinity for C resulting in the formation of Mo_2C. Considering 1200°C as the joining temperature (ΔG_4^0 = -52 kJ), and then combining (7.3) and (7.4) yield

$$SiC + 5\,Mo = Mo_3Si + Mo_2C.....\Delta G_6^0 = \Delta G_3^0 + \Delta G_4^0 = -106\ kJ \quad (7.6)$$

Comparing (7.3) and (7.6), it can be seen that the formation of Mo_2C lowers the total free energy of the system, indicating that (7.6) is more favourable than (7.3).

As the reaction proceeds, the concentration of free Si at the interface increases, which precipitates Mo_5Si_3, as a result of the diffusion of Si into Mo_3Si. The total reaction between SiC and Mo at this point can be expressed by

$$SiC + 5\,Mo = Mo_3Si + Mo_2C$$

$$Mo_3Si + 4/5\,Si = 3/5\,Mo_5Si_3$$

$$4/5\,SiC = 4/5\,Si + 4/5\,C$$

$$8/5\,Mo + 4/5\,C = 4/5\,Mo_2C$$

$$9/5\,SiC + 33/5\,Mo = 3/5\,Mo_5Si_3 + 9/5\,Mo_2C.....\Delta G_7^0 \quad (7.7)$$

For a joining temperature of 1200°C, ΔG_7^0 = -173 kJ. Since $\Delta G_7^0 < \Delta G_6^0$, the reaction expressed by (7.7) proceeds. According to the Mo-Si and Mo-C phase diagrams, and F*A*C*T, the reaction between SiC and Mo would continue with the transformation of Mo_5Si_3 into $MoSi_2$ by addition of Si into the Mo_5Si_3, and with the transformation of Mo_2C into MoC by addition of C into the Mo_2C. F*A*C*T does not contain any data on ternary Mo-Si-C phases, nevertheless, the existence of such a compound has been established and it may prevent the transformation from Mo_5Si_3 to $MoSi_2$ [30,31,32].

A similar thermodynamic analysis can be conducted based on the 1200°C cross-section of the Mo-Si-C phase diagram. The two methods should yield similar results.

Figure 7.2 shows the 1200°C cross-section of the Mo-Si-C phase diagram plotted along with the SiC-Mo interface (dotted line).

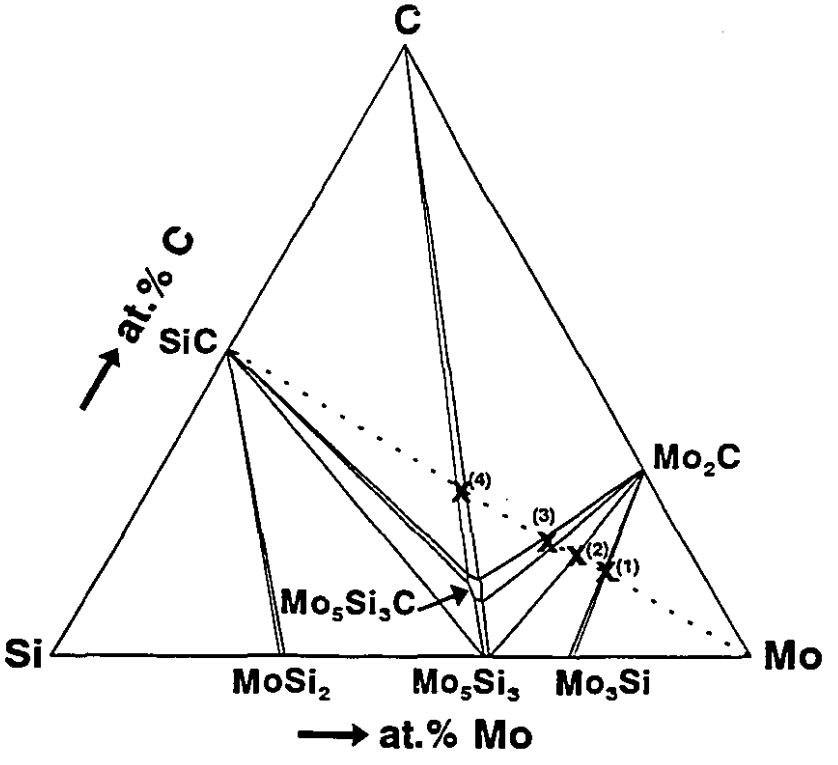

Figure 7.2- The 1200°C cross-section of the Mo-Si-C phase diagram plotted along with the SiC-Mo interface (dotted line). Labels (1) to (4) indicate interfacial reactions [31].

When SiC and Mo are joined at 1200°C, the sequence of events that take place within the interface can be visualized from Figure 7.2. In a ternary cross-section of a phase diagram, the interface between two materials is represented by a straight line connecting them. Every time the interface intercepts a tie-line, reaction occurs and the

corresponding products are the compounds present at the extremities of the tie-line. In this situation the lever rule applies, and it can be used to estimate the relative amounts of each compound. Thus, following the interface line in Figure 7.2 towards SiC, it can be seen that a first reaction between SiC and Mo, labelled (1) in Figure 7.2, produces Mo_2C and Mo_3Si in a wt.% ratio of 0.63 to 1. This result corresponds to the reaction expressed by (7.6), where the wt.% ratio of Mo_2C to Mo_3Si was calculated to be 0.65 to 1. Subsequently, the interface intercepts a tie-line containing Mo_2C and Mo_5Si_3, labelled (2), in a wt.% ratio of 1.09 to 1. This reaction corresponds to equation (7.7) where the wt.% ratio between Mo_2C and Mo_5Si_3 is 1.1 to 1. At this point, the phase diagram analysis complements the data based on F*A*C*T. In the phase diagram, a ternary phase of composition Mo_5Si_3C is seen coexisting with Mo_2C, as indicated by label (3) in Figure 7.2. Hence, the transformation of Mo_5Si_3 into $MoSi_2$ does not take place. Further evidence of this fact is the absence of any tie-line containing $MoSi_2$ as an extremity intercepting the interface in Figure 7.2. Finally, the SiC-Mo interface line intercepts a tie-line containing Mo_5Si_3C and C as its terminal phases. The presence of free carbon within SiC-Mo interfaces has not been reported in the literature, and it may be a consequence of using phase diagrams, *i.e.*, equilibrium conditions, to explain a non-equilibrium situation, such as the continuous diffusion of Si and C into Mo, observed during the production of SiC-Mo diffusion couples.

Considering a higher joining temperature (1600°C), the formation of Mo-silicides (Mo_3Si and Mo_5Si_3) as well as the formation of Mo_2C can be observed by direct

examination of Figure 7.1. Alternatively, this fact can also be observed by plotting the SiC-Mo interface line along with the 1600°C cross-section of the Mo-Si-C phase diagram (Figure 7.3). The same sequence of events observed at 1200°C occurs at 1600°C. However, an important difference is noticed as the interface intercepts a tie-line connecting Mo_5Si_3C to MoC. This indicates that during bonding at 1600°C, a transformation from Mo_2C to MoC is likely to occur. Further evidence of this fact is found in the binary Mo-C phase diagram (Figure 3.7). However, the temperature of stability of the first MoC phase (η-MoC_{1-x}) in that diagram is 1657°C. The presence of MoC within diffusion-bonded SiC-Mo interfaces has not been reported in the literature.

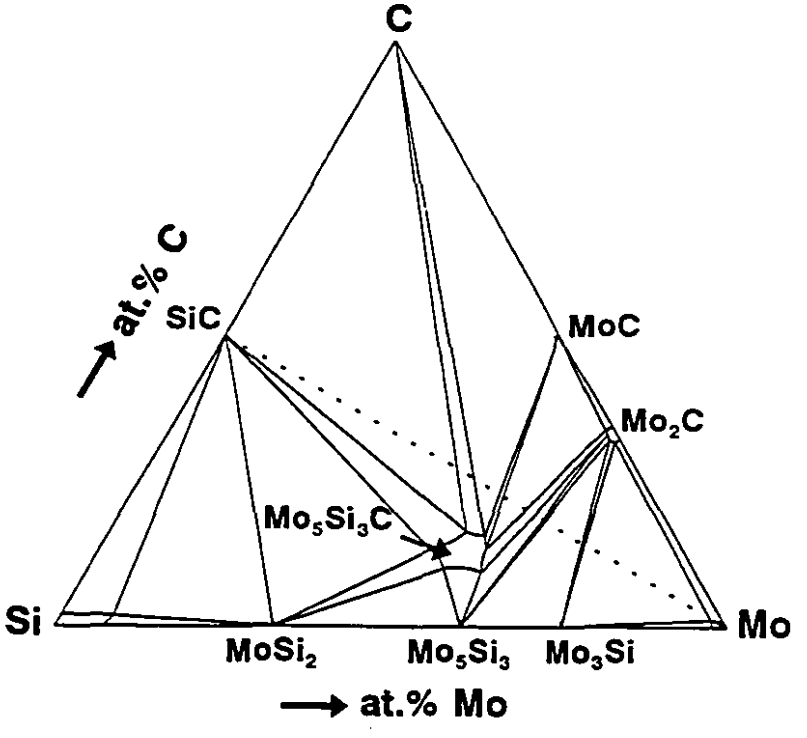

Figure 7.3- The 1600°C cross-section of the Mo-Si-C phase diagram plotted along with the SiC-Mo interface (dotted line) [30].

7.2 INTERFACE CHARACTERIZATION

Diffusion couples of SiC and Mo were hot-pressed in vacuum at temperatures ranging from 1000°C to 1700°C and times varying from 10 minutes to 4 hours. The pressure applied to the sample was limited to values between 10 and 20 MPa, as this range is within the compressive yield strength of Mo. Pressures in excess of 50 MPa resulted in substantial deformation of the Mo foil, especially at relatively high joining temperatures.

Joining of SiC to Mo occurred by the formation of a reactive interface on the Mo side of the sample. The reaction started with the decomposition of SiC into Si and C and diffusion of these species into Mo. Because solid-state diffusion is a thermally activated mechanism, reaction became significant only for relatively high joining temperatures (above 1100°C). The interfaces consisted initially of one reaction layer containing two intermixed phases. EPMA performed on a sample hot-pressed at 1250°C for 2 h showed an interface with 8 μm in thickness and indicated that the two phases formed were Mo_5Si_3 and Mo_2C (Figure 7.4).

Despite the fact that Si is larger in size than C[1], the activation energy for the diffusion of Si in Mo (327 kJ/mol) is lower than the activation energy for the diffusion of C in Mo (348 kJ/mol) [63]. This indicates that upon joining of SiC to Mo, Si probably diffused into Mo faster than C. It has been suggested that the rate of diffusion of non-metals into transition metals is related to the ionization potential of the non-metal species

[1] Carbon has atomic radius 0.77 Å and silicon 1.17 Å [62].

rather than its ionic size [63]. The lower the ionization potential of the non-metal ion, the easier it diffuses into the transition metal. Following this argument, Si diffused into Mo easier than C, as a result of its lower ionization potential (8.28 eV) as compared to that of C (11.24 eV) [63]. However, the high affinity of Mo for Si resulted in ready formation of a silicide, initially Mo_3Si, preventing Si from diffusing extensively into the Mo. Mo_3Si transformed rapidly into Mo_5Si_3 which indicates considerable decomposition of SiC, and a large supply of Si. The diffusion of C into Mo resulted in Mo_2C formation. Although initially present intermixed with Mo_5Si_3 only, Mo_2C extended deeper inside the Mo and, at 1400°C, consisted of a separate interfacial layer [64].

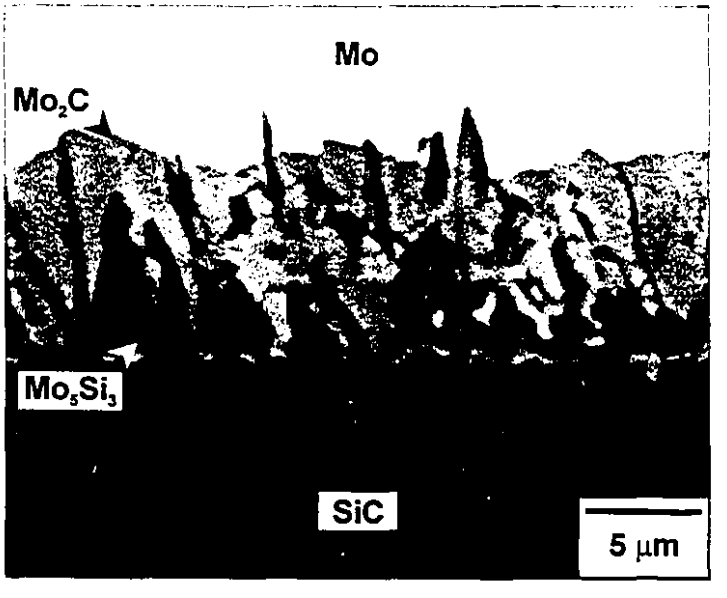

Figure 7.4- Backscattered electron image (BEI) of SiC-Mo interface (vacuum, T = 1250°C, t =2 h, P = 10 MPa).

Figure 7.5 shows the interface of a sample hot-pressed at 1300°C for 1 hour. The average thickness of this interface was 11.25 μm and consisted once more of Mo_5Si_3 and Mo_2C. Back-scattered imaging also showed a contrast effect in the Mo_2C region probably related to texture. This result was later confirmed for samples hot-pressed at higher temperatures. A different contrast was also observed in the Mo_5Si_3 region in contact with SiC. EPMA showed a composition which corresponded to Mo_5Si_3 but contained a trace amount of C. It is believed that this was the beginning of the precipitation of the ternary phase Mo_5Si_3C. This fact became evident when the joining temperature was increased to 1500°C.

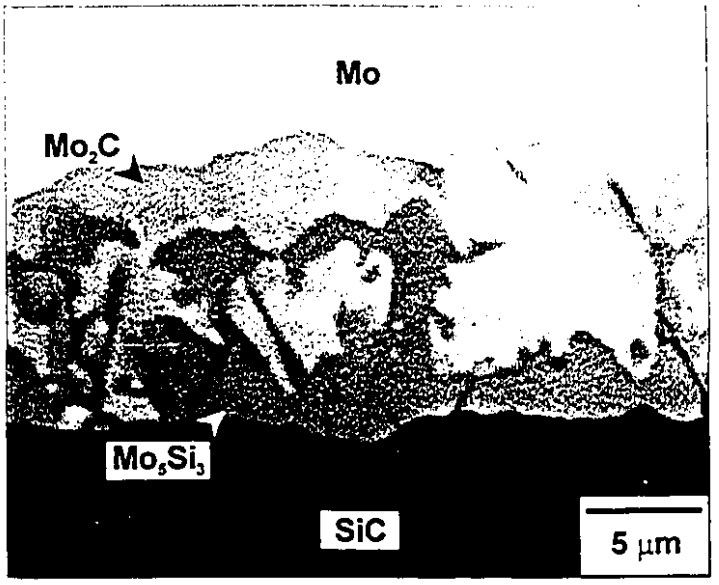

Figure 7.5- BEI of SiC-Mo interface (vacuum, T = 1300°C, t = 1 h, P = 10 MPa).

The interface of a SiC-Mo diffusion couple hot-pressed at 1500°C for 10 minutes is shown in Figure 7.6. A Mo_5Si_3C layer of 3 μm in average thickness was observed in contact with SiC, and identified by EPMA. The total thickness of this interface was 24 μm. Figure 7.6 also illustrates a more defined interface between SiC and Mo, which is composed of three reaction zones: (a) a layer of Mo_2C in contact with Mo; (b) an intermediate reaction zone containing both Mo_5Si_3 and Mo_2C, and (c) a layer of Mo_5Si_3C in contact with SiC [64].

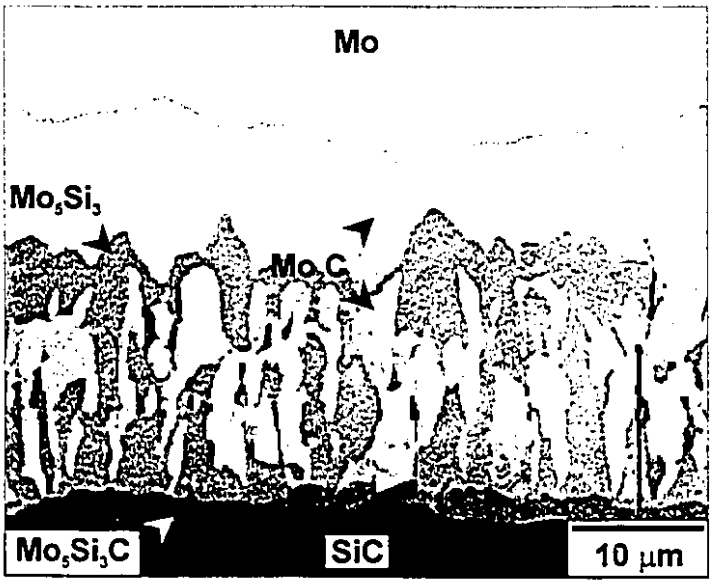

Figure 7.6- BEI of SiC-Mo interface (vacuum, T = 1500°C, t = 10 min, P = 10 MPa).

The presence and position of each reaction layer identified in Figure 7.6 can also be visualized in the WDS line analysis of Mo, Si, and C across that interface

(Figure 7.7). The different reaction layers can be identified through the variation in intensities of the X-ray scans as a function of distance from the original interface.

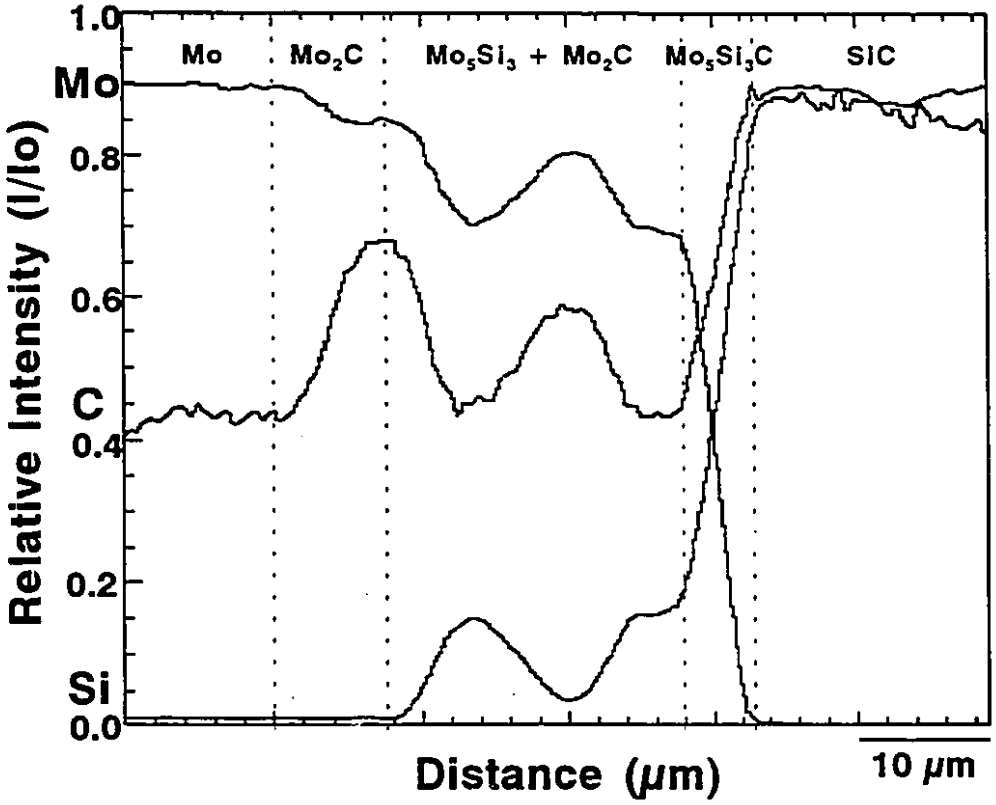

Figure 7.7- WDS line analysis of atomic species across the SiC-Mo interface shown in Figure 7.6 [64].

In Figure 7.7, the Mo_2C layer in contact with Mo is identified by an increase in the relative intensity of the C signal. At the point where the C signal reaches its maximum, the intensity of the Si signal starts to increase, indicating the presence of Mo_5Si_3. At that point, the probe was on the mixed layer, where a second peak in the C signal is seen at the same relative position as a peak in the Mo intensity, indicating the

presence of a Mo_2C region. Subsequently, the relative intensity of Mo abruptly decreases at the same point where the intensities of Si and C increase, indicating the presence of the ternary phase Mo_5Si_3C.

Therefore, the sequence of reaction within a SiC-Mo interface can be summarized as follows: when Mo became saturated with Si, cubic Mo_3Si was probably formed initially, but not observed. Further addition of Si stabilized tetragonal Mo_5Si_3. The next step in the reaction should be the formation of $MoSi_2$, as reported for experiments on siliconizing of Mo [63]. However, the presence of C prevented the formation of $MoSi_2$. Carbon is thought to diffuse preferentially along the grain-boundaries of Mo_5Si_3, however lattice diffusion could also have occurred, and a fraction of C atoms, diffusing through Mo_5Si_3, remained in the structure stabilizing the hexagonal Mo_5Si_3C. In this structure, C occupies interstitial positions at the centre of octahedra formed by the Mo atoms as shown in Figure 3.11.

A common aspect observed for all SiC-Mo interfaces was their irregular pattern with wavy phase-boundaries between Mo_5Si_3 and Mo_2C, between Mo_2C and Mo, and between Mo_5Si_3C and SiC. It has been suggested that this is a ternary diffusion phenomenon related to the kinetics of C diffusion through the Mo_5Si_3 layer [31]. As for the wavy aspect of the Mo_5Si_3C-SiC boundary, it may be related to the asperities present at the original SiC and Mo surfaces. Voids of different sizes are formed when the SiC and Mo surfaces are brought in contact. At the points where large voids are present, the final interface can be expected to be relatively thin.

Bonding experiments carried out for temperatures higher than 1500°C generally resulted in failure of the joints. X-ray diffraction was performed on the SiC and Mo fracture surfaces of a sample hot-pressed at 1650°C, which debonded during cooling from the joining temperature. The corresponding patterns are shown in Figure 7.8. The diffraction spectrum obtained from the SiC fracture surface matched that of the original α-SiC (Figure 6.1) with the addition of residual Mo_5Si_3 and Mo_5Si_3C. Although overlapping of Mo_5Si_3C and SiC occurred, the presence Mo_5Si_3C was established mainly by its (112) peak. Mo_2C peaks were not observed on the SiC fracture surface [64].

Mo_5Si_3 was the main phase observed on the Mo fracture surface. The main peaks observed were (411) and (321), although the (321) peak overlapped with the (102) peak of Mo_5Si_3C. Hexagonal β-Mo_2C was also observed. As the Mo fracture surfaces were characterized by a change in composition with the distance from the surface, and diffraction at high angles included a thicker region of the interface, the relative intensities of the carbide peaks increased with the angle of diffraction, 2θ, due to the increase in the penetration of X-rays. For angles greater than 60°, diffraction originated from the interface layer rich in Mo_2C and, depending on the local thickness of the interface, even the Mo layer diffracted, as can be seen by the Mo (220) peak at 2θ=87.65°. An intense peak observed at 2θ=35.7° was identified as the (006) planes of hexagonal α-SiC, and originated from particles dispersed on the Mo surface. Another relatively intense line was observed at 2θ=20.9°. It was attributed to presence of free C on the Mo fracture surface, as predicted in Figure 7.3. Upon joining at high temperatures, reaction took

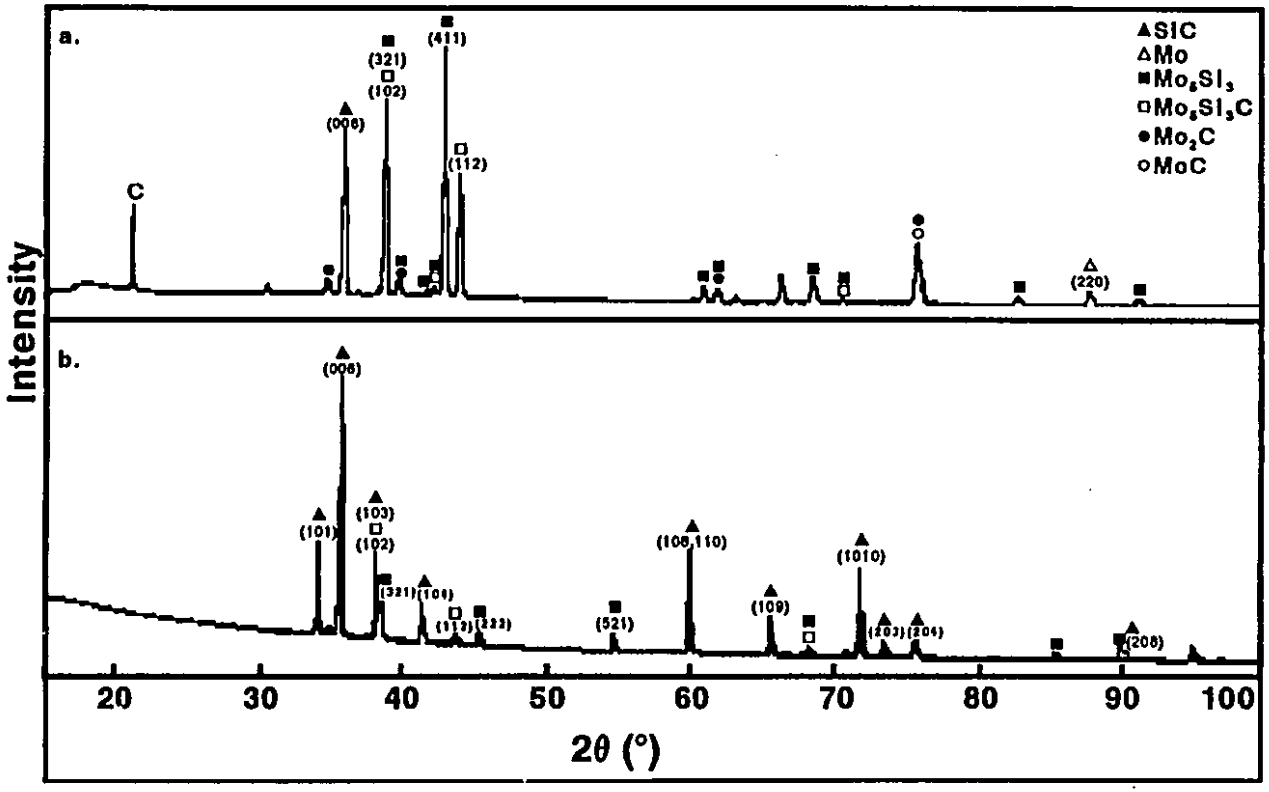

Figure 7.8- XRD pattern of (a) Mo and (b) SiC fracture surfaces. Sample hot-pressed at 1650°C for 10 minutes (10 MPa).

place at the extent that the Mo-Si-C system was approaching the equilibrium conditions represented by its phase diagram, resulting in the formation of Mo_5Si_3C and free C.

At 1700°C, samples were hot-pressed for 1 hour resulting in failure of the joints. X-ray diffraction of the Mo fracture surface of one of those samples indicated that the transformation from β-Mo_2C to η-MoC_{1-x} may have occurred, but the results were inconclusive due to extensive peak overlapping. As SiC-Mo interfaces are characterized by a change in composition with sample depth, it is important to know the effective depth of penetration of X-rays for each compound. An estimate of the depth analyzed by X-ray diffraction can be obtained from the parameter G_x [55]. This parameter represents the fraction of the total diffracted intensity originated from a layer of thickness x, and is expressed by

$$G_x = 1 - e^{\left(\frac{-2\mu x}{\sin\theta}\right)} \tag{7.8}$$

where μ is the mass absorption coefficient of the compound, x is the thickness, and θ is half of the diffraction angle. The method used to calculate the coefficients of mass absorption for Mo_5Si_3C, Mo_5Si_3, and Mo_2C is described in Appendix II. Figure 7.9 shows a plot of G_x as a function of 2θ for Mo_5Si_3C, Mo_5Si_3, and Mo_2C. It can be seen that for all three compounds, more than 95% of the X-rays analyzed were originated in a layer 10 μm thick, which explains the difficulty in obtaining clear Mo-carbides spectra. The variation of G_x with θ also accounts for the preferential presence of Mo and Mo-carbide peaks at high angles of diffraction.

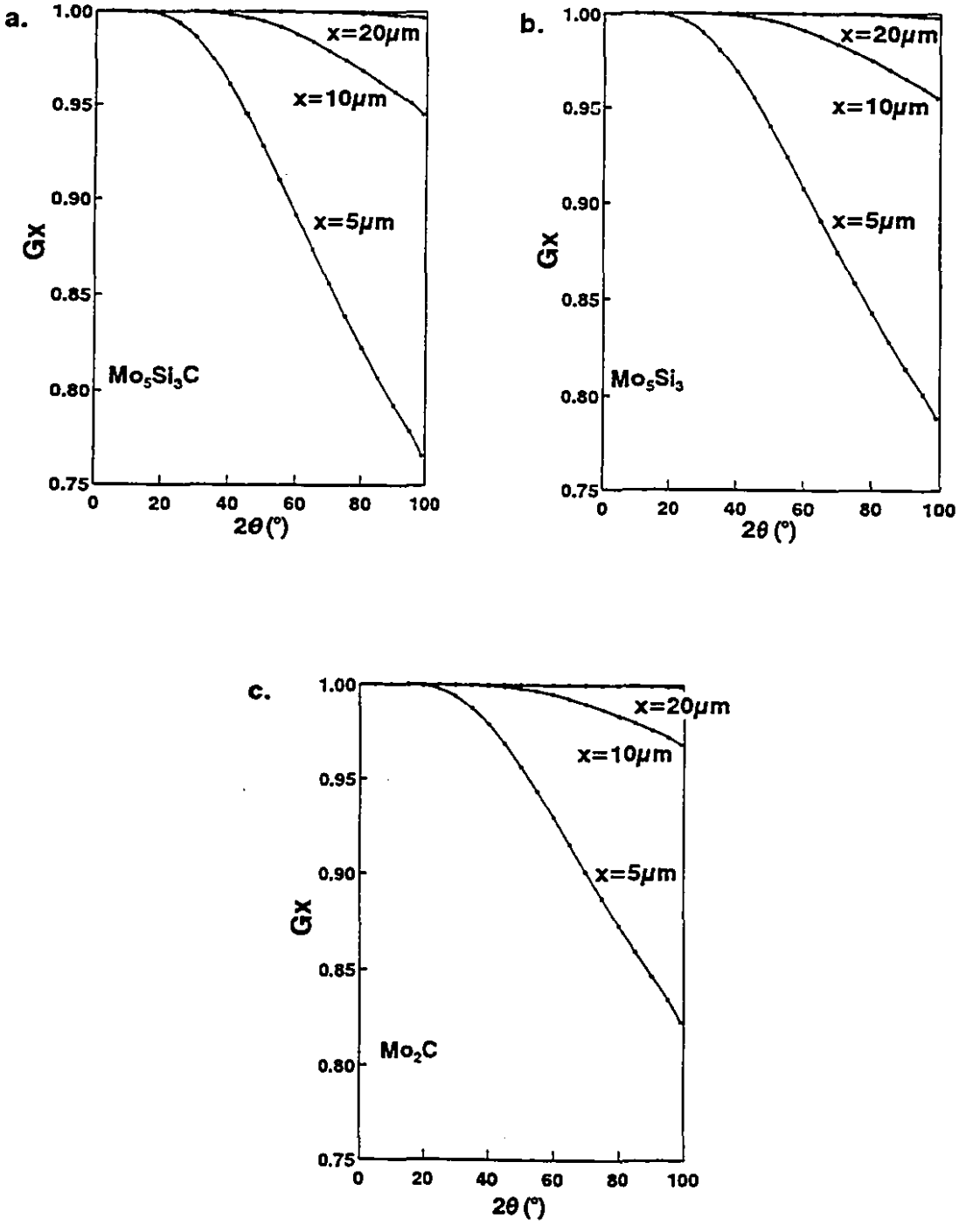

Figure 7.9- Plots of G_x as a function of the angle of diffraction, θ, and thickness, x, for (a) Mo_5Si_3C, (b) Mo_5Si_3, and (c) Mo_2C.

In order to establish whether η-MoC_{1-x} was formed at 1700°C, X-ray diffraction was performed after gradually removing interfacial material from the Mo-fracture surface of a sample hot-pressed for 1 hour. Figure 7.10 shows a cross-section of the Mo-side of the sample [64].

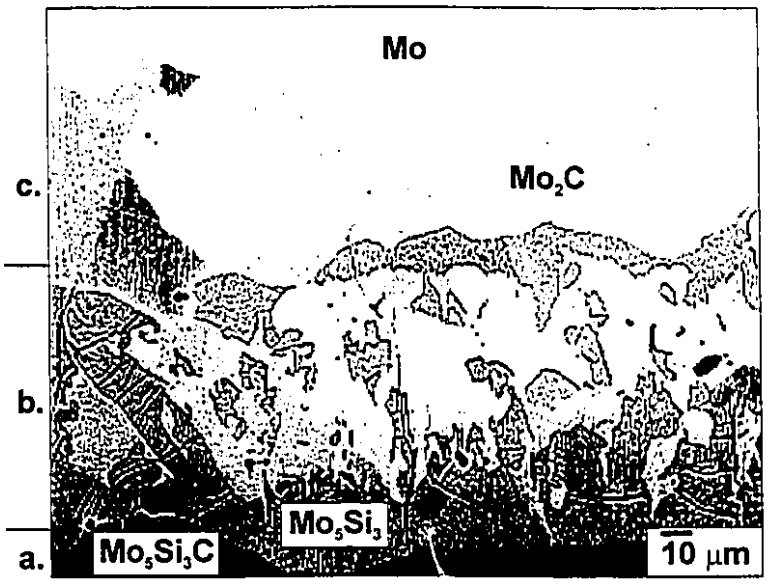

Figure 7.10- BEI of SiC-Mo interface (vacuum, T = 1700°C, t = 1 h, P = 20 MPa).

The labels (a) through (c) in Figure 7.10 correspond to the X-ray spectra contained in Figure 7.11, and they indicate the interfacial layers analyzed. First, the original interface was studied and the presence of Mo_5Si_3C and Mo_5Si_3, as the main phases, was confirmed (Figure 7.11a). Mo_2C was identified at high angles of diffraction. Then, the sample was ground to eliminate the ternary phase, and X-ray diffraction was

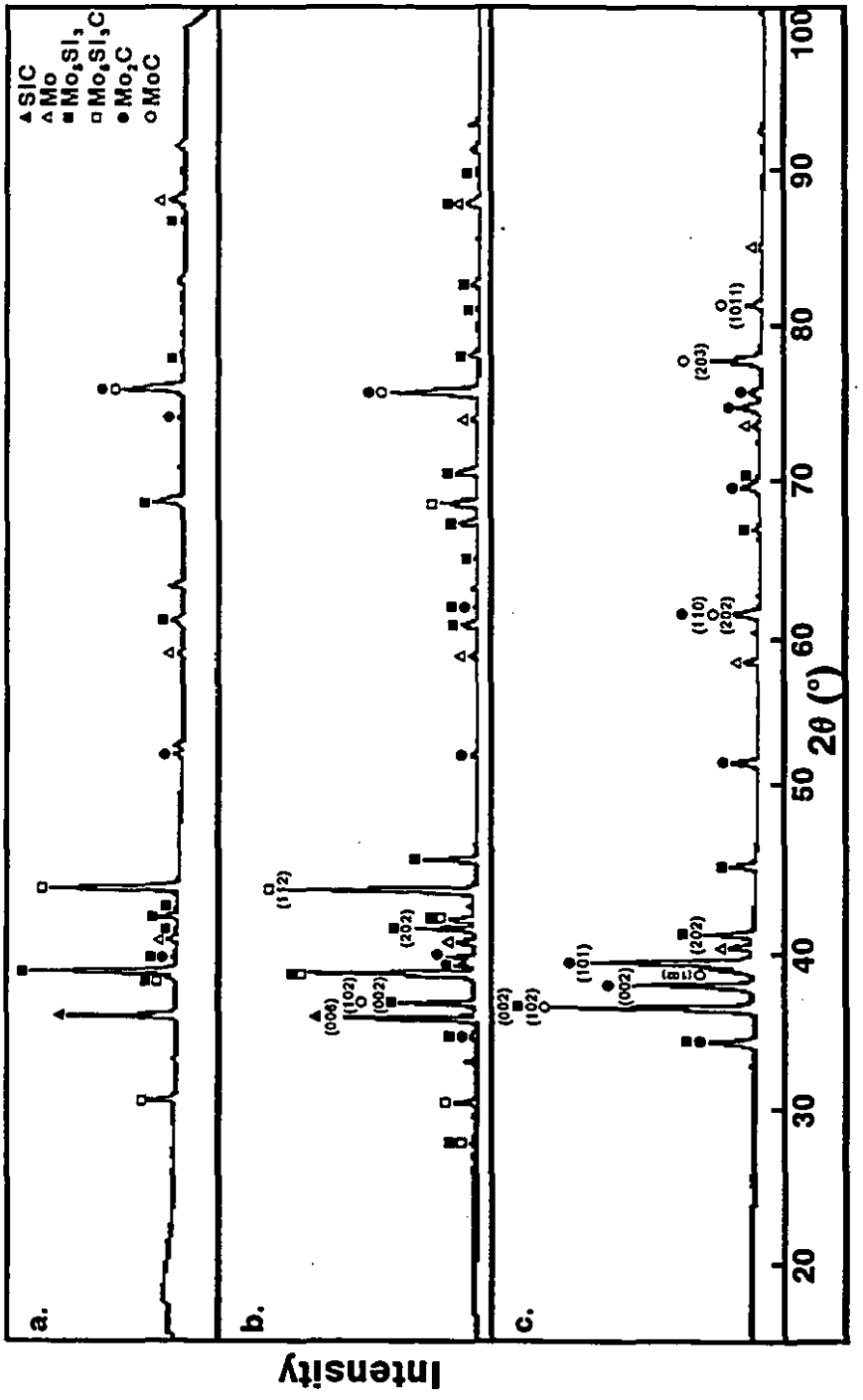

Figure 7.11- XRD spectra of layers indicated by labels (a), (b), and (c) in Figure 7.10.

performed on the mixed layer (Figure 7.11b). Mo_5Si_3 was identified as the main phase, although Mo_5Si_3C was still present as a result of the characteristic wavy aspect of the reaction layers. At $2\theta=36.7°$, the peak (102) of hexagonal η-MoC_{1-x} was observed. However, this position overlapped with the (002) peak of Mo_5Si_3. The last grinding step was performed until optical microscopy of the cross-section of the Mo fracture surface showed only the carbide layer in contact with Mo, at which point about 70 μm had been removed from the sample. X-ray diffraction was then performed resulting in a more accurate determination of the type of carbide present (Figure 7.11c). Although residual Mo_5Si_3 was still detected, carbide peaks were observed over the whole angular range. β-Mo_2C was identified as the main carbide formed, however peaks of η-MoC_{1-x} were also observed [64].

The most intense peak for β-Mo_2C was observed at $2\theta=39.49°$ corresponding to the (101) planes, followed by the (002) which showed some texturing in accordance with previous observations (Figure 7.10). The presence of η-MoC_{1-x} was determined by its most intense peaks: (102) and (103). Although the (102) peak was superimposed with Mo_5Si_3 (002), comparing the relative intensities of Mo_5Si_3 (002) and (202) in Figure 7.11b, it could be seen that the peak at $2\theta=36.78$ (Figure 7.11c) could not be explained solely by the presence of Mo_5Si_3 (002). Moreover, the diffraction pattern for η-MoC_{1-x} shows this peak as its most intense one. Other peaks also corresponded to η-MoC_{1-x}, *i.e.*, the (203) and the (1011) planes. For these peaks there was no overlapping, therefore their presence could not be related to any other phase.

The transformation from β-Mo_2C to η-MoC_{1-x} was predicted in the thermodynamic analysis of the Mo-Si-C system. Mo-carbides are of an interstitial nature. When C diffuses into Mo, it tends to be accommodated in the octahedral interstitial sites of the Mo bcc structure (Figure 3.8). However, these sites are too small for C, especially along the *c* direction. This situation forces a change of crystal structure of Mo from bcc to hcp which contains larger octahedral interstitial sites (Figure 3.9) arranged in a simple hexagonal structure. In the Mo_2C structure, C occupies statistically half of the available interstitial sites. However, the actual amount of C present can vary widely, resulting in a range of compositions for these compounds. Although surface and grain-boundary diffusion usually have lower activation energies compared to lattice diffusion, the formation of MoC_{1-x} showed that the latter process also took place, especially at high temperatures. Diffusion of C into the Mo_2C structure at high temperatures stabilizes the hexagonal and substoichiometric η-MoC_{1-x}. β-Mo_2C crystallizes in the L3' structure where Mo forms a hcp lattice with stacking sequence ABAB... and the C atoms form a simple hexagonal structure by occupying octahedral interstitial sites of the Mo-hcp structure. The complete stacking sequence is AXBXAXBX... (Figure 7.12a). If the C concentration exceeds the homogeneity values for β-Mo_2C, substoichiometric η-MoC_{1-x} precipitates. The similarity of crystal structures observed between the two carbides may also confirm this fact, assuming that β-Mo_2C undergoes a displacive transformation resulting in η-MoC_{1-x}. In the new structure, C occupies statistically two-thirds of the octahedral interstitial sites of the hcp structure. The stacking sequence of Mo is

ABCACBABCACB... and the complete stacking sequence becomes AXBX'CX''AX''CX'BXAXBX'CX''AX''CX'BX... (Figure 7.12b).

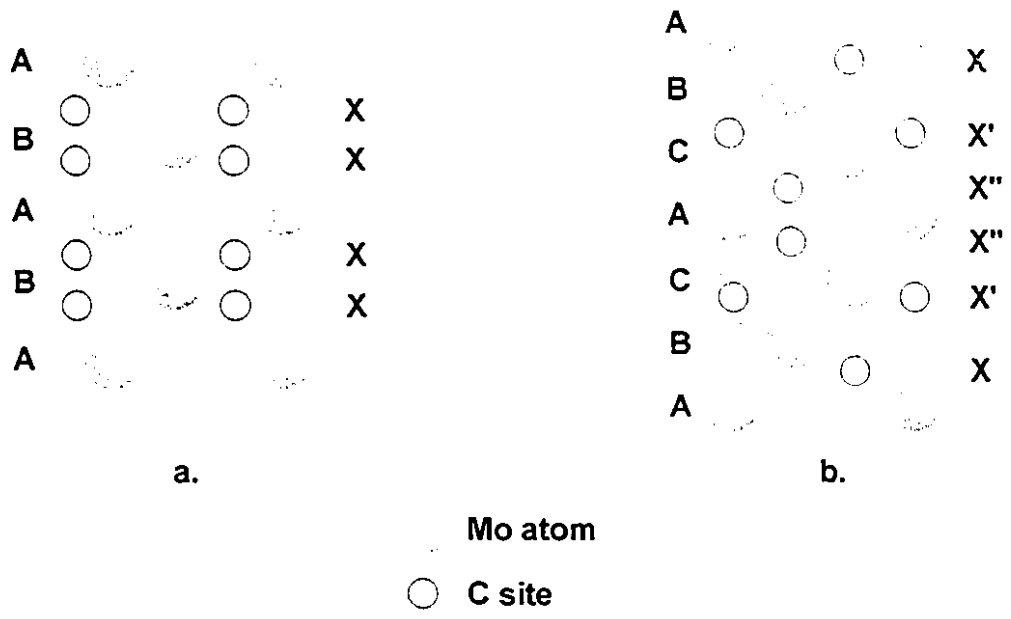

Figure 7.12- Atomic stacking sequence of (a) hexagonal β-Mo_2C and (b) hexagonal η-MoC_{1-x} [38,64].

The activation energy and growth behaviour of SiC-Mo interfaces were also studied. A series of samples was prepared varying the joining temperature from 1200°C to 1500°C, and the holding time from 15 minutes to 4 hours. In order to inhibit the reaction between SiC and Mo during cooling of the diffusion couple, it was necessary to minimize the time that the joints were exposed to elevated temperatures. This was achieved by furnace cooling the samples directly to room temperature, as indicated in Figure 6.6. The thickness of the reaction zones was measured by image analysis.

Figure 7.13 shows a plot of the thickness of the interfaces as a function of the holding time for two joining temperatures: 1200°C and 1400°C. The interfaces grew in a parabolic fashion, resulting in a time exponent equal to 0.5 for equation (3.1). This behaviour is typical of systems where the diffusing species have limited solubility in the host material [20]. Diffusion of Si and C into Mo was immediately followed by reaction, which contributed to the growth of the interfaces. The rate of interfacial growth was higher at 1400°C compared to 1200°C, which accounts for an increase in the value of K_p in equation (3.1), with increase in temperature. As diffusion mechanisms are thermally activated processes, increasing the temperature from 1200°C to 1400°C resulted in substantial mass transport across the interface and faster growth of the reaction zones.

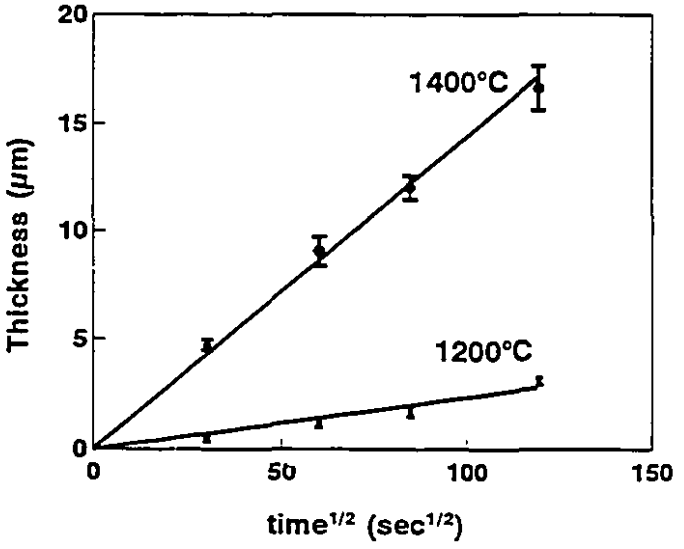

Figure 7.13- Thickness of reaction zone as a function of joining time.

The activation energy for the formation of SiC-Mo interfaces was calculated using equations (3.1) and (3.2). A series of samples was hot-pressed from 1200°C to 1500°C for 1 hour, and furnace cooled. The thicknesses of the corresponding interfaces were measured resulting in a plot of $\ln(K_p)$ as a function of the temperature, as shown in Figure 7.14.

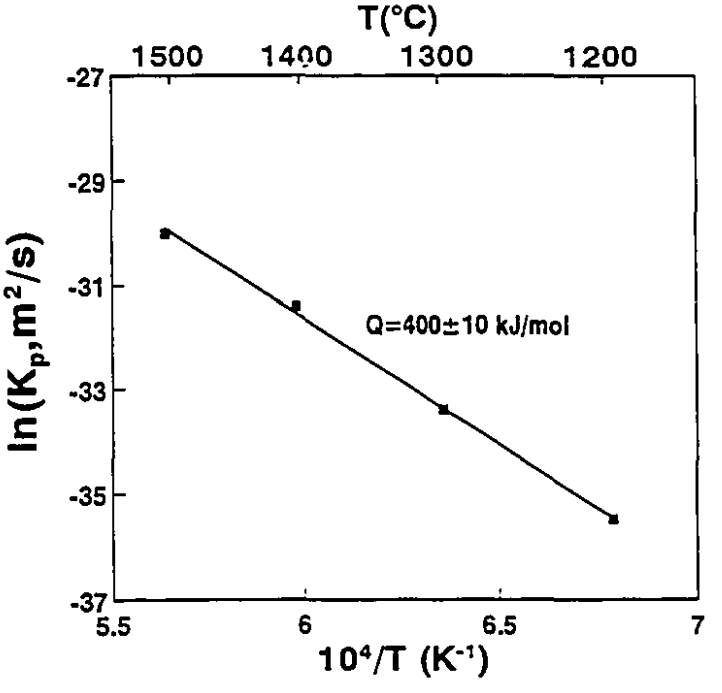

Figure 7.14- Plot of $\ln(K_p)$ *vs.* temperature for diffusion bonded SiC-Mo couples.

A value of 400±10 kJ/mol was obtained for the activation energy, Q. This value is of the same order of magnitude of previously reported results (517 kJ/mol and 477 kJ/mol) [27,33]. The interpretation of activation energies is a controversial topic. It has been suggested that the activation energy for the formation of interfaces can be

obtained by simply summing the energy terms corresponding to the decomposition of the ceramic, and diffusion of the atomic species [65]. Others have reported that the resulting value of activation energy depends solely on the dominating diffusion mechanism [27]. Comparing the activation energy for the formation of SiC-Mo interfaces (400 kJ/mol) with the activation energies for the solid-state diffusion of Si and C in Mo (327 kJ/mol and 348 kJ/mol, respectively) [63,66], it can be observed that the values are of the same order of magnitude, which indicates that the second hypothesis is correct. However, a more positive assessment of the problem would require the values of the activation energy for the diffusion of C through Mo_5Si_3 and Si through Mo_2C, which are not available in the literature. Nevertheless, further evidence to support the second hypothesis was obtained upon studying the Si_3N_4-Mo system, as described in Chapter 8.

7.3 MECHANICAL PROPERTIES

7.3.1 INTERFACIAL STRENGTH

In order to establish a surface preparation procedure, the importance of the surface conditions on joint strength was evaluated. For this experiment, a sample consisting of a Mo foil inserted between two SiC blocks was hot pressed at 1400°C for 1 h (P = 20 MPa). One face of the Mo foil was cleaned and polished to a 1 μm finish, and placed in contact with a SiC surface, also cleaned and polished in the same fashion. The other two faces in contact were cleaned and polished to a 45 μm finish. While the former sample was successfully joined, the latter one containing the rough surfaces was

not. This clearly indicates that solid-state diffusion bonding requires not only surfaces free of contamination, but also intimate contact between the mating materials. Therefore polishing of the surfaces to be joined to a 1μm finish was performed for the remainder of the work.

Joining temperature and time were the main parameters studied. Figure 7.15 shows a matrix of joining conditions used to hot-press SiC-Mo samples. Three distinct regions can be visualized, corresponding to:

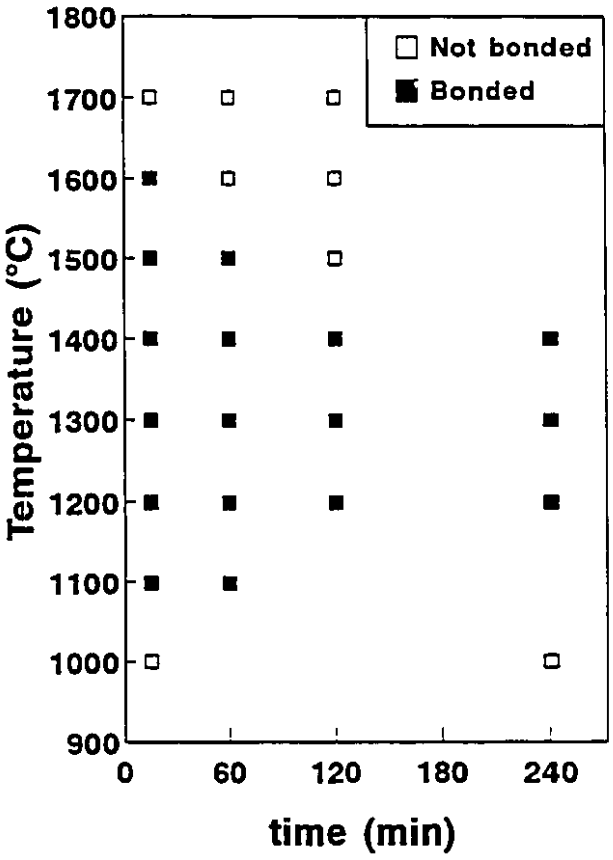

Figure 7.15- Experimental conditions used to hot-press SiC-Mo diffusion couples (P = 20 MPa).

1. **Unbonded samples:** low temperature region (less than 1100°C) which did not result in joining even for holding times of the order of 4 hours.
2. **Bonded samples:** corresponds to intermediate joining temperatures (between 1100°C and 1600°C). Between 1100°C and 1400°C, joining occurred for any length of time between 15 minutes and 4 hours. As the temperature increased, bonding took place only in samples hot-pressed for short times.
3. **Debonded samples:** refers to the high temperature region of the Figure. For such conditions, joining occurred but the samples debonded during cooling. As the joining temperature increased from 1500°C to 1700°C, the time for complete debonding and failure of the joint decreased from 1 hour to less than 15 minutes.

The strength of solid-state diffusion bonded ceramic-metal joints depends on the nature and microstructure of the interface between the joining materials. For non-reactive systems, the interface is either formed by the development of van der Waals forces or it consists of very thin diffusion layers. In such cases, joint strength is primarily a function of the fraction of bonded surface [23]. Maximum strength can then be achieved by optimizing the joining parameters (time, temperature, and applied load) to result in complete bonding as shown in Figure 2.6a. However, reactive systems such as SiC-Mo, develop reaction zones which may be detrimental to the strength of the joints. If the reaction zone is relatively thick, joint strength becomes dependent on the physical and mechanical properties of the reaction products. In particular, the CTE and elastic

modulus mismatch between interfacial reaction products and the original ceramic and metal play a decisive role.

The first indication that the amount of reaction, and consequently the thickness of the interface, drastically affected the strength of SiC-Mo joints was obtained from samples hot-pressed at 1500°C. When the holding time was 1 hour, the average thickness of the interface was 31.8 μm, and the joint debonded during cooling. However, samples hot-pressed reducing the holding time to 10 minutes resulted in reliable interfaces with an average thickness of 24 μm (Figure 7.6). Although the joining temperature was the same for both samples, the concentration of interfacial flaws was severely reduced by decreasing the holding time from 1 h to 10 min. This result indicated that although the concentration of residual stresses in a joint is a function of the joining temperature, the thickness of the reaction zone may dominate in the final joint strength. To verify this assumption, plots of shear strength as a function of bonding temperature and time are showed in Figure 7.16 [67]. Substantial scattering was observed and attributed to the brittle nature of fracture, and to the deflection of the crack path towards the SiC. All sheared specimens fractured in the interface between SiC and the reaction zone, most of which remained attached to the Mo side. However, the occurrence of brittle fracture was characterized by the presence of residual SiC particles on the Mo fracture surface and of interface material on the SiC fracture surface, as shown in Figure 7.17. The SiC particles present on the Mo fracture surface were distributed over the entire area, however, the concentration of these particles was higher close to the corners of the

a.

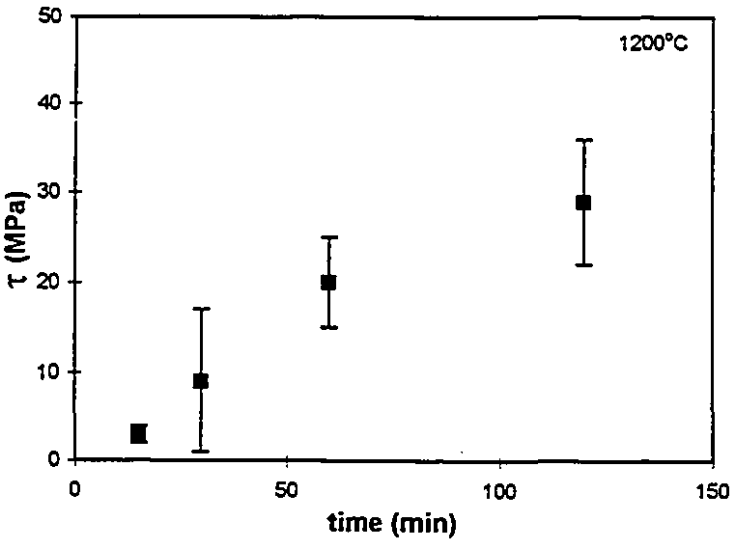

b.

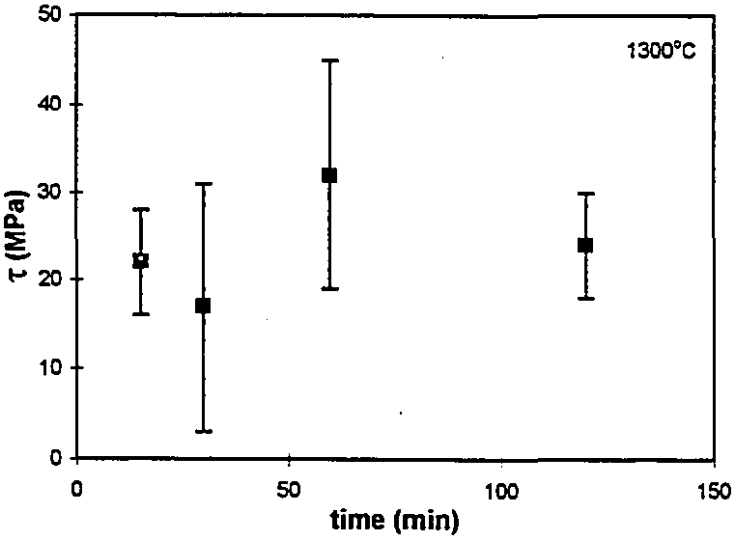

Figure 7.16- Plots of shear strength as a function of time for SiC-Mo samples hot-pressed at (a) 1200°C and (b) 1300°C.

c.

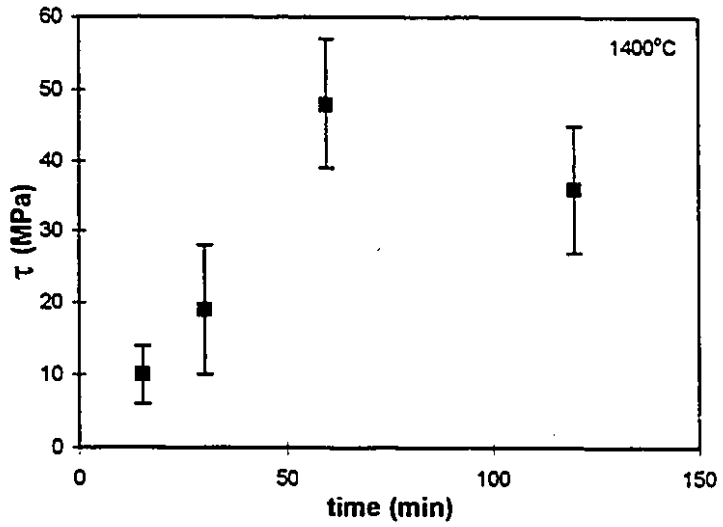

d.

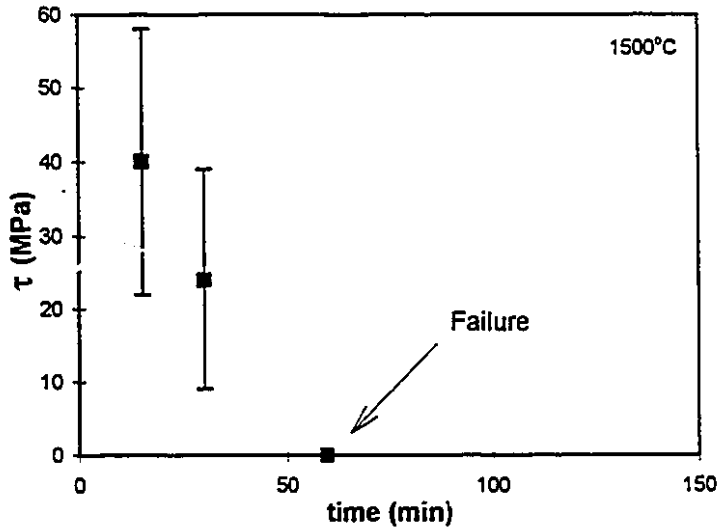

Figure 7.16(cont)- Plots of shear strength as a function of time for SiC-Mo samples hot-pressed at (c) 1400°C and (d) 1500°C.

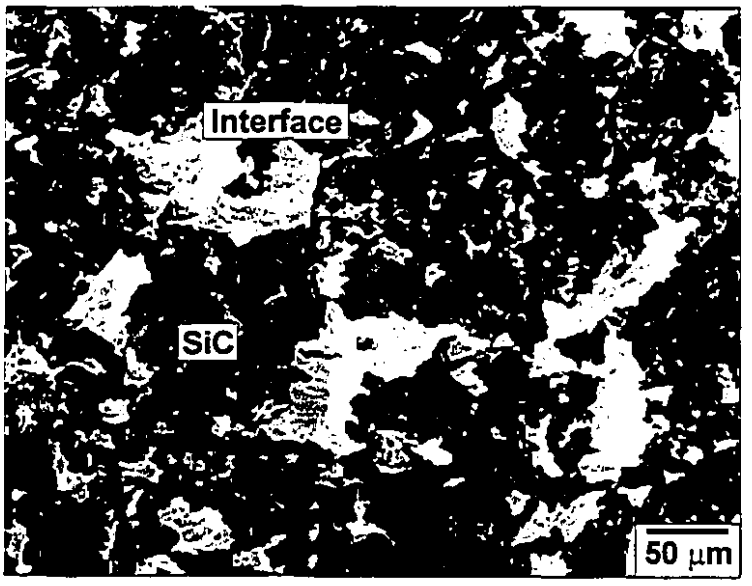

a.

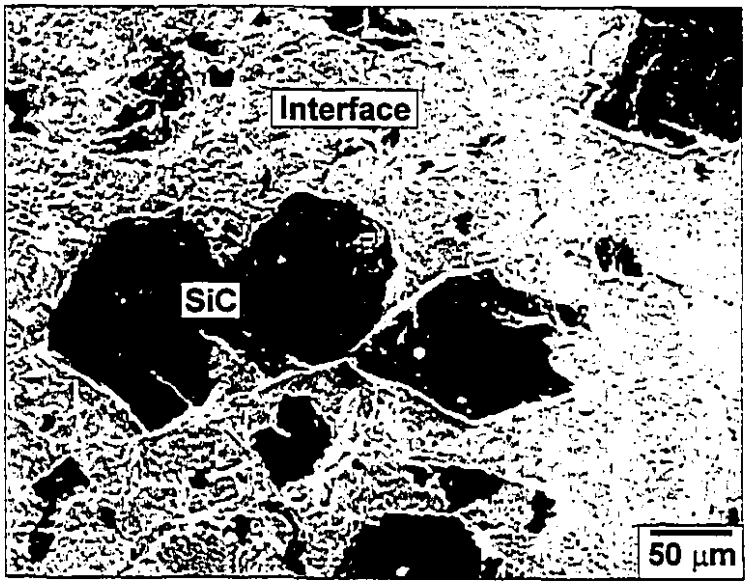

b.

Figure 7.17- BEI of (a) SiC and (b) Mo fracture surfaces (vacuum, T = 1650°C, t = 30 min, P = 10 MPa).

sample. The non-uniform concentration of SiC particles was probably related to the fact that stresses are developed preferentially near the corners of rectangular surfaces. As for the small particles observed on the SiC fracture surface, X-ray diffraction showed that these particles were mainly Mo_5Si_3 and Mo_5Si_3C. This result is consistent with Figure 7.10, where the interface is seen attached to the Mo-fracture surface of the corresponding sample. EPMA was also performed on the interface particles present on the SiC fracture surface depicted in Figure 7.17. The results confirmed the XRD observations, however an excess of C was also detected. The presence of free C within interfaces hot-pressed at high temperatures is predicted by the Mo-Si-C phase diagram, as discussed earlier.

An analysis of Figure 7.16 showed that at 1200°C, the shear strength appeared to increase with time from an average value of 3 MPa to an average value of 29 MPa when the bonding time increased from 15 minutes to 2 hours. At 1300°C, the average shear strength showed a slight increase from 15 minutes to 1 hour, achieving a maximum value of 32 MPa. Although the average value measured for a bonding time of 2 hours was 24 MPa, the range of measured values are well within the error bar of the strength measured for a bonding time of 1 hour. At 1400°C, the shear strength increased initially to reach a maximum of 50 MPa after 1 hour, and then decreased to about 35 MPa, after 2 hours of hot-pressing. At 1500°C, the effect of time was to decrease the shear strength of the samples, resulting in failure of joints hot-pressed for 1 hour or more.

The variation of the shear strength with bonding time for the different bonding

temperatures can be explained in terms of the fraction of bonded surface and growth of the interfacial reaction layer. The growth of the SiC-Mo reaction layer is governed by equations (3.1) and (3.2). Because K_p is an exponential function of the temperature and a parabolic function of time, for low temperatures (1200°C), the growth of the reaction layer was limited even when the bonding time was set to 2 hours. Consequently, at this temperature the strength of the joint was controlled by the amount of bonded surface which increased with time. At 1300°C, the beneficial effect of increasing the fraction of bonded area started to be counteracted by the detrimental effect of the growth of the reaction layer. At 1400°C, the latter growth process began to take over for times longer than 1 hour, and at 1500°C, it was the dominant term [67].

In order to understand the detrimental effect of the growth of the reaction layer on the shear strength of the samples, the microhardness and the elastic modulus of the phases present at the interface were measured, by conducting depth sensing indentation on the interface depicted in Figure 7.6. Representative load-depth plots obtained for the various phases present within that interface, as well as for Mo and SiC, are shown in Figure 7.18.

The different maximum loads and depths indicated differences in the elastic and plastic properties between the various phases analyzed. For instance, SiC which has the highest hardness also has the lowest depth of penetration and the highest maximum load. Mo_5Si_3, on the other hand, has the highest maximum depth of penetration and the lowest maximum load, and consequently is expected to have the lowest hardness. The loading

segments for Mo_5Si_3 and Mo_5Si_3C were different from those of Mo, SiC, and Mo_2C, in that they consisted of two distinct regions: in the first one, the increase in the load is low and that of the depth is high, and in the second region the slope of the load-depth curve increased substantially. Such trends indicated that the plastic and elastic deformation to accommodate the indenter may have occurred first in a soft material and then moved to a harder and more rigid material situated underneath the phase being studied. Because the reactions to produce Mo_2C and Mo_5Si_3 are influenced by local conditions such as the diffusion path of C, they may proceed faster in certain locations than in others. As a result, the thickness of the Mo_2C and Mo_5Si_3 phases may vary drastically from point to point, which explains the differences observed in the loading segments [67].

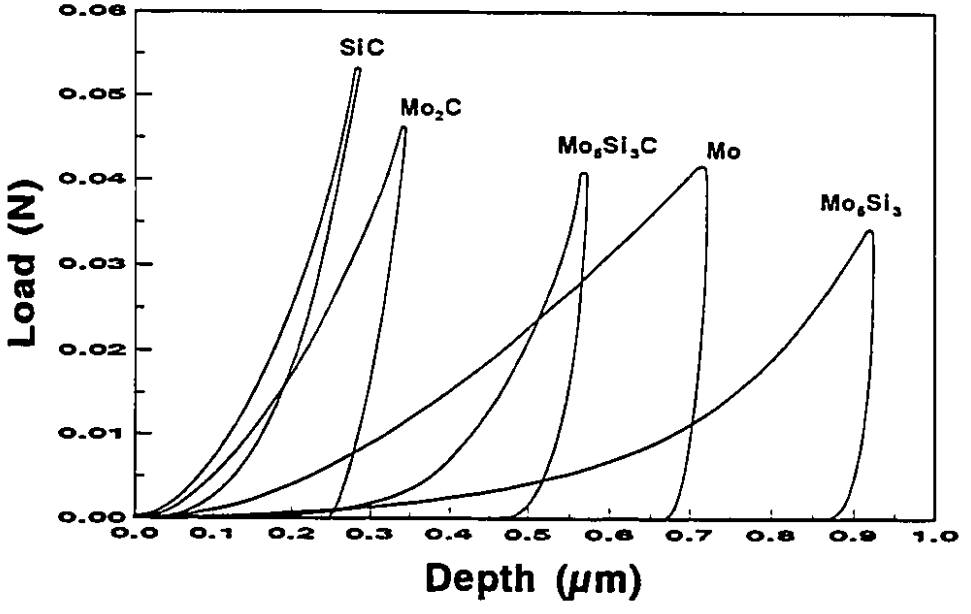

Figure 7.18- Load-depth curves of SiC, Mo, and the reaction products present within the interface illustrated in Figure 7.6.

From the load-depth plots in Figure 7.18, the microhardness and elastic modulus of the different phases were obtained using equations (6.8) and (6.9), respectively. These results are given in Table 7.1 along with published values.

Table 7.1- Hardness and Elastic Modulus of SiC, Mo, and Interfacial Reaction Products [1,16,38,66,68]

Material	$HV_{meas.}$ (GPa)	$HV_{lit.}$ (GPa)	$E_{meas.}$ (GPa)	$E_{lit.}$ (GPa)
Mo	3.83±0.26	2.30	307.0±37.5	324
SiC	44.75±5.36	33.00	402.7±52.5	414
Mo_2C	23.69±8.40	15	339.1±33.4	228
Mo_5Si_3	1.37±0.49	11	231.1±75.1	260
Mo_5Si_3C	3.85	N/A	201.7	N/A

The errors represented in Table 7.1 correspond to plus or minus one standard deviation. The unusually large errors in the measurements reflect the scatter in the data, probably resulting from surface defects such as scratches and voids. Nevertheless, the elastic modulus values determined from unloading segments of load-depth plots were in good agreement with the published values. In the case of the Mo_5Si_3 phase, the scatter may also be due to the variation in the thickness of the layer. The difference between the calculated and published values for the hardness of SiC is due to the fact that the current tests were conducted at a much lower load (approximately 0.055 N) than in the microindentation regime (1 to 10 N). For most ceramics, a change of typical load values

from the microindentation regime to the nanoindentation regime is accompanied by an increase in the measured hardness of the material. This behaviour is referred to as the indent action size effect [67,69].

By examining the elastic moduli obtained for Mo_2C, Mo_5Si_3, and Mo_5Si_3C, the detrimental effect of excessive growth of the reaction layer on the shear strength of SiC-Mo joints could be explained. The presence of an interfacial reaction layer within the SiC-Mo joints results in the existence of two interfaces: one between Mo and Mo_2C and another between SiC and Mo_5Si_3 or Mo_5Si_3C, depending on the joining temperature. Mo has a CTE of $5.35 \times 10^{-6} °C^{-1}$ (between 20°C and 1600°C), and Mo_2C has an average CTE of $6.55 \times 10^{-6} °C^{-1}$. In addition, the elastic modulus of these materials are similar (Table 7.1). For these reasons, the interface between Mo and Mo_2C is not subjected to substantial residual stresses during cooling from the joining temperature. The interface between SiC and Mo_5Si_3, on the other hand, is expected to have high tensile and shear stresses as a result of the mismatch in the CTE and elastic modulus of these two materials. The coefficients of thermal expansion for SiC and Mo_5Si_3, in the temperature range of 20 to 1000°C, are 4.5×10^{-6} and $6.4 \times 10^{-6} °C^{-1}$, respectively. In addition, the elastic modulus of SiC is approximately 403 GPa, and that of Mo_5Si_3 is 231 GPa. A similar situation occurs within the interface between SiC and Mo_5Si_3C. The high tensile and shear stresses generated in the area adjacent to the SiC-Mo_5Si_3/Mo_5Si_3C enhance the propensity to fracture in this region. Hence, a decrease in strength is observed in the joints hot-pressed at 1500°C, where substantial growth of the ternary phase Mo_5Si_3C

occurred. Furthermore, from Figure 7.10 it can also be seen that extensive precipitation of Mo_5Si_3 results in a high concentration of flaws parallel to the interface plane. When cracking occurs perpendicular to the interface it is characteristic of the mismatch in the thermal expansion properties of the joining materials. On the other hand, cracking occurring parallel to the interface is related to a volume expansion corresponding to a phase transformation. The volume change associated with the formation of Mo_5Si_3 from the original Mo is of the order of 46%, whereas the formation of Mo_2C from the original Mo results in a volume change of only 20%. This explains the longitudinal cracking observed within the Mo_5Si_3 layer in Figure 7.10.

Therefore, in the choice of the suitable conditions to prepare ceramic-metal joints, knowledge of the mechanism of reaction between the materials and the evolution of the interface are fundamental requirements. For the case of hot-pressed SiC-Mo diffusion couples, strong bonding was obtained when the joining temperature and time were 1400°C and 1 hour, respectively, with a resulting average shear strength of 50 MPa. Under such conditions total bonding did not occur. Maximum strength resulted when a balance was achieved between the fraction of bonded interface and the growth of the reaction zone. In this case, a more realistic representation of the appearance of the interface can be accomplished by modifying Figure 2.3 to include the effect of time on the shear strength, τ, of a sample joined at a particular temperature, T (Figure 7.19).

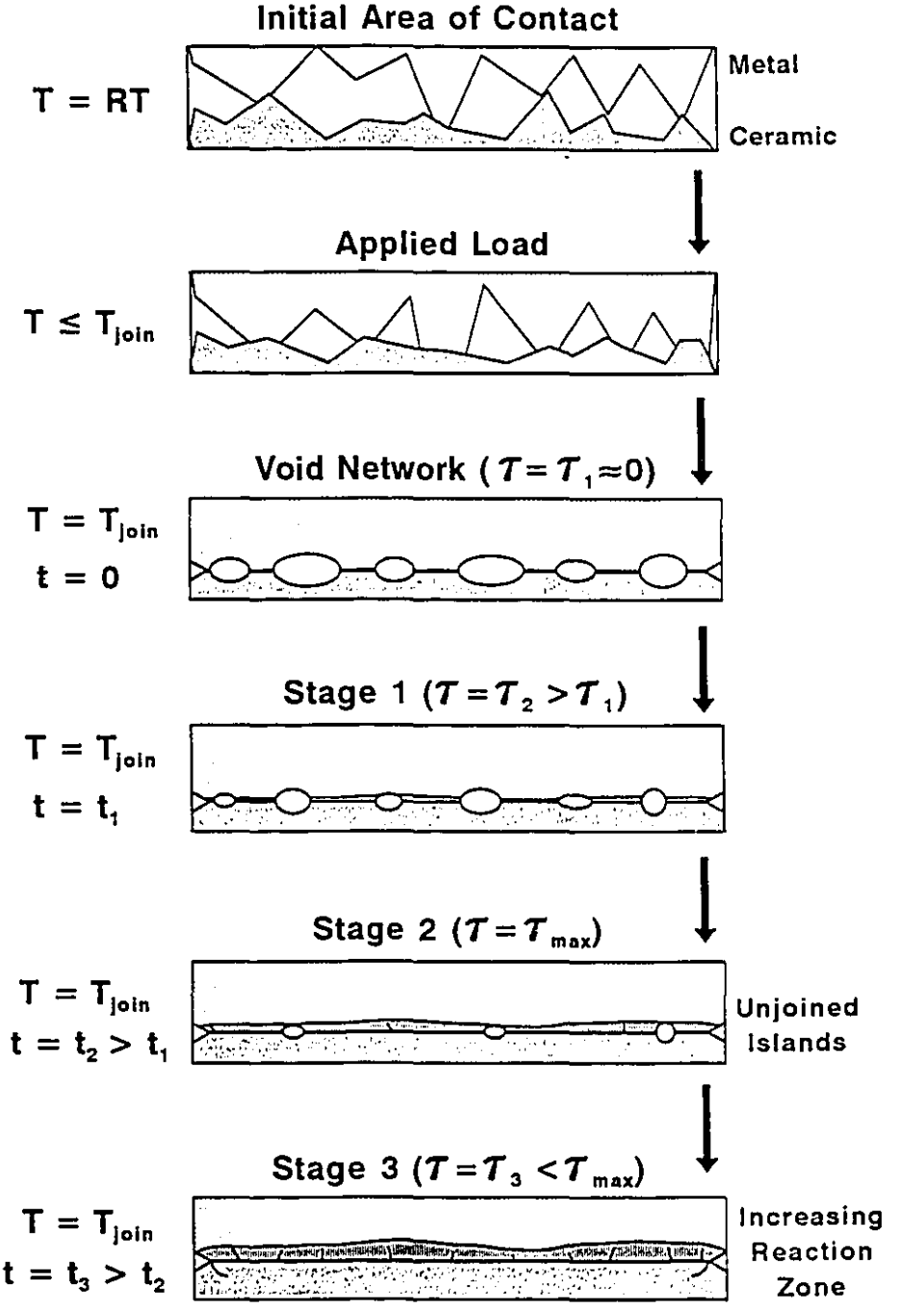

Figure 7.19- Schematics of diffusion bonding taking place on a reactive ceramic-metal system.

7.3.2 RESIDUAL STRESSES

The distribution of residual stresses on SiC-Mo joints was studied using neutron diffraction. Tests were performed on joints hot-pressed under vacuum, at temperatures between 1200°C and 1400°C for 1 hour (P = 10 MPa). In-plane (σ_x), and normal (σ_y) stresses were obtained using equation (6.6) and (6.7). Initially, the distribution of stresses was studied along a line perpendicular tc the interface and far from the corner of the samples, as shown in Figure 7.20.

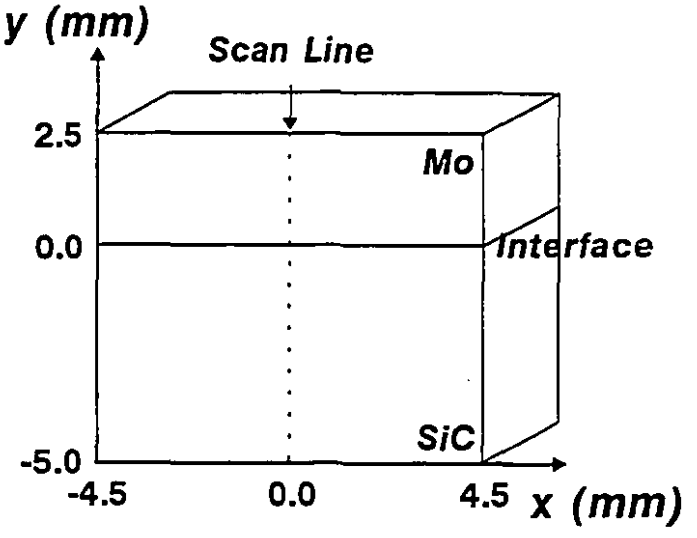

Figure 7.20- Position of scan line for neutron diffraction tests across SiC-Mo interfaces.

From the results of the sample hot-pressed at 1200°C (Figure 7.21), it can be seen that SiC is in compression in the direction of σ_x while Mo is in tension, as ex··· ted

from Figure 4.8. This behaviour is mainly a consequence of the mismatch in the CTEs of these materials. As Mo has a higher CTE than SiC, it contracted more during cooling of the joint from the bonding temperature. However, as its contraction was restrained by the bonding with SiC, compressive stresses resulted on the ceramic side. Mo reacted to that tendency, trying to extend the interface, thus resulting in a concentration of tensile stresses especially near the interface with SiC.

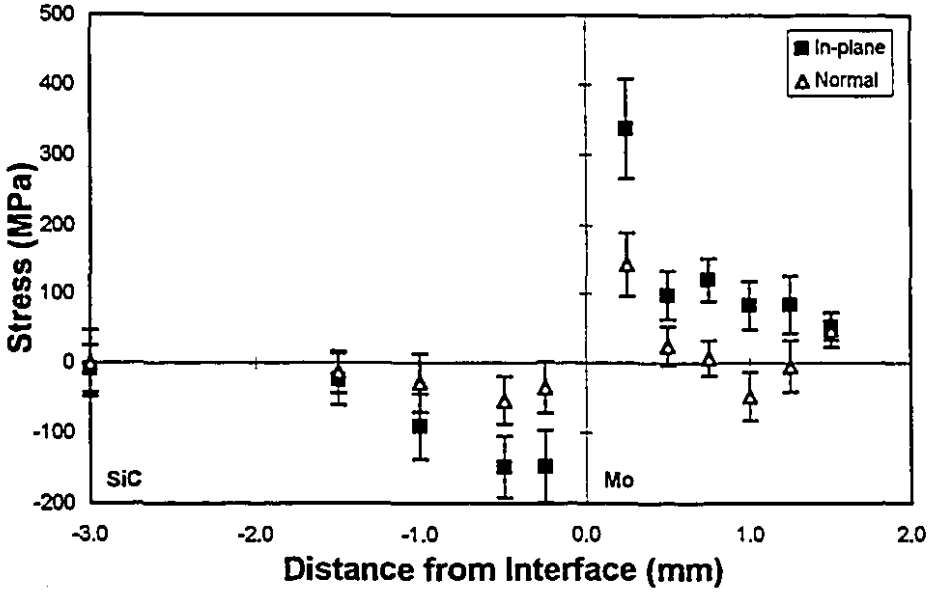

Figure 7.21- Distribution of stresses across SiC-Mo interface. Sample hot-pressed in vacuum (T = 1200°C, t = 1 h, P = 10 MPa), and furnace cooled from the joining temperature.

Also from Figure 7.21, it can be seen that in both the ceramic and metal sides, the amplitude of σ_x decreased with distance from the interface. On the SiC side, the value of σ_x was close to zero at a distance of 1.5 mm from the interface, whereas at the Mo side, residual stresses were measured at an equivalent distance, as a result of the plastic deformation of the metal. Adjacent to the interface, σ_x reached average values of -140 MPa on the SiC side and 330 MPa on the Mo side. By contrast, the normal component remained close to zero (within the margin of error) for most of the region studied, with an oscillating pattern resulting in slight tension on the metal side and compression on the ceramic side. This behaviour has been observed in FEM studies of other ceramic-metal joints prepared by solid-state diffusion. Figure 7.22 shows the FEM results obtained for a Si_3N_4-SM50 stainless-steel diffusion couple, and indicates good agreement with the results of this work for both the σ_x and σ_y components [48].

Increasing the joining temperature to 1400°C, increased the amplitude of σ_x adjacent to the interface to an average value of -550 MPa on the SiC side, and 300 MPa on the Mo side (Figure 7.23). Increasing the joining temperature from 1200°C to 1400°C, increased the ΔT to which the sample was exposed during cooling, which reflected higher values of residual stresses. However, the profile of the stress distribution is similar to that obtained for the sample hot-pressed at 1200°C. A remarkable exception is the presence of high values of the σ_y component far from the interface. As the temperature increased, the compressive yield strength of Mo would decrease, as indicated in Appendix I (Figure AI.12). On the other hand, the pressure applied to the sample

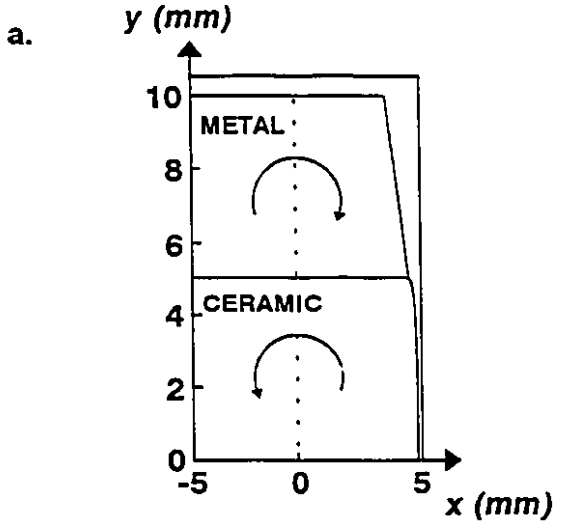

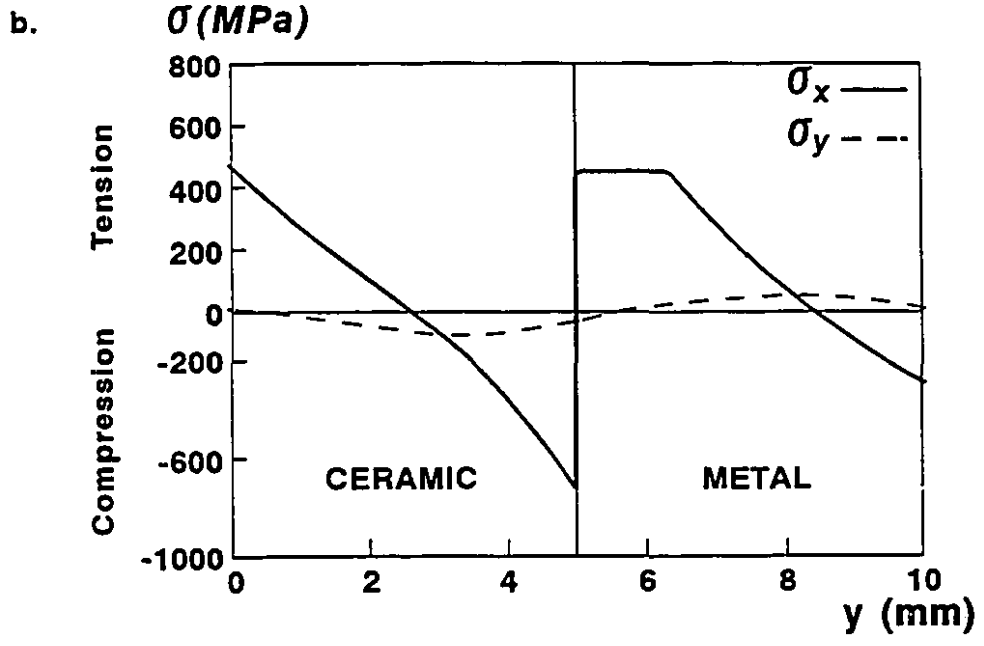

Figure 7.22- (a) Line analyzed by FEM on Si_3N_4-SM50 samples (dotted line). Arrows indicate bending moment originated by the CTE mismatch between ceramic and metal; (b) distribution of resulting stresses [48].

remained constant (10 MPa), resulting in higher plastic deformation of the metal, and consequently, higher values of σ_y.

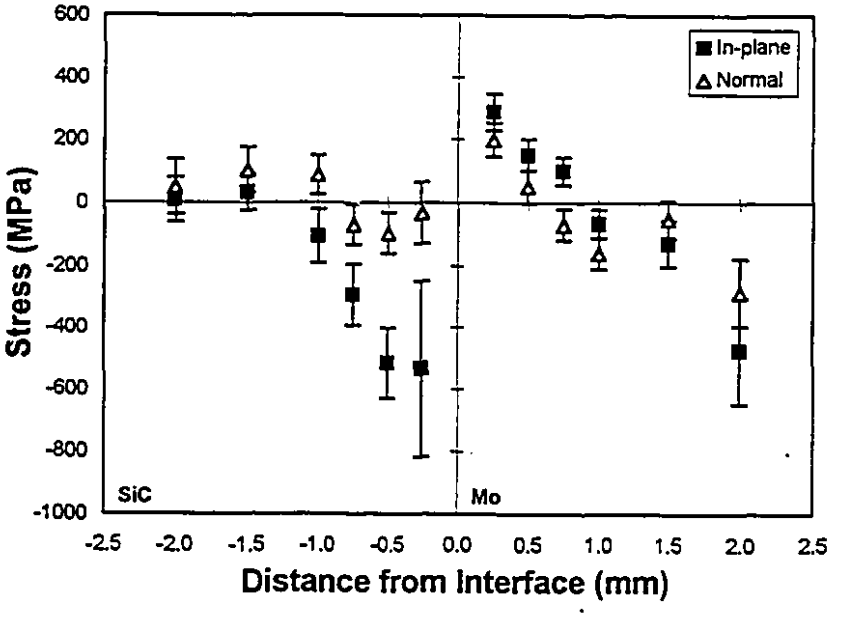

Figure 7.23- Distribution of stresses across SiC-Mo interface. Sample hot-pressed in vacuum (T = 1400°C, t = 1 h, P = 10 MPa), and furnace cooled from the joining temperature.

The results contained in Figure 7.21 and 7.23 refer to samples which were furnace cooled from the joining temperature. Figure 7.24 shows the distribution of stresses on a sample hot-pressed at 1400°C, and cooled according to the two-step profile depicted in Figure 6.6. The distribution of stresses is similar to that from Figure 7.23. However, the amplitude of stresses adjacent to the interface, particularly for the σ_x

component, was significantly reduced. Slow cooling increased the time to which the sample was exposed to elevated temperatures. At high temperatures atomic mobility is enough to promote structural rearrangement of the materials in accommodating residual stresses, *i.e.* creep. Therefore, controlled cooling should decrease the amplitude of σ_x on the SiC side adjacent to the interface. Figure 7.23 provides clear evidence of this phenomenon, since under rapid cooling conditions an average value of σ_x = -550 MPa was obtained, whereas the amplitude of σ_x in the equivalent position in Figure 7.24 is only 50 MPa.

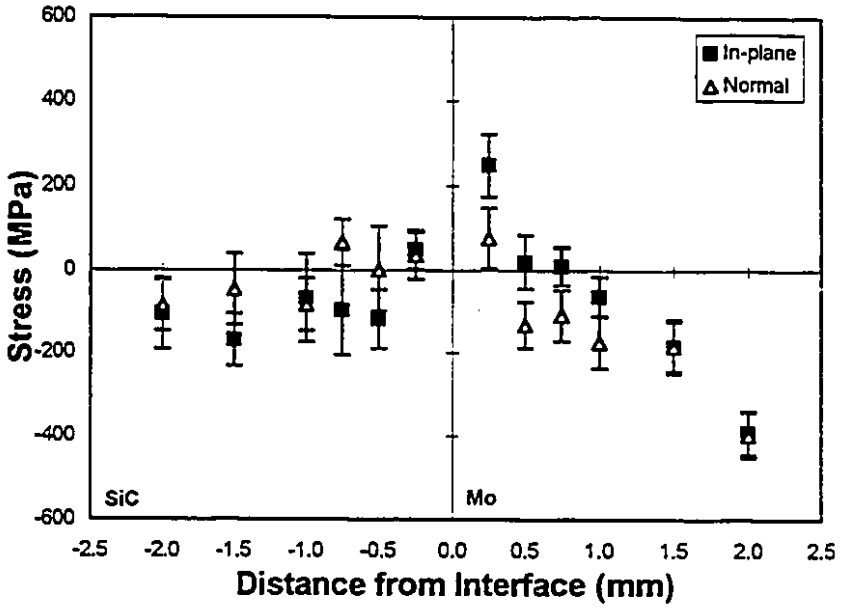

Figure 7.24- Distribution of stresses across SiC-Mo interface. Sample hot-pressed in vacuum (T = 1400°C, t = 1 h, P = 10 MPa), and slowly cooled from the joining temperature.

The presence of residual stresses was also investigated in the direction parallel to the ceramic-metal interface for a sample hot-pressed at 1200°C, as indicated in Figure 7.25a. From the FEM results on Si_3N_4-SM50 stainless-steel [48], σ_x would be expected to increase upon approaching the edge of the sample, where it would reach its maximum value, as it can be seen from Figure 7.25b. However, Figure 7.25c shows that the average value of σ_x is higher at the position corresponding to $x = \pm 1.75$ mm than at $x = \pm 3.5$ mm. This result can be explained by the presence of unjoined edges as illustrated in Figure 4.1 and 7.19. Limited edge bonding can result from mechanical bevelling of the bonding surfaces. Grinding and polishing of SiC and Mo prior to joining may have removed extra material from the region close to the edges, preventing contact of the joining surfaces [2]. Thus, the edge of the joint may not correspond to the edge of the bonded interface, which in this case, would be somewhere between the positions corresponding to 2 and 4 mm in Figure 7.25a. If bevelling occurs, σ_x is expected to reach its maximum at the position corresponding to the edge of the bonded interface, which explains the decrease in the amplitude of stresses observed at the positions $x = \pm 4$ mm in Figure 7.25c.

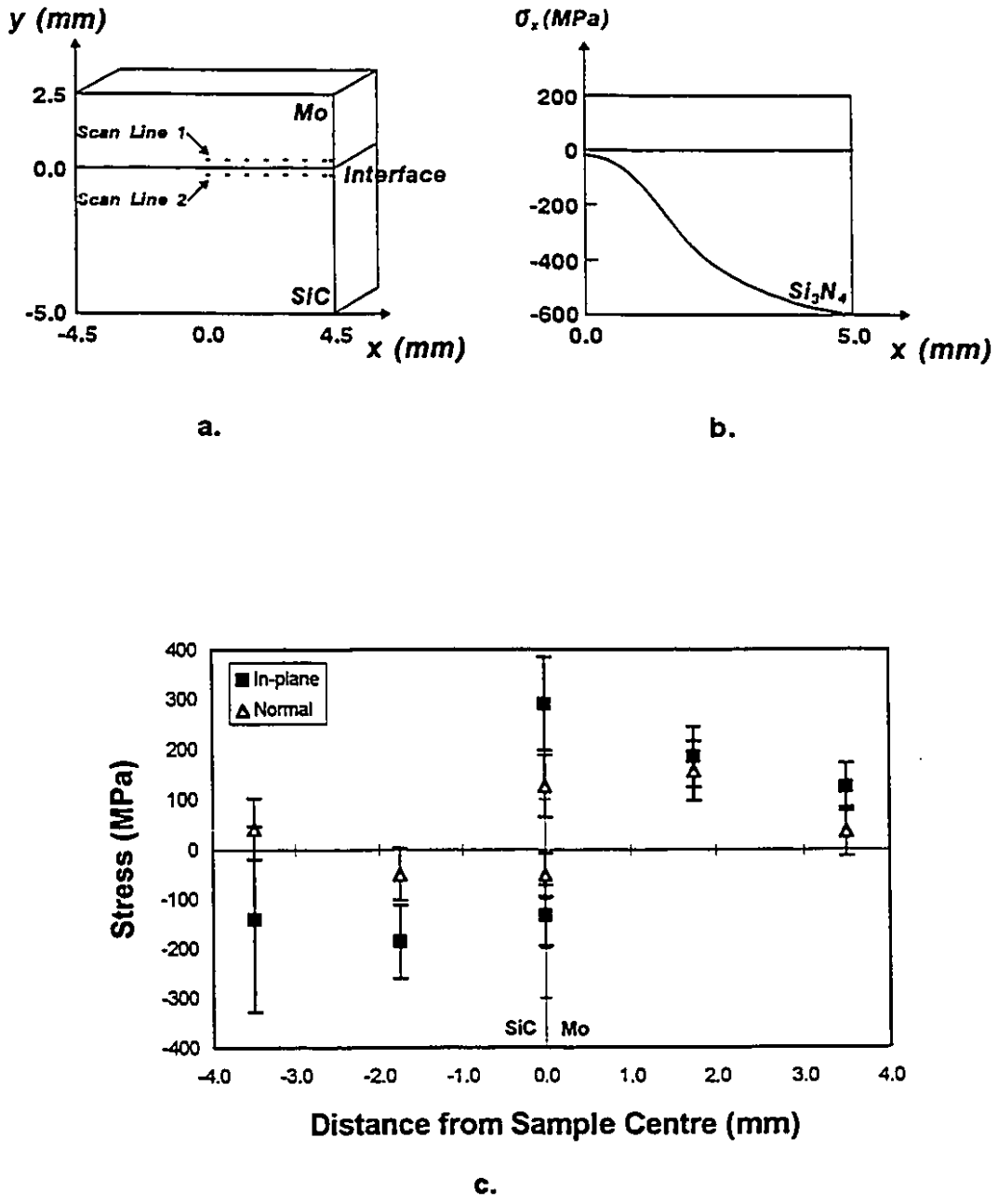

Figure 7.25- (a) Neutron diffraction scan lines parallel to interface; (b) distribution of σ_x for scan line 2 on Si_3N_4-SM50 [48]; (c) stresses on SiC-Mo sample (T = 1200°C, t = 1 h, P = 10 MPa).

CHAPTER 8:

THE Si_3N_4-Mo SYSTEM

A similar approach to that described in Chapter 7 was applied to the Si_3N_4-Mo system. Diffusion couples were hot-pressed and the microstructure of the resulting interfaces was analyzed. The results were then compared to thermodynamic predictions obtained using the F*A*C*T program and database, as well as data from the literature. In addition, the mechanical strength of the joints was investigated by shear testing.

8.1. THERMODYNAMIC EVALUATION OF THE Si_3N_4-Mo SYSTEM

A thermodynamic evaluation of the Si_3N_4-Mo system was carried out using F*A*C*T. The analysis was based on the stability of Mo-Si-N compounds that could possibly result from joining Si_3N_4 to Mo in a vacuum of 10^{-2} atm. (1 kPa). A plot of the standard Gibbs free energy of formation of these compounds as a function of temperature, for this pressure, is shown in Figure 8.1.

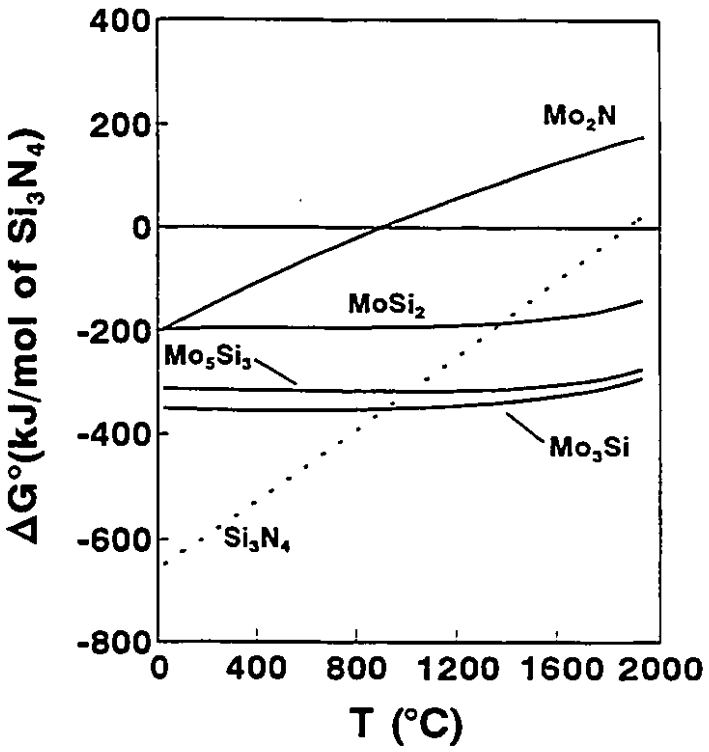

Figure 8.1- Standard free energy of formation of Mo-Si-N compounds as a function of the temperature (data obtained from F*A*C*T).

Si_3N_4 is more stable than any other Mo-Si-N compound from room temperature to approximately 900°C. Hence, no reaction is expected to take place in that temperature

range. At 900°C, Mo_3Si becomes more stable than Si_3N_4, and is expected to form. The reaction starts with the decomposition of Si_3N_4 into Si and N_2,

$$Si_3N_4 = 3\ Si + 2\ N_{2(g)} \ldots\ldots\ldots \Delta G_1^0 \qquad (8.1)$$

where $\Delta G_1^0 > 0$, since the formation of Si_3N_4 has $\Delta G^0 < 0$. In the next step, Si diffuses and reacts with Mo to form Mo_3Si,

$$9\ Mo + 3\ Si = 3\ Mo_3Si \ldots\ldots\ldots \Delta G_2^0 \qquad (8.2)$$

Combining (8.1) and (8.2) and setting the joining temperature to 1300°C results in

$$Si_3N_4 = 3\ Si + 2\ N_{2(g)} \ldots\ldots\ldots \Delta G_1^0 = 216\ kJ$$

$$9\ Mo + 3\ Si = 3\ Mo_3Si \ldots\ldots\ldots \Delta G_2^0 = -345\ kJ$$

therefore,

$$Si_3N_4 + 9\ Mo = 3\ Mo_3Si + 2\ N_{2(g)} \ldots\ldots\ldots \Delta G_3^0 = \Delta G_1^0 + \Delta G_2^0 = -129\ kJ \qquad (8.3)$$

According to reaction (8.3), $N_{2(g)}$ is formed along with Mo_3Si. If $N_{2(g)}$ diffuses into Mo to form Mo_2N, the reaction at 1300°C is expressed by

$$Si_3N_4 = 3\ Si + 2\ N_{2(g)} \ldots\ldots\ldots \Delta G_1^0 = 216\ kJ$$

$$9\ Mo + 3\ Si = 3\ Mo_3Si \ldots\ldots\ldots \Delta G_2^0 = -345\ kJ$$

$$8\ Mo + 2\ N_{2(g)} = 4\ Mo_2N \ldots\ldots\ldots \Delta G_4^0 = 76\ kJ \qquad (8.4)$$

resulting in,

$$Si_3N_4 + 17\ Mo = 3\ Mo_3Si + 4\ Mo_2N \ldots\ldots\ldots \Delta G_5^0 = \Delta G_1^0 + \Delta G_2^0 + \Delta G_4^0 = -53\ kJ \qquad (8.5)$$

However, as $\Delta G_3^0 < \Delta G_5^0$ the reaction expressed by (8.5) is thermodynamically less favourable than the one expressed by (8.3). Therefore, the formation of Mo_2N at the Si_3N_4-Mo interface is not expected to occur during joining experiments at 1300°C in

vacuum. In fact, Figure 8.1 shows that, in a vacuum of 10^{-2} atm., Mo_2N is unlikely to form in the temperature range of 0 to 2000°C. Up to 900°C, Mo_2N is not expected to form because the reaction between Si_3N_4 and Mo is thermodynamically unfavourable. Between 900°C and 2000°C, Mo_2N is not expected to form, as its ΔG^0 of formation is positive, contributing towards making the overall ΔG^0 for the reaction less negative. Therefore Mo-silicides are the only reaction products anticipated to be present at Si_3N_4-Mo interfaces of diffusion couples hot-pressed under a vacuum of 10^{-2} atm..

Depending on the concentration of Si within the interface, Mo_3Si can be converted to Mo_5Si_3. At 1300°C, this reaction is expressed by

$$Si_3N_4 + 9\,Mo = 3\,Mo_3Si + 2\,N_{2(g)} \ldots\ldots \Delta G_3^0 = -129\ kJ \qquad (8.3)$$

$$3\,Mo_3Si + 12/5\,Si = 9/5\,Mo_5Si_3 \ldots\ldots \Delta G_6^0 = -569\ kJ \qquad (8.6)$$

$$4/5\,Si_3N_4 = 12/5\,Si + 8/5\,N_{2(g)} \ldots\ldots \Delta G_7^0 = 173\ kJ \qquad (8.7)$$

resulting in,

$$9/5\,Si_3N_4 + 9\,Mo = 9/5\,Mo_5Si_3 + 18/5\,N_{2(g)} \ldots\ldots \Delta G_8^0 = \Delta G_3^0 + \Delta G_6^0 + \Delta G_7^0 = -525\ kJ \qquad (8.8)$$

Mo_5Si_3, in its turn, can be transformed into $MoSi_2$ following

$$9/5\,Si_3N_4 + 9\,Mo = 9/5\,Mo_5Si_3 + 18/5\,N_{2(g)} \ldots\ldots \Delta G_8^0 = -525\ kJ$$

$$9/5\,Mo_5Si_3 + 63/5\,Si = 9\,MoSi_2 \ldots\ldots \Delta G_9^0 = -1152\ kJ \qquad (8.9)$$

$$21/5\,Si_3N_4 = 63/5\,Si + 42/5\,N_{2(g)} \ldots\ldots \Delta G_{10}^0 = 907\ kJ \qquad (8.10)$$

which gives

$$6\,Si_3N_4 + 9\,Mo = 9\,MoSi_2 + 12\,N_{2(g)} \ldots\ldots \Delta G_{11}^0 = \Delta G_8^0 + \Delta G_9^0 + \Delta G_{10}^0 = -770\ kJ \qquad (8.11)$$

Because $\Delta G_{11}^0 < \Delta G_8^0 < \Delta G_3^0$, the sequence of reactions to convert Mo_3Si into Mo_5Si_3,

and Mo_5Si_3 into $MoSi_2$, by addition of Si into the original silicide, is thermodynamically favourable. This sequence of events is illustrated in Figure 8.2, where the 1300°C cross-section of the Mo-Si-N phase diagram, corresponding to a pressure of 10^{-2} atm. (Figure 3.6), is plotted along with the Si_3N_4-Mo interface (dotted line) [36].

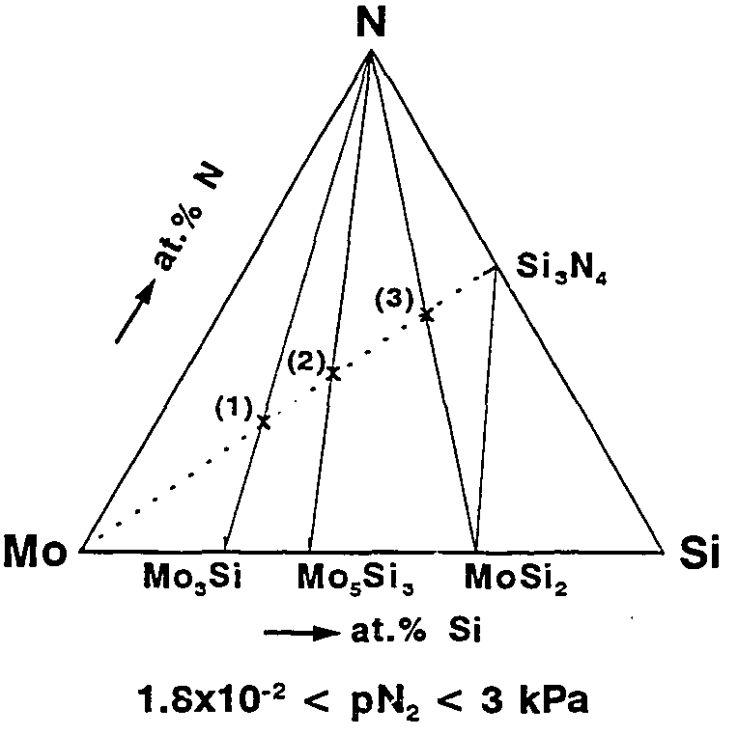

Figure 8.2- The 1300°C cross-section of the Mo-Si-N phase diagram for a total pressure of 1 kPa, plotted along with the Si_3N_4-Mo interface (dotted line). Labels (1) to (3) indicate interfacial reactions [36].

The Si_3N_4-Mo interface intercepts three tie-lines in Figure 8.2. At the extremities of those tie-lines are Mo_3Si and N, Mo_5Si_3 and N, and $MoSi_2$ and N. Thus, the sequence of reactions proposed by (8.3), (8.8), and (8.11) confirms the observations of the

Mo-Si-N phase diagram. The relative concentration of each compound can be found either from equations (8.3), (8.8), and (8.11), or by the lever rule applied to the tie-lines of Figure 8.2, since the two analyses are equivalent. The silicide-to-N ratios calculated from Figure 8.2 were 2.9:1 for Mo_3Si:N, 2.1:1 for Mo_5Si_3:N, and 1.1:1 for $MoSi_2$:N, whereas equations (8.3), (8.8), and (8.11) yielded silicide-to-N ratios of 3:1 for Mo_3Si:N, 2:1 for Mo_5Si_3:N, and 1.1:1 for $MoSi_2$:N.

Because diffusion is the dominating reaction mechanism in solid-state joining, silicide transformations may or may not be observed depending on the joining parameters, especially bonding temperature and time. These parameters affect the concentration of diffusing Si at the interface, and therefore, the nature of the resulting silicide. Upon joining of SiC to Mo, Mo_3Si was not observed at the interface for the joining conditions described in Chapter 7. However, for the same joining conditions, Mo_3Si may be observed during the initial stages of the bonding process between Si_3N_4 and Mo. As Si_3N_4 is more stable than SiC at temperatures between 1200°C and 1500°C, both in vacuum and N_2 (Figure 8.3), the initial concentration of Si within Si_3N_4-Mo interfaces may be low enough to allow the observation of Mo_3Si. Subsequently, diffusion of Si into Mo_3Si produces Mo_5Si_3. In addition, because no ternary phase is known for the Mo-Si-N system, if the concentration of Si reaches 66.67 at.% at any point of the interface, the transformation from Mo_5Si_3 to $MoSi_2$ may also be observed, as indicated in the binary Mo-Si phase diagram (Figure 3.10) [41].

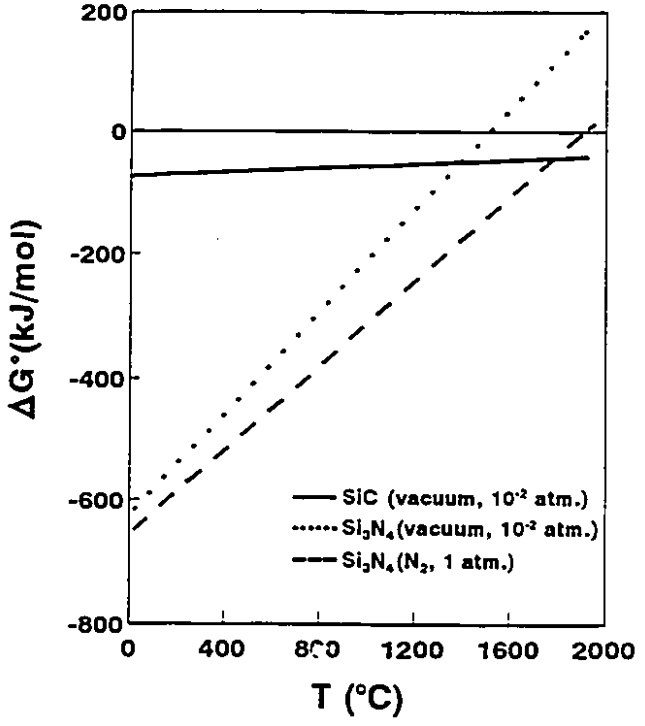

Figure 8.3- Standard free energy of formation of Si_3N_4 and SiC as a function of the temperature (data obtained from F*A*C*T).

8.2 INTERFACE CHARACTERIZATION

8.2.1 MICROSTRUCTURAL EVOLUTION

Si_3N_4-Mo diffusion couples were hot-pressed at temperatures varying from 1100°C to 1800°C, under vacuum and in N_2. Figure 8.4 summarizes the results obtained from these experiments. Bonding was not observed in samples hot-pressed for temperatures lower than 1200°C in either vacuum or N_2. At 1100°C, for example, even for holding times up to 4 hours, the fraction of bonded interface was insufficient to establish a reliable mechanical joint between the ceramic and the metal. As a

consequence of poor bonding, a high concentration of unbonded islands remained at the interface. The fact that SiC was joined to Mo at lower temperatures and shorter times than Si_3N_4, is related to the different thermodynamic stabilities of the ceramics. Si_3N_4 being more stable than SiC (Figure 8.3) required higher temperatures and/or longer times to close a substantial fraction of the voids present within the interface, thus promoting joining.

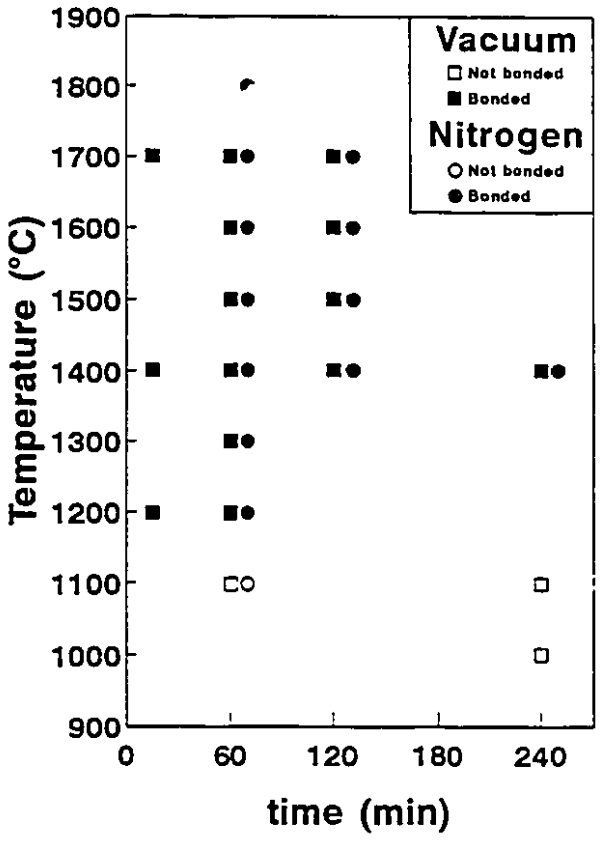

Figure 8.4- Experimental conditions used to hot-press Si_3N_4-Mo diffusion couples (P = 10 MPa).

Between 1200°C and 1800°C, Si_3N_4 was successfully joined to Mo under vacuum and in N_2, for bonding times varying from 15 minutes to 4 hours. All the samples were hot-pressed under a uniaxial pressure of 10 MPa. For the range of bonding times investigated, joining started to take place at 1200°C. Samples prepared between 1200°C and 1400°C developed single-layer interfaces at the sub-micron scale, both in vacuum and in N_2. An example of such an interface is shown in Figure 8.5, which depicts a sample hot-pressed at 1400°C for 1 hour, in N_2. A BEI contrast was observed at some points of the interface. EDS spot analysis performed at different locations indicated that the contrast was due to the precipitation of Mo_3Si.

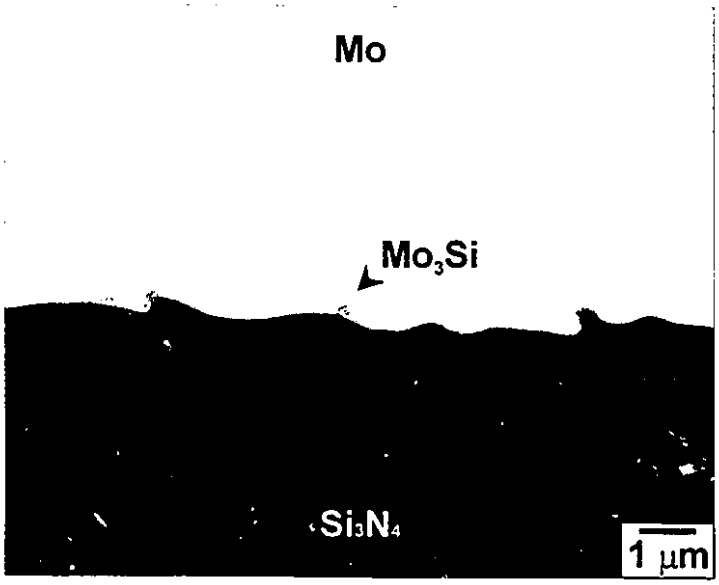

Figure 8.5- BEI of Si_3N_4-Mo interface (N_2, T = 1400°C, t = 1 h).

A plot of the thickness of the interfaces for the samples hot-pressed at 1400°C, as a function of the joining time, is shown in Figure 8.6. The samples were cooled directly to room temperature. The interfaces grew in a parabolic fashion and, as a result, increasing the holding time from 1 to 4 hours did not result in a significant increase in the interface thickness for that temperature.

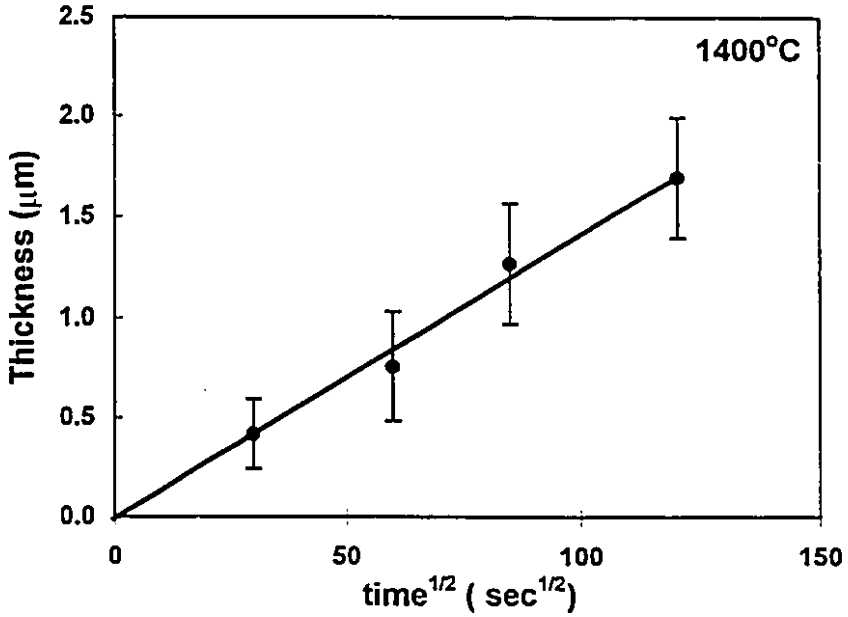

Figure 8.6- Thickness of reaction zone as a function of joining time (T = 1400°C).

On the other hand, increasing the temperature to 1500°C resulted in the development of thicker reaction zones. Figure 8.7 shows two interfaces produced at 1500°C. Figure 8.7a illustrates the interface of a sample hot-pressed for 2 h in N_2, and Figure 8.7b shows the interface of a sample hot-pressed for 1 h under vacuum. BEI and EDS showed that both reaction zones consisted of single Mo_3Si layers. However,

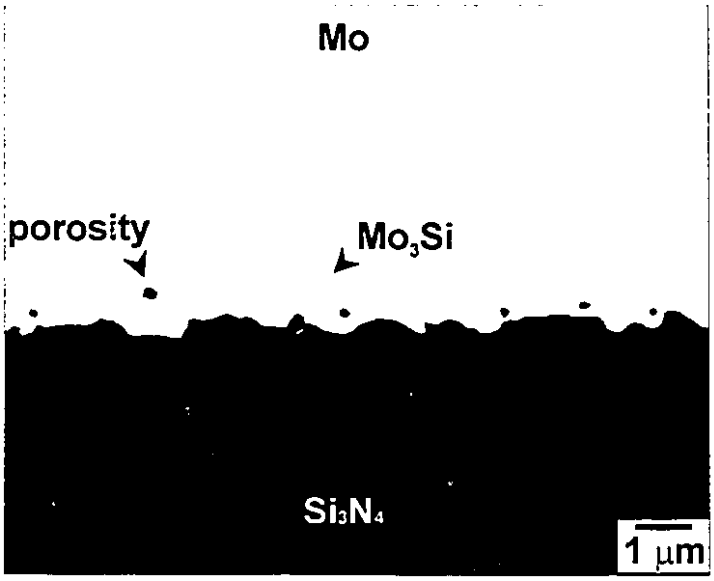

a.

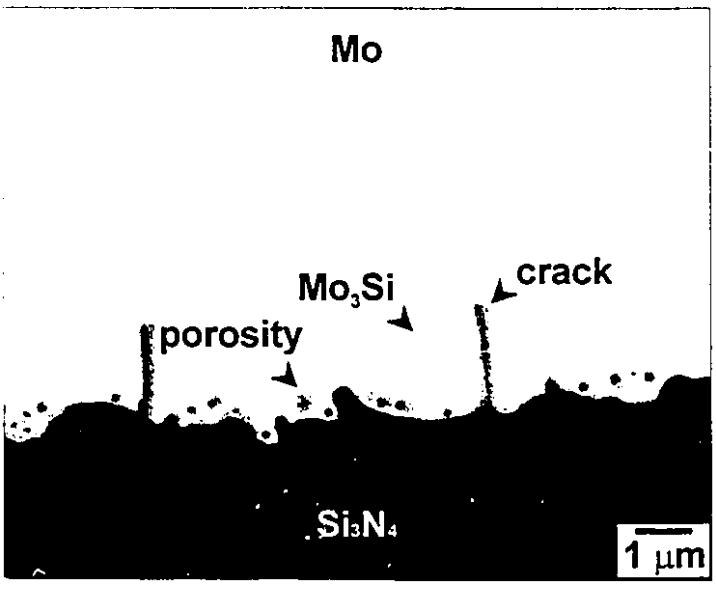

b.

Figure 8.7- BEI of Si_3N_4-Mo interfaces.(a) (N_2, T = 1500°C, t = 2 h); (b) (vacuum, T = 1500°C, t = 1 h).

important differences were noticed between the two specimens. Firstly, the sample hot-pressed in vacuum had a thicker interface (2 μm) than that hot-pressed in N_2 (1 μm), despite the shorter holding time (1 h in vacuum and 2 h in N_2). As a result, transverse thermal cracking can be observed in the Mo_3Si layer of the thicker interface (Figure 8.7b). Secondly, porosity was observed in the Mo_3Si layer adjacent to Si_3N_4, in the region of the original Si_3N_4-Mo boundary line. The concentration of pores was higher in the sample hot-pressed under vacuum (Figure 8.7b), compared to the sample hot-pressed in N_2 (Figure 8.7a). The small concentration of pores in the sample shown in Figure 8.7a, within a relatively thin reaction layer, indicated that the reaction to form Si_3N_4-Mo interfaces proceeded at a slower rate under N_2 than in a vacuum. As the formation of Mo_3Si depended upon the decomposition of Si_3N_4, joining in N_2 changed the stability of the ceramic compared to joining in vacuum.

The equilibrium reaction of Si_3N_4 is expressed by (8.1). By heating up Si_3N_4-Mo couples to the joining temperature, $N_{2(g)}$ is evolved. When joining experiments were carried out in a dynamic vacuum, $N_{2(g)}$ evolved according to (8.1) was continuously pumped out, driving (8.1) towards reestablishing the equilibrium vapour pressure of the system, *i.e.*, from left to right. On the other hand, when joining was carried out in a N_2 atmosphere, lower concentrations of $N_{2(g)}$ evolved as a result of the higher stability of Si_3N_4 (Figure 8.3). In addition, the $N_{2(g)}$ which evolved upon the dissociation of Si_3N_4 remained in the environment. As a result, the equilibrium vapour pressure of the system was easily achieved, and (8.1) proceeded more slowly.

The presence of pores at the interface is also related to the evolution of $N_{2(g)}$ due to the dissociation of Si_3N_4. As the temperature increased from 1400°C to 1500°C, the stability of Si_3N_4 decreased, contributing to the dissociation of Si_3N_4 into Si and $N_{2(g)}$. The Si diffused into Mo resulting in the formation of Mo_3Si. At these temperatures, Si has a very low solubility in Mo (Figure 3.10). Under vacuum, Si_3N_4 dissociated more readily than in the presence of N_2, resulting in thicker interfaces and also in considerable evolution of N_2 gas. As no reaction occurred between Mo and N_2, under the partial pressures of N_2 investigated, the $N_{2(g)}$ resulting from the decomposition of Si_3N_4, could either diffuse into Mo_3Si and/or Mo, or be evolved at the interface between Si_3N_4 and the reaction layer, thus resulting in porosity. Because of the low solubility of N_2 in Mo (less than 10^{-2} at.%, according to Table 3.2), when the continuous dissociation of Si_3N_4 exceeded this critical concentration of N_2, the gas could no longer dissolve in the metal. Consequently, the excess N_2 remained trapped at the interface forming a porous layer. It has been suggested that, depending on the amount of N_2, the gas could build up significant pressures inside the pores [36]. Because the dissociation of Si_3N_4 is strongly dependent on the temperature, increasing the joining temperature would result in a substantial increase in the N_2 pressure within the porous layer (Figure 8.8) [70].

Figure 8.9 shows an interface produced at 1600°C. The sample was hot-pressed for 1 hour under vacuum. The average thickness of the interface was 3 μm. Along with Mo_3Si and the porous layer, both observed previously, a new BEI contrast was present in the interfacial region adjacent to Si_3N_4. EDS area analysis confirmed the composition

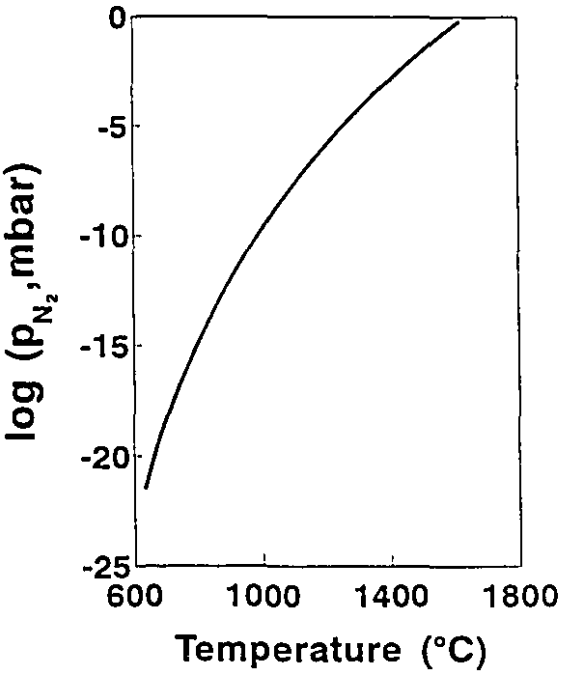

Figure 8.8- Partial pressure of $N_{2(g)}$ as a function of the temperature, for decomposition of Si_3N_4 in vacuum, according to equation (8.1) [70].

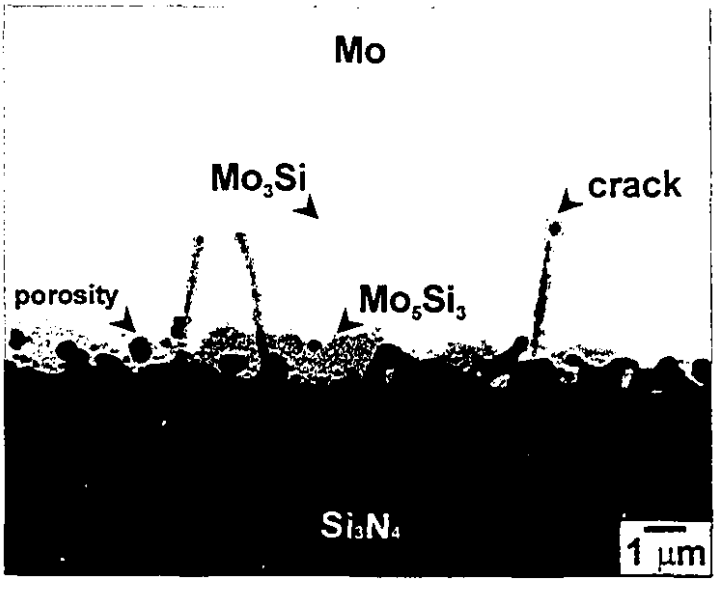

Figure 8.9- BEI of Si_3N_4-Mo interface (vacuum, T=1600°C, t=1 h).

of the new phase as Mo_5Si_3. The formation of Mo_5Si_3 occurred as a consequence of diffusion of Si into Mo_3Si, as anticipated in the thermodynamic analysis of the Mo-Si-N system. However, the transformation of Mo_5Si_3 into $MoSi_2$ was not observed at 1600°C, for holding times up to 4 hours. This indicated that the concentration of diffusing Si in Mo did not reach the minimum necessary to form $MoSi_2$ (66.7 at.%), at any point within the interface. Increasing the temperature to 1700°C, increased the total thickness of the interface, as shown in Figure 8.10 (vacuum hot-pressed for 2 hours). Porosity also increased as a result of the extensive dissociation of Si_3N_4. Within the same interface, substantial transformation of Mo_3Si into Mo_5Si_3 was observed, however, there was no evidence of the formation of $MoSi_2$, even after 4 hours of hot-pressing.

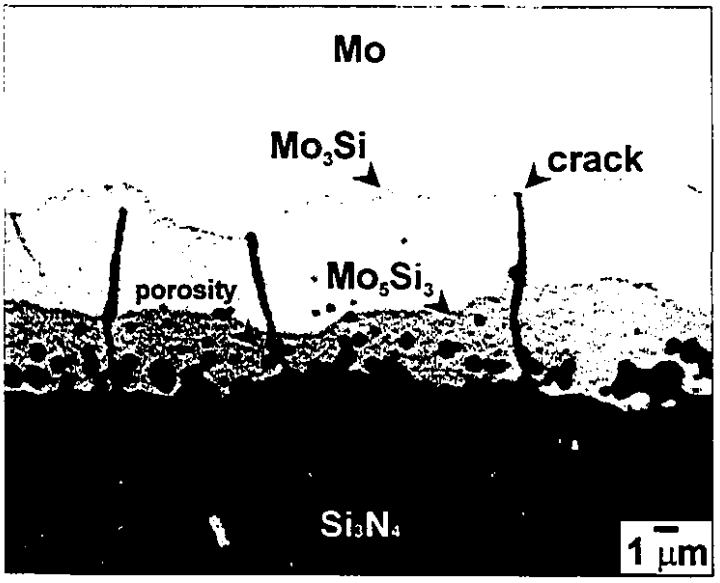

Figure 8.10- BEI of Si_3N_4-Mo interface (vacuum, T = 1700°C, t = 2 h).

8.2.2 EFFECT OF JOINING ATMOSPHERE

Comparing the overall reaction between Si_3N_4 and Mo, under vacuum and in N_2, confirmed that the same sequence of events occurred in both cases. However, in N_2, higher temperatures and longer times were required to obtain the same microstructures observed for samples hot-pressed under vacuum. The higher stability of Si_3N_4 in N_2 compared to vacuum delayed the formation of Mo_3Si, the growth of the porous layer, and the transformation of Mo_3Si into Mo_5Si_3.

However, the environment did not affected the mechanism of diffusion, and consequently, the activation energy for interface formation under the different atmospheres remained unchanged. Figure 8.11 shows a plot of the coefficient of penetration, K_p, as a function of the temperature. The activation energy, Q, for the formation of interfaces was calculated from the slope of the Arrhenius curves obtained for vacuum and N_2 conditions. The curve for the SiC-Mo system is also shown in Figure 8.11. From the Si_3N_4-Mo samples hot-pressed under vacuum, an activation energy of 440 kJ/mol was obtained. Hot-pressing in N_2 did not result in a significant change of the value of the activation energy (450 kJ/mol), indicating that the activation energy is associated with the diffusion mechanism, which remains the same in both environments, and not with the dissociation of the ceramic. The only difference between the curves for vacuum and N_2 was a slight shift of the frequency factor (pre-exponential term, K_o) to a lower value for the samples hot-pressed in N_2, which accounted for the thinner interfaces compared to the specimens produced under vacuum. Furthermore, the values

of Q obtained for the Si_3N_4-Mo system were nearly identical, within the margin of error, to that obtained for the SiC-Mo, despite the significant difference in the thermodynamic stability of the two ceramics (Figure 8.3). This fact confirmed the hypothesis that the determining factor for the activation energy is the dominating diffusion mechanism rather than a combined contribution from diffusion and thermodynamic stability of the ceramic. Therefore, for both the SiC-Mo and Si_3N_4-Mo systems, the activation energy for the formation of interface is directly related to the slowest diffusion process taking place. In the case of SiC-Mo, this may be the diffusion of C through Mo_5Si_3 [31], and in the case of Si_3N_4-Mo, the diffusion of Si through Mo_3Si.

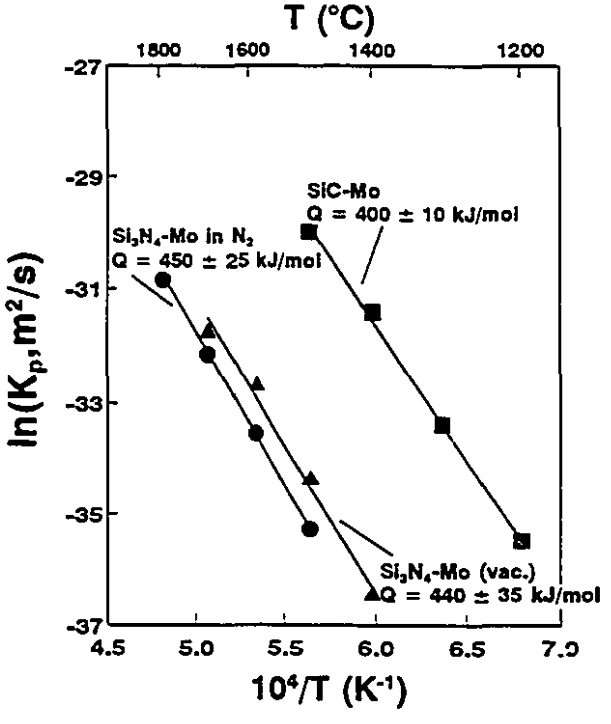

Figure 8.11- Arrhenius plot of the coefficient of penetration, K_p, for the SiC-Mo and Si_3N_4-Mo systems. The activation energy, Q, is obtained from the slope of the curves.

8.2.3 ELECTRON PROBE MICROANALYSIS

The distribution of atomic species across the Si_3N_4-Mo interface was studied by X-ray mapping, using EPMA-WDS on the interface shown in Figure 8.10. The main elements analyzed were molybdenum (Mo), silicon (Si), and nitrogen (N). Since Y_2O_3 and Al_2O_3 were used as additives to sinter Si_3N_4 CERALLOY® 147-3, therefore yttrium (Y), and aluminum (Al) were also analyzed. The corresponding maps are shown in Figure 8.12, where the interface is aligned in the vertical direction; Mo is at the left side and Si_3N_4 at the right. In the Mo-map, the different contrasts from left to right corresponds to the decrease in the concentration of Mo from pure Mo to pure Si_3N_4, passing through Mo_3Si and Mo_5Si_3, where the concentration of Mo was 75 and 62.5 at.%, respectively. No diffusion of Mo into the ceramic is observed, resulting in the dark region corresponding to Si_3N_4. The porous layer can be seen as a dark area indicating that Mo was not present in the regions along and beneath the pores. For the Si map, a decrease in the intensity corresponding to a decrease in the concentration of Si is observed in the direction of Mo. Starting from Si_3N_4 which contained 43 at.% Si, the concentration of the element decreased to 37.5 at.% in Mo_5Si_3, and to 25 at.% in Mo_3Si. The porous layer appears as a zone depleted in Si as compared to the Si_3N_4 region. Residual Si can be observed in the region adjacent to Mo indicating the presence of traces of Si dissolved in Mo, which is consistent with the Mo-Si phase diagram. From the Y and Al maps, an increase in the concentration of these elements can be noticed close to the interface, delineating closely the porous layer. However, no diffusion of Al

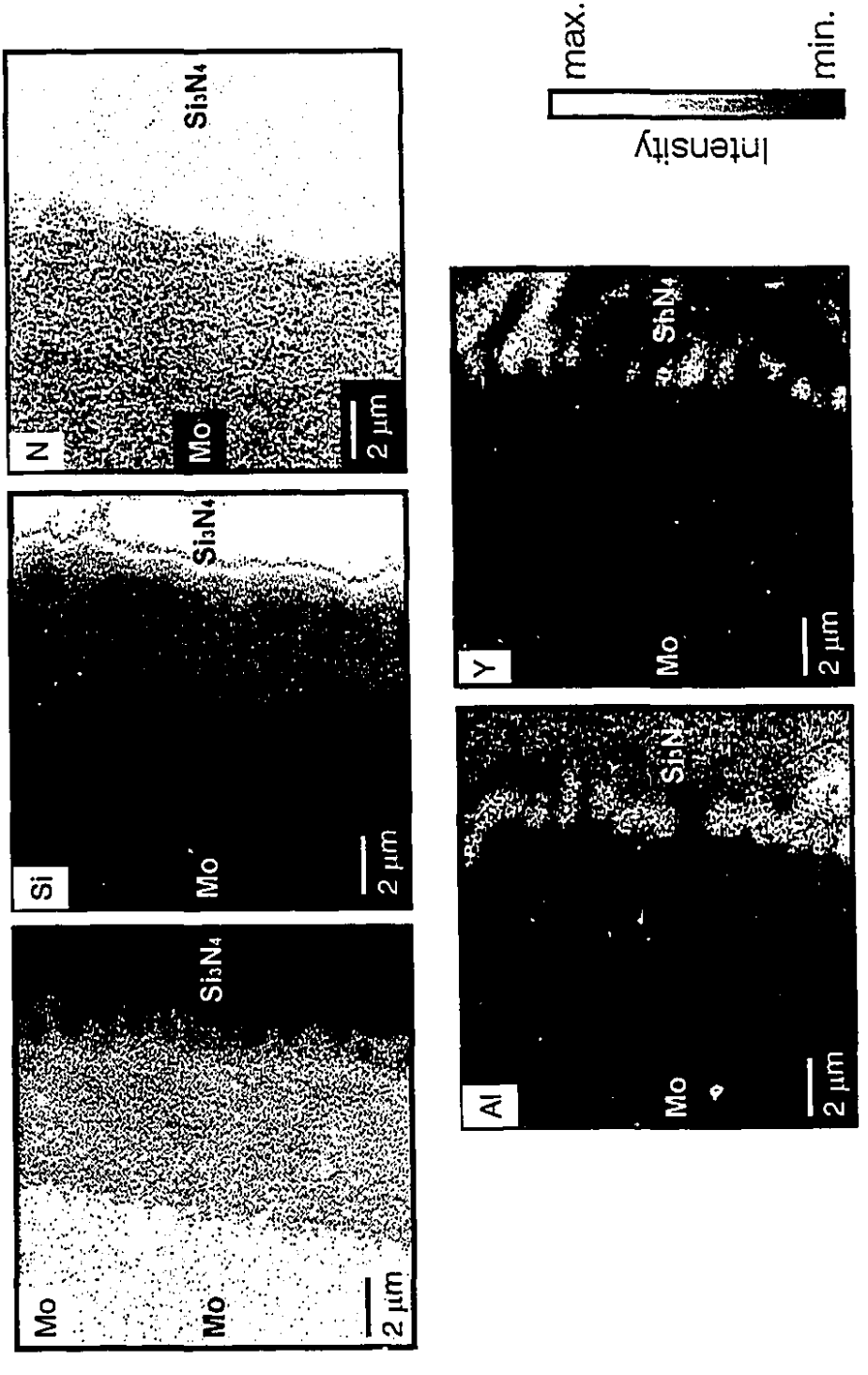

Figure 8.12- WDS mapping of atomic species across interface shown in Figure 8.10.

or Y into Mo can be observed. The N map shows excessive background interference. Part of the noise was eliminated by subtracting the background from each peak during the data acquisition stage, resulting in the map shown in Figure 8.12. Some of the pores contours can be visualized in regions where the concentration of N_2 was probably much higher than its surroundings. In the area corresponding to the Mo-silicides, a slightly higher concentration of N_2 can be observed, as compared to pure Mo, possibly corresponding to the presence of dissolved $N_{2(g)}$. This may be an indication that the Mo-silicides layers had a slightly higher solubility for N_2, as compared to pure Mo. In order to reduce the effect of background interference, diffusion profiles across the interface shown in Figure 8.10 were also obtained by WDS line analysis. This method also permitted obtaining an acceptable profile for oxygen, and consequently, establishing the presence of oxide phases. In order to obtain an overview of the distribution patterns, all the elements were analyzed. The diffusion profiles are illustrated in Figure 8.13. The line was chosen to intercept a large pore (diameter greater than 1 μm), located entirely in the Mo_3Si layer. The distance from one of the extremities of the pore to the Si_3N_4 region had to be close to 0.5 μm. This way, using a spot size of 0.5 μm, it was possible to observe variations in the intensities of all elements corresponding to the different regions analyzed, without significant interference from the surrounding material.

Data was collected starting at a distance of about 6 μm inside the Si_3N_4 region ($x = 0$). Mo was not observed in that area, confirming the results obtained from WDS mapping. Until about $x = 5$ μm, the main elements present were Si and N. At

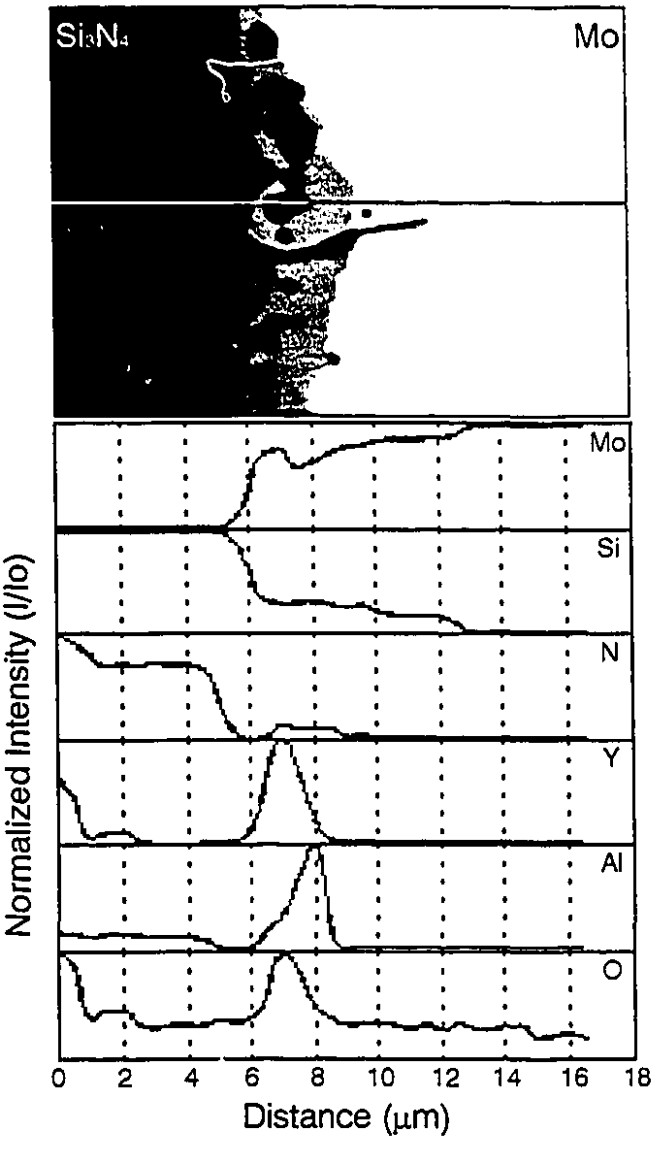

Figure 8.13- WDS analysis across the Si_3N_4-Mo interface depicted in Figure 8.10.

$x = 2\ \mu m$, an increase in the Y and O signals suggested that the probe scanned a grain-boundary area rich in N-melilite. The Al profile indicates the presence of a residual and well distributed concentration of Al across the Si_3N_4 area ($0 \leq x \leq 4\ \mu m$). The Mo and Si profiles show good agreement with the data obtained from the WDS mapping. The different interfacial phases (Mo_3Si and Mo_5Si_3) can be seen through the variation in the intensity of the WDS signal, for these two elements. Increases in the Mo intensity were matched by a decrease in the Si signal, indicating the transition to a different phase, *e.g.*, the Si signal reaches its maximum in the Si_3N_4-Mo_5Si_3 boundary where the Mo signal reaches its minimum. The region corresponding to the pore ($6 \leq x \leq 8\mu m$) shows an abrupt increase in the Al, Y, and O intensities confirming that most Al and Y were deposited along the porous layer in the form of oxides. In the same area, the intensity of N seems to increase slightly while that of Mo appears to decrease, confirming the WDS mapping which showed that the porous region contained N, but was depleted in Mo. The presence of O in the silicide layers and in Mo is not clear. The residual intensity of the profile can be related to surface oxide and/or background noise. Y and Al were not observed outside the porous layer in the direction of Mo, confirming the WDS mapping, which indicated that these elements did not diffuse into the metal. These results indicated that, upon decomposition of Si_3N_4, Si was the main diffusing element into the metal. Due to the limited solubility of N_2 in Mo, gas evolved forming a porous layer where the original Si_3N_4-Mo interface was once located. Y and Al did not diffuse into the metal or the interface, but remained trapped along the porous region, probably

in the form of oxides or oxynitrides. Whether or not O diffused into Mo was not clear, however the Mo-O phase diagram does not indicate the existence of any mutual solid-solubility between these two elements [71].

8.2.4 X-RAY DIFFRACTOMETRY

In order to further identify the phases found in the Si_3N_4-Mo diffusion couples, X-ray diffraction was performed. The specimen used was hot-pressed at 1700°C for 2 hours in N_2. The sample was sheared at the interface resulting in two fracture surfaces. The XRD spectra from these surfaces are shown in Figure 8.14. Comparing the pattern of the Si_3N_4 fracture with that of the original Si_3N_4 material (Figure 6.2), it can be concluded that, upon shearing, most of the interface remained attached to the metal. However, as for the SiC-Mo system, fracture occurred in a brittle manner, and Si_3N_4 particles remained attached to the Mo surface. The dominant peaks in the Si_3N_4 spectrum corresponded to CERALLOY® 147-3 (hexagonal β-Si_3N_4). An intergranular crystalline phase was also observed. This second phase was N-melilite ($Y_2Si_3N_4O_3$), a tetragonal crystalline phase having similar structure to that of melilite ($Ca_2MgSi_2O_7$). Al_2O_3 was not observed, suggesting the presence of an amorphous alumino-silicate intergranular phase. Comparing these results with the WDS line analysis, it can be concluded that, within and beneath the porous layer remained a mixture of N-melilite and an alumino-silicate glass. Low intensity peaks attributed to residual Mo_5Si_3 were also observed at the angular positions $2\theta = 38.26°$, $2\theta = 42.77°$, $2\theta = 66.94°$, and $2\theta = 77.68°$. No peaks could

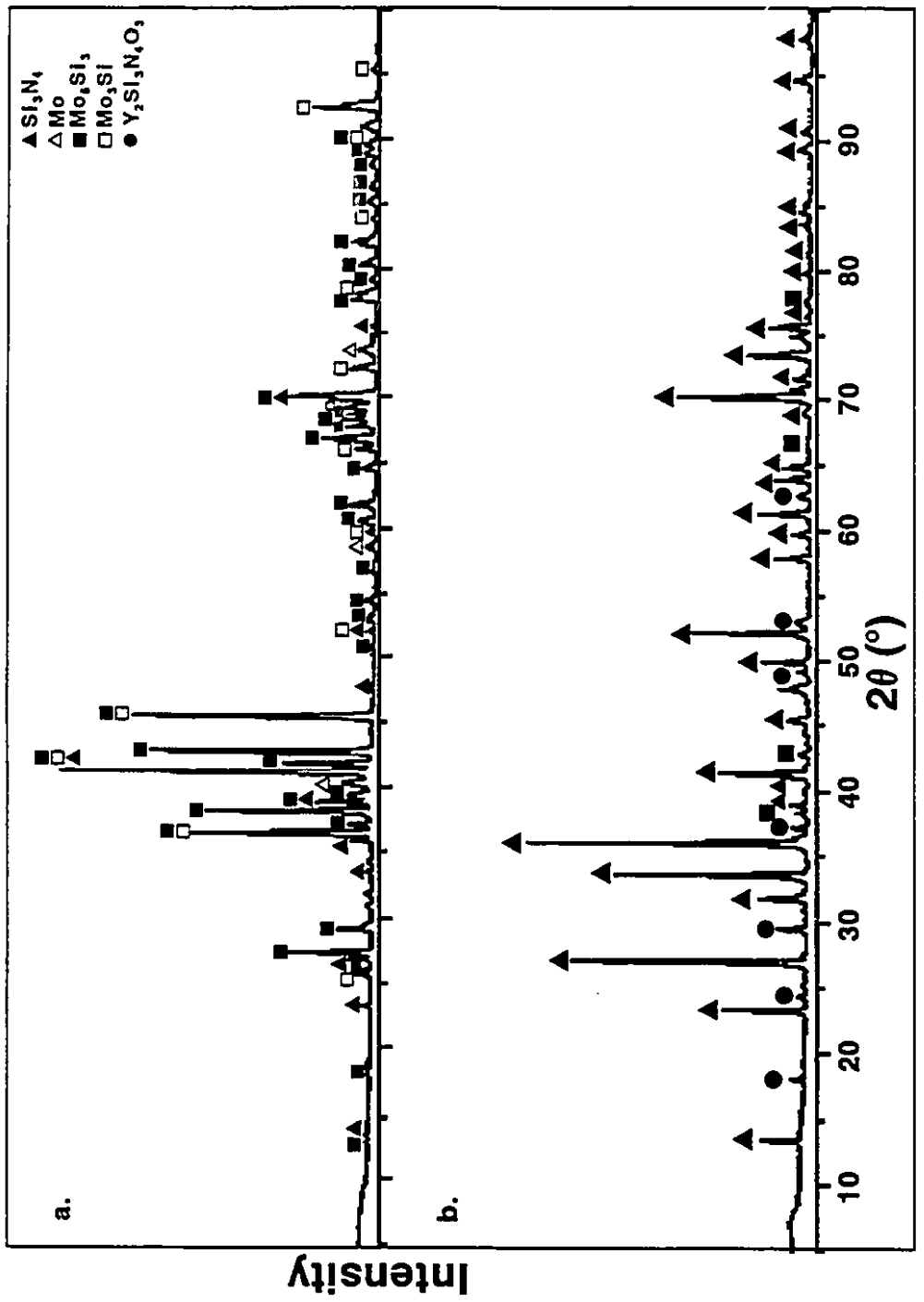

Figure 8.14- XRD pattern of (a) Mo and (b) Si_3N_4 fracture surfaces. Sample hot-pressed in N_2, at 1700°C for 2 hours.

be attributed to any Mo-nitride phases (Mo_2N, MoN and $Mo_{16}N_7$), confirming the thermodynamic predictions and WDS results. The X-ray pattern corresponding to the Mo fracture surface revealed the presence of cubic Mo (bcc structure) by the presence of its most intense peaks $2\theta = 40.52°$, $2\theta = 73.68°$, and $2\theta = 58.62°$. Residual β-Si_3N_4 was also observed by low-intensity peaks, many of which overlapped with other phases, which were present in greater abundance. The intergranular N-melilite phase was not observed on the Mo fracture surface. The main reaction compounds detected on the Mo fracture surface were tetragonal Mo_5Si_3 and cubic Mo_3Si. Apparently, the concentration of Mo_5Si_3 was higher, which confirms the results obtained from BEI and EDS, since substantial transformation from Mo_3Si to Mo_5Si_3 was observed at 1700°C. Also, no Mo-nitrides were identified on the Si_3N_4 fracture surface.

8.3 MECHANICAL STRENGTH

As indicated in Figure 8.4, joining between Si_3N_4 and Mo was achieved for temperatures as low as 1200°C. In addition, the presence of residual thermal stresses close to the interfaces did not result in debonding of the Si_3N_4-Mo joints, even for the highest temperature tested (1800°C), which is contrary to previous investigations [10].

In fact, Si_3N_4-Mo joints endured higher joining temperatures than SiC-Mo, as can be seen comparing Figure 7.15 and 8.4. This fact cannot be explained from an analysis based on the values of CTE for SiC, Si_3N_4, and Mo. If residual thermal stresses depend mainly on the CTE mismatch between parent materials, the amplitude of those stresses

would have to be higher in the Si_3N_4-Mo interfaces than in the SiC-Mo interfaces. SiC has an average CTE of $4.5x10^{-6}°C^{-1}$ and Mo has a CTE of $5.4x10^{-6}°C^{-1}$, resulting in a mismatch of the order of $1.0x10^{-6}°C^{-1}$. On the other hand, Si_3N_4 has a CTE of $3.5x10^{-6}°C^{-1}$ which results in a mismatch with Mo of the order of $2.0x10^{-6}°C^{-1}$. Therefore, this would imply that Si_3N_4-Mo couples should fail at lower joining temperatures compared to SiC-Mo. An explanation of this controversy can be found by examining the thickness of SiC-Mo and Si_3N_4-Mo interfaces (Figure 8.15).

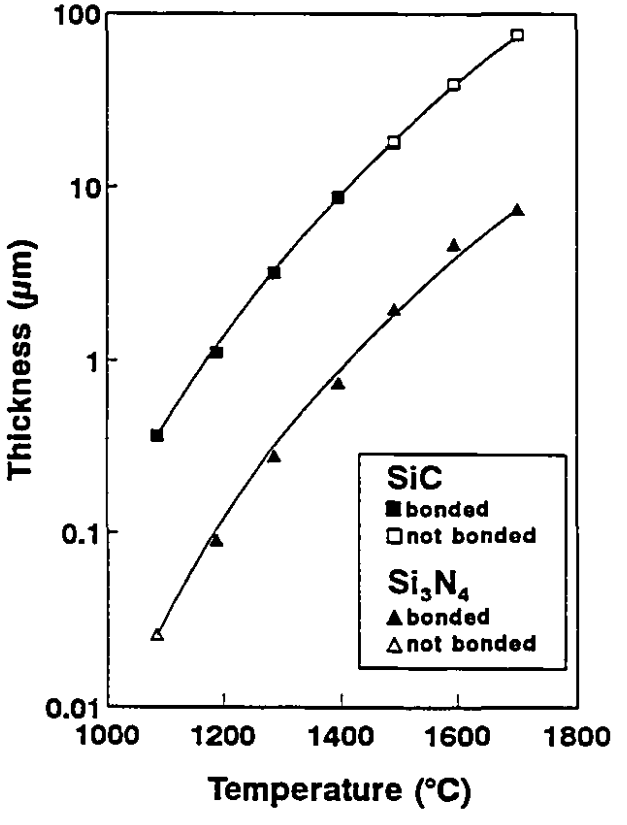

Figure 8.15- Thickness of interface as a function of the temperature for SiC-Mo and Si_3N_4-Mo diffusion couples (t = 1 h).

For both the SiC-Mo and Si_3N_4-Mo systems, the thickness of the interfaces is an exponential function of the joining temperature, however, there is a ten fold difference in the absolute values of the interface thicknesses. Because of the difference in the thermodynamic stability of SiC and Si_3N_4 in vacuum (Figure 8.3), Si and C were more abundant for reaction when SiC was joined to Mo, than Si and N_2 when Si_3N_4 was joined to Mo, for the same bonding temperature and time. As a consequence, the formation of a reaction zone proceeded preferentially for the SiC-Mo system, resulting in thicker interfaces. For this reason, joining of SiC to Mo started at lower temperatures than Si_3N_4 to Mo. This result is depicted in the lower left side of Figure 8.15, which represents a region where insufficient diffusion resulted in no bonding between Si_3N_4 and Mo. On the other hand, as the temperature increased, reaction became significant in the SiC-Mo system, resulting in debonding at lower temperatures (1600°C) as compared to Si_3N_4-Mo, where samples were joined even at 1700°C, in vacuum. This fact can be observed by the open symbols on the upper right region of Figure 8.15, referring to samples where joining occurred and it was followed by debonding of the couple upon cooling.

In summary, the two systems studied showed a significant difference in the absolute thickness of the interfaces, which required different experimental conditions to promote reliable joining. As a consequence of the limited amount of reaction, Mo could be joined to SiC at lower temperatures than for Si_3N_4, however debonding also occurred at lower temperatures. It is clear that the amount of interfacial reaction played a major role in determining the final mechanical properties of the joints. Furthermore, the nature

of the reaction products may also have influenced the mechanical properties of the joints. Significant production of Si and C, from the decomposition of SiC, resulted in the precipitation of Mo_5Si_3 and Mo_5Si_3C. As discussed earlier, the formation of these phases had limited benefit on the final mechanical strength of SiC-Mo joints. Excessive formation of either one decreased the overall strength of the joints, ultimately leading to failure. On the other hand, the concentration of Si present within the Si_3N_4-Mo interfaces was lower than for SiC (for the same joining conditions) which prevented substantial precipitation of Mo_5Si_3. In addition, the absence of C prevented the formation of Mo_5Si_3C, which exhibits undesirable mechanical properties.

The weak link in the Si_3N_4-Mo joints was determined to be the porous zone left by the entrapment of $N_{2(g)}$, within the interface between the Si_3N_4 and the reaction zone. Figure 8.16 shows plots of the shear strength of Si_3N_4-Mo samples as a function of joining temperature, time, and atmosphere. All samples were slowly cooled during the first 500°C, and then furnace cooled to room temperature. For samples hot-pressed at 1400°C under vacuum, it was observed that the average joint strength increased from 30 MPa to 57 MPa, as the bonding time increased from 15 minutes to 1 hour. This improvement was attributed to the initial stages of interface formation, and elimination of interfacial voids. However, as the bonding time increased from 1 to 2 hours, and subsequently to 4 hours, the average joint strength decreased to 20 MPa and 15 MPa, respectively, as a consequence of the increasing porosity present at the interface. An analysis of the joint strength for samples hot-pressed for 1 hour under vacuum revealed

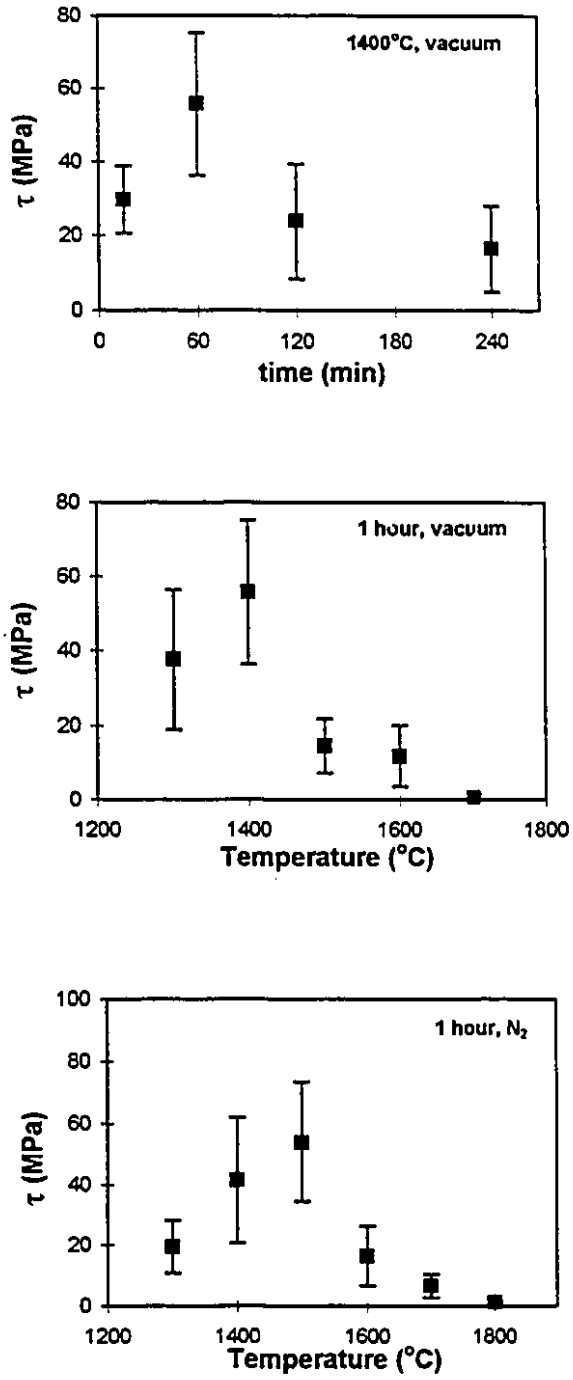

Figure 8.16- Plots of shear strength as a function of joining temperature, time, and environment, for Si_3N_4-Mo joints.

a similar trend, however, the effect of temperature was more drastic than the effect of time. Increasing the joining temperature from 1400°C to 1500°C decreased the average joint strength from 57 MPa to less than 20 MPa. The difference in the effect of temperature and time is related to the growth rate of the reaction zone as a function of these parameters, *i.e.*, exponential *vs.* parabolic, respectively.

Finally, joint strength was measured for Si_3N_4-Mo samples hot-pressed under N_2 for 1 hour. A maximum average strength of 53 MPa was achieved for samples hot-pressed at 1500°C. From that point on, the joint strength decreased as the joining temperature increased. Comparing the results obtained from the samples hot-pressed under vacuum and N_2 for 1 hour, a similar behaviour was observed. However, the samples hot-pressed under N_2 achieved their maximum average strength at 1500°C, whereas the maximum average strength for the samples hot-pressed under vacuum was attained at 1400°C. The fact that the maximum joint strength occurred for a temperature 100°C higher, for the samples hot-pressed in N_2, confirmed that there is a strong relationship between the interface microstructure and joint strength. The absolute values of joint strength for samples hot-pressed under vacuum at 1400°C for 1 hour, and in N_2 at 1500°C, for the same bonding time, were the same when considering the error bars on the strength data. A schematic correlation between the interfacial microstructure and joint strength can be seen in Figure 8.17.

As mentioned earlier, shear tests result in significantly lower strength values than tensile and flexural tests. This implies that the actual service strength of the joints

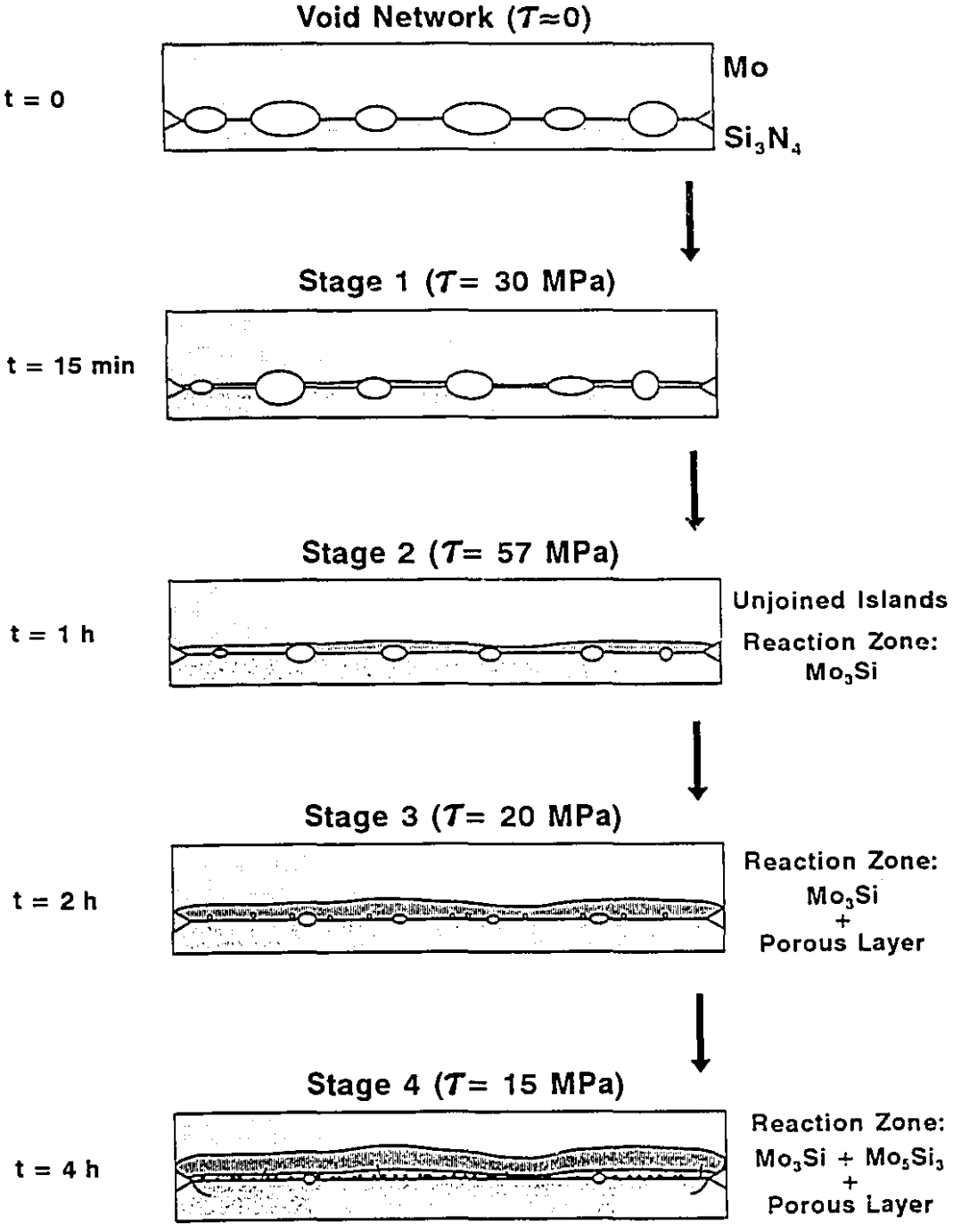

Figure 8.17- Correlation between joint strength and interfacial microstructure for Si_3N_4-Mo (T = 1400°C).

produced in this study are much higher than the values obtained herein. A direct comparison between solid-state bonding and brazing of Si_3N_4 to Mo was obtained. Under optimum conditions (vacuum, 1400°C, 1 hour), an average strength of 57 MPa was measured for Si_3N_4-Mo diffusion couples. This value represents a significant improvement when compared to shear strength values of the order of 28 MPa, reported when Si_3N_4 was brazed to Mo at 1300°C using an Ni-Cr-Si alloy [25]. In addition, no degradation is expected in the high-temperature strength of the diffusion couples, whereas high service temperatures result in a further decrease of the strength of the brazed material.

CHAPTER 9:

CONCLUSIONS

A series of SiC-Mo and Si_3N_4-Mo joints was hot-pressed varying experimental parameters such as, joining temperature, time, and environment. Extensive characterization of the physical and mechanical properties of the corresponding ceramic-metal interfaces was performed. In general, the microstructure of the interfaces could be predicted, with reasonable certainty, using the thermodynamic analyses performed for both the Mo-Si-C and Mo-Si-N systems. Furthermore, important observations were made concerning the relationship between the microstructural evolution

of the interfaces and its effect on the final mechanical properties of the diffusion couples. Finally, the presence of residual stresses was studied, and a simple and effective solution was developed to limit the concentration of residual stresses.

9.1 CONCLUSIONS ON SiC-Mo

1. A thermodynamic analysis of the Mo-Si-C system indicated that SiC-Mo interfaces are reactive. For a joining temperature of 1200°C, the predicted reaction products were Mo_3Si, Mo_5Si_3, Mo_2C, and Mo_5Si_3C. Although the F*A*C*T database does not include any ternary phase for the Mo-Si-C system, the existence of Mo_5Si_3C is well established in the literature. Furthermore, increasing the joining temperature to 1600°C, Mo_2C is likely to transform into MoC.
2. Joining between SiC and Mo did not take place at temperatures lower than 1100°C for the bonding times investigated (between 15 minutes and 4 hours).
3. A reaction zone was observed to form between SiC and Mo, and consisted of two main phases: Mo_5Si_3 and Mo_2C. A ternary phase of composition Mo_5Si_3C was also formed. Although initially identified at 1500°C, there was evidence that traces of this phase were also present at lower temperatures. The suggested sequence of reaction was that, after the formation of tetragonal Mo_5Si_3, C diffused into the octahedral interstitial sites of this phase, causing it to transform into hexagonal Mo_5Si_3C. The main carbide formed was identified as hexagonal

β-Mo_2C. At 1700°C, the formation of MoC was identified by X-ray diffraction. Carbon accommodated in the Mo_2C structure precipitating non-stoichiometric hexagonal η-MoC_{1-x}. Although this is a high-temperature phase, it was present in the final interfaces, probably as a result of the cooling rates employed after the joining experiments.

4. An activation energy of 400 ± 10 kJ/mol was calculated, and is in good agreement with previous reported values. It is believed that this parameter is mainly related to the diffusion mechanism involved in the formation of SiC-Mo interfaces, probably the diffusion of C through Mo_5Si_3.

5. The amount of reaction was an important factor in determining the final mechanical strength of the joints. Initially, the shear strength of SiC-Mo joints increased with joining time and temperature to a maximum average value of 50 MPa, obtained for samples hot-pressed at 1400°C for 1 hour. Increasing the temperature or time caused the strength to decrease, ultimately resulting in failure of the joints by a brittle fracture mechanism. Debonding occurred invariably between SiC and the Mo_5Si_3/Mo_5Si_3C reaction layer. The variation of the shear strength with bonding temperature and time was attributed to the competing effects of interfacial bonding and growth of the interfacial reaction layer. At low joining temperatures, joint strength was controlled by the fraction of bonded surface which increased with time. At higher temperatures, the beneficial effect of increasing the fraction of bonded area was counteracted by the detrimental

effect of the growth of the reaction layer. Excessive growth of the reaction layer decreased joint strength because of the mismatch in the mechanical properties of the reaction products Mo_5Si_3/Mo_5Si_3C and SiC, which enhanced the propensity to fracture.

6. Thermomechanical stresses were measured on SiC-Mo joints by neutron diffraction. High residual compressive stresses parallel to the interface were observed at the SiC side of the joints. These stresses were counteracted by tensile stresses at the proximity of the interface on the Mo side of the joints. The distribution of stresses was affected by the cooling profile to which the diffusion couples were exposed. Slow cooling the samples for the first 500°C was an effective way to reduce the amplitude of in-plane stresses, particularly in the SiC adjacent to the interface. For samples hot-pressed at 1400°C for 1 hour, the absolute value of these stresses was reduced from 550 MPa to 50 MPa by controlling the cooling rate.

9.2 CONCLUSIONS ON Si_3N_4-Mo

1. A thermodynamic analysis of the Mo-Si-N system indicated that reaction is expected to take place within Si_3N_4-Mo interfaces. The nature of the reaction products depends upon the partial pressure of N_2, corresponding to the joining environment. For N_2 environments with pressures up to 1.2 atm. only Mo-silicides will form. For a joining temperature of 1300°C, the formation of

Mo_3Si, Mo_5Si_3, and $MoSi_2$ is thermodynamically favourable in vacuum. The transformation from one Mo-silicide into another takes place by diffusion of Si, depending on the bonding time.

2. Joining of Si_3N_4 to Mo was investigated for temperatures ranging from 1000°C to 1800°C. For the range of bonding times investigated (between 15 minutes and 4 hours), joining did not take place for temperatures lower than 1200°C.
3. Joining started with the dissociation of Si_3N_4 into Si and $N_{2(g)}$. Subsequently, Si diffused into Mo forming Mo_3Si. Further diffusion of Si into Mo_3Si stabilized Mo_5Si_3. The formation of $MoSi_2$ as well as the reaction between Mo and $N_{2(g)}$ were not observed. Initially $N_{2(g)}$ diffused into Mo and Mo-silicides, but as a consequence of limited solubilities, the excess $N_{2(g)}$ remained trapped at the interface between Si_3N_4 and Mo-silicide resulting in a porous layer.
4. Hot-pressing in vacuum produced thicker interfaces than hot-pressing in N_2, for similar joining conditions. Joining in a N_2 atmosphere increased the stability of Si_3N_4 delaying the formation of Mo_3Si and its transformation to Mo_5Si_3, along with the growth of the porous layer.
5. An activation energy of 440 ± 10 kJ/mol was calculated for the samples hot-pressed in vacuum, whereas 450 ± 25 kJ/mol was obtained for samples hot-pressed in N_2. The similarity between these two values and the activation energy calculated for the SiC-Mo system (400 ± 10 kJ/mol), despite the differences in the thermodynamic stability of SiC and Si_3N_4, confirmed the hypothesis that

activation energies are determined by the diffusion process, rather than the free energy of dissociation of the ceramic. For Si_3N_4-Mo, it is possible that the activation energy is directly related to the diffusion of Si through Mo_3Si.

6. Contrary to the observations for SiC-Mo, debonding did not occur for joints hot-pressed at temperature in excess of 1500°C, as a consequence of the limited growth of Si_3N_4-Mo interfaces as compared to SiC-Mo.
7. The extent of the reaction between Si_3N_4 and Mo, and the growth of the porous layer were the determining factors in the mechanical reliability of the joints. Optimum joining conditions were attained by establishing a balance between the fraction of bonded interface (beneficial to joint strength) and the thickness of the interfacial porous region (detrimental to joint strength). Maximum strength was obtained when Si_3N_4 was joined to Mo in vacuum at 1400°C for 1 hour. Shear tests performed on these samples resulted in an average strength of 57 MPa.
8. Shear testing performed on Si_3N_4-Mo joints hot-pressed in a N_2 atmosphere confirmed that there is an intimate relationship between interfacial microstructure and joint strength. Similar shear strength values were obtained for samples hot-pressed in vacuum at 1400°C and in N_2 at 1500°C, despite the different joining temperatures.

CONTRIBUTION TO ORIGINAL KNOWLEDGE

lthough the joining of SiC and Si_3N_4 to Mo has been previously studied to some extent, several important aspects of the diffusion bonding of these materials were addressed here for the first time. In particular, a thorough description of the solid-state diffusion bonding technique as applied to these materials was developed. This chapter summarizes the most important original contributions achieved in this study.

a. SiC-Mo

1. The microstructural evolution of the interfaces was studied as a function of joining parameters, and the results were correlated with the thermodynamic behaviour of the system.
2. The composition and crystal structure of the different reaction products was investigated by successive X-ray diffraction analyses of the interface, which led to the conclusion that β-Mo_2C transformed into η-MoC_{1-x}, as predicted by the thermodynamic analysis.
3. The elastic constants of the reaction products were measured by the nanoindentation technique, and a relationship between these values and the mechanical behaviour of the joints was established.
4. Joint strength was measured as a function of the experimental parameters by shear testing, and the optimum joining conditions were identified.
5. The distribution of residual stresses as a function of experimental parameters was evaluated by neutron diffraction, and a method to reduce these stresses was developed by controlling the cooling rate employed in the joining experiments.

b. Si_3N_4-Mo

1. A comprehensive study of the interfacial microstructure of diffusion couples was provided based on a thermodynamic analysis and experimental data.

2. The microstructural evolution of the interfaces as a function of joining temperature, time, and atmosphere was investigated, and a correlation with the observed joint strength was established.
3. The distribution of atomic species across the interface was investigated by EPMA-WDS, and a complete diffusion profile was provided and included elements such as yttrium, aluminum, nitrogen and oxygen.
4. Shear tests were performed and the experimental conditions necessary to optimize joint strength were investigated.
5. The results obtained for the Si_3N_4-Mo system were correlated with those obtained for SiC-Mo, and existing discrepancies related to bonding temperature and joint strength were explained.
6. The activation energies for the formation of interfaces were calculated, and their determining factor was established to be the dominating diffusion mechanism rather than the dissociation of Si_3N_4.

RECOMMENDATIONS FOR FUTURE WORK

This study provided an important contribution towards extending the available literature on joining of SiC and Si_3N_4 to Mo by solid state diffusion. Although significant questions concerning the microstructure of the interfaces and the mechanical properties of the diffusion couples have been addressed, other important aspects of technological interest remain to be studied regarding these two ceramic-metal systems, some of which are proposed below as topics for further investigation.

1. To obtain the thermodynamic data of the Mo_5Si_3C phase and, to include this information in the F*A*C*T database.
2. To study the use of nitride forming elements, *e.g.* titanium, in conjunction with molybdenum, in order to prevent the formation of interfacial porous zones in Si_3N_4-Mo joints, and to investigate the effect of the new microstructure on the mechanical properties of the diffusion couples.
3. To study the solubility of nitrogen in Mo-silicides.
4. To measure the distribution of residual stresses and joint strength of diffusion couples with cylindrical geometry, in order to eliminate the detrimental corner effects found in joints with rectangular geometry.
5. To measure joint strength and toughness on sandwich-like samples (ceramic-Mo-ceramic) by three or four point bending on pre-notched specimens.
6. To produce functionally graded SiC-Mo-metal and Si_3N_4-Mo-metal samples using structural alloys of technological interest, *e.g.* superalloys or steel, and to evaluate the mechanical properties of these joints.

REFERENCES

[1] D.W. Richerson, *"Modern Ceramic Engineering, 2nd. Edition"*, Marcel Dekker, New York, USA, (1992).

[2] K. Suganuma, "Reliability Factors in Ceramic/Metal Joining", *Mater. Res. Soc. Symp. Proc.* 314, (1993) 51-60.

[3] N.L. Loh and Y.L. Wu, "Diffusion Bonding of Ceramics to Metals, *Mater. Manuf. Proc.* 8, 2 (1993) 159-181.

[4] *"Engineered Materials Handbook V.4 - Ceramics and Glasses"*, ASM International, Materials Park, USA, (1991).

[5] M.P. Boyce, *"Gas Turbine Engineering Handbook"*, Gulf Pub. Company, Houston, USA, (1982).

[6] L.M. Sheppard, "Advances in Automotive Ceramics", *Am. Ceram. Soc. Bull.* 69, 6 (1990) 1011-1021.

[7] G.W. Meetham, *"The Development of Gas Turbine Materials"*, John Wiley & Sons, New York, USA, (1981).

[8] J.P. Angus, "Aeroengine Ceramics — The Vision, the Reality and the Progress", *J. Aerosp. Eng.* 207, 2 (1993) 83-96.

[9] M. Fukutomi, M. Kitajima, M. Okada and R. Watanabe, "Silicon Carbide Coating on Molybdenum by Chemical Vapor Deposition and its Stability under Thermal Cycle Conditions, *J. Nucl. Mater.* 87, (1979) 107-116.

[10] K. Suganuma, M. Takagi, Y. Miyamoto, M. Koizumi, T. Okamoto and H. Nakata, "Joining of Silicon Nitride to Molybdenum under High Pressure", *J. Ceram. Soc. Jpn.* 96, 11 (1988) 1051-1056.

[11] J.M. Howe, "Bonding, Structure, and Properties of Metal/Ceramic Interfaces: Part 2 Interface Fracture Behaviour and Property Measurement", *Int. Mater. Rev.* 38, 5 (1993) 257-271.

[12] G.S. Upadhyaya, "Molybdenum and Tungsten - Their Relative Assessment", *R & HM*, (1987), 168-172.

[13] J.J. Harwood, *in "The Metal Molybdenum"*, ASM International, Cleveland, USA, (1958), 420-461.

[14] R.S. Archer, *in "Rare Metals Handbook"*, Chapman & Hall, London, UK, (1961), 283-303.

[15] *"Metals Handbook, Desk Edition"*, ASM International, Materials Park, USA, (1985), 20.13.

[16] D.M. Shah, D. Berczik, D.L. Anton and R. Hecht, "Appraisal of other Silicides as Structural Materials", *Mater. Sci. Eng.* 155A, 1-2 (1992) 45-57.

[17] M.M. Schwartz, *"Ceramic Joining"*, ASM International, Materials Park, USA, (1990).

[18] K. Suganuma, Y. Miyamoto and M. Koizumi, "Joining of Ceramics and Metals", *Ann. Rev. Mater. Sci.* 18, (1988) 47-63.

[19] M.G. Nicholas and D.A. Mortimer, "Ceramic/Metal Joining for Structural Applications", *Mater. Sci. Technol.* 1, 9 (1985) 657-665.

[20] T. Okamoto, "Interfacial Structure of Metal-Ceramic Joints", *ISIJ Int.* 30, 12 (1990) 1033-1034.

[21] R.W. Rice, J.H. Enlor, J.W. Lau, E.Y. Luh and L.E. Dolhert, "Hot Pressing—A New Route to High-Performance Ceramic Multilayer Electronic Packages", *Ceram. Bull.* 71, 7 (1992) 751-755.

[22] B. Derby, "The Formation of Metal/Ceramic Interfaces by Diffusion Bonding", *Acta Scr. Metall. Proc. Ser.* 4, (1990) 161-167.

[23] J.M. Howe, "Bonding, Structure, and Properties of Metal/Ceramic Interfaces: Part 1 Chemical Bonding, Chemical Reaction, and Interfacial Structure", *Int. Mater. Rev.* 38, 5 (1993) 233-256.

[24] A.G. Evans and B.J. Dalgleish, "The Fracture Resistance of Metal-Ceramic Interfaces", *Mater. Sci. Eng.* 162A, 1-29 (1993) 1-13.

[25] G. Ellsner and G. Petzow, "Metal/Ceramic Joining", *ISIJ Int.* 30, 12 (1990) 1011-1032.

[26] A. Hill and E.R. Wallach, "Modelling Solid-State Diffusion Bonding", *Acta Metall.* 37, 9 (1989) 2425-2437.

[27] O.M. Akselsen, "Diffusion Bonding of Ceramics", *J. Mater. Sci.* 27, 3 (1992) 569-579.

[28] R.E. Loehman and A.P. Tomsia, "Jcining of Ceramics", *Am. Ceram. Soc. Bull.* 67, 2 (1988) 375-378.

[29] M. Naka, T. Saito and I. Okamoto, "Effect of a Silicon Sintering Additive on Solid State Bonding of SiC to Nb", *J. Mater. Sci.* 26, 7 (1991) 1983-1987.

[30] W.J. Boettinger, J.H. Perepezka and P.S. Frankwicz, "Application of Ternary Phase Diagrams to the Development of $MoSi_2$-Based Materials", *Mater. Sci. Eng.* 155A, 1-2 (1992) 33-44.

[31] F.J.J. Loo, F.M. Smet, G.D.Rieck and G.Versoi, "Phase Relations and Diffusion Paths in the Mo-Si-C System at 1200°C", *High Temp.- High Pressures* 14, (1982) 25-31.

[32] A. Horiguchi, K. Suganuma, Y. Miyamoto, M. Shimada, and M. Koizumi, "Solid-State Interfacial Reaction in Molybdenum Carbide Systems at High Temperature-Pressure, and its Application to Bonding Technique", *J. Soc. Mater. Sci. Jpn.* 35, 388 (1986) 35-40.

[33] K. Kurokawa, "Interfacial Reactions of Metals and Alloys with Si-Based Ceramics", *Nippon Kinzoku Gakkai Kaiho* 29, 11 (1990) 931-938.

[34] K.K. Schulze, H.A. Jehn and G. Horz, "High-Temperature Interactions of Refractory Metals with Gases", *J. Met.* 40, 10 (1988) 25-31.

[35] J.C. Schuster, "Silicon Nitride-Metal Joints: Phase Equilibria in the Systems Si_3N_4-Cr, Mo, W and Re", *J. Mater. Sci.* 23, 8 (1988) 2792-2796.

[36] E. Heikinheimo, A. Kodentsov, J.A. Beek, J.T. Klomp and F.J.J. Loo, "Reactions in the Systems Mo-Si_3N_4 and Ni-Si_3N_4", *Acta Metall. Mater.* 40, (1992) S111-S119.

[37] J. Kouvetakis and L. Brewer, "Temperature Stability Range of the Binary MoC Phase", *J. Phase Equilib.* 13, 6 (1992) 601-604.

[38] L.E. Toth, *"Transition Metal Carbides and Nitrides"*, Academic Press, New York, USA, (1971).

[39] C.S. Barrett and T.B. Massalski, *"Structure of Metals"*, McGraw Hill, New York, USA, (1966).

[40] A.L. Ivanovski, D.L. Novikov and V.A. Gubanov, "Electronic Properties of Carbides, Nitrides, and Oxides of Subgroup VIa Transition Metals", *Phys. Status Solidi* 141B, 1 (1987) 9-33.

[41] M. Hansen, *"Constitution of Binary Alloys"*, McGraw Hill, New York, USA, (1958).

[42] A.K. Vasdevan and J.J. Petrovic, "A Comparative Overview of Molybdenum Disilicide Composites", *Mater. Sci. Eng.* 155A, 2 (1992) 1-17.

[43] E. Parthe, W. Jeitschko and V. Sadagopan, "A Neutron Diffraction Study of the Nowotny Phase $Mo_{\leq 5}Si_3C_{\leq 1}$", *Acta Crystallogr.* 19, (1965) 1031-1037.

[44] J.T. Klomp and G. With, "Strong Metal-Ceramic Joints", *Mater. Manuf. Processes* 8, 2 (1993) 129-157.

[45] J. Dundurs, "Edge Bonded Dissimilar Orthogonal Elastic Wedges under Normal and Shear Loading", *J. Appl. Mech.* 36, (1969) 650-652.

[46] C. Woeltjen, C.F. Shih and S. Suresh, "Cyclic Near Tip Fields for Fatigue Cracks along Metal-Metal and Metal-Ceramic Interfaces", *Acta Metall. Mater.* 41, 8 (1993) 2317-2335.

[47] J.D. Cawley, *in "Metal-Ceramic Joining"*, TMS, Chicago, USA, (1991), 3-22.

[48] Y.C. Kim, T. Yamamoto and T.H. North, "Generation and Reduction of Residual Stresses in Ceramic-Metal Joints", *Trans. JWRI* 21, 2 (1992) 285-291.

[49] G.E. Bacon, *"Neutron Diffraction"*, Clarendom Press, Oxford, UK, (1975).

[50] W.T. Thompson, A.D. Pelton and C.W. Bale, *"F*A*C*T - Guide to Operations"*, École Polytechnique, Montreal, (1985).

[51] *"Supplier's Data"*, Carborundum Co., Niagara Falls, NY, USA, (1990).

[52] J.R. McDermid, *"A Thermodynamic Approach to the Brazing of Silicon Carbide"*, Ph.D. Thesis, McGill University, Montreal, Canada, (1991).

[53] *"Supplier's Data"*, Ceradyne Inc., Costa Mesa, CA, USA, (1994).

[54] *"Supplier's Data"*, Johnson & Matthey, Toronto, Canada, (1992).

[55] B.D. Cullity, *"Elements of X-Ray Diffraction"*, Addison-Wesley, Reading, USA, (1978).

[56] *"Supplier's Data"*, Speer Canada Inc., Montreal, Canada, (1993).

[57] B. Powell, *Private Communication*, Neutron and Condensed Science Division, AECL, Chalk River, (1994).

[58] R. Rogge, *Private Communication*, Neutron and Condensed Science Division, AECL, Chalk River, (1994).

[59] R. Berriche, "Evaluation of Advanced Aerospace Materials by Depth Sensing Indentation and Scratch Methods", *Can. Aeronautics Space J.* 40, 4 (1994), 163-170.

[60] R. Berriche, "Vickers Hardness from Plastic Energy", *Scr. Metall. Mater.* 32, 4 (1995) 617-620.

[61] J.L. Loubet, J.M. Georges and G. Meille, *in "Microindentation Techniques in Materials Science and Engineering"*, ASM International, Materials Park, (1979), 771.

[62] J. Emsley, *"The Key to the Elements"*, Clarendom Press, Oxford, UK, (1991).

[63] G.V. Samsonov and A.P. Epik, *"Coatings of High-Temperature Materials"*, Plenum Press, New York, USA, (1966).

[64] A.E. Martinelli and R.A.L. Drew, "Microstructural Development during Diffusion Bonding of α-Silicon Carbide to Molybdenum", *Mater. Sci. Eng.* 191A, (1995) 239-247.

[65] B.T.J. Stoop and G. Ouden, "Diffusion Bonding of Silicon Nitride to Austenitic Stainless Steel without Interlayers", *Metall. Trans.* 24A, (1995) 1835.

[66] G.V. Samsonov and I.M. Vinitskii, *"Handbook of Refractory Compounds"*, Plenum Press, New York, USA, (1980).

[67] A.E. Martinelli, R. Berriche and R.A.L. Drew, "Correlation between the Strength of SiC-Mo Diffusion Couples and the Mechanical Properties of the Interfacial Reaction Products", *J. Mater. Sci. Lett.*, in press.

[68] *"Metals Handbook V.2, 9th. Edition"*, ASM International, Materials Park, USA, (1990), 771-776.

[69] C.A. Brookes, *in "The Science of Hard Materials"*, Plenum Press, New York, USA, (1983), 181.

[70] E. Lugscheider and W. Tillmann, "Methods for Brazing Ceramic and Metal-Ceramic Joints", *Mater. Manuf. Processes* 8, 2 (1993) 219-238.

[71] *"Binary Alloy Phase Diagrams, 2nd. Edition"*, ASM International, Materials Park, USA, (1990).

[72] A.M. Hadian, *"Joining of Silicon Nitride-to-Silicon Nitride and to Molybdenum for High-Temperature Applications"*, Ph.D. Thesis, McGill University, Montreal, Canada, (1993).

[73] H.E. Helms, P.W. Heitman, L.C. Lindgren and S.R. Thrasher, *"Ceramic Applications in Turbine Engines"*, Noyes Pub., Park Ridge, USA, (1986).

[74] N.S. Jacobson, "Corrosion of Si-Based Ceramics in Combustion Environments", *J. Am. Ceram. Soc.* 76, 11 (1993) 3-28.

[75] K. Upadhya, *in "Processing, Fabrication, and Applications of Advanced Composites"*, ASM International, Materials Park, USA, (1993), 1-9.

[76] H.G. Nelson, *in "Processing, Fabrication, and Applications of Advanced Composites"*, ASM International, Materials Park, USA, (1993), 11-20.

[77] A. Brooks and A.I. Bellin, "Benefits of Ceramics to Gas Turbines", *Proc. AGARD Conf. 276*, (1980), 1.1-1.25.

[78] L. Gavoret, *"Processing of SiC Whisker Reinforced Reaction Bonded Silicon Nitride Composites"*, M.Eng. Thesis, McGill University, Montreal, Canada, (1992).

[79] R.A.L. Drew, "Silicon Nitride and Sialon Ceramics - A Review", *Can. Metall. Q.* 27, 1 (1988) 59-64.

[80] G. Ziegler, "Thermo-Mechanical Properties of Silicon Nitride and their Dependence on Microstructure", *Mater. Sci. Forum* 47, (1989) 162-203.

[81] G. Ziegler, J. Heinrich and G. Wotting, "Relationships between Processing, Microstructure and Properties of Dense and Reaction-Bonded Silicon Nitride, *J. Mater. Sci.* 22, 9 (1987) 3041-3086.

[82] N.L. Hecht, D.E. McCullum and G.A. Graves, "Investigation of Selected Silicon Nitride and Silicon Carbide Ceramics", *Ceram. Eng. Sci. Proc.* 9, 9-10 (1988) 1313-1332.

[83] J. Weiss and W.A. Kaysser, *in "Progress in Nitrogen Ceramics"*, M. Nijhoff Pub., Boston, USA, (1983), 169-187.

[84] R.N. Katz and E.M. Lenoe, "Ceramics for Small Airborne Engine Applications", *Proc. AGARD Conf. 276*, (1980), 2.1-2.13.

APPENDIX I:

PROPERTIES OF SiC, Si_3N_4, AND Mo

This chapter reviews the main physical and mechanical properties of SiC and Si_3N_4. Emphasis is given to the high-temperature behaviour and oxidation mechanisms of these materials. Lastly, the properties of the metal Mo are also addressed.

AI.1 SILICON CARBIDE

AI.1.1 GENERAL ASPECTS

SiC is a highly covalent ceramic with three possible crystallographic symmetries:

cubic, hexagonal and rhombic [4]. Several SiC polytypes have been identified so far. The simplest one has a cubic diamond-like structure in which alternate carbon (C) atoms are replaced by silicon (Si). This structure is referred to as β-SiC. All other structures show either hexagonal or rhombic symmetry and are collectively called α-SiC. Every α-SiC polytype is made up of C atoms arranged in an hexagonal closed-packed (hcp) pattern placed above a second layer of C atoms in another hexagonal pattern as shown in Figure AI.1.

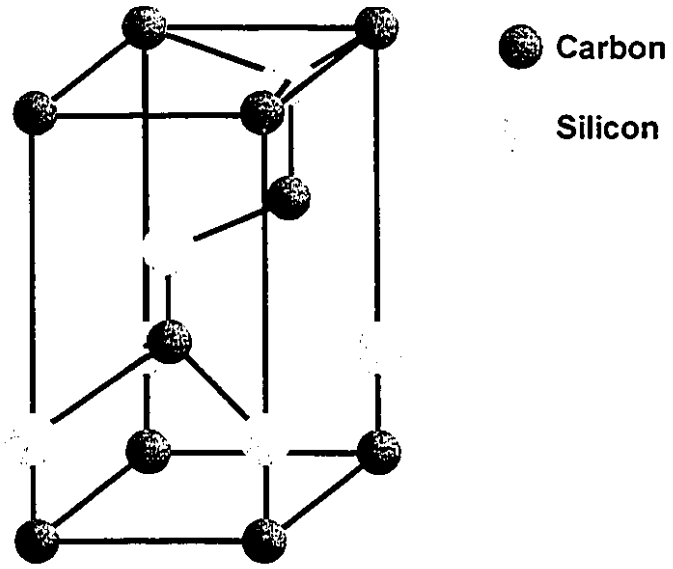

Figure AI.1- Crystal structure of the hexagonal α-SiC polymorph [52].

The Si atoms fit into the tetrahedral interstitial positions of the hcp structure. Every C atom is surrounded tetrahedrally by four Si atoms and every Si atom is also surrounded

tetrahedrally by four C atoms (coordination 4). Differences between the α-polymorphs arise from the different stacking arrangements of C and Si atoms, resulting in different lengths of the c-axis [52]. In this study, the polymorph 6H was used (space group $P6_3mc$). The lattice parameters for this hexagonal variety are: a=3.073 Å and c=15.08 Å.

Although SiC is rarely found naturally, it can be synthetically produced from almost any source of Si and C [1]. The most widely used technique to produce SiC powder is the Acheson process [52]. In this method, SiC is formed from the reaction of high-purity silica (SiO_2) and coke (C) according to

$$SiO_2 + 3\ C = SiC + 2\ CO \qquad \text{(AI.1)}$$

Depending on the time and temperature of the reaction, the resulting SiC is either in the form of a fine powder or as a large chunky mass. After crushing, milling, and separation into specific size fractions, the powder is roasted to oxidize traces of residual C and washed with hydrofluoric acid (HF) to remove SiO_2 to the required purity [4].

Commercial SiC products can be reaction bonded or sintered. In this work, the SiC was sintered by the manufacturer using boron (B) and carbon (C) as additives. Sintering is usually carried out at temperatures between 2000°C and 2200°C, and proceeds via solid-state densification. The presence of C as an additive apparently aids the removal of the SiO_2 layer from the surface of the SiC particles. The use of B is based on its low solid-solubility in SiC, enhancing material transfer between adjacent SiC grains, thus increasing the rate of diffusion and sintering [1]. Sintered SiC is the choice

for structural applications because of its superior mechanical properties and good oxidation resistance. Although SiC decomposes, in vacuum or inert gas, into volatile Si and C (that reverts to graphite) between 2300°C and 2500°C, the mechanical integrity of structural SiC components becomes compromised at around 1650°C, this being accepted as the maximum service temperature for this material [17].

AI.1.2 PROPERTIES OF SINTERED α-SiC

Table AI.1 includes a collection of physical and mechanical properties of sintered α-SiC. Among the most attractive properties, the low CTE of SiC makes it a dimensionally stable material, useful in applications where close tolerances are required. SiC is also chemically stable at high temperatures, and it has been used in the presence of radiation and combustion gases, and in oxidizing atmospheres. For example, SiC has been used as lining material for chemical equipment, as electrical contacts for hostile environments, and as coating of nuclear reactor structures [52,74].

However, one of the main attractions of SiC is its oxidation resistance. In several applications, SiC components are required to work in air at high temperatures, or in the presence of combustion gases and deposit-forming corrodents, such as in heat exchanger tubes for glass remelting, and aluminum reclamation furnaces [74]. SiC is inherently unstable in air and, as a result, whenever the material is exposed to an oxidizing atmosphere, passive oxidation takes place resulting in the formation of a thin superficial layer of SiO_2 according to,

$$SiC_{(s)} + 1.5\ O_{2(g)} = SiO_{2(s)} + CO_{(g)}^{1} \quad \text{(AI.2)}$$

Because SiO_2 has the lowest permeability to oxygen of any of the common oxides, it forms an effective reaction barrier, which gives SiC the potential of substantially better high-temperature oxidation behaviour than metals.

Table AI.1- Properties of Sintered α-SiC [4,52,73]

Physical Properties	
Molecular Weight	40.07 g/mol
Decomposition Temperature	2300 - 2500°C
Density	3.21 g/cm^3
CTE	4.4 - 4.8x10^{-6}°C^{-1} (20°C - 1000°C)
Maximum Service Temperature	1650°C
Electrical Resistivity	10^2 - 10^6 Ω.cm
Thermal Conductivity	126 W/m.K at Room Temperature (RT) 78 W/m.K at 400°C
Oxidation at 1450°C	0.01 - 0.25 wt. gain% / 1000 h
Mechanical Properties	
Elastic Modulus	395 - 420 GPa at RT
Modulus of Rupture	300 - 400 MPa (RT to 1500°C)
Vickers Microhardness	26.00 - 28.00 GPa
Poisson's Ratio	0.14
Fracture Toughness	4.60 MPa$\sqrt{m}$
Compressive Strength	4600 MPa

[1] Further oxidation may take place transforming $CO_{(g)}$ into $CO_{2(g)}$.

The upper temperature limit of the chemical stability of SiC is related to the melting point of SiO_2 (1700°C). When the protective SiO_2 layer melts, it begins to flow and rapid transport rates are attained in non-protective environments. Figure AI.2 illustrates the presence of the SiO_2 layer on the surface of SiC.

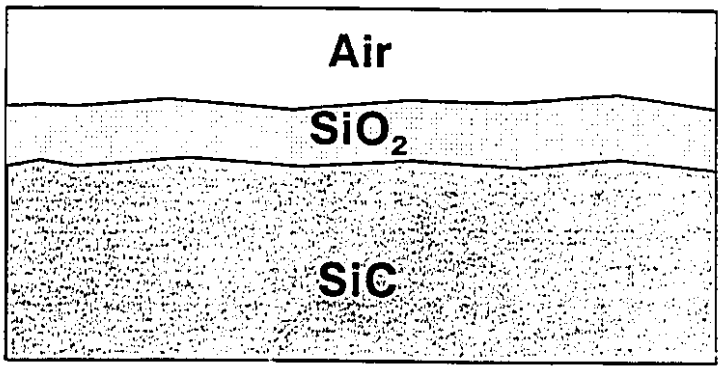

Figure AI.2- Schematic of protective SiO_2 layer on SiC [74].

Passive oxidation occurs only if a minimum partial pressure of oxygen is achieved (Figure AI.3). However, most combustion processes involve large concentrations of the oxidant (molecular oxygen, carbon dioxide, and water), generally resulting in passive oxidation. Nevertheless, in a few cases, such as coal combustion, the partial pressure of oxygen may fall below that needed for a stable SiO_2 film to form. In that case, active oxidation takes place which causes degradation of the ceramic, according to

$$SiC_{(s)} + O_2 = SiO_{(g)} + CO_{(g)} \qquad \text{(AI.3)}$$

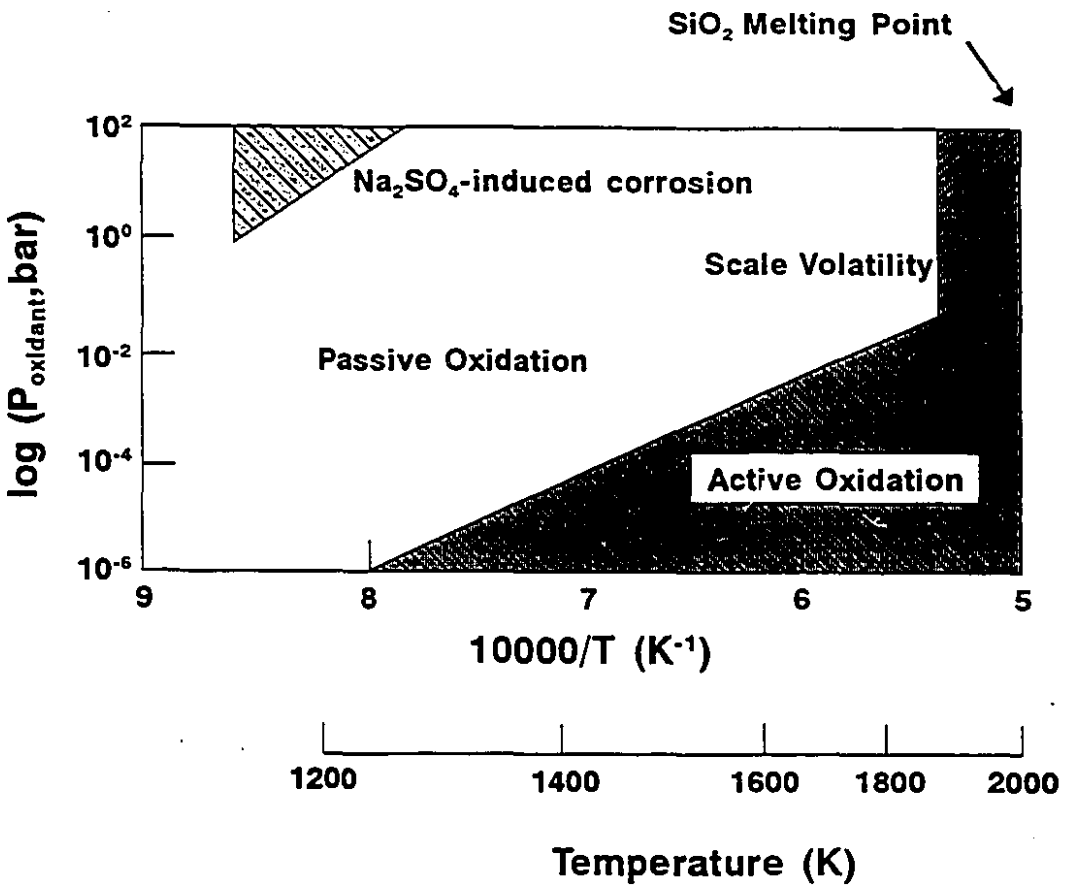

Figure AI.3- Main routes of corrosive attack and degradation of SiC [74].

Degradation of SiC can also be caused by the formation of corrosive deposits. The most common deposit encountered in engines, for example, is sodium sulphate (Na_2SO_4). Deposits of Na_2SO_4 form when Na reacts with S, usually present as a fuel impurity. The Na may also be present as a fuel impurity, or, most commonly, it can originate from a marine environment or from a salted roadway. Na_2SO_4 is corrosive

between its melting point (884°C) and its dewpoint for deposition, which varies according to the combustion conditions. However, as indicated in Figure AI.3, the temperature region for Na_2SO_4 corrosion is very limited. With the use of SiC components, engines can easily operate at high-temperatures, exceeding the dewpoint of Na_2SO_4 and preventing its deposition.

Another important aspect of SiC is its low density combined with superior mechanical properties at high temperatures. SiC is becoming an increasingly important structural ceramic, especially for the aerospace and automotive industry. For example, sintered α-SiC has been evaluated by General Motors for the production of hot sectional structural components of land-vehicle gas-turbines and piston engines. The material revealed excellent oxidation resistance at temperatures in excess of 1200°C, without degradation of its modulus of rupture (335 MPa, at room temperature). Specimens oxidized for 500 hours at 1250°C were tested at 1150°C and showed an average modulus of rupture of 318 MPa [73]. The low density of SiC also contributes to a high strength-to-weight ratio at high temperatures, which improves engine performance. Although other structural materials have higher specific strength than SiC at low temperatures, SiC outmatches the metallic alloys and intermetallics as the temperature approaches 1000°C (Figure AI.4). In that region, only carbon-carbon and SiC-C composites have a higher specific strength than sintered SiC, however these materials have severe limitations concerning their oxidation resistance [75,76].

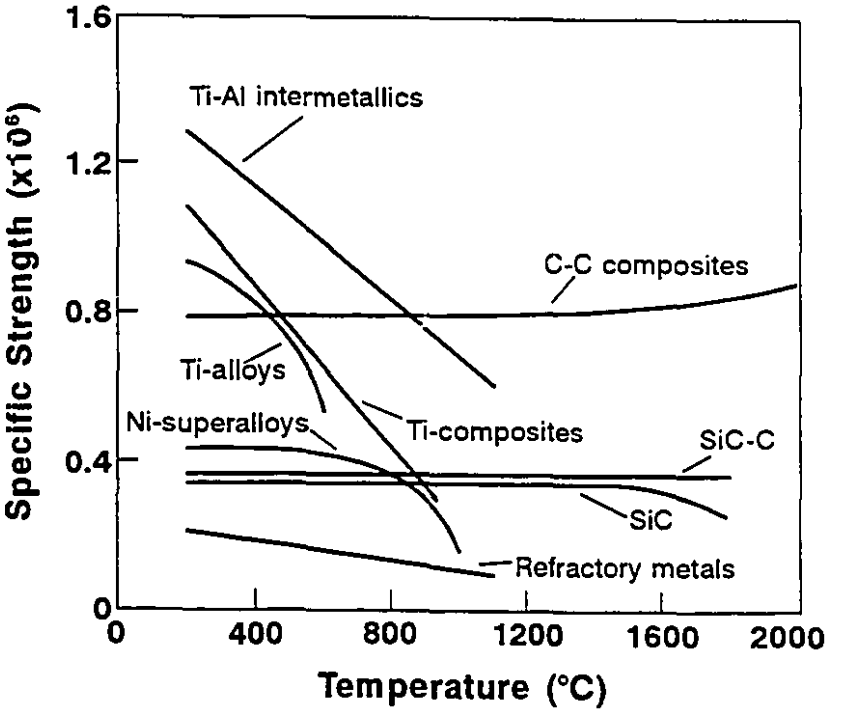

Figure AI.4- Strength-to-weight ratio of structural materials as a function of the temperature [75,76].

Finally, SiC has a low steady-state creep rate as compared to structural superalloys and other ceramics (Figure AI.5). This property contributes to the mechanical resistance of the material at high temperatures and increases the potential engine operating temperatures by as much as 500°C [77].

The reason for the low creep rate of SiC, as compared to superalloys, is that metals and ceramics have different creep mechanisms. In metals, creep is controlled by the movement of dislocations, which increases significantly at high temperatures. In

polycrystalline ceramics, creep is controlled by the rate of grain boundary sliding, which is determined by the nature of the intergranular phases. If a ceramic is sintered with additives, such as Si_3N_4 sintered with MgO, Y_2O_3, or Al_2O_3, its creep behaviour may be significantly degraded. Additives usually form intergranular glassy phases which soften at relatively low temperatures, allowing sliding to occur along grain boundaries at temperatures well below the temperature at which the matrix material would creep. On the other hand, α-SiC can be sintered at temperatures in excess of 1800°C with low levels of additives, which results in extremely low creep rates [1].

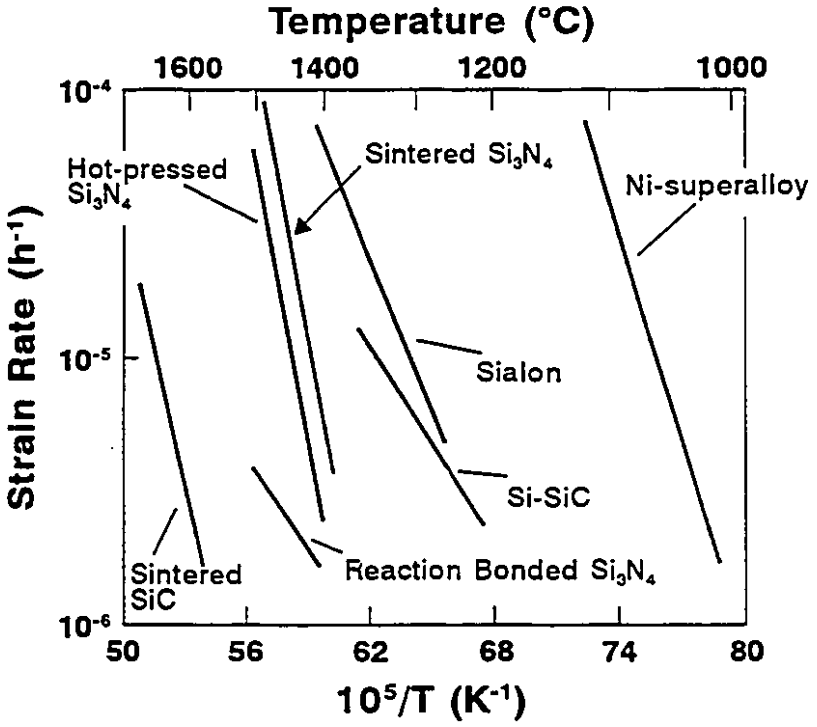

Figure AI.5- Creep behaviour of structural materials at high temperatures [77].

The importance of incorporating SiC components into engineering devices has already been recognized by numerous manufacturers. Efforts have been made to overcome the inherent difficulties of handling ceramics, such as their brittle behaviour and failure mode, by tailoring the microstructure of the materials to optimize performance. Moreover, new joining techniques have also been developed in order to attach ceramic components to metallic elements, thus creating mechanically sound hybrid structures.

AI.2 SILICON NITRIDE

AI.2.1 GENERAL ASPECTS

Si_3N_4 crystallizes in two hexagonal forms, designated α and β. Both phases have similar hexagonal crystal structures but different cell dimensions, especially in the c direction. For the α-phase, $a=b=7.753$ Å and $c=5.623$ Å. For the β-phase, $a=b=7.603$ Å and $c=2.906$ Å. The crystallographic densities of the α and β phases are 3.185 and 3.196 g/cm^3, respectively [78]. The α and β-Si_3N_4 structures are built of SiN_4 tetrahedra in which the four nitrogen (N) atoms are arranged around a central silicon (Si) atom [79]. Because the nitrogen atoms are shared at the corner of each tetrahedron, a three dimensional network is produced [78]. The β-Si_3N_4 polymorph was employed throughout this study, and Figure AI.6 shows a schematic of this structure.

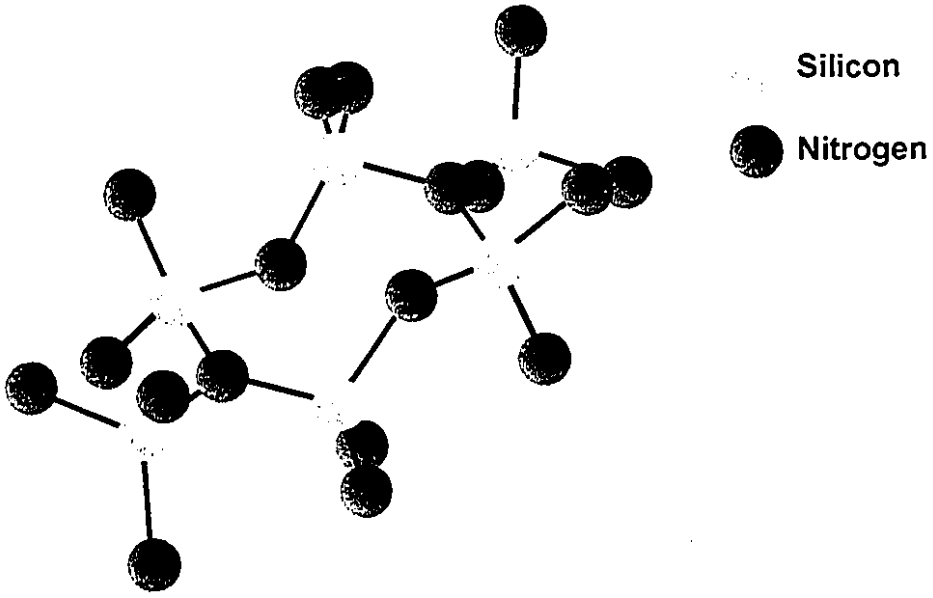

Figure AI.6- Crystal structure of β-Si_3N_4 [78].

The SiN_4 tetrahedra of the β-Si_3N_4 structure are linked together forming rings which surround large voids. In the α-phase, the bond lengths and angles are less uniform compared to the β-phase, and the N atoms are slightly drawn in towards the centre of structural voids [80]. The structure of the β-phase layers alternates in the sequence AB, forming hexagonal tunnels in the *c* direction. In the α-structure, the layers alternate with mirror inverted layers in the sequence ABCD, resulting in a lattice parameter, *c*, which is about twice as large as for the β-phase. The hexagonal tunnels are not present in the α-phase [81]. The α-phase is considered a defect structure where one N atom in 30 is replaced by an oxygen (O) atom, whereas β-Si_3N_4 is the stoichiometric form [79].

Si_3N_4 does not occur naturally. It is, instead, produced synthetically by combining

Si and N_2 using various processes. Two types of Si_3N_4 are commonly used: porous reaction-bonded Si_3N_4 (RBSN) and dense sintered Si_3N_4, which differ in both density and microstructure, resulting in different mechanical properties [81]. RBSN is formed by the reaction of elemental Si with N_2 gas. Nitridation of the starting Si powder compact occurs at temperatures between 1250°C and 1450°C. The resulting material is a porous Si_3N_4 matrix formed with no sintering additives. The ceramic matrix usually has between 65 and 85% of the theoretical density. These parts are easy to machine and therefore, complex shapes can be made. When the desired shape is achieved, the strength of the material can be increased by post-reaction sintering or by the use of ceramic reinforcements in the form of particles, whiskers or fibres [17].

Dense Si_3N_4 is produced by pressureless or pressure-assisted sintering. Si_3N_4 is difficult to sinter because of its high degree of covalent bonding. For this reason, high sintering temperatures (around 1850°C) are used. In addition, Si_3N_4 has a high vapour pressure at high temperatures which promotes decomposition rather than densification. If Si_3N_4 powder is heated up to 1900°C in 1 atm. of N_2, $N_{2(g)}$ gas will form and disperse, forcing the reaction

$$Si_3N_{4(s)} = 3Si_{(l)} + 2N_{2(g)} \qquad \text{(AI.4)}$$

to proceed to the right. There are two alternatives to resolve this densification problem: sintering under an overpressure of N_2 or application of external pressure to assist densification [1]. In pressureless sintering, Si_3N_4 powder compacts containing sintering additives are densified at high temperatures in N_2. The capillary pressure created by the

presence of an intergranular liquid phase and particle dissolution are the driving forces for diffusion [78]. However, even in N_2, Si_3N_4 will decompose if Si-vapour is not prevented from escaping the system and if, as a result, the equilibrium partial pressure of Si cannot build up. To overcome this difficulty, the ceramic compact can be embedded in a powder with the same composition of the body, *i.e.*, including the same amount of sintering additives [81].

Pressure-assisted sintering can be subdivided into hot-pressing and hot isostatic-pressing. Hot-pressing involves the use of uniaxial pressure at high temperatures to aid densification. Fully dense hot-pressed Si_3N_4 (HPSN) with good mechanical properties are produced by this technique, however, only simple shapes can be designed [78]. Lower sintering temperatures are required due to the application of an external pressure. In hot-isostatic pressing, the pressure is applied by a gas surrounding the sample instead of a mechanical load.

During sintering of Si_3N_4, the formation of the β-phase is the result of a solution-reprecipitation process. Upon nitridation of Si, the reaction between SiO-vapour and N_2 results in the formation of α-Si_3N_4. Sintering at high temperatures causes the α-phase to become unstable with respect to β-Si_3N_4. As the α-phase cannot be transformed into the β-phase by a displacive process, the transformation is reconstructive, occurring by solution-precipitation through a liquid phase [81]. For this reason, oxides are used as sintering additives. At high temperatures, they react with Si_3N_4 and SiO_2 (usually present as a passive oxide layer on the surface of Si_3N_4), promoting the formation of an

intergranular liquid phase where the α-Si_3N_4 particles dissolve and β-Si_3N_4 precipitates [79]. After the first component melts, a rapid densification occurs by a creep process that involves the movement of solid particles closing a large fraction of the voids present in the compact (primary rearrangement). The densification rate due to this rearrangement depends on the mobility of the solid particles and on the kinetics of the solution-reprecipitation process [82]. The melting temperature and the amount of liquid phase depends on the nature and composition of the additives. During the initial stages of sintering, the amount and composition of the melt undergoes a continuous change by the dissolution of Si_3N_4 and residual additives. This changes the viscosity of the liquid silicate which influences the particle movement and densification rate. With increasing sintering temperature, the viscosity of the melt decreases, increasing the shrinkage rate [82].

When primary rearrangement is complete, further densification is controlled by secondary rearrangement. In this stage, the particle geometry changes at the contact regions by flattening or dissolution of small particles and the reprecipitation of large ones [82]. The process is controlled by the slower dissolution-reprecipitation kinetics. The driving force responsible for grain growth is the dissolution of α-Si_3N_4 particles and the reprecipitation of the material as β-Si_3N_4. The growth of the β-grains at the expense of the α-particles include directional grain growth if the β-particles are much smaller than the starting α-particles, or Oswald ripening if the β-particles become much larger than their adjacent α-grains [82]. Upon cooling, the liquid phase transforms into a glassy or

partially crystallized phase arranged in thin layers at the grain boundaries or at triple junctions [79,83]. The presence of this second phase is deleterious to the mechanical properties of the final material (particularly its creep behaviour), and to its oxidation resistance. Therefore, in the production of mechanically reliable Si_3N_4 components, it is important to sinter the material using a minimum amount of additives [17].

The most common additives used to sinter Si_3N_4 are Y_2O_3, Al_2O_3, and MgO. The type and amount of additives determine the onset sintering temperature and the densification rate. The nature of the sintering additives also influence the morphology of the β-grains and the characteristics of the grain-boundary phase, which controls the high temperature properties of the final material [81]. Y_2O_3 promotes considerable shrinkage at temperatures higher than 1600°C. The softening temperature is high and consequently, densification starts at higher temperatures. For this reason, an increased N_2 pressure is required to suppress decomposition of Si_3N_4. The melt is stable but because of the high viscosity of the liquid phase, the densification rate is low [1]. Softening temperature and viscosity can be adjusted by adding a second oxide, such as Al_2O_3. A mixture of Y_2O_3 and Al_2O_3 results in a decrease of the softening temperature and viscosity as compared to pure Y_2O_3, but also in a reduction of the thermal stability of the liquid phase. Consequently, the densification rate and total shrinkage increase but the final mechanical properties of the material are somewhat compromised [1]. The sintering mechanism of Si_3N_4 and the precipitation of the β-phase is illustrated in Figure AI.7.

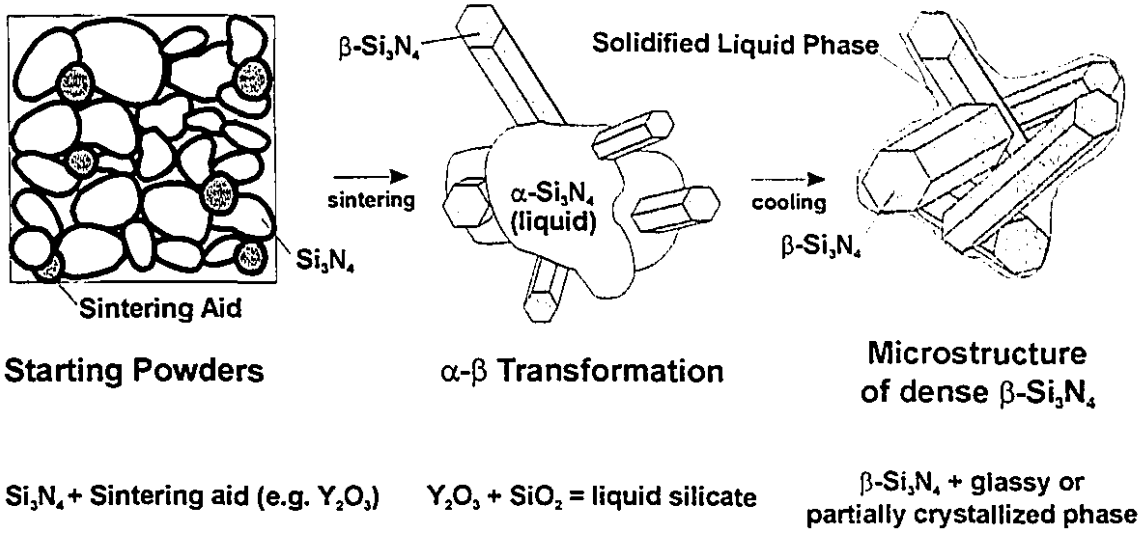

Figure AI.7- Sintering mechanism of Si_3N_4 [81].

AI.2.2 PROPERTIES OF SINTERED Si_3N_4

Table AI.2 shows a collection of physical and mechanical properties of sintered Si_3N_4 materials. Similarly to SiC, Si_3N_4 has a low coefficient of thermal expansion, which implies in good dimensional stability at high temperatures and, consequently, close tolerances can be achieved. In addition, Si_3N_4 has high toughness, which combined with its low expansion characteristics, makes it an excellent material for the production of bearings and cutting tools. On the other hand, the hardness of Si_3N_4 is lower than that of SiC, which makes the latter a better choice for the manufacture of grinding wheels and abrasives [1].

Table AI.2- Properties of Sintered Si_3N_4 [1,4,72]

Physical Properties	
Molecular Weight	140.28 g/mol
Density	3.19 g/cm^3
CTE	3.0 - 3.5x10^{-6}°C^{-1} (20°C - 1000°C)
Electrical Resistivity	$>10^{14}$ Ω.cm
Thermal Conductivity	15 - 45 W/m.K at RT 5 - 20 W/m.K at 1000°C
Mechanical Properties	
Elastic Modulus	260 - 320 GPa at RT
Modulus of Rupture	600 - 1200 MPa at RT 340 - 550 MPa at 1350°C
Vickers Microhardness	13 - 17 GPa
Poisson's Ratio	0.28
Fracture Toughness	5.0 - 8.5 MPa$\sqrt{m}$

Si_3N_4 is an attractive structural material for high-temperature applications, and where corrosion and oxidation resistance are required. Similarly to SiC, Si_3N_4 also undergoes passive oxidation, which results in the formation of a protective SiO_2 layer on its surface. In the case of Si_3N_4, an oxynitride (Si_2N_2O) layer is also formed under the SiO_2 layer, as shown in Figure AI.8 [74]. The reactions that control the passive oxidation of Si_3N_4 are expressed by,

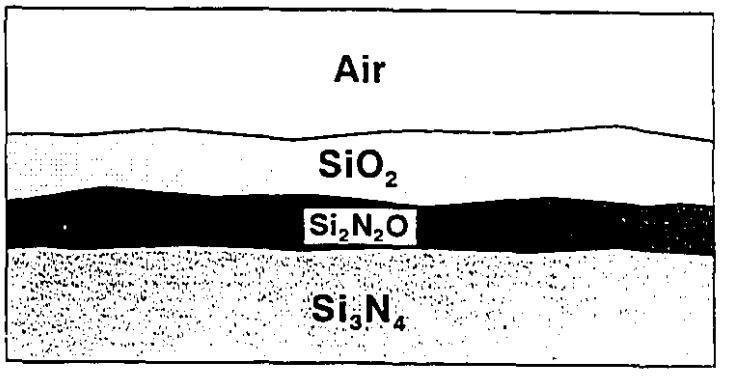

Figure AI.8- Protective oxide layer on Si_3N_4 surface [74].

$$Si_3N_{4(s)} + 0.75\ O_{2(g)} = 1.5\ Si_2N_2O_{(s)} + 0.5\ N_{2(g)} \quad \text{(AI.5)}$$

$$Si_2N_2O_{(s)} + 1.5\ O_{2(g)} = 2\ SiO_{2(s)} + N_{2(g)}^{1} \quad \text{(AI.6)}$$

As for the case of SiC, the chemical stability of Si_3N_4 is also limited by the melting point of SiO_2, and the main chemical attack routes, as illustrated in Figure AI.3, also take place. If the oxygen potential falls below that needed to establish a stable SiO_2 layer, active oxidation of Si_3N_4 occurs following

$$Si_3N_{4(s)} + 1.5\ O_2 = 3\ SiO_{(g)} + 2\ N_{2(g)} \quad \text{(AI.7)}$$

however, as stated earlier, conventional applications seldom lead to this situation.

The use of Si_3N_4 improves the high-temperature oxidation and corrosion resistance of engineering devices. Figure AI.9 shows a plot of the weight gain per unit area for structural superalloys and Si_3N_4 materials, at 1400°C in air. It can be seen that Si_3N_4 has

[1] $NO_{(g)}$ may also been produced in addition to $N_{2(g)}$.

demonstrated an improvement of three to four orders of magnitude in the oxidation resistance as compared to the superalloys. In fact, sintered Si_3N_4 has even shown better oxidation behaviour than SiC at that temperature [77].

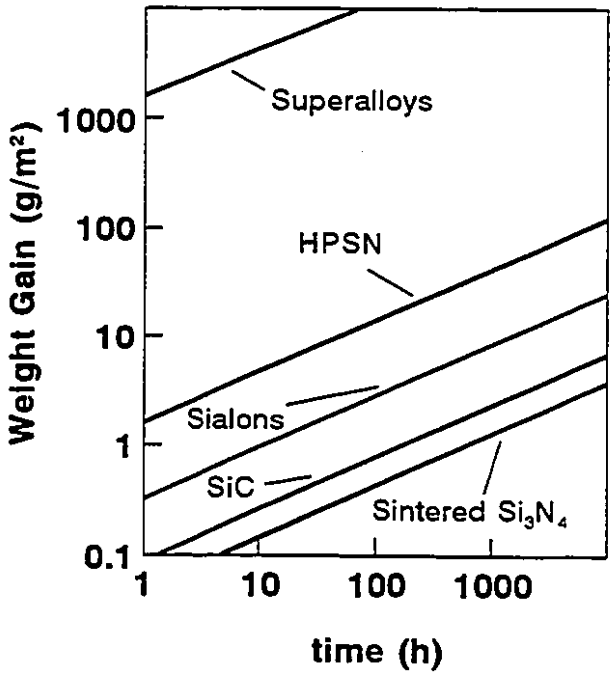

Figure AI.9- Weight gain per unit area of Si_3N_4 and high-temperature structural superalloys at 1400°C in air [77].

Corrosion resistance is another area where Si_3N_4 has better properties than conventional superalloys. Figure AI.10 shows a comparison between sintered and hot-pressed Si_3N_4 with a Ni-based superalloy. It can be seen that the sintered Si_3N_4 has better properties than the bare alloy, although coating the same alloy improved its corrosion behaviour, exceeding the capabilities of the sintered Si_3N_4. However, the

corrosion behaviour of hot-pressed Si_3N_4 (HPSN) was still better than that of the coated alloy. In addition, coatings may erode and lose their integrity with time, degrading the properties of the metallic component [77].

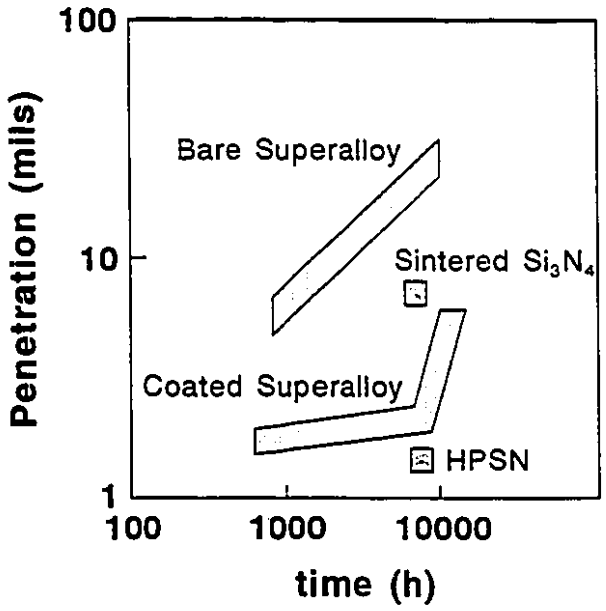

Figure AI.10- Hot-corrosion of Si_3N_4 and Ni-based superalloy [77].

In addition to superior oxidation and corrosion resistance, Si_3N_4 has also excellent mechanical properties at high temperatures. On the other hand, Si_3N_4 is also a brittle material and it requires a precise definition of the stress map throughout a component. However, engineers have improved their skills in producing ceramic parts avoiding notches and other sources of highly localized stress gradients [84]. In fact, the overall number of Si_3N_4 components in naturally aspirated, turbine, and diesel engines has increased in the past few years. Si_3N_4 has demonstrated better high-temperature

properties than conventional superalloys, and acceptable strength values for practical applications as demonstrated by Figure AI.11 for the case of turbine components [77].

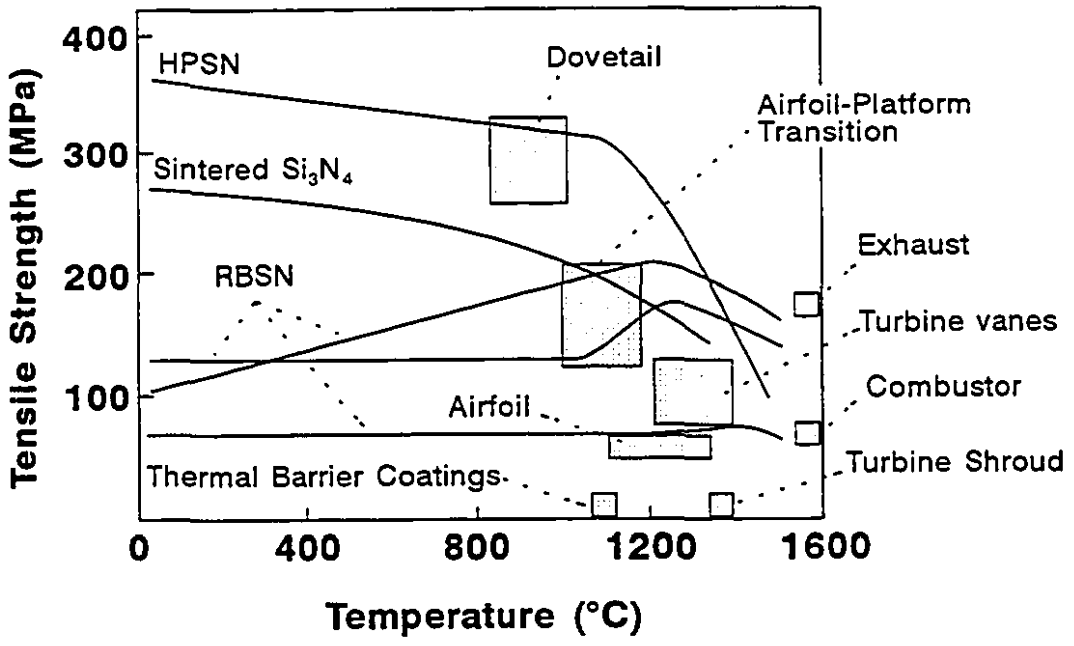

Figure AI.11- High-temperature strength of Si_3N_4 materials plotted along with the required strength for turbine engine components [77].

Si_3N_4 also has a low creep rate at high temperatures compared to structural superalloys. However, in this particular aspect, sintered SiC outmatches Si_3N_4. SiC can be sintered with lower amounts of additives than Si_3N_4 resulting in significantly less grain boundary sliding. For the case of Si_3N_4, as discussed earlier, sintering additives such as MgO, Y_2O_3, and Al_2O_3, frequently result in the formation of intergranular glassy phases

which degrades the creep resistance of the material. Nevertheless, alternative processing routes, such as reaction bonding, allow Si_3N_4 to be sintered without additives, significantly reducing the propensity for grain-boundary sliding, and consequently improving the high-temperature creep resistance of the material (Figure AI.5) [1,77].

In summary, the use of Si_3N_4 as a structural material is already a reality. Nevertheless, research in processing techniques and joining of this material is still quite extensive, which will contribute to a further increase in the number of Si_3N_4 components integrated to engineering devices, resulting in better overall performance.

AI.3 MOLYBDENUM

Molybdenum is a transition metal from the VI-A series (Z = 42). Its coordination number is eight and valences from +2 to +6 have been observed. The crystal structure of Mo is cubic (bcc) with two atoms per cell, with no known allotropic transformations. Because of its high melting point, Mo is often produced by a powder metallurgy process. Pure Mo is obtained converting molybdenite (MoS_2) to molybdenum trioxide (MoO_3), which is subsequently reduced to Mo by hydrogen. The powder is compacted and sintered in hydrogen or vacuum at temperatures around 1100°C [14].

As a consequence of its strong interatomic cohesion, Mo is considered a refractory metal, and it possesses high strength at ambient and elevated temperatures, and relatively small CTE compared to other metals. Mo is used in the fabrication of electrical and electronic parts, and missile and aircraft components. Because of its small cross

section for thermal neutrons, Mo is also a suitable material for nuclear reactor applications. Elsewhere, Mo is used in hostile environments due to its resistance to attack by most types of molten glass and acids [12]. Although Mo shows high strength at high temperatures, it undergoes a ductile to brittle transition as the temperature is lowered. Under certain conditions of purity, fabrication methods, and stress patterns, the transition in unalloyed Mo may take place even at room temperature. For this reason, the room temperature properties of Mo are very sensitive to mechanical and thermal history [14].

At elevated temperatures, unprotected Mo oxidizes rapidly in air or oxidizing atmospheres at ordinary pressures that its continued use under such conditions is impractical. The final product of the oxidation reaction is not a self-protective oxide. The oxidation of Mo is a two-step process which results in the formation of molybdenum dioxide (MoO_2) as the internal layer and MoO_3 as the outer layer. Below 500°C, a parabolic oxidation law is followed indicating some degree of self-protection. Above 500°C, MoO_3 begins to volatilize and at 770°C it evaporates at the same rate as it forms, offering no protection to the base metal [14]. To overcome this difficulty, Mo can be coated with oxidation-resistant Mo-silicides, such as $MoSi_2$. Alternatively, when Mo is used in combination with SiC or Si_3N_4, as an interlayer between the ceramic and a metal-alloy, the ceramic can also function as a protective coating to the metal, depending on the joint design. A summary of the properties for Mo is presented in Table AI.3 and Figure AI.12.

Table AI.3- Properties of Molybdenum [12,14]

Physical Properties	
Molecular Weight	95.94 g/mol
Melting Point	2617°C
Density	10.2 g/cm^3
CTE	7.2×10^{-6}°C^{-1} (20°C - 2000°C)
Thermal Conductivity	80 - 140 W/m.K at RT
Mechanical Properties	
Elastic Modulus	330 GPa at RT
Vickers Microhardness	2.50 GPa
Poisson's Ratio	0.293
Compressive Yield Strength	Figure 2.12
Tensile Strength	830 MPa at RT

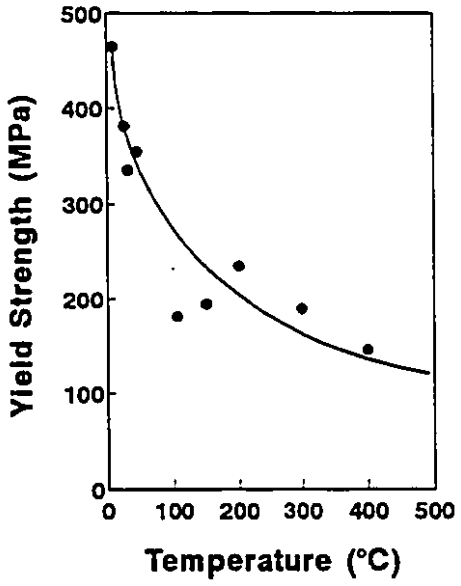

Figure AI.12- Compressive yield strength of unalloyed Mo as a function of the temperature [68].

APPENDIX II:

MASS ABSORPTION COEFFICIENTS OF Mo-Si-C COMPOUNDS

In order to estimate the depth of penetration of X-rays in the SiC-Mo reaction products present within the interfaces, it was necessary to determine the mass absorption coefficient, μ, for each of these compounds. These values were then used in equation (7.8) to obtain the parameter G_x.

For an element, μ is calculated multiplying tabulated values of (μ/ρ) by the density of the material, ρ [55]. For a compound, μ is given by

$$\frac{\mu}{\rho} = w_1(\frac{\mu}{\rho})_1 + w_2(\frac{\mu}{\rho})_2 + \ldots \qquad \text{(AII.1)}$$

where w_i is the weight fraction of element *i* in the compound, and $(\mu/\rho)_i$ is the tabulated mass absorption coefficient of element *i* for the wavelength of CuKα radiation (λ = 1.54 Å).

Using equation (AII.1), and the mass absorption coefficients of Mo, Si, and C (158.3 cm^2/g, 65.32 cm^2/g, and 4.219 cm^2/g, respectively [55]), The values of μ for Mo_5Si_3C, Mo_5Si_3, and Mo_2C, were calculated as follows:

a. Mo_5Si_3C:

Molecular weight- 575.97 g/mol.

Density- 7.86 g/cm^3 (Table 3.5)

weight fraction of Mo- 0.833 wt.%

weight fraction of Si- 0.146 wt.%

weight fraction of C - 0.021 wt.%

Hence,

$$(\frac{\mu}{\rho})_{Mo_5Si_3C} = w_{Mo}(\frac{\mu}{\rho})_{Mo} + w_{Si}(\frac{\mu}{\rho})_{Si} + w_C(\frac{\mu}{\rho})_C$$

$$(\frac{\mu}{\rho})_{Mo_5Si_3C} = 0.833(158.3) + 0.146(65.32) + 0.021(4.219) = 141.48\ cm^2/g$$

$$(\mu)_{Mo_5Si_3C} = (\frac{\mu}{\rho})_{Mo_5Si_3C} \cdot (\rho)_{Mo_5Si_3C} = (141.48) \cdot (7.86) = 1112.03\ cm^{-1} \qquad \text{(AII.2)}$$

b. Mo_5Si_3:

Molecular weight- 563.96 g/mol.

Density- 8.24 g/cm^3 (Table 3.5)

weight fraction of Mo- 0.851 wt.%

weight fraction of Si- 0.149 wt.%

Hence,

$$\left(\frac{\mu}{\rho}\right)_{Mo_5Si_3} = W_{Mo}\left(\frac{\mu}{\rho}\right)_{Mo} + W_{Si}\left(\frac{\mu}{\rho}\right)_{Si}$$

$$\left(\frac{\mu}{\rho}\right)_{Mo_5Si_3} = 0.851(158.3)+0.149(65.32) = 144.45\ cm^2/g$$

$$(\mu)_{Mo_5Si_3} = \left(\frac{\mu}{\rho}\right)_{Mo_5Si_3} \cdot (\rho)_{Mo_5Si_3} = (144.45) \cdot (8.24) = 1190.27\ cm^{-1} \qquad \text{(AII.3)}$$

c. Mo_2C:

Molecular weight- 203.89 g/mol.

Density- 9.06 g/cm^3 (Table 3.4)

weight fraction of Mo- 0.941 wt.%

weight fraction of C- 0.059 wt.%

Hence,

$$\left(\frac{\mu}{\rho}\right)_{Mo_2C} = W_{Mo}\left(\frac{\mu}{\rho}\right)_{Mo} + W_{C}\left(\frac{\mu}{\rho}\right)_{C}$$

$$\left(\frac{\mu}{\rho}\right)_{Mo_2C} = 0.941(158.3)+0.059(4.22) = 149.21\ cm^2/g$$

$$(\mu)_{Mo_2C} = \left(\frac{\mu}{\rho}\right)_{Mo_2C} \cdot (\rho)_{Mo_2C} = (149.21) \cdot (9.06) = 1351.84\ cm^{-1} \qquad \text{(AII.4)}$$